Effective theory of the yielding transition in amorphous solids

Saverio Rossi

▶ **To cite this version:**

Saverio Rossi. Effective theory of the yielding transition in amorphous solids. Statistical Mechanics [cond-mat.stat-mech]. Sorbonne Université, 2023. English. NNT : 2023SORUS250 . tel-04241288

HAL Id: tel-04241288
https://theses.hal.science/tel-04241288

Submitted on 13 Oct 2023

HAL is a multi-disciplinary open access archive for the deposit and dissemination of scientific research documents, whether they are published or not. The documents may come from teaching and research institutions in France or abroad, or from public or private research centers.

L'archive ouverte pluridisciplinaire **HAL**, est destinée au dépôt et à la diffusion de documents scientifiques de niveau recherche, publiés ou non, émanant des établissements d'enseignement et de recherche français ou étrangers, des laboratoires publics ou privés.

SORBONNE UNIVERSITÉ

THÈSE DE DOCTORAT
DE SORBONNE UNIVERSITÉ

Spécialité : Physique

École Doctorale n°564: Physique en Île-de-France

réalisée

au Laboratoire de Physique Théorique de la Matière Condensée

présentée par

Saverio ROSSI

Sujet de la thèse:

Effective theory of the yielding transition in amorphous solids

Théorie effective de la transition yielding dans les solides amorphes

Soutenue le 10 juillet 2023

Devant le jury composé de

M.	Jean-Louis BARRAT	Rapporteur
M.	Itamar PROCACCIA	Rapporteur
M^{me}	Elisabeth AGORITSAS	Examinatrice
M.	Damien VANDEMBROUCQ	Président de jury
M.	Gilles TARJUS	Directeur de Thèse
M.	Giulio BIROLI	Invité

Acknowledgments

I am indebted to many individuals who have provided their help and support during the last years. I would like to start by thanking my supervisor, Gilles, who patiently answered the same questions many times with unwavering calm and patience. His precious guidance helped me navigate the complexities of the field and broaden my perspectives. I am also grateful to our collaborators, Giulio and Francesco, who consistently made themselves available for discussions and provided insightful suggestions. Special thanks are owed to Misaki, who generously shared his time and computer skills with me. I have no doubt that he will become an exceptional supervisor in the near future. My gratitude goes to Jean-Louis Barrat and Itamar Procaccia for agreeing to review my manuscript, and to Damien Vandembroucq and Elisabeth Agoritsas for accepting to be part of the "jury de thèse". I would like to thank the LPTMC for welcoming me during the months of my stage first, and the years of my thesis second. In particular, I am thankful to Bertrand and Pascal, members of my "Comité de suivi", who supported me along this path. I would also like to express my gratitude to the fellow PhD students and postdocs of the lab who have shared with me the anguish and joy that characterize a PhD thesis. Thanks to Adriano, Alex, Anna, Aurélien, Brieuc, David, Davide, Etienne, Federico, Hugo, Jérémie, Julien, Léo, Louise, Lucija, Marc, Moulay, Pierre, Romain, and Tim. With Marc and his bikes, I have shared an office for the past few years, engaging in countless conversations that delved into the cultural and culinary differences between France and Italy.

I am grateful to all the friends in Paris who have accompanied me throughout this journey, including Alessandro, FrancescaM, FrancescoM, Hélène, Leonardo, and Lorenzo. I am also thankful to Francesca, Arne, and Mascha for their hospitality in France, which made my transition to a new country much smoother. I thank my friends in Italy, including Alessandro, Aurora, Benedetta, Edoardo, Elena, Elisa, Gianpiero, GiulioB, GiulioR, Irene, Leonardo, Marco, Giovanni, Rebecca, Samuele, SaverioC, SaverioD, and Simone. Despite the distance between us, we have managed to maintain strong connections, and I am deeply grateful for their friendship. I would like to express my heartfelt gratitude to my family. Thanks to my grandmothers, Elena and Ada, who provided me with both emotional and physical support by preparing delicious food that I could take with me. I thank my parents, Luciano and Barbara, as well as my sister, Maria Vittoria, whose warm welcome every time I returned home made the journey back very refreshing. I am thankful for their love and constant presence.

To Giulia, with whom I have shared these past years, sometimes in a small studio in Paris, sometimes in a small studio in L'Aquila, I am grateful for her continuous encouragement and support. On a more practical note, I would also like to thank her for reading and providing

suggestions on various pieces of this work.

To all these individuals and many others who have contributed in various ways, I extend my deepest appreciation for their assistance and support.

Résumé long en Français

Les solides amorphes sont présents dans la vie de tous les jours. Cette dénomination est utilisée pour définir les matériaux qui sont solides, c'est-à-dire, qui résistent à l'application d'une force (parfois faible) sans s'écouler, mais dont les composants ne sont pas arrangés dans un réseau régulier comme dans les cristaux. Au delà de l'absence d'ordre à longue portée qui est la caractéristique principale des solides amorphes, les matériaux peuvent être très différents. Un premier sous-groupe est celui des verres. Il est possible d'obtenir un verre en abaissant la température d'un liquide en dessous du point de fusion tout en évitant la cristallisation (cela peut se faire, par exemple, avec des vitesses de refroidissement élevées). Le liquide entre d'abord dans l'état de surfusion, et si la température est encore abaissée, il finit par atteindre l'état vitreux. Dans cet état, les particules ont une organisation spatiale irrégulière analogue à celle des liquides. Cependant, les verres sont solides et, au niveau macroscopique, ils se comportent d'une manière totalement différente des liquides. En raison de leur module élastique élevé, cette première catégorie de matériaux est souvent qualifiée de solides amorphes "durs", par opposition au sous-groupe "mou". Les colloïdes, les mousses et les émulsions sont des exemples de ce deuxième groupe. Les suspensions colloïdales [1] sont des fluides dans lesquels sont dispersées des particules solides qui, sous l'effet d'une compression suffisamment rapide, présentent une transition vitreuse [2]. Dans les mousses, un gaz est confiné dans un liquide ou un solide, comme par exemple dans la mousse sur le dessus d'un cappuccino ou dans les mousses métalliques. Enfin, les émulsions, comme la mayonnaise, sont obtenues en mélangeant deux liquides normalement non miscibles. Ces matériaux présentent certaines propriétés caractéristiques des solides, car ils sont capables de conserver leur forme si des petites forces sont appliquées, et certaines caractéristiques des liquides, puisqu'ils s'écoulent après l'application d'une charge externe suffisamment importante.

Dans notre travail, nous avons étudié la réponse des solides amorphes, durs ou mous, à une déformation imposée. Les protocoles de préparation, la taille des constituants, la nature de la déformation et d'autres détails peuvent conduire à des résultats très différents. Nous nous intéressons plus particulièrement au changement de la réponse lorsqu'un *même* matériau est préparé de manières différentes, ce qui joue sur sa stabilité et son degré de désordre. Les deux principales quantités dont on a besoin pour décrire la réponse du solide sous une charge sont la contrainte et la déformation. Le champ de contrainte quantifie les forces agissant en chaque point du matériau, tandis que le champ de déformation caractérise la déformation qui en résulte. Afin d'étudier les propriétés mécaniques des matériaux, nous nous sommes concentrés sur le cisaillement simple dans lequel le solide commence au repos et est ensuite soumis à une déformation par cisaillement qui est progressivement augmentée. Le résultat de ce protocole est une courbe contrainte-déformation qui caractérise les

propriétés mécaniques du matériau. A faible déformation le solide se comporte de manière essentiellement élastique, c'est-à-dire que sa contrainte est linéairement proportionnelle à la déformation appliquée. Lorsque la déformation augmente, la courbe s'écarte du comportement linéaire et devient saccadée, en raison de la présence d'une déformation plastique. Le passage d'un comportement élastique à un comportement plastique est appelé transition de "yielding". A la différence des cristaux, l'origine de la plasticité dans les solides amorphes vient de réarrangements non affines se produisant dans une région localisée de l'espace [3]. Ces événements localisés agissent sur le reste du système, y compris à grande distance, générant un champ de déformation qui est décrit par le propagateur d'Eshelby, doté d'une symétrie quadrupolaire. Le champ de déformation résultant d'un seul réarrangement permet à d'autres zones de subir un événement plastique, créant un phénomène collectif d'avalanche. En raison de la forme anisotrope du propagateur d'Eshelby, les événements plastiques peuvent se localiser dans une bande de cisaillement. Lorsque la déformation s'accroit, deux scénarios sont possibles : alors que les mousses et autres solides amorphes mous peuvent s'écouler indéfiniment sans se rompre (comportement ductile), les solides durs tels que les verres de silicate se brisent brutalement (comportement fragile). L'existence de ces deux types de réponse soulève la question des facteurs qui contrôlent la nature de la transition de yielding. Des simulations de dynamique moléculaire [4] ont apporté une première réponse, en montrant que le comportement d'un même matériau vitreux peut être ductile (yielding continu) ou fragile (yielding discontinu) en fonction de sa préparation. En outre, il a été suggéré qu'il existe un point critique qui sépare les deux comportements.

Du point de vue de la physique statistique, un système au point critique possède une propriété d'invariance d'échelle (la longueur de corrélation spatiale est infinie), ce qui se traduit par l'existence de lois de puissance, caractérisées par des exposants critiques. Ces exposants, ainsi que d'autres propriétés du système au point critique, sont indépendants des détails microscopiques. Deux systèmes différents du point de vue microscopique peuvent avoir un point critique avec les mêmes propriétés, auquel cas on dit qu'ils appartiennent à la même classe d'universalité. Le cas qui nous intéresse, la transition de yielding associée à la déformation des solides amorphes, est cependant plus compliqué que les systèmes purs habituellement considérés en mécanique statistique, à cause du désordre gelé associé à la nature amorphe des matériaux et du caractère hors équilibre du processus. Il est notamment nécessaire d'introduire les concepts de susceptibilité déconnectée et connectée, qui permettent de comprendre la contribution relative des différentes sources de désordre et d'identifier les propriétés critiques du système. Ces idées ont été utilisées dans [4], où il a été proposé que le comportement des solides amorphes cisaillés à proximité de la transition de yielding est analogue à celui d'un autre modèle bien connu en physique statistique : le modèle d'Ising en champ aléatoire (RFIM) forcé loin de l'équilibre par un champ appliqué à température nulle. Cependant, le coût de calcul des simulations de dynamique moléculaire et la limitation de la taille des systèmes et du nombre d'échantillons accessibles, est un obstacle majeur qui empêche une étude approfondie par analyse d'échelle des effets de taille (finite-size scaling analysis) des propriétés critiques des solides amorphes cisaillés. Notre travail repose sur l'idée qu'il est alors nécessaire d'utiliser une modélisation mésoscopique du phénomène et de chercher à développer une théorie effective reposant sur le RFIM.

Dans la première partie de notre travail, nous avons étudié le changement dans la transition de yielding des solides amorphes cisaillés, d'un comportement de premier ordre (dis-

continu) à un comportement continu, au moyen d'un modèle élasto-plastique (EPM) en 2 et 3 dimensions [5]. Dans ce modèle phénoménologique, le solide est considéré au niveau mésoscopique comme composé de nombreux blocs, chacun portant une valeur locale de contrainte. Ces éléments se comportent selon des règles simples, mais donnent lieu à un comportement macroscopique complexe capable de reproduire des résultats réalistes. Nous n'avons retenu que les ingrédients minimaux du modèle, qui devraient suffire à capturer la physique essentielle en jeu dans la transition de yielding et le comportement à grande échelle. Les blocs évoluent élastiquement au fur et à mesure que la déformation appliquée augmente, jusqu'à ce qu'ils atteignent une valeur de limite d'élasticité au-delà de laquelle ils subissent un événement plastique et redistribuent une partie aléatoire de leur contrainte vers les autres sites par le biais du propagateur quadrupolaire d'Eshelby. Nous avons constaté que, comme dans les résultats des simulations de dynamique moléculaire, la courbe contrainte-déformation obtenue change avec la préparation du matériau, qui, dans notre version de l'EPM, est codée dans la distribution initiale des contraintes pour chaque bloc. Pour un désordre faible (petite variance de la distribution initiale des contraintes), la courbe contrainte-déformation obtenue présente un saut d'ordre 1 de la contrainte moyenne, accompagnée de la localisation de l'activité plastique dans une bande de cisaillement. Au fur et à mesure que la variance initiale augmente, le saut se réduit et disparaît pour laisser place à une courbe continue avec un maximum puis enfin, pour un désordre encore plus important, à une courbe monotone. Nous avons étudié avec soin le régime fragile (discontinu), en examinant la phénoménologie qui conduit à la formation de la bande de cisaillement pendant la plus grande avalanche. Nous avons mesuré l'évolution du profil de la bande de cisaillement en fonction de la taille du système, ainsi que la contribution à la chute macroscopique de contrainte des sites situés à l'intérieur et à l'extérieur de la bande. Notre analyse a également démontré que la caractérisation des propriétés de la transition de premier ordre peut être difficile en raison des effets importants de taille finie, en particulier l'influence de régions statistiquement rares qui sont présentes dans la limite thermodynamique mais pas dans des systèmes de taille limitée. Nous avons ensuite abordé le point principal de cette première partie, à savoir l'étude du passage entre les comportements fragile et ductile. En étudiant la susceptibilité déconnectée, nous avons confirmé numériquement que dans ce modèle mésoscopique, comme dans les simulations de dynamique moléculaire, ce passage correspond à un point critique hors équilibre. En outre, grâce à la nature mésoscopique du modèle, il nous a été possible d'effectuer une analyse d'échelle en taille finie afin d'obtenir une première estimation des exposants critiques en jeu. Nous avons pu réaliser des simulations de très grands systèmes (jusqu'à environ 100 fois plus grands que les quelques échantillons les plus grands étudiés par la dynamique moléculaire) avec un très grand nombre d'échantillons et une grande précision dans la discrétisation de l'amplitude du désordre. Nous avons mesuré les exposants critiques de la susceptibilité déconnectée de différentes manières, ce qui donne une estimation des barres d'erreur. Il a été récemment avancé [6] que ce point critique n'est dû qu'à des effets de taille finie, et qu'il devrait disparaitre dans la limite thermodynamique. Pour vérifier la persistance du point critique lorsque la taille du système augmente, nous avons réussi à borner sa position par la valeur du désordre nécessaire pour observer un dépassement ("overshoot") dans la courbe contrainte-déformation. Nous avons ainsi pu renforcer la conclusion que la valeur critique du désordre est finie dans la limite thermodynamique à la fois en 2D et 3D. Nous avons conclu l'étude de l'EPM en examinant deux variantes du modèle. Tout d'abord, nous avons évalué l'effet de rares régions peu stables sur l'évolution du matériau dans le régime fragile. Pour ce

faire, nous avons inséré artificiellement une région de ce type à l'intérieur du matériau. Nous avons vu que la présence d'une telle région induit la formation de la bande de cisaillement et suffit à modifier non seulement la valeur moyenne de la déformation à laquelle le matériau cède, mais également sa distribution. Nous avons discuté les conséquences sur le comportement de la susceptibilité connectée avec la taille du système. Nous avons enfin considéré la version de l'EPM proposée par [7]. Nous avons effectué la même analyse et trouvé à nouveau des preuves numériques de la présence d'un point critique entre les régimes fragile et ductile.

Nous avons ensuite testé l'idée que la transition de yielding est analogue à la transition hors équilibre d'un modèle d'Ising en champ aléatoire forcé. La possibilité d'établir un parallèle entre les deux modèles serait essentielle pour développer une théorie effective de la transition de yielding et pour appliquer alors à l'étude de la réponse mécanique en cisaillement toutes les techniques analytiques et numériques développées pour le RFIM. Ceci permettrait également de surmonter une limitation actuelle de l'EPM, à savoir l'absence de description hamiltonienne, en autorisant l'utilisation d'outils de la théorie des champs, y compris le groupe de renormalisation. Cependant, en dehors de la similarité entre EPM et RFIM dans l'existence de deux régimes de transition discontinue et continue avec un point critique contrôlé par l'amplitude du désordre entre les deux, l'organisation des événements est qualitativement différente. Nous avons considéré un RFIM hors équilibre à température nulle dans lequel les interactions entre les spins sont régies par le propagateur d'Eshelby et ont donc un caractère quadrupolaire. Nous avons étudié ce modèle "Eshelby-RFIM" par des simulations numériques à 2 et 3 dimensions afin de comprendre dans quelle mesure il reproduit la phénoménologie de yielding. La dynamique commence avec une grande valeur négative du champ externe, de sorte que tous les spins sont négatifs (-1) et le champ externe est augmenté de manière quasistatique jusqu'à ce que tous les spins soient positifs ($+1$). A faible désordre les courbes d'aimantation montrent une transition discontinue, comme dans le RFIM ferromagnétique standard. Cependant, l'avalanche associée au saut macroscopique de l'aimantation n'a pas la forme isotrope observée dans le cas ferromagnétique, mais est organisée sous la forme d'une bande, semblable à la bande de cisaillement observée dans les solides amorphes. Nous avons alors étudié la façon dont la plus grande avalanche se propage dans le système et mesuré l'évolution de la largeur de la bande en fonction de la taille du système. Bien que la phénoménologie soit qualitativement très similaire à l'EPM, certaines différences importantes doivent être notées. En particulier, dans le cas de l'EPM, on a observé que chaque site pouvait céder plusieurs fois au cours de l'évolution du système, alors que ce mécanisme est clairement absent dans le Eshelby-RFIM, où les spins ne peuvent se retourner qu'une seule fois. De plus, dans ce dernier cas, la contribution au saut d'aimantation provient des sites à l'intérieur de la bande, puisque la valeur de leur spin change, plutôt que des sites en volume, au contraire de ce qui se passe dans l'EPM. Ces différences peuvent affecter l'analogie entre les deux modèles dans le régime de désordre faible, mais ne jouent pas nécessairement un rôle à proximité du point critique. Comme pour l'EPM, les effets de taille finie sont très importants dans le régime de désordre faible. Nous sommes ensuite passés à la partie principale du chapitre, qui est l'étude du comportement critique observé lorsque l'évolution de l'aimantation passe de discontinue à continue sous l'effet de l'amplitude du champ aléatoire. Nous avons mesuré la susceptibilité déconnectée et nous avons effectué une analyse d'échelle en taille finie afin d'estimer les exposants critiques. Comme pour la criticalité de l'EPM, il reste difficile d'obtenir avec une bonne certitude la valeur des exposants.

L'estimation faite à partir de 3 méthodes différentes indique que les exposants du RFIM sont systématiquement plus grands que ceux de l'EPM à la fois en 2D et 3D, mais il est peut-être prématuré de conclure que les deux systèmes sont dans des classes d'universalité différentes. Pour le Eshelby-RFIM également, nous avons remarqué que, lorsque la taille du système augmente, le point critique se déplace lentement vers des valeurs plus grandes de l'intensité du désordre. Comme pour l'EPM, nous avons utilisé l'apparition d'une bosse dans la courbe d'aimantation pour borner le déplacement du point critique et nous avons conclu qu'il semble avoir lieu à un désordre fini dans la limite thermodynamique. Pour conclure l'étude du modèle, nous avons envisagé deux variantes possibles. Tout d'abord, nous avons ajouté artificiellement une région de spins positifs dans le système dès le début du processus, afin d'imiter la présence d'une région statistiquement rare qui pourrait altérer la dynamique dans la limite thermodynamique. Nous avons observé que la présence de cette région affecte la valeur moyenne du champ externe à laquelle le saut d'aimantation macroscopique a lieu, mais nous n'avons pas pu conclure sur sa distribution générale. Nous nous sommes ensuite concentrés sur l'effet du réseau sur le modèle. Il a été montré précédemment que le RFIM standard souffre de certains effets de facettage lorsqu'il est simulé dans un réseau carré [8]. Un effet similaire pourrait également modifier les résultats de notre modèle, puisque le noyau d'Eshelby considéré est orienté le long d'un axe particulier du réseau. Pour vérifier si nos résultats sont robustes par rapport à une modification du réseau, nous avons simulé le modèle en changeant l'orientation du noyau d'Eshelby, ce qui revient à incliner le réseau. Nous avons montré que la même phénoménologie est observée dans ce cas et que le point critique est à nouveau présent.

Dans la dernière partie du projet, nous avons travaillé sur une approche analytique du problème en étudiant les deux modèles dans une limite de champ moyen. Nous avons commencé par définir la version champ moyen de l'EPM, en choisissant celle spécifiée dans [4]. Dans cette approximation, les blocs interagissent entre eux de manière totalement connectée et ferromagnétique. Une description plus précise de la limite du champ moyen devrait prendre en compte la nature anisotrope du noyau d'Eshelby. Une solution a été proposé dans [9], mais elle fait intervenir un désordre supplémentaire et ne se prête pas à l'étude des fluctuations qui est le cœur de notre travail. Dans le modèle que nous avons étudié, le désordre est produit au niveau de la distribution initiale des contraintes et de la distribution des sauts après déformation, comme dans le cas à dimension finie que nous avons considéré dans la première partie. Les courbes contrainte-déformation reproduisent la même phénoménologie que le cas en dimension finie, avec deux régimes, fragile et ductile, selon l'amplitude du désordre initial. Nous avons analysé en parallèle la limite du champ moyen du RFIM hors équilibre avec le protocole quasistatique athermique, basé sur [10]. Nous avons pu caractériser analytiquement les fluctuations d'échantillon à échantillon des deux modèles. Nous avons montré directement que, au voisinage de la transition de yielding, l'EPM peut être décrit comme un RFIM dans lequel le champ magnétique appliqué joue le rôle de la déformation appliquée. Nous avons également montré que le champ aléatoire effectif qui se couple linéairement à la stabilité locale (c'est-à-dire à la distance au seuil d'élasticité locale jouant le rôle de paramètre d'ordre local semblable à l'aimantation locale dans le RFIM) est une propriété émergente : il n'est pas présent au niveau "nu" dans le système avant déformation et survient à un stade ultérieur à partir d'une combinaison des conditions initiales et de l'histoire de la déformation impliquant une séquence d'événements plastiques locaux.

Nous avons ensuite étudié l'influence des différents types de désordre introduits dans l'EPM pour imiter l'effet de l'inhomogénéité structurelle locale d'un solide amorphe (contraintes locales initiales aléatoires, sauts de contrainte locaux aléatoires, ...) sur l'amplitude du champ aléatoire effectif.

Dans une partie de conclusion, nous avons résumé les résultats marquants de notre travail et envisagé plusieurs perspectives possibles pour aller au-delà.

Contents

Acknowledgments i

Résumé long en Français iii

Introduction 1
1 A brief introduction to sheared amorphous materials . . . 2
1.1 Materials deformation . . . 2
1.2 Simulations and Theoretical models . . . 12
1.3 The yielding transition and the influence of the preparation conditions 16
2 A brief introduction to critical phenomena . . . 16
2.1 Equilibrium . . . 17
2.2 Out of equilibrium . . . 23
3 Summary of the introduction and structure of this work . . . 33

1 The Elasto-Plastic Model and the yielding transition 37
1 Introduction . . . 38
1.1 The key ingredients of an Elasto-Plastic Model . . . 38
1.2 Our version of the model . . . 41
1.3 Stress-vs-strain curves . . . 44
2 The brittle regime and the shear band formation . . . 46
2.1 Inside the shear band formation . . . 46
2.2 Before and after the macroscopic drop . . . 48
2.3 Characterizing the brittle transition . . . 51
3 Critical point between brittle and ductile regime . . . 54
3.1 Characterizing the brittle-to-ductile transition . . . 54
3.2 Bounding the location of the critical point . . . 59
4 Variations of the model . . . 61
4.1 Effect of a seed . . . 61
4.2 The Popović-de Geus-Wyart version of the EPM . . . 65
5 Conclusion . . . 67

2 The athermally driven Eshelby Random-Field Ising model 69
1 Introduction . . . 70
1.1 The Eshelby-like interactions . . . 71
1.2 Magnetization curves . . . 72

2 The "brittle" regime and the "shear band" formation . . . 75
2.1 Inside the "shear band" . . . 76
2.2 Before and after the macroscopic jump . . . 78
2.3 Characterizing the discontinuous transition . . . 79
3 Disorder-controlled critical point . . . 82
3.1 Characterizing the "brittle-to-ductile" transition . . . 82
3.2 Bounding the location of the critical point . . . 87
4 Variations of the model . . . 89
4.1 Effect of a seed . . . 89
4.2 Rotated Eshelby-RFIM . . . 92
5 Conclusion . . . 94

3 Mean-field results: Emergence of a random field in an EPM 97
1 Introduction . . . 98
1.1 Mean-field limit of the EPM . . . 98
1.2 Mean-field limit of the RFIM . . . 104
1.3 Contrasting EPM and RFIM . . . 106
2 Sample-to-sample fluctuations and strength of the effective random field . . . 108
2.1 Illustration for the RFIM . . . 108
2.2 Susceptibilities in the mean-field EPM . . . 110
3 Results for the mean-field EPM . . . 113
3.1 Stress-vs-strain curves and the role of various types of disorder . . . 113
3.2 Connected and disconnected susceptibilities . . . 115
3.3 Strength of the effective random field . . . 118
4 Conclusion . . . 123

Conclusions and perspectives 125

A The Eshelby kernel 130
1 Fourier transform convention . . . 130
2 Derivation of the Eshelby propagator . . . 131
2.1 Value at the origin and properties of the Eshelby strain field . . . 134
3 Implementation of the kernel . . . 135
3.1 The Eshelby kernel in the EPM . . . 137
3.2 The Eshelby kernel in the Eshelby-RFIM . . . 138

B Details on the code 139
1 Code for the EPM . . . 139
1.1 Adding a seed . . . 140
2 Code for the standard RFIM . . . 143
3 Code for the Eshelby-RFIM . . . 145
3.1 Adding a seed . . . 145

C Mean-field Calculations 148
1 Details for the AQS driven mean-field soft-spin RFIM . . . 148
2 Details for the AQS driven mean-field EPM . . . 149
2.1 Expression of the disconnected susceptibility . . . 150

2.2 Solving different models . . . 153
2.3 Annealed average over the random jumps . . . 157
3 Direct mapping between correlation functions in MF-EPM and MF-RFIM . . 158
3.1 Mean-field EPM starting from finite strain . . . 158
3.2 Mean-field RFIM starting from a finite field . . . 161
3.3 Tentative mapping between the two models . . . 163
3.4 Results and test of the hypothesis of a single plastic event per site . . 163

D Avalanches **165**
1 Avalanche size distribution for the EPM . . . 165
2 Avalanche size distribution for the Eshelby-RFIM . . . 167

Bibliography **170**

Introduction

Contents

1 A brief introduction to sheared amorphous materials 2
1.1 Materials deformation 2
1.1.1 Start-up experiments 5
1.1.2 Other protocols 9
1.1.3 Terminology conventions 11
1.2 Simulations and Theoretical models 12
1.3 The yielding transition and the influence of the preparation conditions 16
2 A brief introduction to critical phenomena 16
2.1 Equilibrium 17
2.1.1 Pure case 17
2.1.2 Adding quenched disorder 20
2.2 Out of equilibrium 23
2.2.1 Interface depinning 27
2.2.2 Athermally driven Random Field Ising model 29
3 Summary of the introduction and structure of this work 33

1 A brief introduction to sheared amorphous materials

Amorphous solids are present in everyday life. They represent materials that are solid, i.e. resisting to the application of a (sometimes small) force without flowing, but whose components are not arranged in a precise lattice as in crystals. The lack of long-range order is their defining characteristic, but they encompass a diverse range of materials with distinct properties. For example, a first subgroup is glasses. When the temperature of a liquid decreases below its freezing point, the irregular structure of the particles changes to the well-defined organization of a crystal. The process for this transition involves the nucleation of a crystal seed growing and spanning the whole system. It is however possible to maintain the temperature of a liquid below its freezing point while avoiding nucleation of these seeds (this can be done, for example, with large cooling rates). The liquid enters the supercooled state, and if the temperature is lowered even more it ends up in a glassy state. In this state the particles are not organized in a precise way on a lattice and they have an irregular structure analogous to the one of liquids, so that no sharp distinction between the two states can be found by simply looking at the arrangement of particles. However, glasses are solids, and at the macroscopic level they behave in a completely different way from liquids. Silicate glasses are the oldest manufactured and most common type of glasses. They are used to make everyday items such as windows, bottles, and eyeglasses. Other examples of glasses are metallic glasses [11]. In this case the elemental constituents of the material are at the atomic scale (see Fig. I.1). Due to their large elastic moduli, this first category of materials is often referred to as "hard" amorphous solids, as opposed to "soft" ones. Examples of this second group are colloids, foams, and emulsions. Colloidal suspensions [1], are fluids in which solid particles (of typical size between tens of nanometers and microns) are dispersed. It has been shown that, under a sufficiently fast compression, these materials show a glass transition as well [2]. Foams are formed by confining a gas in a liquid or solid medium, as seen in the foam atop a cappuccino or in metal foams. Emulsions, on the other hand, are created by mixing typically immiscible liquids, such as oil, vinegar, and egg yolks in the case of mayonnaise. These materials show some properties characteristic of solids, in that they are able to retain their shape if small forces are applied, and some characteristic of liquids, in that they can flow upon the application of a sufficiently large external load. Because of this dual nature the term of yield-stress fluids is also used [12].

The response of hard and soft amorphous solids to an imposed deformation is quite diverse between these two subgroups, but also between elements of the same subgroup. Preparation protocols, constituent size, driving, and other details can indeed lead to very different results. However, as discussed in the following, amorphous solids also share common features when subject to deformation.

1.1 Materials deformation

In this work we are interested in the properties of amorphous materials when they are subject to a deformation. To obtain any kind of deformation some forces need to be applied. When considering the resulting dynamics of an object under the effect of applied forces one often makes the rigid body hypothesis, in which the material is considered undeformed. In this way one can focus only on the evolution of its position. The study of deformations focuses instead on the other face of the coin, i.e., on how forces change the shape of a material.

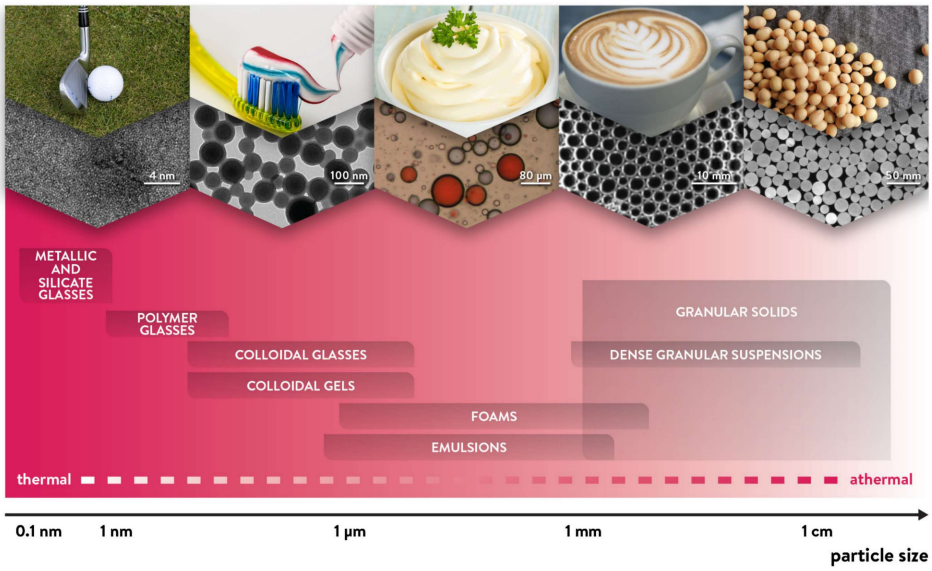

Figure I.1: General overview of different types of amorphous solids. From left to right, top row: golf club made of metallic glass, toothpaste, mayonnaise, coffee foam, and soya beans. Second row: fractured bulk metallic glass, nanoparticles obtained by miniemulsion polymeritation, emulsion of water droplets, soap foam, thin nylon cylinders. Adapted from [5] (see references therein).

Imagine the solid as composed by many infinitesimal elements defined by their position $\boldsymbol{r}$ in some reference system ($\boldsymbol{r}$ is a vector in d-dimensions, with $d = 2$ or 3 usually). A local stress tensor σ_{ij} can be defined at any point $\boldsymbol{r}$ as the force per unit area applied on the face i in the direction j (in 3D i and j are either x,y or z) of that infinitesimal block. When the object is at rest, each point is stationary and the following conditions,

$$\sum_{i=x,y,z} \frac{\partial \sigma_{ij}}{\partial r_i} = 0 \tag{I.1}$$

$$\sigma_{ij} = \sigma_{ji}, \tag{I.2}$$

need to be satisfied for every axis i and j in order to impose force and momentum equilibrium. Notice that the equations above do not imply that $\sigma_{ij} = 0$ everywhere in order to have a stationary solid, so that residual stress can be present even in objects at rest [13]. As we will discuss below, this has important consequences on the material's properties (a known example being Prince Rupert's drops [14]). The stress field quantifies the forces acting at each point of the material, and what is left is to quantify its deformation. When some forces are applied to the solid, the position of each point in the system changes as $\boldsymbol{r} \to \boldsymbol{r} + \boldsymbol{u}$, where the vector $\boldsymbol{u}$ is called displacement and contains information on both the rigid-body motion and the shape's change. In order to only focus on the deformation part and avoid the rigid-body motion one considers the displacement gradient, or deformation tensor, $\boldsymbol{\nabla u}$. This tensor can be split into a symmetric and an antisymmetric part as $\partial u_i/\partial r_j = \varepsilon_{ij} + R_{ij}$ with

$$\varepsilon_{ij} = \frac{1}{2}\left(\frac{\partial u_i}{\partial r_j} + \frac{\partial u_j}{\partial r_i}\right) \quad \text{and} \quad R_{ij} = \frac{1}{2}\left(\frac{\partial u_i}{\partial r_j} - \frac{\partial u_j}{\partial r_i}\right), \tag{I.3}$$

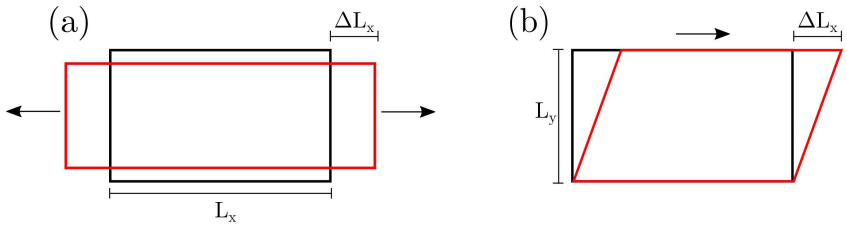

Figure I.2: Sketch of two possible deformation geometries in 2D: in (a) the solid is subject to uniaxial tension along the x-axis. The applied strain tensor has diagonal entries $\varepsilon_{xx} = \Delta L_x/L_x$ and $\varepsilon_{yy} = \Delta L_y/L_y$, while the non-diagonal entries are 0. In (b) a simple shear deformation is applied instead. In this case we have $2\varepsilon_{xy} = 2\varepsilon_{yx} = \gamma = \Delta L_x/L_y$, while the diagonal entries are 0.

which are the Cauchy's strain tensor and a rigid-body rotation, respectively. By focusing on the strain tensor ε_{ij} one can eliminate all the rigid-body motion from the picture, as only changes in the shape act on this quantity. To understand the physical interpretation of this strain tensor let us look at its components. The elements in the diagonal part of ε_{ij}, called normal strains, represent the change in length of the side of an infinitesimal block, while the off-diagonal terms measure the change in angle between two axes that were orthogonal before deformation, cf. Fig. I.2. This strain tensor can then be divided in two tensors as $\varepsilon_{ij} = \varepsilon'_{ij} + \varepsilon_{\mathrm{M}}\delta_{ij}$, with $\varepsilon_{\mathrm{M}} = \sum_i \varepsilon_{ii}/3$ the volumetric strain, related to volume change, and $\varepsilon'_{ij} = \varepsilon_{ij} - \varepsilon_{\mathrm{M}}\delta_{ij}$ the deviatoric strain, related to all deformations that change the shape but not the volume. One has to remember that the definition of strain we gave above is based on the small displacement hypothesis $|\boldsymbol{\nabla u}| \ll 1$, while different definitions are necessary when this condition cannot be assumed. In the following we will not discuss this possibility and we will define strain as in Eq. (I.3). The two fields $\sigma_{ij}(\mathbf{r})$ and $\varepsilon_{ij}(\mathbf{r})$ describe the local forces and deformations occurring at each point $\mathbf{r}$ in the material. The macroscopic strain and stress tensors that the solid is subject to are obtained by integrating over the whole volume. In the following we will use the same notation for microscopic and macroscopic stresses, but the difference will be clear from the context.

Based on the definition of the strain and stress tensors, different choices on the deformation protocol of the material are possible. First of all, the orientation of the forces acting on the system leads to many deformation geometries, as sketched in Fig. I.2. Common choices include for example compression (tension), in which inward (outward) forces are applied to sides of a material, with zero net sum and torque, trying to reduce (increase) its volume. In a bending deformation the load is instead applied perpendicularly to the longitudinal axis of the solid. This type of geometry is often chosen to study metals and hard amorphous solids to be used as structural elements. Finally there are shear deformations, in which parallel surfaces inside the material slip on each other while remaining parallel and at the same distance. In this last case the volume of the solid does not change, so that $\varepsilon_{\mathrm{M}} = 0$. This type of deformation is often used in the study of yield stress fluids like foams and emulsions and other soft amorphous solids. In general, many choices of the deformation geometry are possible and relevant for applications in engineering, but they are out of the scope of this work. In the following we will focus only on the *simple shear* case, defined in 2D by the

displacement gradient $\boldsymbol{\nabla u} = \left(\begin{smallmatrix} 0 & \gamma(t) \\ 0 & 0 \end{smallmatrix}\right)$. The important variable is the xy component of the strain tensor $\boldsymbol{\varepsilon} = 1/2\left(\begin{smallmatrix} 0 & \gamma(t) \\ \gamma(t) & 0 \end{smallmatrix}\right)$. When the deformation is applied uniformly to the whole material, the value of $\gamma(t)$, which is the only non-zero entry of the strain tensor, is the only variable describing the shape change and the problem can be treated as a scalar one to a good approximation. This situation is illustrated in Fig. I.2(b). Then $\gamma(t) = \Delta L(t)/L$ with ΔL the displacement of the top plane and L the distance between planes.

For a given geometry the loading can be applied in several ways. Deformations can be controlled in two different manners: by imposing strain and measuring stress and viceversa. Moreover, as the loading is applied the system adapts to the new conditions and tries to relax to a mechanical equilibrium. The difference between the time rate at which the loading increases and the one at which the system relaxes is then important when characterizing the properties of the system. In a similar way, the operating temperature at which the experiment is carried on plays a role in the response to loading. From these brief considerations it is clear that the observations obtained from a deformation experiment depend not only on the solid under study, but also on the conditions under which the experiment is being performed. In the study of metals and hard amorphous materials the usual choice is to start with the system at rest and apply the load by imposing the strain, while measuring the whole stress response. This is also done in the case of soft amorphous materials. In the latter case another possibility is to apply an external load and measure the resulting strain-rate once the system reaches a flowing stationary state. Other protocols are also studied in the literature, such as the oscillatory strain protocol, where the strain is applied by increasing from 0 to some value γ_1, then decreasing to $-\gamma_1$ and then repeating the procedure periodically between these two values. Finally, in creep experiments the transient behavior of the system at fixed applied stress is studied. In our work we focus on the case of a system that is sheared under a strain-controlled protocol, starting at rest, in what is called shear start-up experiment. We will also refer to other choices and more general properties later on.

1.1.1 Start-up experiments

A start-up experiment is one in which the loading is applied by imposing a certain macroscopic strain to the material. The solid starts at rest with no strain applied to it, hence with zero macroscopic stress. As the strain increases, at a fixed rate $\dot{\gamma} = \partial\gamma/\partial t$, with t representing time, the stress evolves. The result of this protocol is a stress-vs-strain curve that characterizes the relation between forces and deformation and the material's mechanical properties, see Fig. I.3. In the first part of the evolution the solid behaves elastically and the stress is linearly proportional to the applied strain. A solid body is said to be elastic when it returns to its original shape after the forces acting on it are removed, which means that the deformation is reversible and the solid behaves like a spring. Under the hypothesis of linear elasticity the stress is linearly proportional to the strain so that, for a general deformation geometry,

$$\sigma_{ij} = C_{ijkl}\varepsilon_{kl}, \tag{I.4}$$

where C_{ijkl} is called the stiffness tensor. In the case of an isotropic and homogeneous system some symmetries can be exploited and the stiffness tensor can be reduced to $C_{ijkl} = K\delta_{ij}\delta_{kl} + \mu(\delta_{ik}\delta_{jl} + \delta_{il}\delta_{jk} - 2/3\delta_{ij}\delta_{kl})$, with δ_{ab} the Kronecker delta, K the bulk modulus and μ the shear modulus. These two coefficients characterize the stiffness of the material:

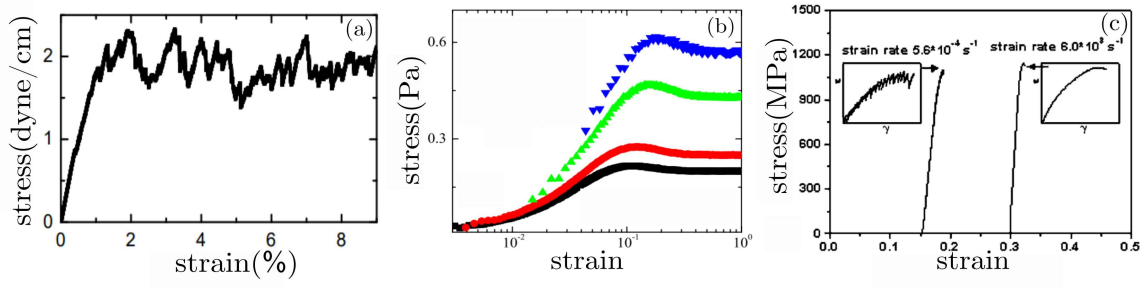

Figure I.3: Stress-vs-strain curves for three different amorphous solids. In (a) the result for a two-dimensional foam under shear deformation is shown. The experiment is performed with fixed strain rate $\dot{\gamma} = 3.1 \times 10^{-3}\text{s}^{-1}$. Panel (b) is instead obtained for a colloidal glass under shear deformation. The different curves correspond to different straining rates, increasing from bottom to top. Notice that the x-axis is logarithmic. Finally, in panel (c) the stress-vs-strain curves for the same metallic glass driven with different strain rates. The images are adapted from [15], [16] and [17] respectively.

the larger the value of μ the stiffer the material. The assumption of a purely homogeneous material is clearly problematic in amorphous solids which may have local inhomogeinities, so that this linear elasticity relation holds but with locally different shear and bulk moduli [18]. In the following we will neglect this type of elastic inhomogeneity.

As the load increases, the curve departs from the linear behavior and becomes jerky (as we will show in Section 2.2 this is characteristic of out-of-equilibrium driven systems with cooperative interactions). This is due to plastic deformation, which is an irreversible phenomenon that occurs in most materials for large enough loads. As soon as the load is removed, elastic deformations disappear completely, while plastic ones do not. The transition from elastic to plastic behavior is called "yielding", and is the main topic of this work. Plasticity has been studied from the macroscopic point of view [19] where the system is considered homogeneous, but this hypothesis has to be lifted in order to understand how plastic deformation emerges at the microscopic level. First of all, the mechanism behind plasticity at small scales depends on the type of material. For example, in crystals, where every atom occupies some site in a precise lattice, plasticity originates from dislocations, i.e., topological defects in the ordered lattice, that propagate through the system as the loading is applied [20]. In amorphous solids, plastic deformation is also observed, but cannot be described by topological defects anymore, due to the lack of periodic long-range order. A first important result in this direction was obtained in the study of a bidisperse bubble raft (that should be representative of metallic glasses) where the non-affine rearrangements occur in a localized region of space [3]. Following this work, such confined rearrangements have been observed in many other materials, such as colloidal glasses [22] and emulsions [23]. The number of elements taking part in the plastic rearrangement can vary, from just a few tens of particles in colloidal glasses [24] to hundreds of them in some metallic glasses [25]. In foams, under slow driving, the simplest kind of rearrangement observed is in form of a T1 event in which bubbles switch neighbors [21], as depicted in Fig. I.4(a). The details of the microscopic origin of plastic behavior in amorphous solids can change with the material, but plastic events essentially always originate in localized rearrangements (unlike dislocations in

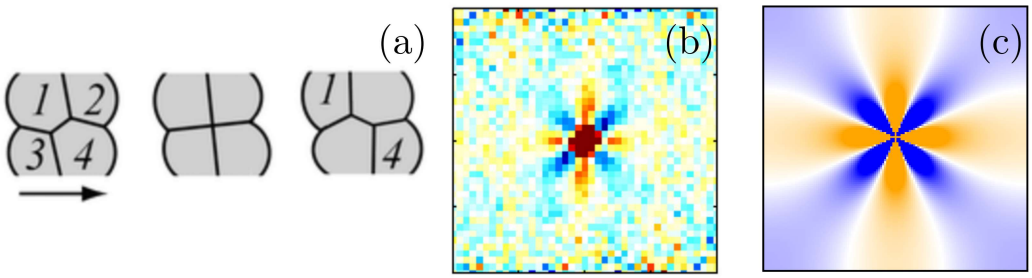

Figure I.4: (a) Form of a T1 event, the simplest plastic rearrangement observed in foams, adapted from [21]. (b) Strain autocorrelation computed for a colloidal glass, adapted from [22]. (c) Form of the Eshelby strain field in Eq. (I.5). Dark orange stands for a positive value, while blue stands for a negative one.

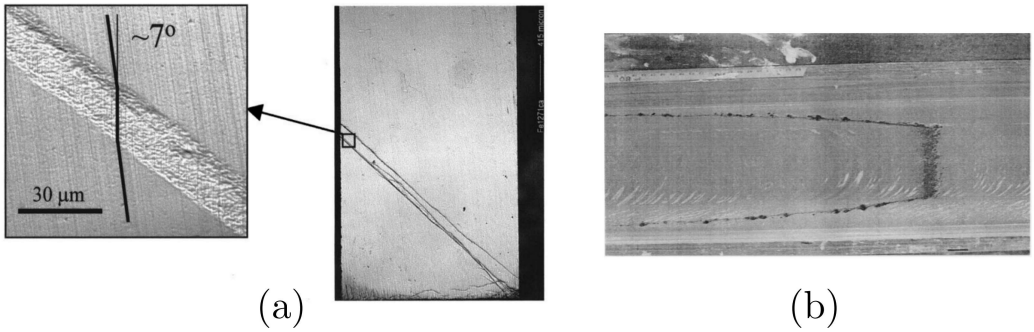

Figure I.5: Shear bands in a metallic glass (a) during a compression experiment from [26] and in a suspension (b) sheared inside a rheometer from [27].

crystals). Yet such localized events affect space around them. Even if the rearrangement is localized in a small region (infinitesimal in the thermodynamic limit) its effect may be felt at long distances from its location. These rearrangements act as a deformation on the rest of the solid that, as a first approximation, can be considered as reacting elastically. The typical strain field resulting from this kind of events has both a volume-changing and a shear component. The volumetric part is generally much smaller for the amorphous solids described here, so that only the shearing part is usually considered (we will neglect dilatation and contraction of the rearranging regions). This additional strain field, which is non-affine with respect to the externally imposed deformation, is called plastic strain. The typical form of the resulting strain at large distance from the plastic event can be computed by considering the effect of an ellipsoidal inclusion in a purely elastic medium and has the form (in 2D)

$$\varepsilon_{xy}(r,\theta) = \frac{\cos(4\theta)}{\pi r^2}, \tag{I.5}$$

where (r,θ) are the polar coordinates with respect to the event in $r = 0$. The above expression was first obtained by Eshelby [28], who also computed near-field corrections (see Ap-

pendix A). This propagator is long-ranged and has a quadrupolar nature that originates from the symmetry of the shear deformation in $r = 0$, which consists of an elongation in a direction and a contraction in the perpendicular one. This quadrupolar form has been confirmed by experiments and simulations on different materials [22, 23, 29], as shown in Fig. I.4(b). As discussed in Appendix A, the form of the far-field propagator has been obtained in the hypothesis of a uniform, isotropic, and purely elastic medium, which is questionable for an amorphous solid (see [30, 31]). Nonetheless, the overall picture seems to hold well. The strain field resulting from a single rearrangement makes it possible for other zones to undergo a plastic event, thereby creating a collective avalanche of plastic events. Avalanches of large sizes can be seen as serration in the stress-vs-strain curves for finite size samples. In amorphous solids, due to the cooperativity and the quadrupolar symmetry of the strain field, large avalanches can in some cases lead to the formation of shear bands. Instead of having a homogeneous distribution of the activity, the material accumulates the majority of strain in these zones, which have the form of a band, and it has been shown that it is indeed energetically favorable to do so [32]. This phenomenon is observed both in hard [33] and in soft [34, 35] solids, as shown in Fig. I.5.

Two types of behavior under loading are observed, depending on the characteristics of the material under consideration and its preparation. In hard solids as silicate glasses the deformation is almost completely elastic and the solid may break even before plastic deformation can take place. Metallic glasses show some plasticity before failure, which allows to predict to a certain degree when the system will break. The plastic events are localized in shear bands, where strain grows quickly and eventually drives the system to failure [33, 36]. After fracture occurs the stress drops to 0 since the material cannot sustain forces anymore, see Fig. I.3(c). On the other hand foams and other soft amorphous solids can flow without failing. As the applied strain increases the material cannot increase its stress, which then fluctuates around a constant value, the fluctuations being associated with avalanches given by plastic rearrangements (see Fig. I.3(a,b)). However, in some conditions, the flow of soft solids is not homogeneous and shear bands appear [27, 34, 37]. Depending on the material under consideration, these shear bands can then die out or characterize permanently the flow, which is then divided into a solid-like phase that does not move and a liquid-like phase inside the shear band.

We now briefly consider the role of testing conditions introduced before, such as the operating temperature and the strain rate. To understand the effect of temperature one can consider the local zone where the rearrangement takes place as a system sitting in one of two possible states, described by the position of the particles, at zero temperature. (As an example one can take the T1 event in Fig. I.4(a), where the first state is the one in which particles 1 and 4 are neighbors, while in the second one 2 and 3 are.) Each of the states has its own energy value, and the two values are separated by a barrier. As the system is in one state, it can rearrange to go in the other one if it is more favorable, but at zero temperature this can only happen if the initial state becomes unstable due to the loading that tilts the landscape. However, if the solid is at finite temperature, it is easier to jump over the barrier between the states thanks to the kicks given by thermal fluctuations. Whether or not this thermal contribution is important for the plasticity of the solid depends on many factors controlling the ratio of the thermal fluctuation kicks to the typical size of the barriers, for example the size of constituents. In foams and suspensions the thermally

activated processes can be neglected, while in metallic and colloidal glasses they could have important consequences [38, 39]. Similarly, the strain rate affects the mechanical properties of the system. In particular, for smaller strain rates the maximum amount of stress reached in the transient evolution is smaller [16, 40]. A driven system at zero temperature and vanishing strain rate only visits local minima (at which mechanical equilibrium is satisfied) that are made accessible by the applied force. Finally, material's preparation also plays an important role. This can be understood when thinking about glasses, that are disordered systems with a huge number of local minima in the energy landscape. Due to this large number of states, the system can be trapped in a given configuration even if this is not the most stable one, and relaxation to the global minimum takes a very long time (experimentally inaccessible). A glass is then out-of-equilibrium, and, as a consequence, its properties depend on the process through which it was obtained. For example, cooling rate [41], preparation temperature [42, 43] and aging [44] are important factors. In general, a well annealed glass, obtained with a very small cooling rate, a low preparation temperature, or after waiting a long time after its formation, will have a sharp transition from elastic to plastic response, with the plastic strain localized in a shear band. On the other hand, a poorly annealed glass, obtained with a large cooling rate, a high preparation temperature, or by deforming just after its formation, shows a more gradual passage from elastic to plastic regime.

From these considerations we retain mainly three concepts that are at the core of this work:

- When the loading is small, amorphous solids evolve apparently elastically, with the stress growing linearly with the strain (this linear elasticity is only apparent, since it has been proven that plastic activity is present for any minute strain [45]). As the loading increases, plastic behavior becomes more prominent and takes place in the form of localized rearrangements that affect the rest of the material via a long-ranged anisotropic strain field.
- The material may reach a point of failure or may continue to flow plastically. Hard solids such as glasses usually behave in the former way, and yield stress fluid in the latter. The two cases have historically been studied as different fields: plasticity mechanics and material science for hard solids and rheology and soft matter physics for soft ones. However, some features, as for example the localized nature of the plastic events and the nucleation of shear bands, are common to many amorphous solids across the categories.
- For a given deformation setup the material's preparation may have important effects on the resulting mechanical response.

1.1.2 Other protocols

We have described the shear start-up setup, in which the loading (in our case the external strain) is increased over time with a certain rate, and the reaction of the system (in our case the stress) is measured at the same time. This means that the transient response of the system is taken into consideration. However, in some cases (often for soft amorphous solids), only the steady-state flow of the system is considered. This case is studied in a different setup, in which some shear stress is usually imposed on the system and the resulting value of the strain rate $\dot{\gamma}$ is measured in the steady state. For a liquid the simple relation $\sigma = \eta\dot{\gamma}$ is observed, where η is the viscosity: since a liquid cannot sustain any force, any value of

applied force induces a flow. In the soft amorphous solids the system instead does not flow ($\dot{\gamma} = 0$) if the applied stress is below a certain threshold (called yield stress σ_y), just as a solid would do. When $\sigma \gtrsim \sigma_y$, the solid starts to flow as a liquid, with the relation

$$\dot{\gamma} \approx (\sigma - \sigma_y)^{\beta}, \tag{I.6}$$

where β is called Herschel-Bulkley exponent. (In a thermal system, such as a glass close to T_g, thermal fluctuations can obscure this sharp transition at σ_y and the solid can flow very slowly also for smaller stresses.) As discussed in the next section, this relation is typical of systems close to critical points. The passage from $\sigma < \sigma_y$ to $\sigma > \sigma_y$ is usually called yielding transition. The critical behavior around this point has received a lot of attention in recent years, and many results have been found regarding the avalanche distribution [15].

The strain rate form in Eq. (I.6) is however not representative of every material. In some cases, the yield stress fluid under external stress abruptly changes from a solid-like behavior to a liquid-like one with a jump from $\dot{\gamma} = 0$ for $\sigma < \sigma_y$ to $\dot{\gamma} = \dot{\gamma}_c$ for $\sigma > \sigma_y$. An experiment in which the solid is driven by fixing the value of the strain rate is needed to access this region in which $0 < \dot{\gamma} < \dot{\gamma}_c$ and one observes that in this case the solid shows a shear band, in which the flow is localized, and a solid region, in which $\dot{\gamma} = 0$ [46, 47]. This separation is permanent, since it is measured in the steady state.

Let us summarize the differences between the two testing protocols that we just presented: in the stress-vs-strain curve obtained from the shear start-up experiment the stress is measured as the strain increases, while in the flow-curve the strain rate is measured at the steady state for each value of the stress. In the former framework the transient behavior is accessible and one can study all types of solids, while in the latter only stationary regimes are observed, which can be measured only if the material flows instead of breaking. Moreover, two definitions of "yielding" also arise. In the strain driven case, the "static yielding" is defined as the continuous or discontinuous passage of the stress-vs-strain curve from the elastic regime to the plastic one, as discussed above. On the other hand, in the strain rate flow curve experiment one defines the "dynamic yielding" as the value of the stress at which the system starts to flow (this is analogous to what happens at the depinning transition of an interface, as we will described below). We will briefly discuss this and other terminology issues in the following. Finally, a bit of care is required when discussing the formation of a shear band. The localization of plastic activity may be observed both in the study of amorphous solids during start-up experiments [34, 40] and in the rheology of yield stress fluids in the steady state. Even if the phenomenon is qualitatively similar, the two appearances are quite different in their duration. In the start-up case strain localization may occur at some value of the applied strain but then disappears in some soft matter systems as the deformation further increases. The resulting shear band is transient, as the plastic deformation eventually invades the whole sample and strain is uniform in the final steady state. In the imposed-stress case instead, the heterogeneous flow in the form of a shear band is permanent, since one considers the steady state of the system. Recently, it has however been suggested that in some cases the transient shear bands observed in the shear start-up experiments can transform into permanent ones in the steady-state flow [46].

1.1.3 Terminology conventions

The subject that we treat is often studied in the realm of mechanics and materials science. However, our goal is to more specifically look at the yielding phenomenon through the lens of statistical mechanics and critical phenomena, in order to understand what the minimal ingredients to describe the yielding transition of amorphous solids are. This different perspective may lead to give a different meaning to same terms, so that some clarification is needed. In materials science, a solid is said to be brittle if, when a load is applied, it deforms elastically and then breaks, with little or no plastic deformation. This is the case of silicate glasses and cast iron, for example. On the other hand, if a material is able to undergo a significant plastic deformation before breaking, it is said to be ductile. According to this, there is not a clear-cut definition of brittle or ductile solids, but just a degree of ductility (or brittleness) for each material under some condition. Morevoer, this definition assumes that the solid eventually breaks, which is not the case for the yield stress fluids, where the systems can flow forever. In some computer simulations, one may define a brittle behavior when the stress has a discontinuous jump of order 1 at a precise value of the applied strain. This corresponds to the appearance of a macroscopic shear band, but without the formation of vacuum regions (no "cracks") so that the solid does not really break. In this work we define brittle and ductile along the latter lines. Ductile behavior refers to a (shear start-up) stress-vs-strain curve that is continuous in the macroscopic limit whereas brittle behavior is associated with the presence of a discontinuous stress jump that persists in the thermodynamic limit and can be followed by the establishment of a steady state.

Another discussion is needed for the notion of yielding. We already mentioned how dynamic yielding observed in the rheology of soft amorphous solids is different from the static one, defined during start-up experiments. In this latter case however, yielding is only loosely defined as the passage from the linear elastic behavior to the plastic one in which stress does not increase anymore. This concept is somewhat vague, as the point of the stress-vs-strain curve at which the behavior passes from elastic to plastic is not crisply defined. In addition, recent works in the statistical physics community showed that the linear elastic regime is still punctuated by plastic events, which makes the previous definition problematic [45, 48–50]. Another definition of yielding, used in the study of yield stress fluids, is the maximum value of stress attained during a start-up deformation experiment. Even if this value could coincide with the dynamic yield stress of the flow curve set-up, the two are actually different [46]. Here we will define yielding as a transition when there is an $O(1)$ stress discontinuity in the stress-vs-strain curve and a not precised crossover otherwise. This is reminiscent of the definition of the paramagnetic to ferromagnetic transition from the magnetization versus applied field curve.

Finally, we also note that some materials undergo a rather sharp increase in the amount of plastic deformation they can sustain before breaking as the working temperature increases above a certain value. This phenomenon is often called brittle-to-ductile transition. Its effects can be quite drastic, as for example in the sinking of the RMS Titanic [51]. In any case, the material breaks after some given loading. Our definition of brittle, ductile, and brittle-to-ductile transition is different. First of all, in what we will discuss, it is the *preparation* temperature that produces the observed change in the behavior from ductile to brittle. In the standard context of materials science, the phenomenon is caused instead by a change in the *working* temperature, so that the two concepts are quite different. Secondly, in our

language passing from brittle to ductile means having a material that abruptly fails for some preparation temperatures and plastically flows for others, while in the engineering field the material always fractures eventually.

1.2 Simulations and Theoretical models

The experimental results just discussed show salient features that are common to many types of amorphous solids. Since the non-affine motions that are at the origin of the plastic rearrangements are very localized in space, it is difficult to observe and track such displacement in experiments with a precise spatio-temporal resolution (even if it is possible for solids with large constituents, like colloids [52]).

The main advantage of Molecular Dynamics (MD) simulations method is that one can follow the trajectory of each particle and compute both global and local quantities easily. Since the goal is to mimic an amorphous solid, particles of different sizes are considered to avoid crystallization. The particles interact through a pair potential, and a common choice is the Lennard-Jones form,

$$v(i,j) = 4\epsilon_{ij}\left[\left(\frac{\sigma_{ij}}{r_{ij}}\right)^{12} - \left(\frac{\sigma_{ij}}{r_{ij}}\right)^{6}\right] + C(r_{ij}), \tag{I.7}$$

with ϵ_{ij} and σ_{ij} energy and size parameters that depend on the nature of particle i and j. The function $C(r_{ij})$ ensures a smooth behavior of the potential as it goes to 0 after some r_{cutoff}. Another possibility for the interaction potential is to consider the hard-sphere limit, in which particles are simply forbidden to overlap. In simulations one can only study a finite number of particles (thousands to sometimes millions) so that one should specify the boundary conditions. At equilibrium, in order to avoid boundary effects one usually takes periodic boundary conditions. In the case of sheared systems the natural generalization is given by the Lees-Edwards boundary conditions [53]. In this case the copies of the original simulation box move so that the conditions can be used also for large values of strain. To produce a glass, one starts from equilibrating a liquid at high temperatures, and then cools it down to the glass transition. This can be done by means of molecular dynamics or Monte Carlo algorithms, but it is hard to approach the glass transition temperature as the equilibration time increases very rapidly. New algorithms have been devised that allow one to reach extremely stable glasses, such as the Swap Monte Carlo (SWAP), in which the moves to be accepted with the Metropolis rule are not only displacements of a particle, but also exchanges between two particle sizes (see [54] and references therein). A similar problem arises when considering the strain rate in a deforming system. Small rates are hard to simulate. This issue can be sidestepped by performing the simulations with the athermal quasistatic protocol (AQS). The external strain is increased by a small quantity (chosen in such a way that the parallel occurence of multiple non-affine displacements is avoided). The system relaxes completely toward the closer energy minimum through a steepest descent method before the strain is increased again. This means that the timescale for the relaxation of an energy input to the whole system is much shorter than that given by the strain rate. At the same time, the aging that occurs in the system as a consequence of the thermal relaxation is assumed to have a much longer timescale. In the AQS one has then $\dot{\gamma} \to 0$ and $T \to 0$ and the timescale of the driving is completely decoupled from those of plastic events

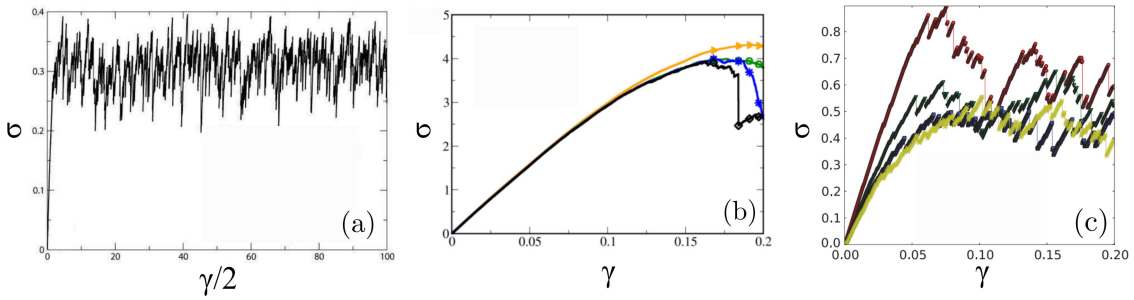

Figure I.6: Stress-vs-strain curves from MD simulations of amorphous solids. One can see a first elastic regime following by a plastic one in which the stress is constant on average. In (a) for a 2D system in the AQS limit, no overshoot is observed in the curve (from [55]). In (b) the system is in 3D and the different curves represent different values of the strain rate (decreasing from top to bottom, which is AQS). Adapted from [56]. Finally in (c) the curves are for different cooling rates during glass preparation, increasing from top to bottom. Adapted from [57].

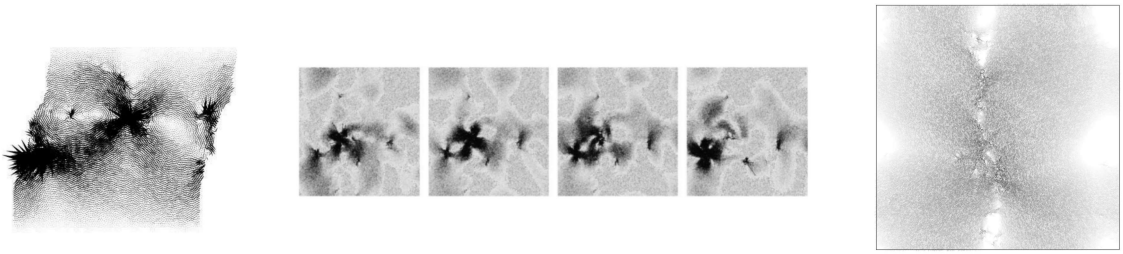

Figure I.7: (a) Displacement field associated to a localized plastic event. Larger arrows correspond to larger displacements. Adapted from [55]. (b) Instantaneous velocity field, in which an event occurs, triggers another one and then dies out, from [58]. (c) Organization of the events to form a shear band, from [59].

and aging processes. Time is therefore completely absent. As will also be seen for general out-of-equilibrium systems, the advantage of looking at the evolution of the system in this limit is that one is sure that the events that take place are associated with a mechanical instability that changes a local minimum into a saddle point. The concepts of metastable states, avalanches and discontinuous phase transitions are then crisply defined. In this sense removing temperature and driving rate is very important. The AQS protocol is considered for the rest of this work.

Let us now look at some results obtained with this approach in the shear start-up setup with controlled strain. Stress-vs-strain curves compatible with experiments are reproduced, see Fig. I.6. One observes an elastic region for small values of the applied strain and an increase in the plastic activity for larger values. Due to the latter the resulting curve shows the same jerky behavior as in experiments associated with avalanches of plastic activity.

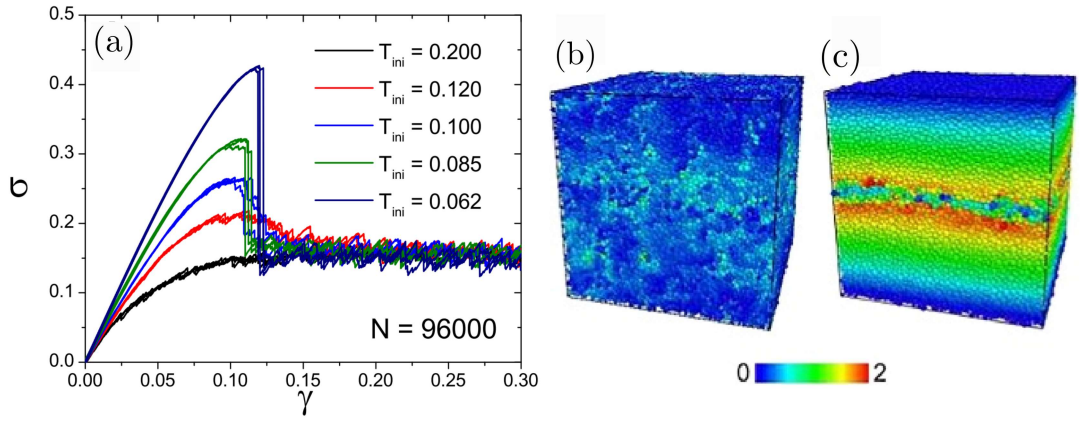

Figure I.8: (a) Stress-vs-strain curves obtained in the start-up shearing of a 3D polydisperse solid with MD simulations in the AQS limit. Different curves correspond to different preparation temperatures that affect the stability of the glass. Snapshot of non-affine displacements between $\gamma = 0$ and $\gamma = 0.13$ for $T_{\rm ini} = 0.120$ (b) and $\gamma = 0.119$ for $T_{\rm ini} = 0.062$ (c). As the preparation temperature decreases below a certain value the stress-vs-strain curve displays an $O(1)$ jump which is associated with the localization of the plastic activity in a shear band. The fact that the stress is finite after the jump is a consequence of imposing a fixed volume with Lees-Edwards periodic boundary conditions. The system is composed by $N = 96000$ particles. Figures are taken from [4].

Plastic events are localized and the strain field that is generated is compatible with the Eshelby form in Eq. (I.5) [60, 61]. The correlation between plastic events has been shown to hold also when $\dot{\gamma} > 0$ and gives rise to avalanches that are sensitive to the strain rate value [58]. As in the start-up experiments, also in this case the organization of plastic events into transient shear bands is observed [59, 62, 63]. The plastic activity accumulates in a stripe, that slowly diffuses in the whole system until a steady-state independent of the initial configuration is reached. The effect of initial preparation and testing conditions has also been studied in MD simulations [4, 57, 64–67]. Another investigation made possible by MD simulation is the study of precursors of plastic events. The rearrangements are at the origin of plastic deformation, but predicting where one such event will take place is still a difficult task. Recent progresses on this issue have been done in simulations and with machine learning approaches [68, 69].

In [4], the simple shear of glass samples formed over a wide range of preparation temperature, and as a consequence of stability, or annealing, is studied thanks to the SWAP algorithm. The samples are then instantaneously quenched to $T = 0$ before being deformed. By varying the preparation temperature one can simulate the behavior of different amorphous solids, from wet foams to ultrastable glasses. Since the system is prepared at some temperature and quenched instantaneously to $T = 0$, aging cannot take place. Moreover, the loading is imposed according to the AQS protocol, so that also the effects of the strain rate and the operating temperature are disregarded. In this way it is possible to isolate the role of only one control parameter, the fictive temperature $T_{\rm ini}$, at which the liquid fell out of

equilibrium to form a glass. As shown in Fig. I.8(a) the stress-vs-strain curve changes qualitatively with $T_{\rm ini}$, going from a monotonic curve for large values (as in foam experiments [15]) to displaying an overshoot for smaller values (as in colloids experiments [16]). The real space organization of the plastic strain is quite homogeneous during the whole evolution when the preparation temperature is high. However, as the overshoot appears, the plastic activity localizes in a shear band, as already observed previously [62]. When the external strain is increased even more this band grows and eventually spans the whole system, so that the strain is again homogeneous. For even smaller values of $T_{\rm ini}$ the stress-vs-strain curve shows a jump of order 1 that seems to survive after averaging over many samples and taking the thermodynamic limit. This jump is also associated with the nucleation of a shear band, but one which forms abruptly, during a single strain increment, and grows with the system size. This picture corresponds to a nonequilibrium first-order transition [70, 71]. For large enough values of $T_{\rm ini}$ yielding instead appears to be a smooth crossover. The order parameter defined in [4] (the maximum stress drop during the evolution) is 0 for large values of $T_{\rm ini}$ and it starts to grow to a finite value as $T_{\rm ini}$ gets smaller than a certain value $T_{\rm ini,c}$. Moreover, the fluctuations of this order parameter show a clear peak at $T_{\rm ini,c}$. These properties are indicative of the presence of a critical point that in this case separates brittle from ductile behavior. The values of $T_{\rm ini}$ for which the stress curve displays an overshoot are then larger than $T_{\rm ini,c}$, since in this case the maximum stress drop is still 0 in the thermodynamic limit.

We now discuss analytical approaches. Due to the huge number of degrees of freedom, a direct microscopic approach is impossible, and one needs to resort to approximate models built on phenomenological observations. Many of the models that have been studied analytically are furthermore considered in the mean-field limit. For the shear start-up case an important theoretical approach is the Hébraud-Lequeux model [72], which is based on a Fokker-Planck-like equation to study the distribution of stresses as the system evolves. This model has been refined by considering the nature of the Eshelby kernel [9, 73]. Other models have been proposed for soft amorphous solids. In the Soft Glassy Rheology (SGR) model [74, 75] (based on the so-called trap model introduced to describe aging in glasses [76]) the material is divided into mesoscopic elastic blocks characterized by a local strain and a maximal yield elastic energy. The contribution to each block from the plastic events occurring elsewhere in the system is considered as a thermal noise, with an effective temperature (see [77] for a discussion on the role of thermal and athermal sources of noise). In order to capture the permanent heterogeneous flow observed in some yield stress fluids the thermal fluidity model has also been proposed [78, 79].

The MD simulations can help understanding amorphous solids under deformation, but their relevance is limited by the huge computational cost needed to simulate large systems. Other complementary approaches that correspond to a mesoscopic rather than microscopic description are necessary. One such approach is provided by Elasto-Plastic Models (EPMs). The EPM has been first introduced in [80] (see [5] for a review). It is a phenomenological model in which the solid is considered at the mesoscopic level as composed by many elasto-plastic elements that interact between themselves. The blocks are taken as large enough to have a local strain, but small enough to be considered as local. Such elements behave following simple rules, but lead to a complex macroscopic dynamics. This kind of approach is common in the context of statistical mechanics, where one trades the microscopic details, specific of each particular case, in order to get a more general insight on the phenomenon

at study. The simplicity of these models allows for analytical treatment in mean-field limit and for computer simulations of large systems that would be otherwise impossible. A large part of our work makes use of such models to investigate how the preparation conditions affect the resulting mechanical properties of a sheared amorphous solid, and in particular its yielding transition, which we now describe.

1.3 The yielding transition and the influence of the preparation conditions

The study of soft amorphous solids has been focused for a long time on the properties of their steady state flow. On the other hand, in the start-up protocol, the stress of these solids increases with the applied strain until yielding occurs, after which the stress does not increase anymore. This yielding transition or crossover is generic in amorphous solids, which we have seen encompass a wide variety of materials. A successful theory for this phenomenon should then be as much as possible free of details of the specific solids and one may adopt a statistical mechanics point of view and look for an effective coarse-grained picture.

An important step is to characterize yielding and try to devise a quantity, akin to an order parameter, that distinguishes the state of the system before and after yielding takes place. Mean-field calculations on glasses in infinite dimensions [81, 82] and numerical and theoretical analyses [70, 71] have suggested that yielding corresponds to a spinodal point, i.e., a limit of stability, and that the overlap or similarity among configurations is a good order parameter. As shown in computer simulations studying a wide range of preparation conditions [4], yielding does not seem to always be a spinodal and can instead be continuous, in the form of a mere crossover, or even critical for a fine-tuned preparation condition (see above).

The effect of the initial preparation on the yielding transition is the main focus of the present work. We will in particular investigate the existence of a critical point for a fine-tuned preparation temperature and the possibility to develop an effective theory for its description. The existence of such a critical point and the occurrence of a continuous overshoot in the stress-vs-strain curves have been recently challenged, both from the theoretical side through arguments about a shear-banding instability [6] and from the numerical side by showing the presence of very strong finite-size effects in MD simulations [83, 84]. We will address this issue by studying mesoscopic models such as the EPM already introduced and models with the explicit presence of quenched disorder. Before delving more into this we first briefly introduce the field of critical phenomena and concepts that will be useful in the rest of this work.

2 A brief introduction to critical phenomena

We now introduce basic concepts of critical phenomena for systems at equilibrium, first in the "pure" case and then with the addition of some quenched disorder. We then consider out-of-equilibrium systems, focusing on the case of athermal driving, which is the relevant situation for sheared amorphous solids.

2.1 Equilibrium

2.1.1 Pure case

Let us start by reviewing the general case of a system in equilibrium at a temperature T, which is for instance defined on a discrete lattice of linear size L in d-dimensions. To each site i of the lattice a local variable s_i is associated, and the model is described by a Hamiltonian $\mathcal{H}_0(\{s_i\})$. For simplicity we only consider the case in which s_i is a scalar. When $T = 0$ the system occupies the configuration that minimizes the energy, also called the ground state (if there is a degeneracy, it occupies one of these states) and $s_i = s_{i,\mathrm{gs}}$. In this case any function of the local variables $Q(\{s_i\})$ simply takes the value $Q(\{s_{i,\mathrm{gs}}\})$. As the temperature increases, more configurations become available for the system due to thermal fluctuations, so that $Q(\{s_i\})$ is now a random variable that oscillates around a mean value $Q = \langle Q(\{s_i\})\rangle$. The notation $\langle\cdot\rangle$ stands for the average over thermal fluctuations which is computed as

$$Q = \langle Q(\{s_i\})\rangle = \sum_{\{s_i\}} Q(\{s_i\}) \frac{\exp\{-\beta\mathcal{H}_0(\{s_i\})\}}{\mathcal{Z}}, \tag{I.8}$$

with $\exp\{-\beta\mathcal{H}_0(\{s_i\})\}$ the Boltzmann factor and $\beta = 1/(k_B T)$, with k_B the Boltzmann constant. Finally, $\mathcal{Z}$ is the normalization defined as

$$\mathcal{Z} = \sum_{\{s_i\}} \exp\{-\beta\mathcal{H}_0(\{s_i\})\} \tag{I.9}$$

and is called the partition function, which is a function of temperature and of the parameters that enter the Hamiltonian $\mathcal{H}_0$. From $\mathcal{Z}$ one defines the free energy of the system as $\mathcal{F} = (-1/\beta)\ln(\mathcal{Z})$. The partition function turns out to be also extremely useful in computing the average of thermodynamic quantities. An example of $Q(\{s_i\})$ is the system-averaged quantity $s = 1/N \sum_{i=1}^{N} s_i$, with $N = L^d$ the total number of sites, and $\langle s\rangle$ its thermal average. The value of $\langle s\rangle$ can be found directly from $\mathcal{Z}$ by applying to the system under consideration a uniform source field H directly coupled with the s_i's. The Hamiltonian now becomes $\mathcal{H}(\{s_i\}) = \mathcal{H}_0(\{s_i\}) - H\sum_i s_i$. At this point one can see that the average of the system-averaged quantity s can be computed as

$$\langle s\rangle = \left.\frac{\partial \mathcal{Z}_{\mathcal{H}}}{\partial H}\right|_{H=0}, \tag{I.10}$$

and similar relations hold for higher moments of s (the subscript $\mathcal{H}$ is used here to specify that the partition function is computed for the whole Hamiltonian $\mathcal{H}$). With the addition of appropriate applied fields or sources the partition function is the generating function of all the thermodynamic quantities and correlation functions of the system.

At this point let us add the hypothesis that $\mathcal{H}_0(\{s_i\})$ is translationally invariant (as a consequence, $\langle s\rangle = \langle s_i\rangle$) and favors cooperation between s_i's at different sites (in the following we will say that such interactions are ferromagnetic, in analogy with what happens in models for magnets). This means that at $T = 0$, in the configuration that minimizes the energy, one observes the same value $s_i = s_{\mathrm{gs}}$ at every site, and the system is said to be in the ordered phase. On the other hand, when the temperature is very large, all the configurations will be almost equally probable and the system is said to be in the disordered phase, with

$\langle s \rangle = s_{\rm ds}$. Qualitatively, at equilibrium and finite temperature T, there is a competition between order, required to minimize energy, and disorder, required to maximize entropy. At small temperatures the order wins, while at large temperatures disorder does. If the quantity $\langle s \rangle$ is able to distinguish between the two states of the system it can be used as an order parameter: by looking at the value of $\langle s \rangle$ one can understand whether the system is in the ordered or in the disordered state. The temperature acts as the control parameter, and a phase transition occurs at a special value $T = T_c$. The order parameter $\langle s(T) \rangle$ is a function of temperature, and in going from $T > T_c$ to $T < T_c$ it changes from $\langle s(T \to \infty) \rangle = s_{\rm ds}$ to $\langle s(T = 0) \rangle = s_{\rm gs}$. If $\langle s(T) \rangle$ is discontinuous at $T = T_c$, the phase transition is of first order, while if it is singular but continuous it is of second-order (or higher). We will mainly focus on the latter case in the following.

Since thermal fluctuations are responsible for the destruction of the ordered phase, quantifying their strength is fundamental to understand what happens at the phase transition. This can be done by looking at the correlation function $G_{ij} = \langle s_i s_j \rangle - \langle s_i \rangle \langle s_j \rangle$ that measures how much thermal fluctuations of the local order parameter $\delta s_i = s_i - \langle s \rangle$ at some point i are related to those at point j. One expects that for close-by sites this quantity is positive and close to 1, while as the distance r_{ij} between the sites increases G_{ij} is expected to go to zero. The asymptotic behavior for large r_{ij} is given by $G_{ij} \sim \exp(-r_{ij}/\xi)$, where ξ is the correlation length. In the vicinity of a critical point, inside the region of volume ξ^d the correlation function decreases as a power law with the distance between sites, so that

$$G_{ij} \sim \begin{cases} r_{ij}^{-(d-2+\eta)} & r_{ij} \ll \xi \\ \exp(-r_{ij}/\xi) & r_{ij} \gg \xi, \end{cases} \tag{I.11}$$

where η is an exponent characterizing the model. When $T \neq T_c$ the value of ξ is finite and one can imagine dividing the system into many blocks of volume ξ^d that can be considered to be independent one from the other due to the exponential decay of correlations. However, as the critical point is approached the correlation length diverges, so that the correlations have a power law decay everywhere and fluctuations become scale free and therefore relevant on all the system sizes. Another important quantity to characterize the state of the system is its response to an external perturbation. To this end, let us add again a source field H that is linearly coupled to the order parameter and acts uniformly on every site, favoring some value of the s_i's. In the low-temperature phase this effect decides which value of the order parameter the system chooses, breaking the symmetry (if present) between the possible choices, while for some $H = H_c$ the field is not favoring any value. This allows one to define the response function of the system with respect to an external source, which is called the susceptibility and is defined as $\chi(T, H) = \partial \langle s \rangle (T, H)/\partial H$. As the system approaches the critical point, i.e. when $t = (T - T_c)/T_c \to 0$ at fixed $H = H_c$, both the correlation length and the susceptibility, ξ and χ, diverge. In the study of second-order phase transitions one defines the usual scaling relations

$$\begin{aligned} &\langle s(t, H = H_c) \rangle - s_{\rm ds} \sim (-t)^{\beta}, \\ &\chi(t, H = H_c) \sim |t|^{-\gamma}, \\ &\xi(t, H = H_c) \sim |t|^{-\nu}, \\ &C_v(t, H = H_c) \sim |t|^{-\alpha}, \end{aligned} \tag{I.12}$$

where $C_v(t, H = H_c) = -T\partial^2\mathcal{F}/\partial T^2$ is the specific heat and α, β, γ, and ν are the exponents that characterize the universality class of the critical behavior. These exponents are not independent as one can find relations between them. For example, for systems at equilibrium and finite temperature, the fluctuation-dissipation theorem gives a link between χ and G_{ij}, stating that

$$\chi = \frac{1}{Nk_BT}\sum_{i,j} G_{ij} = \frac{N}{k_BT}\langle(s - \langle s\rangle)^2\rangle. \tag{I.13}$$

The response of the system to an external field is then proportional to the thermal fluctuations of the system-averaged order parameter s. From Eq. (I.13) and Eq. (I.12) it follows that both the response function and the correlations diverge in the same way when approaching the critical point, which also gives the relation $\gamma = \nu(2 - \eta)$. Other relations between the critical exponents involve the physical dimension d, and take the name of hyperscaling relations. For example let us imagine the system as composed of many blocks with linear size of the order of the correlation length ξ. The free energy density inside this block of volume ξ^d is of the order of the temperature $\mathcal{F}_\xi \sim T$. By expressing the singular part of the free energy with the help of the specific heat exponent α (defined in Eq. (I.12)) one finds

$$2 - \alpha = d\nu. \tag{I.14}$$

In the majority of cases, the critical behavior cannot be solved exactly and one then resorts to approximate approaches. As a first step the system is usually considered in a mean-field approximation. This method amounts to substituting the interaction between s_i's with the interaction between each s_i and the mean value s. The system is then homogeneous and spatial fluctuations are neglected. The effect of such fluctuations is generally weaker at large values of d, so that above an upper critical dimension d_{uc} the mean-field predictions of the exponents are correct. However, for small values of d, thermal fluctuations can be so strong that the ordered phase is destroyed as soon as $T > 0$, which means $T_c = 0$. The value of d at which an ordered phase is no longer observed at finite temperature is called the lower critical dimension d_{lc}. For $d_{\text{lc}} < d < d_{\text{uc}}$ the mean-field approximation fails and more powerful methods need to be employed. One method that has proved particularly successful and provides a powerful framework to study critical behavior and scale invariance is the Renormalization Group approach [85, 86]. The main idea is to apply a sequence of coarse-graining and parameter-rescaling operations to progressively average out the thermal fluctuations at every scale. The fixed points of this series of operations will then be scale-invariant. One particular nontrivial fixed point is then associated to the critical point. Systems starting from different points in the parameter space can end up in the same fixed point after the renormalization procedure, in which case they are said to be in the same universality class and they share the same critical properties. Critical properties are thus quite robust with respect to changes in the details of the model and can be shared by models that have different microscopic descriptions. Due to this property, simplified effective models may be able to describe the large-scale critical physics of real physical systems, provided they fall in the same universality class.

To get a more concrete insight into these concepts we consider the archetypal example of a system at equilibrium that shows a second-order phase transition: the ferromagnetic Ising model. Here the s_i's are spins that take $+1$ or -1 values and that interact ferromagnetically following the Hamiltonian $\mathcal{H}_0(\{s_i\}) = -J\sum_{\langle i,j\rangle} s_i s_j$, where the coupling constant

J is positive and $\langle \cdot, \cdot \rangle$ denotes nearest neighbors sites. It can be shown [87] that in this case a ferromagnetic (ordered) phase in which all spins are oriented in the same direction is stable with respect to formation of a droplet with opposite sign in $d > d_{\rm lc} = 1$. When the temperature increases the system ends up in a paramagnetic (disordered) phase in which the spins are randomly oriented, so that $\langle s \rangle = 0$. Notice that the Hamiltonian function $\mathcal{H}_0(\{s_i\})$ is symmetric with respect to the inversion of all spins, i.e. $\mathcal{H}_0(\{s_i\}) = \mathcal{H}_0(\{-s_i\})$. This means that the Boltzmann weight associated to some configuration does not change if we reverse all the spins in the configuration, so that if we compute $\langle s_i \rangle$ we see that it is equal to $\langle -s_i \rangle$, which in consequence means that $\langle s_i \rangle = 0$. However, as the temperature goes below T_c, the spins conspire to align along a common direction. The system has a finite value of $\langle s_i \rangle$ (either positive or negative), and the inversion symmetry is spontaneously broken by the phase transition. Notice that this is not the only way to break a symmetry: as soon as an external field is applied to the system the term $H \sum_i s_i$ is added to $\mathcal{H}_0(\{s_i\})$. The alignment of the spins along the field is now favored, which explicitly breaks the symmetry. The Ising model can be exactly solved in $d = 2$ [88], and in $d = 3$ precise estimations of the critical exponents have been found [89, 90]. Mean-field predictions are correct for $d > d_{\rm uc} = 4$ which is the upper critical dimension in this case [91].

2.1.2 Adding quenched disorder

We now consider what happens when frozen-in (or quenched) disorder is added to the system. Indeed, no material is perfect and no magnet is pure. The effect of impurities and more generally quenched disorder on the otherwise pure system can be benign or modify the behavior. The modification of the critical properties can be small as a slight change in the exponents, or strong as completely changing the nature of the system's phases. Depending on the physical situation, disorder can be added to the system in many ways. For example, an interesting phenomenon that can be described as a disordered system is percolation, where disorder comes in at the geometrical level as the probability of having a certain number of edges in a network [92]. In spin systems as the Ising model described above, impurities are typically introduced in the Hamiltonian as lattice-site or bond dilution [93], random interactions between spins [94] or random fields coupled to each spin [95]. Another example of systems with disorder is the random manifold, where the elastic energy is minimized by a flat surface, but pinning due to the disorder compete with this ordered phase [96–98]. There are also many disordered models outside physics, for example in neuroscience [99] and computer science [100].

Let us go back to the general system described above by the Hamiltonian $\mathcal{H}_0$, adding disorder to the picture. The kind of disorder we will consider is quenched, which means that the random variables that enter in the Hamiltonian are fixed at the beginning of the dynamics and do not evolve (as opposed to annealed disorder in which they are allowed to change on a certain timescale). Since an additional source of randomness (other than temperature) is now present, it is important to consider an average over different realizations of this quenched disorder in order to reach meaningful conclusions and obtain quantities that are representative of the typical situation in the thermodynamic limit (so-called self-averaging quantities). The generic quantity $Q^\alpha(\{s_i\})$ depends of both sources (the superscript α stands for a particular realization α of the disorder) and its average over thermal fluctuations is still a random variable. The average over all the disorder realizations is hereafter indicated by an

overline, so that the fully averaged quantity is $\overline{\langle Q^\alpha(\{s_i\})\rangle}$. In the pure case we described the competition between order and (thermal) disorder, which gives rise to the phase transition. In the present case the new source of noise at play also conspires to destroy the ordered phase. Applying both averages, we define the correlation function as $G_{ij} = \overline{\langle s_i s_j\rangle} - \overline{\langle s_i\rangle}\,\overline{\langle s_j\rangle}$. In order to quantify the contribution of each source of fluctuations we can split this correlation function in two terms, which read

$$\begin{aligned} G_{\mathrm{c},ij} &= \overline{\langle s_i s_j\rangle} - \overline{\langle s_i\rangle\langle s_j\rangle} \\ G_{\mathrm{d},ij} &= \overline{\langle s_i\rangle\langle s_j\rangle} - \overline{\langle s_i\rangle}\,\overline{\langle s_j\rangle}, \end{aligned} \tag{I.15}$$

with $G_{ij} = G_{\mathrm{c},ij} + G_{\mathrm{d},ij}$. The function $G_{\mathrm{c},ij}$, called connected correlation function, is the average over the frozen-in disorder of the correlation function defined for the pure system and it quantifies the effect of thermal fluctuations as in the pure case. On the other hand, $G_{\mathrm{d},ij}$, called disconnected correlation function, is a measure of the sample-to-sample fluctuations coming from the addition of quenched disorder. In this case the fluctuation-dissipation theorem still holds, but the response function is proportional to the connected part of the correlation $G_{\mathrm{c},ij}$ alone, so that the connected susceptibility is $\chi_{\mathrm{conn}} = \partial\overline{\langle s\rangle}/\partial H = N\beta\overline{\langle(s^\alpha - \langle s^\alpha\rangle)^2\rangle}$. Once again, the thermal fluctuations scale at the critical point as the response function, but the critical exponents are in general different from the pure case. The disconnected correlation function is a priori not related to any response function, but by symmetry one can define the disconnected susceptibility as $\chi_{\mathrm{disc}} = N\beta(\langle s^\alpha\rangle - \overline{\langle s^\alpha\rangle})^2$. The disconnected susceptibility χ_{disc} can be defined in general for any kind of quenched disorder following the definition in Eq. (I.15), but it is not always a relevant quantity. To see why, let us consider for example the case of the Edwards-Anderson [94] model, with Hamiltonian given by

$$\mathcal{H}(\{s_i\}) = -\sum_{\langle i,j\rangle} J_{ij} s_i s_j \tag{I.16}$$

where J_{ij} is a random variable of 0 mean and standard deviation J. In this case, as in the pure Ising model, the Hamiltonian is still symmetric with respect to the inversion of the spins. Once again one can then prove that $\langle s_i\rangle^\alpha = \langle -s_i\rangle^\alpha = 0$ for any realization α of the disorder. From the definition in Eq. (I.15), the disconnected susceptibility is always 0. Let us now consider a different kind of disorder, obtained by adding a local random field h_i linearly coupled to the s_i's. The Hamiltonian is no longer symmetric with respect to the inversion of the spins, as the contribution coming from $h_i s_i$ changes sign under this transformation. The symmetry is only recovered after an average over the disorder realization, if the distribution of the random fields is symmetric around 0. In this case there is one extra exponent to describe the scaling of the correlations close to the critical point, since here there are two functions which can both diverge. The scaling relations are

$$\begin{aligned} G_{\mathrm{c},ij} &\sim r_{ij}^{-(d-2+\eta)}, \quad & \chi_{\mathrm{conn}} &\sim t^{-\gamma} \\ G_{\mathrm{d},ij} &\sim, r_{ij}^{-(d-4+\bar{\eta})}, \quad & \chi_{\mathrm{disc}} &\sim t^{-\bar{\gamma}}, \end{aligned} \tag{I.17}$$

where, $\gamma = \nu(2-\eta)$ as in the pure case, and $\bar{\gamma} = \nu(4-\bar{\eta})$ (with the exponent ν defined as in Eq. (I.12)).

In the following we will discuss the case in which the quenched disorder comes in the form of random fields coupled to the order parameter. One can show that the disconnected

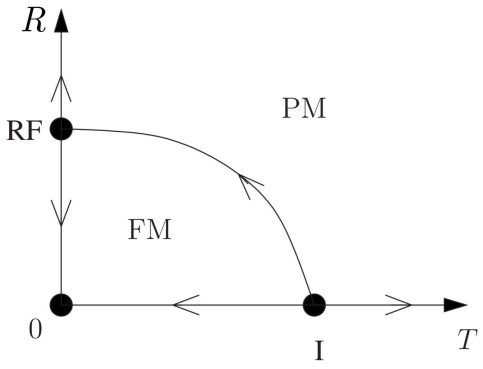

Figure I.9: Schematic renormalization flow of the RFIM in the disorder strength-temperature plane. The fixed point I at $R = 0$ is the one of the standard Ising model and is unstable with respect to a small random-field perturbation. The other fixed point is found at $R = R_c$ and $T = 0$. Adapted from [104].

susceptibility associated with fluctuations that originate from such a kind of disorder diverge faster than the connected part near the critical point [101]. This can also be seen by considering again the hyperscaling relation that we discussed in Eq. (I.14). The difference in the case with random fields is that inside a block of the system of size ξ^d, the variation of the free-energy density is proportional to the random field fluctuations which dominate over the thermal ones and grow as ξ^θ [102] (using the central limit theorem one would argue for $\theta = d/2$, but we have to remember that the random field gets renormalized as one approaches the critical point). From this consideration one finds the modified hyperscaling relation

$$2 - \alpha = (d - \theta)\nu, \tag{I.18}$$

with θ another critical exponent, which describes the (dangerous) irrelevance of temperature [103]. Such exponent is related to the ones introduced before by the equation $\bar{\eta} = 2 + \eta - \theta$. The inequality $\bar{\eta} \leq 2\eta$ has been further proven [101], which confirms that indeed $\bar{\gamma} \geq \gamma$ for systems with a random field.

Let us more specifically focus on the random-field Ising model (RFIM) [103], whose Hamiltonian is given by

$$\mathcal{H}(\{s_i\}) = -\sum_{\langle i,j \rangle} J s_i s_j - \sum_i (H + h_i) s_i \tag{I.19}$$

where h_i's are the local random fields. Here and in the following we assume that the random fields are independent variables chosen from a Gaussian distribution of average zero and standard deviation R. Changing the average value just amounts to shifting the homogeneous external field H, while changing R controls the strength of the quenched disorder. Different random field distributions have been studied [105] but, loosely invoking universality, we only consider Gaussian random fields. It is easy to imagine that when $R/J \gg 1$ the interaction with the local random field dominates over the interaction with the neighboring spins, making the system evolve as a collection of independent entities. When instead $R/J \ll 1$, one can show via the Imry-Ma argument [106] that an ordered phase in which $\langle s \rangle = \pm 1$ is destroyed

by a droplet of opposite sign of radius r for $d < 2$ (a more refined argument that takes into account the roughness of the droplet's surface shows that this is the case also for $d = 2$ [107]). We can already see here a confirmation of the result $\bar{\gamma} > \gamma$ that we discussed above: disorder fluctuations are more important than thermal ones. The Imry-Ma argument is indeed based on the energetic advantage of creating a droplet with spins with opposite sign with respect to the overall magnetization compared to the energetic cost of creating an interface, but it neglects the entropic contribution given by the multiple possible contours. The lack of this term is distinct from the Peierls argument used for the pure Ising model in which this is precisely the term that destroys order [87]. Nonetheless, the Imry-Ma argument provides the correct prediction, as it has been rigorously shown that the lower critical dimension of the RFIM is indeed $d_{\rm lc} = 2$. The model was solved in the mean-field fully-connected limit [108] by using the replica trick. In this case a critical point at $(R_c, T = 0)$ is observed, in addition to the one of the pure case at $(R = 0, T = T_c)$. Moreover, in the solution one observes once again that the thermal fluctuations are less important with respect to the disorder-related ones, as $\eta = \bar{\eta} = 0$, so that $\chi_{\rm disc} \propto \chi^2_{\rm conn}$. Finally, results from renormalization group approaches show that the addition of a random field is a relevant perturbation to the fixed point associated with the pure system critical point, and the renormalization flow brings the whole line of critical points when $R > 0$ to a new fixed point at zero renormalized temperature [109]. At $T = 0$ the disorder strength R is the control parameter and $R = R_c$ is the critical point (see Fig. I.9). When $R > R_c$ the system is in the paramagnetic phase, while for $R < R_c$ a spontaneous magnetization appears. This is compatible with the absence of an entropic term in the Imry and Ma argument on the stability of ordered phase. The contribution of quenched disorder to the correlations is more important than the one from thermal fluctuations, so that the system can be effectively considered at $T = 0$. Within the Non-Perturbative Functional Renormalization Group (NPFRG) approach [110] one can also compute the scaling of the two susceptibilities. In the RFIM the inequality $\bar{\eta} \leq 2\eta$ saturates in $d = 2$, while for $d \geq d_{\rm DR} \approx 5.1$ we have $\bar{\eta} = \eta$. For $2 < d < d_{\rm DR}$ it is difficult to obtain exact results, but analytical [111] and numerical [112, 113] methods show that the relation $\bar{\eta} = 2\eta$ does not hold anymore.

An important consequence of the link between the dominance of the disorder-related fluctuations over the thermal ones and the presence of a random field is that one can use this relation in the other direction. By measuring and comparing the two susceptibilities (disconnected and connected) for a system in which there are no obvious random fields at the microscopic level, one can detect whether there is the emergence of effective random fields linearly coupled to the local order parameter. This idea of comparing the connected and disconnected susceptibilities has been already used to study different systems in which a random-field like disorder is not present a priori [114, 115].

2.2 Out of equilibrium

In the previous section we gave a basic introduction to the study of critical phenomena in systems at equilibrium, starting with the case of a pure system and then taking disorder into consideration, with a particular focus on the RFIM. However, this situation is not representative of the case we study here, i.e., that of solids under deformation, where energy is directly inserted into the system from the outside. We then consider the case of a system that is driven by an external field H, without possibility to relax and hence out of equilibrium.

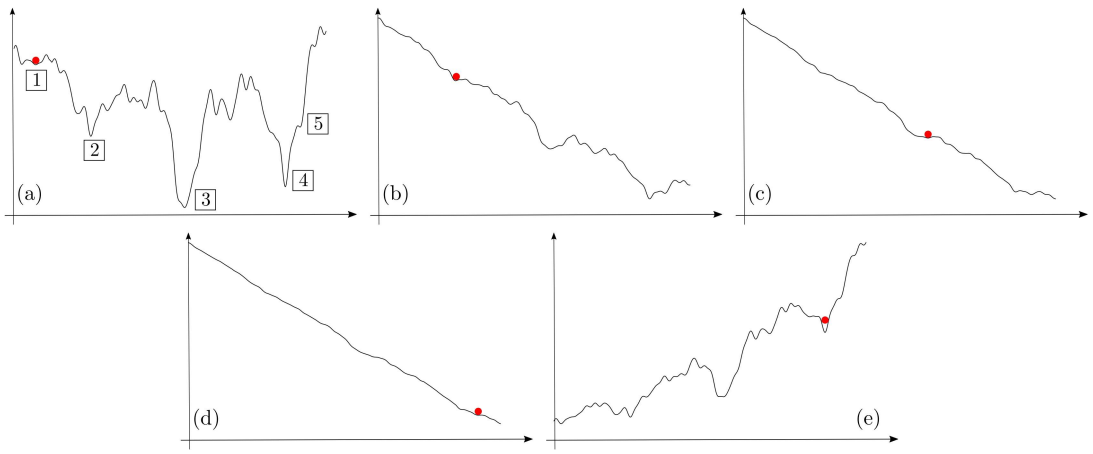

Figure I.10: Energy landscape for a disordered system (a). As the external field increases the system moves to the next minimum when the metastable state it occupies becomes unstable (b-d). As the external field is decreased, the system stays in the last metastable state it visited until it becomes unstable at a different value of the external field (e). Notice that this picture is a crude approximation, as one should imagine the energy landscape in N^d dimensions.

There is a huge amount of work on systems out of equilibrium, which correspond to a very broad range of situations. A different way of bringing a system out of equilibrium is for example encountered in active matter, when energy is injected in the system at the microscopic level. In some other cases the disorder is so strong that the system cannot relax to the minimum of its energy and keeps evolving out of equilibrium, as for example aging in glasses. Here we will focus on the case in which the system is driven by an external field and is moreover at zero temperature. We will comment on the role of temperature later on.

Consider a pure system at zero temperature which has two metastable states, namely states 1 and 2, separated by an energy barrier. The system starts its evolution from state 1 for the initial value of the applied external field $H = H_0$. As H increases, the energy landscape tilts. However, due to the absence of temperature, the system remains in state 1, as jumping over a barrier is not possible. Only when the barrier disappears, making state 1 unstable, will the system jump to state 2 (at $H = H_{1\to 2}$). However, if we now start to decrease the field, the system does not jump back from 2 to 1 at the same value of H, for the same reason as before. Only when state 2 becomes unstable at $H_{2\to 1}$ the system will jump back to the original state 1. The evolution of the system then depends on the states it visited before. This history dependence is called hysteresis. Notice that this reasoning is true in general for a simple athermal driven system. When one adds disorder to the picture the energy landscape becomes much more complex and many local minima appear, some of which will have an energy value close to the one of the ground state, without necessarily being in the same neighborhood in the configurational space. The system (schematized in Fig. I.10) evolves then through sequences of discontinuous jumps from one metastable state to the other, called *avalanches*. Studying the distribution of such avalanches is important to characterize the dynamical properties of the system. (The rapid increase in the number of metastable states

following the addition of disorder has also important consequences in systems that are not driven, but try to relax to the ground state from a metastable state; the needed relaxation time increases very rapidly giving rise to glassy dynamics.) In some cases, such avalanches can become so large that they span the whole system. The size distribution of avalanches can change drastically depending on the disorder and/or the value of the driving field. The divergence of the avalanche size implies strong correlations over all the system size and is reminiscent of the power-law behavior of the correlation functions observed at critical point in equilibrium. This scale invariance naturally leads one to use similar language and tools as for equilibrium critical behavior to describe these systems which are far from equilibrium. It is valuable to use ideas from the Renormalization Group (RG) also in this case. The RG equations for the flow in the parameter space can be obtained with the help of the Martin-Siggia-Rose-Janssen-de Dominicis (MSRJD) formalism [116–118], which allows one to build a generating functional (in the same spirit as the partition function in equilibrium) based on the dynamic Langevin equation [119]. The advantage of this approach is that the system can be studied in a similar fashion to the equilibrium case, making the comparison between the two cases more direct. (This is particularly important for the RFIM, since the equilibrium and non-equilibrium critical exponents are very close and it is difficult to decide if the two critical points are in the same universality class [120, 121].) This framework can be used for any system in which a self-consistent equation of motion for the order parameter can be derived. In the following we will show how this method can be used to find a relation between the connected and disconnected susceptibilities in a general system with random-field disorder. To this end, let us once again consider the system that we discussed in the equilibrium case, described by a Hamiltonian such as $\mathcal{H}(\{s_i\}) = \mathcal{H}_0(\{s_i\}) - \sum_i h_i s_i$, where random fields h_i are linearly coupled to the local order parameters. The dynamics of spin s_i under a drive by an applied field H is described by

$$\partial_t s_i(t) = -\frac{\partial \mathcal{H}_0(\{s_i\})}{\partial s_i(t)} + h_i + H(t), \tag{I.20}$$

By using the Martin-Siggia-Rose-Janssen-de Dominicis formalism and introducing the auxiliary variables $\widehat{s_i}$ one can define a dynamical partition function as well as a dynamical action [110] as

$$\mathcal{Z}_h[\boldsymbol{H}, \widehat{\boldsymbol{H}}] \equiv e^{\mathcal{W}_h[\boldsymbol{H},\widehat{\boldsymbol{H}}]} = \int \prod_i \mathcal{D}s_i \prod_i \mathcal{D}\widehat{s}_i e^{-\mathcal{S}_h[\boldsymbol{s},\widehat{\boldsymbol{s}}]+\sum_i \int_t [\widehat{H}_i(t)s_i(t)+H_i(t)\widehat{s}_i(t)]}, \tag{I.21}$$

where we have used the Ito prescription [122], and where

$$\mathcal{S}_h[\boldsymbol{s}, \widehat{\boldsymbol{s}}] = \sum_i \int_t \widehat{s}_i(t)[\partial_t s_i(t) + \frac{\partial \mathcal{H}_0(\boldsymbol{s}(t))}{\partial s_i(t)} - h_i - H(t)], \tag{I.22}$$

with $\int_t \equiv \int_{-\infty}^{+\infty} dt$. We also added site-dependent sources $H_i(t)$ and $\widehat{H}_i(t)$ in order to generate the correlation functions that we are interested in. At the end of the process we will take $\widehat{H}_i(t) = H_i(t) = 0$ and $H(t) = H + \Omega t$ with $\Omega \to 0^+$. Brackets indicate that we are now dealing with functionals of the variables considered at all times. Due to the presence of the random fields, the action $\mathcal{S}_h$ and the free energy $\mathcal{W}_h$ both depend on the disorder realization (in this case $\alpha \equiv \{h_i^\alpha\}$) and can be characterized by their cumulants. With the

choice of Gaussian random fields, the action is also a Gaussian random functional which is characterized by its first two cumulants given by

$$\begin{aligned} S_1[\boldsymbol{s},\widehat{\boldsymbol{s}}] &= \overline{\mathcal{S}_h[\boldsymbol{s},\widehat{\boldsymbol{s}}]} = \sum_i \int_t \widehat{s}_i(t)[\partial_t s_i(t) + \frac{\partial \mathcal{H}_0(\boldsymbol{s}(t))}{\partial s_i(t)} - H(t)], \\ S_2[\boldsymbol{s},\widehat{\boldsymbol{s}}] &= \overline{\mathcal{S}_h[\boldsymbol{s},\widehat{\boldsymbol{s}}]^2}^{\rm cum} = \Delta_{\rm B} \sum_i \int_t \int_{t'} \widehat{s}_i(t)\widehat{s}_i(t'), \end{aligned} \tag{I.23}$$

where the superscript "cum" indicates a cumulant average. For further use, we note that the variance of the bare random field $\Delta_{\rm B}$ (the B subscript is used to distinguish this from the renormalized disorder that will be introduced later and $\Delta_{\rm B}$ correspond to the square of the standard deviation R considered above) is then obtained by differentiating the second cumulant twice,

$$\Delta_{\rm B}\delta_{ij} = \frac{\partial^2 S_2[\boldsymbol{s},\widehat{\boldsymbol{s}}]}{\partial\widehat{s}_i(t)\partial\widehat{s}_j(t')}, \tag{I.24}$$

or equivalently, since the second derivative is purely local,

$$\Delta_{\rm B} = \frac{1}{N}\sum_{ij} \frac{\partial^2 S_2[\boldsymbol{s},\widehat{\boldsymbol{s}}]}{\partial\widehat{s}_i(t)\partial\widehat{s}_j(t')}, \tag{I.25}$$

where the second cumulant is here independent of time: This expresses the property that the disorder is purely static (quenched). The cumulants of the random free energy $\mathcal{W}_h$ can also be introduced, with $W_1[\boldsymbol{H},\widehat{\boldsymbol{H}}]$ the first cumulant, $W_2[\boldsymbol{H},\widehat{\boldsymbol{H}}]$ the second cumulant, etc., and one then has

$$W[\boldsymbol{H},\widehat{\boldsymbol{H}}] = \ln \overline{\mathcal{Z}_h[\boldsymbol{H},\widehat{\boldsymbol{H}}]} = W_1[\boldsymbol{H},\widehat{\boldsymbol{H}}] + \frac{1}{2}W_2[\boldsymbol{H},\widehat{\boldsymbol{H}}] + \frac{1}{3!}W_3[\boldsymbol{H},\widehat{\boldsymbol{H}}] + \cdots \tag{I.26}$$

For a complete description of the functional dependence of the cumulants on their arguments and a more transparent introduction of the expansion in cumulants one could introduce copies or replicas of the system with the same random field but coupled to different sources [110, 119, 123]. However, this is not really needed here and we proceed without replicas to alleviate the notations. As in the equilibrium case, one obtains all the correlation functions from $W[\boldsymbol{H},\widehat{\boldsymbol{H}}]$ by functional differentiation. For the connected susceptibility we have

$$\chi_{\rm conn}(H) = \frac{1}{N}\sum_{i,j} FT_{\omega=0}\, \overline{\widehat{s}_i(t)s_j(t')}\big|^{\rm cum}_{\rm unif} = \frac{1}{N}\sum_{i,j} FT_{\omega=0}\, \frac{\partial^2 W_1[\boldsymbol{H},\widehat{\boldsymbol{H}}]}{\partial H_i(t)\partial\widehat{H}_j(t')}\Big|_{\rm unif}, \tag{I.27}$$

while for the disconnected one,

$$\chi_{\rm disc}(H) = \frac{1}{N}\sum_{i,j} \lim_{|t-t'|\to+\infty} \overline{s_i(t)s_j(t')}\big|^{\rm cum}_{\rm unif} = \frac{1}{N}\sum_{i,j} \lim_{|t-t'|\to+\infty} \frac{\partial^2 W_2[\boldsymbol{H},\widehat{\boldsymbol{H}}]}{\partial\widehat{H}_i(t)\partial\widehat{H}_j(t')}\Big|_{\rm unif}, \tag{I.28}$$

where the subscript "unif" indicates uniform sources with, for all sites i, $\widehat{H}_i = 0$ and $H_i(t) = H$ (in the limit $\Omega \to 0^+$), and FT_ω denotes a Fourier transform over the time difference $t - t'$. If one wishes to evaluate the strength of the renormalized random field once fluctuations on all scales have been taken into account, one must substitute the bare action with the effective

action or Gibbs free energy $\Gamma[\widehat{\boldsymbol{m}}, \boldsymbol{m}]$. The latter is obtained from the free energy $W[\boldsymbol{H}, \widehat{\boldsymbol{H}}]$ through a Legendre transform,

$$\Gamma[\widehat{\boldsymbol{m}}, \boldsymbol{m}] = -W[\boldsymbol{H}, \widehat{\boldsymbol{H}}] + \sum_i \int_t [H_i(t)\widehat{m}_i(t) + \widehat{H}_i(t) m_i(t)] \tag{I.29}$$

where $\widehat{m}_i(t) = \partial W[\boldsymbol{H}, \widehat{\boldsymbol{H}}]/\partial H_i(t) = \overline{\widehat{s}_i(t)}$ and $m_i(t) = \partial W[\boldsymbol{H}, \widehat{\boldsymbol{H}}]/\partial \widehat{H}_i(t) = \overline{s_i(t)}$. Just like the free energy $W[\boldsymbol{H}, \widehat{\boldsymbol{H}}]$ in Eq. (I.26)), the effective action can be expanded in cumulants (again, a more precise connection is obtained by introducing replicas),

$$\Gamma[\widehat{\boldsymbol{m}}, \boldsymbol{m}] = \Gamma_1[\widehat{\boldsymbol{m}}, \boldsymbol{m}] - \frac{1}{2}\Gamma_2[\widehat{\boldsymbol{m}}, \boldsymbol{m}] + \frac{1}{3!}\Gamma_3[\widehat{\boldsymbol{m}}, \boldsymbol{m}] - \cdots \tag{I.30}$$

with

$$\begin{aligned} \Gamma_1[\widehat{\boldsymbol{m}}, \boldsymbol{m}] &= -W_1[\boldsymbol{H}, \widehat{\boldsymbol{H}}] + \sum_i \int_t [H_i(t)\widehat{m}_i(t) + \widehat{H}_i(t) m_i(t)], \\ \Gamma_2[\widehat{\boldsymbol{m}}, \boldsymbol{m}] &= W_2[\boldsymbol{H}[\widehat{\boldsymbol{m}}, \boldsymbol{m}], \widehat{\boldsymbol{H}}[\widehat{\boldsymbol{m}}, \boldsymbol{m}]], \end{aligned} \tag{I.31}$$

etc., where $H_{i,t}[\widehat{\boldsymbol{m}}, \boldsymbol{m}] = \partial \Gamma_1[\widehat{\boldsymbol{m}}, \boldsymbol{m}]/\partial \widehat{m}_i(t)$ and $\widehat{H}_{i,t}[\widehat{\boldsymbol{m}}, \boldsymbol{m}] = \partial \Gamma_1[\widehat{\boldsymbol{m}}, \boldsymbol{m}]/\partial m_i(t)$ are non-random sources. By analogy with Eq. (I.25), one can define the component of the variance of the renormalized random field that is local in space and independent of time as

$$\Delta_{\text{eff}}(m) = \frac{1}{N} \sum_{ij} \frac{\partial^2 \Gamma_2[\boldsymbol{m}, \widehat{\boldsymbol{m}}]}{\partial \widehat{m}_i(t) \partial \widehat{m}_j(t')}\Big|_{\text{unif}}, \tag{I.32}$$

where the subscript "unif" now indicates uniform variables with $\widehat{m}_i = 0$ and $m_i(t) = m$. (Remember that we consider the quasi-static limit, for which it can be shown that the above defined quantity for such uniform variables is indeed purely static [110].) By using the properties of the Legendre transform and Eq. (I.31), it is straightforward to relate $\Delta_{\text{eff}}(m \text{ or } H)$ to the connected and disconnected susceptibilities introduced in Eqs. (I.27) and (I.28):

$$\Delta_{\text{eff}}(H) = \frac{\chi_{\text{disc}}(H)}{\chi_{\text{conn}}(H)^2}\,. \tag{I.33}$$

This allows us to define the strength of the renormalized random field, i.e., the effective random field obtained after having included all fluctuations. This effective random field of course needs not be Gaussian nor purely local, and the renormalized disorder may include other forms of randomness, but Eq. (I.33) provides us with an estimate of the dominant contribution. This equation gives us the possibility to assess the presence and the strength of the random field in systems in which this is not easy detectable. Notice that this holds even if the random field is not present explicitly in the microscopic definition of the system. In such cases one can imagine that the random field is emergent and arises as the system evolves. In Chapter 3 we will use this formula to study the effective field strength in a mean-field version of the Elasto-Plastic model.

2.2.1 Interface depinning

A first example of athermally driven systems is interface depinning. In this case an elastic interface is forced to move through a disordered medium. The role of the external field is

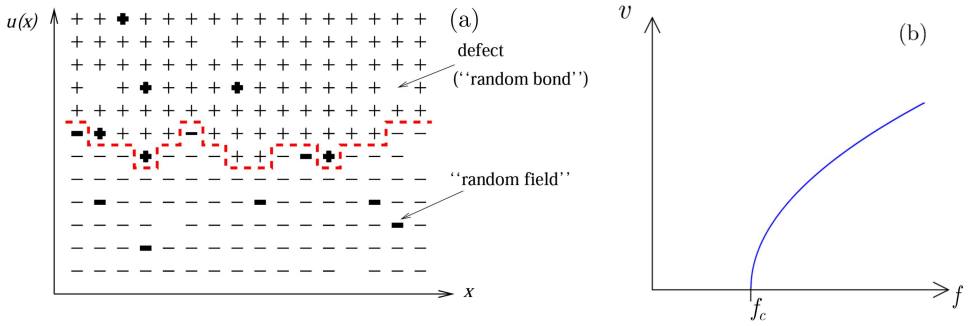

Figure I.11: (a) Schematic representation of an interface in a disordered environment, with both random bonds and random fields represented. Figure taken from [124]. (b) Average velocity of the pinned interface as a function of the applied force. Depinning takes place at $f = f_c$.

played by the force pulling the interface, while the role of the disorder is played by some pinning sites. It is the competition between disorder and elasticity that creates a complex energy landscape with many metastable states. Let us consider for simplicity the case of a one-dimensional ($d_{\mathrm{I}} = 1$) interface moving in a two-dimensional space ($d_{\mathrm{S}} = 2$). We call x the direction along which the interface is defined and $u(x)$ its position (see Fig. I.11(a)). We also make the hypothesis that $u(x)$ does not differ too much from a flat surface in that there are no overhangs and no bubbles in the interface, so that $u(x)$ is a single-valued function. The Hamiltonian of this model is

$$\begin{aligned}\mathcal{H}[u] &= \mathcal{H}_{\mathrm{el}}[u] + \mathcal{H}_{\mathrm{dis}}[u] = \\ &\frac{1}{2}\int_0^L dx[\nabla u(x)]^2 + \int_0^L dx \int_0^{u(x)} dz V(x,z),\end{aligned} \tag{I.34}$$

where the first part is given by short-range elasticity and the second one describes a pinning potential due to some random-field disorder. Here, the elastic constant is equal to 1. In the equilibrium case, one can show [125] that below $d = 4$ and at large enough L, the disorder dominates the elastic energy and the interface is therefore pinned and characterized by a roughness exponent. The system can then be brought out of equilibrium by applying a force to the interface. Its evolution is described by the overdamped Langevin equation

$$\partial_t u(x,t) = \partial_x^2 u(x,t) + F(x, u(x,t)) + f_{\mathrm{ext}}, \tag{I.35}$$

where $F(x, u(x,t)) = -\partial_u V(x,u)$ is a random force and f_{ext} is the external forcing. One can imagine that if the force is small enough the interface will stay pinned. On the other hand, for a very large applied force, all the energy landscape will be tilted and the interface will move ballistically at some velocity v. These two regimes are separated by a critical value of the force f_{c} at which the depinning of the interface occurs. The behavior of the average velocity close to the transition is very similar to what is observed in a second-order phase transition, so that one can define a critical exponent β such that $v \sim (f_{\mathrm{ext}} - f_c)^{\beta}$ (sketched in Fig. I.11(b)). Due to the presence of many metastable states the motion of the interface is characterized by a succession of avalanches of characteristic size ξ, for which one can define

the critical exponent ν as $\xi \sim (f_{\text{ext}} - f_c)^{-\nu}$. Moreover the system shows hysteretic behavior as one changes the sign of the applied force, as one would expect. Once again an approach based on the MSRJD formalism leads to flow equations of the Functional Renormalization Group, that predict critical exponents and scaling functions [126]. Many variations of this model are possible, for example: long-range elasticity, different types of disorder, different dynamics, etc. [127, 128].

2.2.2 Athermally driven Random Field Ising model

Let us now go back to the example of the RFIM, introduced in the previous section, and let us drive the system out of equilibrium at $T = 0$, by slowly applying an external field $H(t)$. The Hamiltonian for this model is the same one in Eq. (I.19) and the athermal quasistatic evolution is described by

$$s_i = \text{sgn}(h_i^{\text{eff}}) = \text{sgn}(J \sum_{j/i} s_j + H + h_i) \tag{I.36}$$

where $\text{sgn}(\cdot)$ is the sign function, the sum over j/i stands for the neighbors of i and we defined the local effective field h_i^{eff} [10, 129–131]. Imagine to start the evolution of the system from a situation in which the applied field $H(t = 0) \to -\infty$, so that all the spins will be pointing down. As one increases H, one increment δH will in some cases change the sign of the effective field somewhere in the lattice, inducing a new spin flip. This process, if repeated, can then lead to an avalanche. Due to the presence of such avalanches the magnetization-versus-field curve is not smooth, but is instead composed of discontinuous jumps of different amplitude which however disappear in the thermodynamic limit (unless an extensive number of spins flip, which correspond to a magnetization jump of $O(1)$). Such reorganizations of regions of multiple spins can be very broadly distributed in size: very often there will be only few spins flipping and more rarely a larger region will rearrange. In the quasistatic protocol, which implies $H(t) = \Omega t$ with $\Omega \to 0^+$, after the external field is increased by δH the subsequent avalanche takes place at fixed value of the external field and the field H is increased again only once the avalanche has completely relaxed. Due to the hysteresis property, the value of the external field at which the average magnetization jumps by $O(1)$ changes sign is not $H = 0$ as in the equilibrium case, but is in general $H = H_{\text{co}}(R) > 0$ ($H_{\text{co}}(R) < 0$) for the ascending (descending) branch. The evolution finally stops once all spins are pointing upwards and the total magnetization reaches $s = 1$. The distribution of the avalanche sizes is then an important quantity to be studied. One can expect that for a very strong disorder the spins evolve as if they were independent and they flip when the condition $H = -h_i$ is realized. On the other hand if no disorder is present, the spins flip all together as in the pure Ising model. In the limit of a quasistatic driving, a critical point is found for a specific value of the disorder strength R_c and separates a low-disorder phase in which the magnetization curve has a discontinuous behavior and a high-disorder phase in which it is instead continuous (in the thermodynamic limit) [10, 130, 131]. For $R = R_c$ the distribution of the avalanches shows a power law with a critical exponent that characterizes the universality class of the model. A convenient order parameter to capture this transition is the largest jump in the magnetization curve, defined as $\Delta m^{\alpha}_{\text{max}} = \max_H(m^{\alpha}(H + \delta H) - m^{\alpha}(H))$. The average of the order parameter, defined as $\Delta m_{\text{max}} = \overline{\Delta m^{\alpha}_{\text{max}}}$, shows a continuous decrease from a finite value for $R < R_c$ to 0 as $R > R_c$, similarly to what one would observe in an equilibrium

second-order phase transition (see Fig. I.12(b)). As for the equilibrium case, one can then write $\Delta m_{\max} \sim (R - R_c)^{\beta}$ with β a critical exponent. One can also define other critical exponents to characterize scale invariance. For the susceptibilities one has for example

$$\begin{aligned} \chi_{\text{conn}}(r, H_c) &\sim r^{-\gamma} \\ \chi_{\text{disc}}(r, H_c) &\sim r^{-\bar{\gamma}}, \end{aligned} \tag{I.37}$$

with $H_c = H_{co}(R_c)$ the critical field and $r = (R - R_c)/R_c$ the reduced disorder strength. The critical properties of the RFIM in and out of equilibrium are very similar, to the point that for a long time it was believed that the two critical points belonged to the same universality class. Only recently, by means of the MSRJD formalism and the NonPerturbative-Functional Renormalization Group critical exponents and scaling functions have been shown to be different for the equilibrium and non-equilibrium critical points, except when $d > d_{\text{DR}} \approx 5.1$ (the value of d below which dimensional reduction breaks down) [110].

Before moving on we make use of this well known model to show the procedure that we are going to use in the rest of this work to capture the critical properties of the other AQS driven model under study. Since precise results on the RFIM under AQS driving exist both from RG theoretical arguments and from numerical simulations, this is a good playground to illustrate how the analysis of an out-of-equilibrium system close to the critical point can be performed. The code we used to simulate the standard RFIM is detailed in Appendix B and is based on [129]. The results for this model are shown in Fig. I.12. In the simulations one cannot access the thermodynamic limit, and the available system sizes are usually quite limited. Yet, a true phase transition cannot take place in a finite-size system and only exists in the thermodynamic limit. As a consequence, the predicted scaling cannot be observed arbitrarily close to the critical point since we only have access to a finite system. The usual procedure in this case, which we will also apply, is to study these properties for different system sizes and consider that, if we are sufficiently close to the critical point, the correlation length ξ becomes very large. It follows that the characteristic spatial extent of the fluctuations correlations will be limited by the system size L, so that we can substitute $\xi \sim L$ in the scaling relations. We can then measure the exponent γ via $\chi_{\text{conn},L} \sim L^{\gamma/\nu}$ and similarly the exponent $\bar{\gamma}$ via $\chi_{\text{disc},L} \sim L^{\bar{\gamma}/\nu}$ by a careful finite-size scaling analysis with the hope that it properly captures the thermodynamic limit. With this in mind, we focus on the computation of the disconnected susceptibility and on the related exponent. We first compute the sample-to-sample fluctuations of the order parameter $\Delta m^{\alpha}_{\max}$, depicted in Fig. I.12(c). It is clear from the figure that the variance of the fluctuations grows very large as one increases the system size, which is a signature of the critical point. We then perform the finite-size scaling analysis by collapsing the curves for different system sizes onto a single master curve, with the scaling ansatz

$$\chi_{\text{disc,L}}(r) \sim L^{\bar{\gamma}/\nu} \Psi(r L^{1/\nu}), \tag{I.38}$$

where $\bar{\gamma}$ and ν are the critical exponents introduced before and $\Psi(\cdot)$ is a scaling function. This procedure gives us an estimate of the critical exponents, which match with previous results from NPFRG [110]. Note that this approach is not the only possible one. For example, in [129, 131], a similar analysis has been carried on for the connected susceptibility. In this case the order parameter that is used is the magnetization and the collapse is performed directly for $\overline{m}(H, r) = M_c + |r|^{\beta} F((h + Br)/|r|^{\beta\delta})$, with β and δ critical exponents, $h = H - H_c$

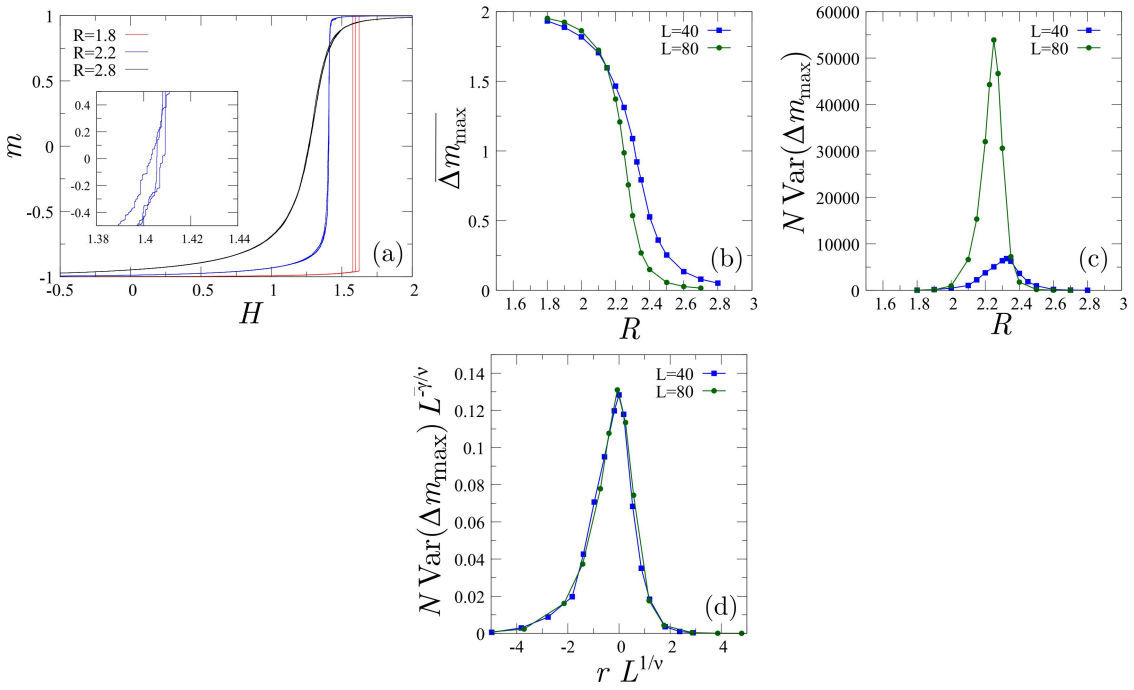

Figure I.12: Results from computer simulations of the 3D AQS driven random-field Ising model. (a) Magnetization curves for 3 samples for different values of the disorder strength R. When R is small the magnetization displays a jump of order 1, while for stronger disorder the curve is smoother. Inset: zoom on the magnetization curve for $R \approx R_c$, showing the jumps (avalanches) that occur at all sizes. Curves obtained with $L = 120$. (b) Average of $\Delta m_{\max}$ as a function of R for two different system sizes. (c) Sample-to-sample fluctuations of the order parameter, that show an unbound growth when approaching the critical point. (d) Collapse of the variance of the sample-to-sample fluctuations on a single master curve. From the collapse we extract the exponents $\bar{\gamma}/\nu \approx 2.95$ and $\nu \approx 1.3$, compatible with analytical results from NPFRG [110].

the reduced external field and $F(\cdot)$ another scaling function. Finally a similar approach has also been used to discuss the criticality of the model in 2D [132]. (The results presented here are only meant to illustrate the procedure and are not intended to give precise estimates of the 3D-RFIM exponents.)

The above procedure allows us to get an estimate of the critical behavior of the model. Let us now move to the regime in which the magnetization (per spin) displays a jump of order 1, i.e., for $R < R_c$. The model then undergoes a non-equilibrium first-order (or discontinuous) transition [134] as the external field reaches some value $H = H_{\mathrm{co}}^{\alpha}$ that depends on the disorder realization. This corresponds to a well-defined zero-temperature spinodal. During the evolution, each sample has a macroscopic jump, but the resulting magnetization curve is always smooth after averaging over many samples. We can then define the disorder-averaged coercive field $H_{\mathrm{co}} = \overline{H_{\mathrm{co}}^{\alpha}}$ where the average magnetization has the largest slope. From the results described above using the MSRJD formalism (in particular from Eq. (I.33)), the simplest assumption is that the disconnected susceptibility should go as the squared

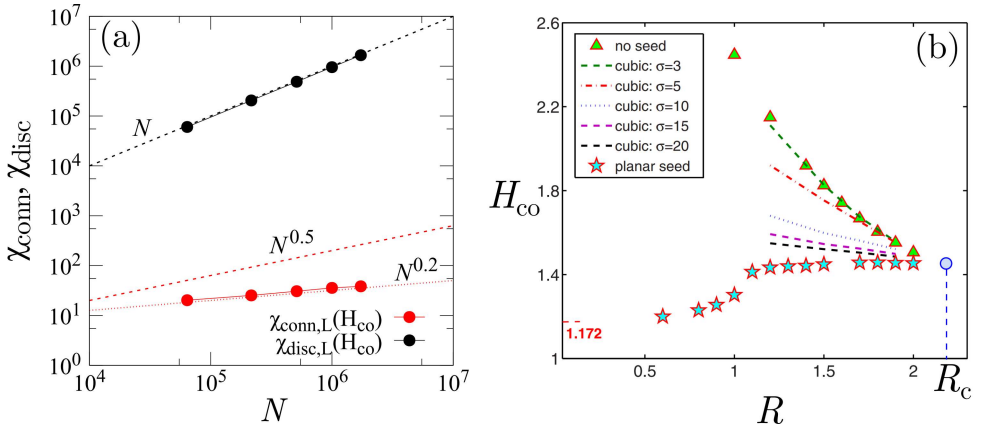

Figure I.13: Results from computer simulations of the 3D AQS driven random-field Ising model in the $R < R_c$ regime. (a) Scaling of the peak (at $H = H_{co}$) of the connected and disconnected susceptibility with the system size, for $R = 1.8$. The disconnected one follows the expected scaling $\chi_{disc,L} \sim N$, while the connected one increases much slower than the expected $\sqrt{N}$. (b) Value of the coercive field for a 3D RFIM with $R < R_c$ where a seed of up-spins has been inserted at the beginning of the dynamics. Such seed would be present in the thermodynamic limit, but is absent in finite-size simulations. Dashed lines are for a cubic seed of linear size σ. Stars are for a planar seed, which seems to give the correct limit as $R \to 0$. Adapted from [133].

connected one. Then, one would expect $\chi_{dis,L}(R < R_c, H_{co}) \sim N$ and $\chi_{conn,L}(R < R_c, H_{co}) \sim \sqrt{N}$, with $N = L^3$ in the present case. This can be easily verified by computing the two susceptibilities as

$$\begin{aligned} \chi_{conn,L}(R < R_c, H) &= \frac{\partial \overline{m}(H)}{\partial H} \\ \chi_{disc,L}(R < R_c, H) &= N(\overline{m^2}(H) - \overline{m}^2(H)). \end{aligned} \tag{I.39}$$

The outcome, however, is that while the expected scaling is observed for χ_{disc}, the connected susceptibility does not follow the $\sqrt{N}$ scaling, as displayed in Fig. I.13(a). In order to understand this issue one has to take into consideration the role of rare events. In the thermodynamic limit it is possible to have regions of the system where the local random fields are particularly large and positive. This is possible since when N gets larger and larger some otherwise improbable realizations of the disorder occur somewhere in the system. These regions flip before the rest and form a seed for the macroscopic avalanche that takes place at H^{α}_{co}. As discussed in [133], one loses the effect of such rare regions in computer simulations, in particular when R is small, since the systems that can be simulated are not large enough to contain them. As we will see, a similar issue is encountered in the study of amorphous solids. In order to get an idea of the effect of such rare realizations, one can add a seed of positive spins to the system before starting the dynamics and observe how this affects the resulting evolution. In Fig. I.13(b) we observe how the presence of such a seed dramatically affects the value of H^{co}, which, without considering the rare regions, would go to the wrong limit as $R \to 0$. More generally, the absence of such regions not only changes the average value H_{co}, but the whole the distribution $\rho_{co}(H^{\alpha}_{co})$ of the sample-dependent coercive field,

which in turn changes the scaling of the connected susceptibility. To see how $\rho_{\rm co}(H^\alpha_{\rm co})$ and $\chi_{\rm conn}(R < R_c, H)$ are linked, we consider that the magnetization of the system simply evolves as

$$m^\alpha(H) = -1 + 2\theta(H - H^\alpha_{\rm co}), \tag{I.40}$$

with $\theta(\cdot)$ the Heaviside function. This is clearly a crude approximation but it works well for small enough values of the disorder strength R. By averaging over the disorder realizations we then get

$$m(H) = \overline{m^\alpha}(H) = -1 + 2\int_{-\infty}^{H} \rho_{\rm co}(H')dH'. \tag{I.41}$$

From this equation the relation $\chi_{\rm conn}(R \ll R_c, H) = 2\rho_{\rm co}(H)$ follows easily. The solution proposed in [133] helps us getting an idea of how the rare regions affect the value of the average coercive field but it does not give us more insight about $\rho_{\rm co}(H)$. In the thermodynamic limit this distribution will depend more generally on the distribution of the rare regions in the system, which is inaccessible via computer simulations.

From the above considerations we gathered some intuition on how to compute exponents and scaling functions close to a critical point as well as on how to study some features of first-order (discontinuous) transitions. Before concluding this part on the driven RFIM, we briefly mention that the dynamical choice used to simulate the system is not unique. The one we just described for this model is proposed in [129, 130]. Another possibility is for example to consider the case in which an full $(d-1)$-dimensional interface of $+1$ spins is already formed in the system where all the other spins are negative at $t = 0$. As the external field increases the positive value of the spin are favored, so that the interface will propagate. In this case however only spins in contact with the interface are allowed to flip [135]. This dynamics correspond to interface depinning in a bulk RFIM system.

In what we said until this point, and in the two examples we presented, temperature was not taken into consideration. The reason is that when we put these systems in contact with a thermal bath, we need to add another source of noise to the Langevin equations Eq. (I.35). This thermal noise then allows the system to jump to different metastable states overcoming energy barriers with the help of thermal fluctuations. Allowing for this possibility blurs the transition, which is no longer strictly defined, neither the discontinuous one and the associate spinodal, nor the critical point. Although the influence of temperature would be interesting per se [136], we focus on the transition and choose the athermal quasistatic dynamics in order to have crisper conclusions on the presence and properties of the critical point.

3 Summary of the introduction and structure of this work

In the first part of this introduction we discussed amorphous solids and the physics that arises when such materials are deformed. We then argued that even if the origin of plasticity is qualitatively similar in all amorphous materials, different responses can occur when deformation is applied. Mechanical properties, and in particular the yielding transition, depend on the initial preparation of the sample. We discussed the results obtained in computer simulations of an atomistic glass prepared over a wide range of stability [4], where the presence of a critical point for a specific value of the preparation temperature separating a brittle regime from a ductile one was proposed. We then described the statistical physics framework to study systems close to a critical point, both in and out of equilibrium, with some examples.

The main point of our work is to provide a theoretical description of the yielding transition of amorphous solids and to try to derive an appropriate effective theory of the phenomenon. The purpose of an effective theory is not to reproduce the phenomenology of the model in all its details but rather to focus on the main features that characterize the behavior of the system at long length scales, which is adequate near a critical point. By focusing on universal aspects, the effective theory is able to describe the system's behavior in a simpler and more general way. This is for example what the ϕ^4 field theory does for systems in the universality class of the Ising model. In principle, to obtain an effective theory one starts from a microscopic description that captures the relevant physics at small scales and integrates out the effect of small scales to obtain an effective description of the system at large scales. The task of constructing such a theory for the yielding transition in amorphous solids is complicated by the initial challenge of creating a microscopic theory that accurately describes the relevant physics and by the intrinsically out-of-equilibrium nature of the process. To bypass this issue we turn to phenomenological models, and in particular to the Elasto-Plastic Model (EPM), that was shown to provide a surprisingly good description of solids under deformation even with few ingredients. The EPM is defined by a set of rules in the spirit of cellular automata. It does not have a Hamiltonian description, so that it is not easy to come up with an effective theory starting from it. Following earlier suggestions, we will develop the analogy between the behavior of solids under deformation and the athermally driven random-field Ising model. The possibility of building an effective theory of the yielding transition starting from the RFIM is particularly appealing as this model can be investigated in depth by means of simulations and theoretical methods such as the Non-Perturbative Functional Renormalization Group [119].

The rest of the work is organized as follows:

In Chapter 1, we study a version of the elasto-plastic model. We start by describing the choices made in devising the model and compare them with what has already been done. We then look at the resulting stress-vs-strain curves and we compare them with results from Molecular Dynamics simulations. We focus first on the brittle regime, where a macroscopic stress drop is observed, concomitantly with the formation of a shear band. We carefully discuss how such a band forms and how it affects the rest of the system. The main part of the chapter is focused on the study of the putative critical point that separates brittle and ductile regimes of yielding in amorphous solids. The existence of such a critical point has already been presented in previous works [4, 137], but due to the limited system sizes accessible to MD simulations, it was not possible to properly characterize the critical properties. We then use our EPM and we study the role of the initial disorder, which is a proxy for the preparation conditions in realistic amorphous solids, on the yielding transition. The mesoscopic nature of this approach allows us to investigate much larger system sizes and a much larger number of samples, thereby allowing a bona fide finite-size scaling analysis. We give a first estimate of the critical exponents that characterize this transition. As the presence of a critical point has been challenged [6, 83, 84], we take particular care to establish its existence when going to the thermodynamic limit. We conclude by showing two variations of the model. First, in the same spirit of what we showed above for the standard RFIM, we look at how the first-order transition is affected by the presence of weak but rare regions. We finally show the signature of the critical point in another (quite different) version of the model, defined in [7].

In Chapter 2, we push the analogy between the yielding transition and the AQS driven random-field Ising model (RFIM) by numerically investigating a specially tailored version of the latter, in which the nearest-neighbor ferromagnetic interactions are replaced by the Eshelby kernel. This allows to mimic the symmetry of the avalanches of quadrupolar plastic events and the appearance of a shear band. We follow the evolution of the model under an athermal quasistatically applied external field. We first look at the magnetization-vs-field curves and study the dependence of these curves on the variance of the local random fields. We highlight the similarities with what we observed in the EPM. Here too we proceed with a careful analysis of the weak-disorder phase, revealing and characterizing the formation of a band of positively magnetized spins as the external field increases. We discuss similarities and differences with the EPM. We then move to the analysis of the critical point, which is controlled by the variance of the local random fields. We carefully confirm its existence and study the properties of the system as it gets closer to criticality. We perform a similar finite-size scaling analysis to determine the critical exponents of the model. While the transition scenarios for the EPM and the Eshelby-RFIM are qualitatively the same we are unable to safely decide whether the critical points of the two models are in the same universality class or not despite the very large system sizes used in both cases. To conclude the study of this model we also discuss two variations. First we look at the effect of seeds of positive spins on the value of the coercive field at which the magnetization jumps in the weak-disorder regime. We find that the effect of such seeds is similar to the one discussed in the standard RFIM [133]. Lastly, we try to assess the effects of the lattice by studying a slightly different model. In particular we consider the Eshelby kernels when aligned along a different axis with respect to the standard one, and we check how this affects the critical point.

Chapter 3 presents an analytical study of the EPM and RFIM models that are obtained in the mean-field approximation. Defining the mean-field version of the EPM is not an easy task, due to the anisotropic nature of the Eshelby interactions. For simplicity, we use the ferromagnetic version defined in [4] for the EPM, while we choose the one introduced in [10] for the RFIM. We first compute the average evolution of the models and we discuss the stress-vs-strain and the magnetization-vs-field curves, for the EPM and the RFIM respectively. Changing the disorder strength changes the average evolution and in both cases a well-defined critical point reached for a specific disorder strength separates a discontinuous from a continuous regime. The core of the calculation is to obtain the disconnected susceptibility which quantifies the sample-to-sample fluctuations. We do this analytically and from the comparison between the disconnected and the connected susceptibilities we provide an estimate of the effective strength of the random field that emerges in the vicinity of the yielding transition. We also study how the strength depends on the various sources of disorder present in the EPM. We conclude by proposing a direct mapping at the average level between the EPM and the RFIM in the mean-field limit.

We conclude the main part by summarizing the salient results obtained in the present work. We highlight the questions that are left open and we propose some future directions to tackle these issues and to explore different problems.

In Appendix A we explain the procedure that leads to the definition of the Eshelby kernel and we discuss its implementation. In Appendix B we give details on the code used to perform the numerical simulations of the EPM and of the Eshelby-RFIM, with their respective variations. A pseudocode version of each algorithm is presented to clarify the procedure.

Appendix C is dedicated to the calculation details that lead to the results in Chapter 3. Finally, in Appendix D we discuss the avalanche-size distribution for the EPM and for the Eshelby-RFIM.

Chapter 1

The Elasto-Plastic Model and the yielding transition

Contents

1 Introduction 38
1.1 The key ingredients of an Elasto-Plastic Model 38
1.2 Our version of the model 41
1.3 Stress-vs-strain curves 44
2 The brittle regime and the shear band formation 46
2.1 Inside the shear band formation 46
2.2 Before and after the macroscopic drop 48
2.3 Characterizing the brittle transition 51
3 Critical point between brittle and ductile regime 54
3.1 Characterizing the brittle-to-ductile transition 54
3.2 Bounding the location of the critical point 59
4 Variations of the model 61
4.1 Effect of a seed 61
4.2 The Popović-de Geus-Wyart version of the EPM 65
5 Conclusion 67

1 Introduction

In this chapter we introduce and numerically study an elasto-plastic model (EPM) that we use as a mesoscopic approach to describe the yielding transition of amorphous solids and how it changes with the preparation of the material. As mentioned in the Introduction, our focus is on universal behavior and we choose an EPM to be able to access much larger system sizes and to consider a much larger number of samples so that a proper finite-size scaling analysis of the results can be performed. Part of the work described in this chapter resulted in the publication of a paper, that can be found here [138].

1.1 The key ingredients of an Elasto-Plastic Model

The original idea of elasto-plastic models is to mix the linear elastic response of a solid to an external shear deformation with the internal rearrangements associated with plastic events [139, 140]. This arises from the observation that plastic activity in amorphous solids is localized. Many versions of the EPM have been devised and in this introductory part we briefly discuss the key common ingredients. (We follow the presentation of the comprehensive review [5].) In the elasto-plastic model the solid is divided into mesoscopic blocks of size similar to that of a typical plastic rearrangement. Each of these elements can then be found in two states: elastic or plastic. To represent these states, a binary variable p_i is introduced, such that if $p_i = 0$ the block at site i is in the elastic state, whereas for $p_i = 1$ it is in the plastic one. When in the elastic state the block responds linearly to deformations, while as soon as $p_i = 1$ it releases part of its stress and redistributes it to the other blocks. The passage from $p_i = 0$ to $p_i = 1$ and viceversa is dictated by some conditions $C1$ and $C2$, respectively, that we discuss below. In general, the evolution of a single element is then composed of four steps:

1. Elastic response to external stimulus and plastic reorganization elsewhere in the system, valid if a certain condition $C1$ is satisfied;
2. Passage to the plastic regime, when $C1$ is not true anymore;
3. Redistribution of its stress, if a certain condition $C2$ is satisfied;
4. Return to the elastic regime when $C2$ is not true anymore.

As often happens in statistical mechanics, even such a simple dynamics for an elementary constituent gives a non-trivial behavior when a collection of interacting blocks is considered. In this first part we discuss the possible choices to implement these rules as well as the relative justifications and applications to different kinds of materials. First of all, in this type of models a single component of the stress and of the strain tensors is often considered when focusing on the shear deformation (if the loading is uniformly applied). In this way the problem is reduced to a scalar one and is hence easier to treat. However, a more careful treatment of the tensorial nature of these quantities can be introduced to take into account the possibility that some other component of the stress and strain tensors comes into play during the deformation procedure and in particular after a plastic event. The advantage of this more realistic approach is that it also allows for the simulation of many types of deformation, giving rise to different forms of plasticity localization. In this way it becomes possible to study the properties of amorphous solids under different deformation protocols [141].

In the majority of EPMs found in the literature, an additional simplification is often made

where each elementary block is assumed to be fixed at some lattice site during the dynamics. This approximation can be relaxed [142] to include the motion of the constituents. For our purpose here, we nonetheless consider a scalar description for a simple shear deformation with a local stress σ_i and a shear strain γ. As already mentioned we furthermore consider the athermal and quasistatic limit with $\dot{\gamma} \to 0$: the system is allowed to reach the bottom of the metastable state before the strain is increased again. The timescales of avalanches and elastic propagation are completely separated from the timescale of the driving. It is in this setting that the yielding transition can be crisply defined. Different protocol choices are possible, as for example stress-controlled EPMs [7, 143]. Some other types of test described in the Introduction, such as the study of the steady state flow curve, have also been carried on in the EPM setting [144]. One looks in this case for the relation between strain rate and stress, of the type $\dot{\gamma}(\sigma) \propto (\sigma - \sigma_{\rm y})^{\beta}$. In this setup the analogy with the depinning transition gives interesting insights [144]. Recently, oscillatory-strain deformation protocols have also been studied in order to deal with stationary states properties instead of transient behaviors [145, 146].

The first step of the algorithm is a linear response of each block to an increase of strain from γ to $\gamma+\delta\gamma$: the local stress then increases from σ_i to $\sigma_i+\mu\delta\gamma$, with μ the shear modulus of the material.

Steps 2 and 4 of the list above describe the fact that each elementary component behaves elastically until its local stress value is too large to sustain. Usually the conditions $C1$ and $C2$ discussed above are built such that the stress at each block has a threshold value $\sigma_i^{\rm th}$, so that if $\sigma_i > \sigma_i^{\rm th}$ the block at site i enters in the plastic state ($p_i = 0 \to p_i = 1$) with a certain rate $\tau_{\rm in}$ (condition C1) and exits ($p_i = 1 \to p_i = 0$) with a certain rate $\tau_{\rm out}$ (condition C2). Different choices for these values are possible, as well as different rules. Such local yielding rates are usually taken as constants. However, recent studies have pointed out that a dependence on the local stress value of such rates should be considered, as it may change the dynamical exponents (even if the static ones seem unaffected) [147]. It has been shown that this choice is related to the form of the random potential acting on the system [148]: depending on the shape of the potential well that each block sits in, the form of the yielding rates change. We do not dive into these issues as we are interested in universal features that should be robust to detail changes.

Stress redistribution in the plastic state is a key factor as it is responsible for the organization of plastic events in the form of shear bands. Each block in the plastic state releases an amount of stress proportional to its local value σ_i in a typical time τ, which is then redistributed to the other sites of the system. While block i relaxes it can still receive the kicks coming from the other relaxing sites in the lattice. The standard choice for the stress redistribution is the Eshelby kernel in the far-field approximation. This propagator was first obtained by considering the strain field generated by a single ellipsoidal inclusion in a completely elastic medium [28]. In the real space in 2D the propagator takes the form introduced in Eq. (I.5), which we repeat here,

$$G_{ij} = \frac{\cos(4\theta_{ij})}{\pi r_{ij}^2}, \tag{1.1}$$

with (r_{ij}, θ_{ij}) the polar coordinates of the vector between site i and j. This form is obtained with the hypothesis of an infinite solid, while in general the boundary conditions play an

important role [149]. It is easily generalized to higher dimensions. Notice that the propagator is not defined in $r_{ii} = 0$, but since the block that relaxes loses stress the choice $G_{ii} = -1$ is usually made. Due to the long-range character of the interaction, the implementation of such a stress propagator on a lattice is not straightforward when periodic boundary conditions are taken. The two main solutions to this issue are the Fourier-space discretization and the finite element method [141, 150]. Another possibility is also to perform the sum over the periodic interactions in some clever way, in order to have a convergence [151]. More details about the Eshelby propagator and its implementation in the simulations are given in Appendix A.

We can finally summarize the evolution equations for the local stress σ_i and activity p_i at site i in the strain-driven protocol as

$$\dot{\sigma}_i = \mu\dot{\gamma} + \sum_j G_{ij} p_j \frac{\sigma_j}{\tau} \tag{1.2}$$

$$\dot{p}_i : \begin{cases} 0 \to 1 & \text{at rate } \tau_{\text{in}}^{-1} \text{ if } \sigma_i > \sigma_i^{\text{th}} \\ 1 \to 0 & \text{at rate } \tau_{\text{out}}^{-1}, \end{cases} \tag{1.3}$$

for the most general case.

The last component that is missing is the disorder associated to the amorphous nature of the material that one wants to describe, which enters the description in many ways. First, one has to choose how to initialize the local stress variables, which are assumed to be randomly chosen from a certain probability $\mathcal{P}_0(\{\sigma_i\})$. As we previously discussed, the behavior of glasses, both in experimental setups and molecular dynamics (MD) simulations, exhibits variations based on the preparation protocol, which includes factors such as preparation temperature, cooling rate, and aging. In order to mimic this dependence one may change the characteristics of the distribution of the initial stress. The only constraint is that if the solid is at mechanical equilibrium and no strain is applied, one has a macroscopic stress $\sigma = 0$. In addition, recent results showed that also the local stress thresholds follow a certain distribution, which is itself influenced by the sample preparation [152] and may even change during the dynamics [153]. In order to reproduce this in the EPM setting, each site should have different stress thresholds, which can possibly change during the evolution, with a threshold distribution of the type $\mathcal{P}_{\text{th}}(\{\sigma_i^{\text{th}}\}, \gamma)$ (see also [77]). After the local stress overcomes the threshold σ_i^{th} the block finds itself in the plastic state and redistributes its stress. The time that the block spends in the plastic state depends on the rates τ_{in} and τ_{out} and is also random. As a consequence, the amount of stress redistributed is another source of disorder. One more source of randomness comes from the shear modulus μ. Usually μ is fixed in the study of EPMs, but in reality its value is nonuniform inside the material [154] due to the elastic heterogeneity. Therefore, in principle, it should also be chosen according to some distribution to account for its variability. Finally, the orientation of the Eshelby kernels could be considered as another source of noise. The solid obtained after the quenching procedure is isotropic. However, as soon as an infinitesimal loading is applied in some direction, the Eshelby propagators tend to align in this same direction. Still, they need not be perfectly aligned [155], so that a disorder on their orientation should be taken into account.

This gives a brief overview of some of the possible variations of the EPM that can be built. As it is clear from all the possible choices that we listed, there are many details that could be taken into account when defining the model. In general, different EPMs have proved

useful in different contexts: each ingredient has to be chosen depending on the scope of the work. If one wants the most accurate version of the EPM this can be done by taking into consideration all the possibilities listed above. Studies in this direction have been performed by calibrating an EPM with results coming from the probing of MD simulations [156, 157], which showed how well this model works when all the previous points are taken into account. However, this multiplicity of choices is also a drawback of EPMs that may be criticized as involving too much arbitrariness or too much fine-tuning. It has furthermore been argued in recent years [30, 31, 158] that the Eshelby kernel and the linear elasticity description of interacting quadrupoles may not be sufficient to capture the behavior of amorphous solids in some situations.

In our work where we focus on the yielding transition and its universal features, we neglect many of the details. As we discussed in the Introduction, the predictive power about critical properties is due to their independence of the details of the model. If one can capture the interesting large scale behavior with a model in which, for example, μ is constant and homogeneous, one can argue that the results will be also valid for a case in which a small perturbation is added to this quantity. We focus on properties that are robust to detailed changes of the model.

1.2 Our version of the model

We consider a system in both two-dimensional (2D) and three-dimensional (3D) cubic lattices under a simple shear deformation protocol with periodic boundary conditions. The tensorial nature of the mechanical quantities is neglected, so that the local stress $\sigma_i = \sigma_{i,\mathrm{xy}}$ and the local strain $\gamma_i = 2\epsilon_{i,\mathrm{xy}}$ are scalar quantities. The blocks are fixed at their position and convection is neglected. These choices may already seem quite drastic, but it has been shown previously that they do not affect the critical properties of the system [141, 142]. For the reasons we already explained, we use the athermal quasistatic (AQS) protocol in our simulations. Since the strain is imposed to the whole system uniformly, we have $\gamma_i = \gamma$ for every site i. Notice that in this limit time does not enter, since the only two timescales present (the one of the driving and the one of the avalanches) are completely separated. At each step the macroscopic strain γ applied to the system is increased by the smallest quantity sufficient to drive the weakest site outside the stability condition, and make it yield. The ensuing avalanche of plastic activity takes place at fixed γ and only once the system has completely relaxed the applied strain is increased again.

Regarding the passage from the elastic to the plastic state we choose it to be instantaneous, so that as soon as $|\sigma_i| > \sigma_i^{\mathrm{th}}$, the block at site i yields and redistribute a portion of its stress, before going back in the elastic state. We also assume that the stress redistribution is instantaneous. Consequently, the timescale between a single plastic event and the propagation of its effect are decoupled, which means that within an avalanche there is no concept of physical time and the evolution is only dictated by the avalanche step l. At $l = 0$ one site yields and (possibly) makes other sites unstable. At step $l = 1$ all the unstable sites yield at the same time (this choice, referred to as "parallel update", is the one that gives a faster algorithm, see Appendix A) and they redistribute their stress, creating some more instabilities in the system. This process goes on until some step $l_{\max}$ at which no more sites are unstable and the local stresses $\sigma_{i,\gamma+\delta\gamma} = \sigma_{i,l_{\max},\gamma}$ are stable. To take into account the randomness given by the three rates that we are ignoring (namely τ_{in}, τ_{out}, and τ) we

choose the stress drop at each site to have a contribution from a random variable η chosen independently for each site and for each rearrangement. The total stress drop $\delta\sigma_{i,l,\gamma}$ at site i, avalanche step l, and external strain γ is given by

$$\delta\sigma_{i,l,\gamma} = \mathrm{sgn}(\sigma_{i,l,\gamma})(|\sigma_{i,l,\gamma}| - \sigma_i^{\mathrm{th}} + \eta_{i,l,\gamma}), \tag{1.4}$$

where $\mathrm{sgn}(\cdot)$ is the sign function. The local plastic strain $\gamma^{\mathrm{pl}}_{i,l,\gamma}$ increases accordingly by an amount $\delta\gamma^{\mathrm{pl}}_{i,l,\gamma} = \delta\sigma_{i,l,\gamma}/\mu$ each time the block yields. The system is considered at $T = 0$ so that no thermal activation takes place.

Once the local stress at site i drops, it is redistributed to the rest of the system via a discrete version of the Eshelby propagator G_{ij}, for each site j, such that $\sigma_{j,l+1,\gamma} = \sigma_{j,l,\gamma} + G_{ij}\delta\sigma_{i,l,\gamma}$. We choose $G_{ii} = -1$ and we implement a discretization in the Fourier space to compute the kernel (more details in Appendix A).

The general local evolution in our case is then

$$\sigma_{i,\gamma+\delta\gamma} = \sigma_{i,\gamma} + \mu\delta\gamma + \sum_j G_{ij}\delta\sigma_{j,\gamma} \tag{1.5}$$

$$\delta\sigma_{j,\gamma} = \sum_{l=0}^{l_{\max}} \delta\sigma_{j,l,\gamma}. \tag{1.6}$$

In our model we neglect the time needed for the local plastic event to propagate its influence to the rest of the system, so that this perturbation affects instantaneously the whole system. This approximation is in general not realistic, but should not affect our conclusions. (In the energy landscape picture proposed by [147, 148] this amounts to consider the potential in the deep well approximation [159].)

Let us come back to the issue of disorder. As we discussed in the Introduction, the main interest in studying systems as it is done in [4] is that one can study the deformation of a given material for different preparations characterized by a unique control parameter, in this case the fictive temperature. We use a similar approach here. First of all, we consider the initial stress values of the system to be independent and identically distributed (i.i.d.) so that $\mathcal{P}_0(\{\sigma_i\}) = \prod_i P_0(\sigma_i)$, with

$$P_0(\sigma) = \frac{(1-\sigma^2)}{\mathcal{N}} \exp\Big\{-\sigma^2/(2R^2)\Big\}, \tag{1.7}$$

with $\mathcal{N}$ a normalization constant (notice that this i.i.d. hypothesis is also an approximation, as stresses have been shown to be slightly correlated in glasses after quench [160, 161]). The average initial value of the macroscopic stress $\sigma = 1/N\sum_{i=1}^N \sigma_i$ is then $\langle\sigma\rangle = 0$ and the distribution is symmetric around this value (no direction is preferred at $\gamma = 0$). As there are no thermal fluctuations (as $T = 0$), the only average is performed with respect to disorder realizations (i.e., different samples) and is denoted by $\langle\cdot\rangle$. (In this chapter we use brackets $\langle\cdot\rangle$ to denote an average over samples, contrary to the Introduction and Chapter 3 where one has to be more specific and use an overline $\overline{(\cdot)}$ to distinguish it from other types of averages.) The parameter R of the distribution $P_0(\sigma)$ controls the disorder strength. When R is small the stress values will not deviate much from the typical value at 0, which mimics a stable system. On the other hand larger values of R describe less stable samples. In this sense

R plays the same role as the fictive temperature in [4] (representing the disorder related to the fictive temperature as a distribution of the initial value of stress is reasonable in view of the results in [157] and the fact the we use a fixed threshold, see below). This is the main source of disorder. Note also that for small values of R, this distribution $P_0(\sigma)$ is very similar to a Gaussian, while it gets closer to a parabola as R increases. The factor $(1-\sigma^2)$ that multiplies the Gaussian term is only present to ensure that at the beginning of the dynamics all sites are stable. However, this also bounds the dispersion of the distribution, limiting the maximum value of the variance. As a consequence, the model saturates to a maximum strength of disorder as $R \to \infty$, as has also been argued in MD simulations of glasses [84]. To limit the number of different ingredients the values of the local stress thresholds and of the local elastic moduli are chosen to be uniform and fixed for all sites, with $\sigma_i^{\text{th}} = 1$ and $\mu = 1$ during the whole dynamics. The value of η is chosen from an exponential distribution (as observed in atomistic simulations [152]) of average $\overline{\eta} = 1$. More details regarding the implementation of the EPM as well as a pseudocode describing the simulation of our model are presented in Appendix B. We stress that of the several possible sources of randomness, only the initial disorder strength R will be varied and taken as a control parameter.

We conclude this part by discussing the issue of force balance. In the AQS limit the system has to be stable before each increase of strain. The mechanical equilibrium condition imposes that $\nabla \cdot \sigma = 0$. Going back to the continuum description of the stress tensor, this condition reads in 2D

$$\frac{\partial \sigma_{\text{xx}}(x,y)}{\partial x} + \frac{\partial \sigma_{\text{xy}}(x,y)}{\partial y} = 0 \ . \tag{1.8}$$

Integrating this relation over x, we obtain

$$\int dx \frac{\partial \sigma_{\text{xy}}(x,y)}{\partial y} = -\int dx \frac{\partial \sigma_{\text{xx}}(x,y)}{\partial x} \ . \tag{1.9}$$

Since the right-hand side of Eq. (1.9) vanishes due to periodic boundary conditions for any y, we obtain

$$\frac{\partial}{\partial y} \int dx \, \sigma_{\text{xy}}(x,y) = 0 \ , \tag{1.10}$$

which implies that the total shear stress $\sigma_{\text{xy}}(x,y)$ along x must be constant over all values of y. A symmetric relation can be obtained by exchanging x and y. The mechanical equilibrium condition imposes that the total stress along each row (or column) of the system is the same. A similar derivation can be obtained in 3D. We can now go back to our model, which lives in a discrete lattice. In the discrete 2D version, averaging the evolution of the local stress (in our case we only have shear stress, so that $\sigma_i = \sigma_{(x_i,y_i)} = \sigma_{\text{xy}}(x_i,y_i)$ at lattice site i) in Eq. (1.5) over x, we obtain

$$\begin{aligned} \frac{1}{L}\sum_{x_i} \sigma_{(x_i,y_i),\gamma+\delta\gamma} = & \frac{1}{L}\sum_{x_i} \sigma_{(x_i,y_i),\gamma} + \mu\delta\gamma - \delta\sigma_\gamma \\ & + \frac{1}{N}\sum_{q_y \neq 0} \hat{G}_{q_x=0,q_y} \delta\hat{\sigma}_{(q_x=0,q_y),\gamma} \, e^{iq_y y} \ , \end{aligned} \tag{1.11}$$

where $\delta\hat{\sigma}_{(q_x,q_y),\gamma}$ is the Fourier transform of $\delta\sigma_{(x_j,y_j),\gamma}$, $\hat{G}_{q_x,q_y}$ is the Fourier transform of the Eshelby kernel, and $\delta\sigma_\gamma = 1/N \sum_{x_j,y_j} \delta\sigma_{(x_j,y_j),\gamma}$ is the average stress relaxed by plastic

sites during the step $\gamma \to \gamma + \delta\gamma$. Since the Eshelby kernel in Fourier space vanishes when $q_x = 0$ for all $q_y \neq 0$ (see Appendix A) the second line vanishes and the average stress along all rows changes by the same quantity $\mu\delta\gamma_{\text{ext}} - \delta\sigma_\gamma$ [162]. The same result is obtained for columns. This means that the difference between the average stress along a given row and along a different row or column remains constant during the dynamics. Therefore, to impose mechanical equilibrium, or force balance condition, it is sufficient to ensure that the sum of the stresses along rows and columns is the same everywhere at $\gamma = 0$. For 3D, a similar argument holds for the average local shear stress over an x-z (or y-z) plane. In our version of the model, we initialize the local stresses by a nearly Gaussian distribution with zero mean. Thus, the force balance condition is satisfied only asymptotically at large L since the average stress over a single row or column (at $\gamma = 0$) goes to zero when $L \to \infty$. However, since we are not dealing with systems in the thermodynamic limit, this condition does not hold exactly. We therefore checked the results obtained with our code by strictly imposing the mechanical equilibrium condition at the beginning of the dynamics as explained in [7] and we observed that in the limit of large system sizes the difference between the two choices disappears. The only approximate force balance condition in our version of the model does not affect our conclusions on the critical point.

1.3 Stress-vs-strain curves

Before showing the results, it is useful to introduce a quantity that greatly characterizes the yielding transition and how it changes with the initial disorder strength. In our study we follow the evolution of the macroscopic stress $\sigma = 1/N \sum_{x_i,y_i} \sigma_{(x_i,y_i)}$ (in 2D) as the system is strain-driven. However, the stress alone is not sufficient to characterize the presence of the transient shear band so we need another quantity that measures "how close" the system is to form a complete shear band that spans the whole system. We then define a quantity $n_{(x_i,y_i)}(\gamma)$ which takes the value 1 if the site i already had a plastic event, and 0 otherwise. We then define the sum along rows, $n^{\text{x}}_{y_i}(\gamma) = 1/L \sum_{x_i=1}^{L} n_{(x_i,y_i)}(\gamma)$, and columns, $n^{\text{y}}_{x_i}(\gamma) = 1/L \sum_{y_i=1}^{L} n_{(x_i,y_i)}(\gamma)$, and choose the row or column that had the maximum number of events as $n(\gamma) = \max_{x_i,y_i}(n^{\text{x}}_{x_i}(\gamma), n^{\text{y}}_{y_i}(\gamma))$. One has $n(\gamma = 0) = 0$ at the beginning, while $n(\gamma) = 1$ when every site in at least one row or column has yielded at least once. One can generalize this quantity to 3D, now checking each plane with normal vector parallel to x,y, and z and choosing the one with the larger number of yielded sites. The quantity $n(\gamma)$ shows a discontinuous jump when $\sigma(\gamma)$ shows a discontinuous jump, so that the two give the same information in the characterization of the yielding transition, but $n(\gamma)$ has some advantages that will appear clear in the following. In Fig. 1.1 we show stress-vs-strain curves for typical samples of the 2D and 3D EPM for different values of the disorder strength R. As expected, when R is small one observes the $O(1)$ stress drop characteristic of brittle materials (brittle as defined in the Introduction) for an external strain γ_{y}, called yield strain in the following. As R increases the stress-vs-strain curve becomes continuous but shows an overshoot and for even larger values of the disorder strength the stress reaches the steady state monotonically. In the insets we show the behavior of the quantity $n(\gamma)$ as well as the real space configuration of the plastic strain, which displays a clear organization in the form of a shear band for small R. One can then clearly distinguish between the two types of behavior, brittle and ductile, by only changing one parameter, similarly to what observed in MD results [4]. After its formation, the shear band grows until it spans the whole space.

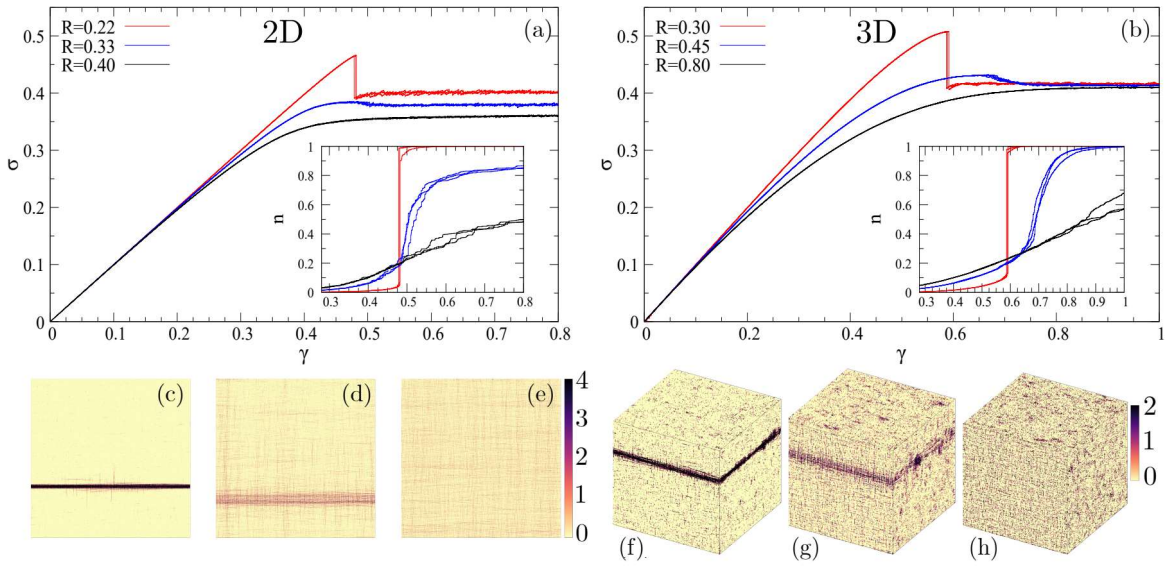

Figure 1.1: Top row: stress-vs-strain curves for our version of the EPM in 2D (a) and 3D (b), with respectively $L = 4096$ and $L = 200$, for three independent samples. One can see a monotonic curve for large values of R, while as the disorder strength decreases an overshoot and then a jump appear. In the inset we show the behavior of the order parameter n defined in the text for the same samples. Bottom row: real space organization of the plastic strain, which shows the shear band formation in the brittle case. The color map shows the plastic strain at each site, with darker colors meaning more strain. (c),(d), and (e) correspond to the configurations found in a 2D system at $\gamma = 0.55$ for $R = 0.22, 0.33$ and 0.4 respectively. (f), (g), and (h) correspond to the configurations found in a 3D system at $\gamma = 0.7$ for $R = 0.3, 0.45$ and 0.8 respectively. For small value of R the majority of events occur around the shear band, while for large values they are homogeneously distributed. For intermediate values (corresponding to an overshoot without a jump) the plastic activity also organize in a shear band, which however does not nucleate instantly.

At large values of γ the system reaches a steady state and the dependence on the initial conditions disappears. Comparing the stress-vs-strain curve with the evolution of $n(\gamma)$ for the brittle case, one can see that the macroscopic stress drop indeed occurs at the same time as the jump in n, which indicates the formation of the system spanning shear band. For the intermediate value of disorder one finds that the plastic strain still accumulates in one particular region during the descending part of the stress curve. The last case, with a large value of R, shows uniformly distributed events. The main goal of this first chapter is then to determine whether a critical point separates the brittle from the ductile regime, as suggested by MD results in [4]. However, before discussing this, we focus on the characteristics of the yielding transition in the brittle regime in the next part.

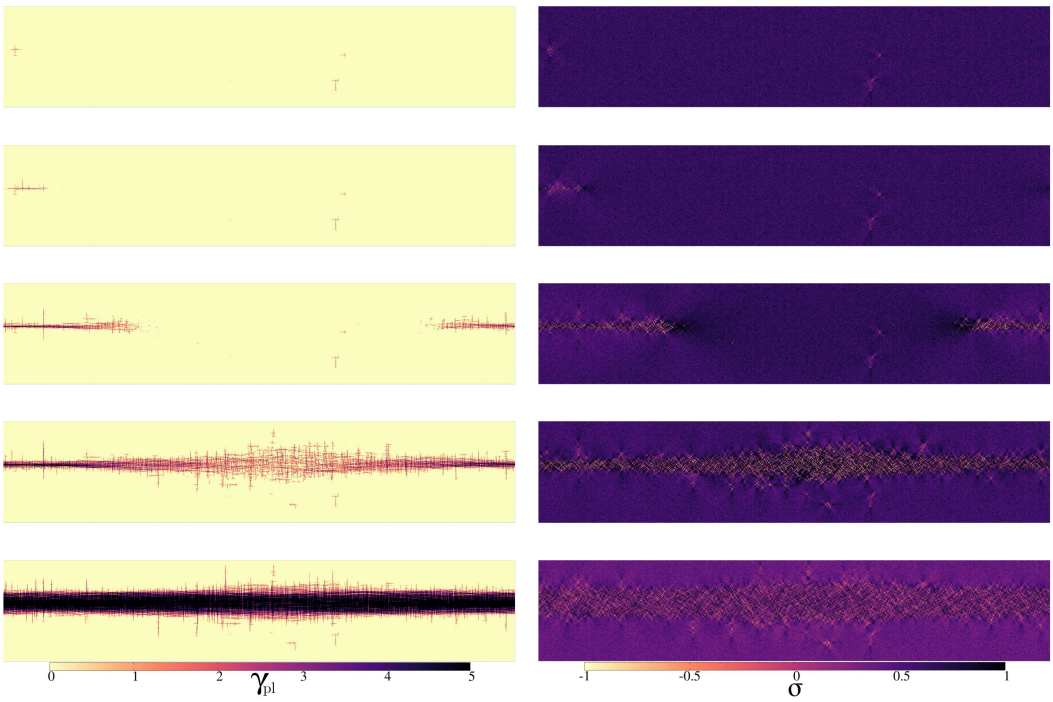

Figure 1.2: Evolution of the shear band inside the largest avalanche, measured via plastic strain (left) and stress (right). It starts from a weak region and picks a direction (here, horizontal) to propagate. One can see that it evolves starting from the end points of the active region, where the local stress is higher on average. Avalanche steps are $l/l_{max} = 0, 0.16, 0.32, 0.41$ and 1. The plot is from $y_{SB} - 100$ to $y_{SB} + 100$ with y_{SB} the location of the shear band. Obtained in 2D with $L = 1024$ and $R = 0.10$.

2 The brittle regime and the shear band formation

When the value of R is small enough the system is in the brittle regime, where in each sample the stress-vs-strain curve shows an $O(1)$ stress drop at γ_y, accompanied by the localization of plastic activity in the form of a shear band. In this section we focus on how such a shear band forms in the EPM, its properties, and the description of the associated discontinuous yielding transition.

2.1 Inside the shear band formation

The organization of the plastic activity in a shear band is observed both in experiments and in MD simulations and is a consequence of the anisotropic (here, quadrupolar) form of the stress redistribution that follows plastic events. First let us get a qualitative understanding of how this series of events proceeds. In Fig. 1.2 the evolution of the local plastic strain (left) and of the local stress (right) of the sites in the vicinity of the shear band location is shown for a system of linear size $L = 1024$ at disorder strength $R = 0.10$ (deep inside the brittle regime). The two top images show the sample at γ_y at the beginning of the largest stress avalanche, while those at the bottom correspond to the final result, just after the $O(1)$ stress drop. From these configurations we visualize the typical process that leads

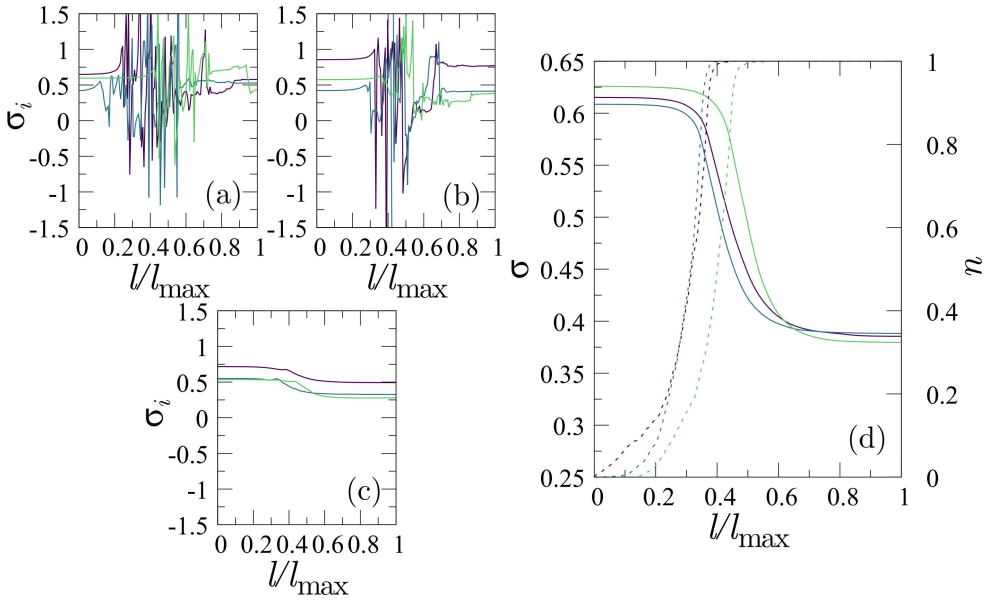

Figure 1.3: Evolution of the local stress of a site inside (a), on the boundary (b), and outside (c) the shear band during its formation. In (d) the evolution of the system-averaged stress (full line) and of the order parameter n (dashed line). We see that the main contribution to the total stress occurs once the avalanche has already spanned the whole system length L. The plot is obtained in 2D with $L = 1024$ and $R = 0.10$, with different colors corresponding to 3 different samples.

to the formation of the shear band: the band starts propagating from a weak region in the material, where some sites have usually already yielded, and selects a direction in which it grows based on the stability of the nearby blocks (in our simulations of simple shear strain with periodic boundary conditions, this direction can be either horizontal or vertical). The growth then proceeds from the endpoints of the band, where we find that the stress is on average larger than in the bulk and, as a result, sites are closer to instability. The reason for this is that the aligned Eshelby kernels induce contributions to the local stress that add up along the direction of the shear band embryo. Due to the decay of the propagator at large distance, the stress is maximum close to the tips of the region, so that if the system is sufficiently homogeneous (which is the case for small values of R), the sites close to the tips yield before those in the bulk. This in turn makes the stress at the new tips even larger, and so on [163]. When the avalanche finally spans the whole system, the band starts thickening. It is in this second part of the avalanche that the majority of events take place and the sites activity peaks. Similar results have been obtained both in MD simulations [163] and in related elasto-plastic models [83].

We now focus on specific sites and look at the evolution of their stress. In Fig. 1.3 the value of σ_i during the avalanche is shown for a site in the middle (a), at the boundary (b), and outside the shear band (c). We see that sites inside the shear band undergo many events and end up with a stress value that is almost uncorrelated with respect to the one they started with, while sites in the bulk of the sample just display a small but steady decrease of their stress value. Finally, in Fig. 1.3(d) we show how the average stress and the average order

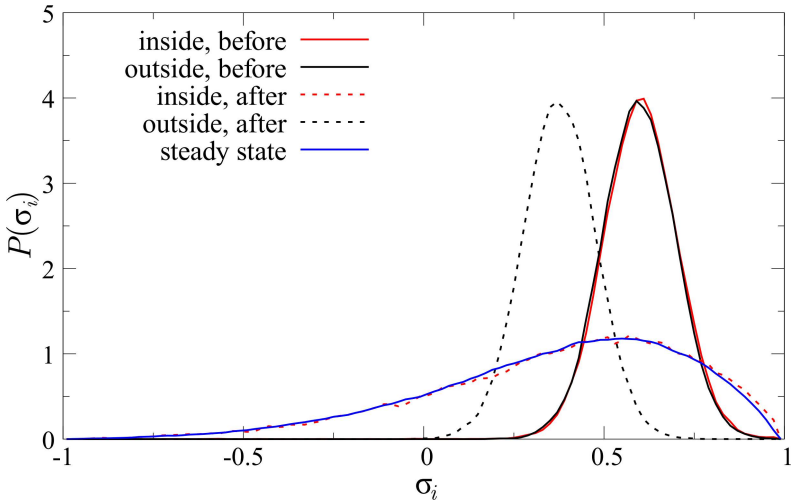

Figure 1.4: Distribution of the local stress for sites that are inside (red) and outside (black) the shear band, before (full) and after (dashed) yielding. In blue the distribution of stress at the steady state. Obtained in 2D with $L = 1024$, $R = 0.10$ and averaged over 30 samples. The steady state distribution is instead obtained with $R = 0.40$ at $\gamma = 5$.

parameter $n(\gamma)$ evolve during the avalanche. One observes that the main contribution to the stress drop comes when the avalanche has already spanned the whole system, i.e., when $n(\gamma)$ is already very close to 1. This occurs roughly at $l = l_{\max}/2$, while for $l > l_{\max}/2$ the shear band thickens. The latter plot is very similar to what is observed in MD simulations, for example in Fig. 3 of [163]. We stress that these curves are, as the snapshots in figure Fig. 1.2, obtained at fixed external strain γ during the largest avalanche.

2.2 Before and after the macroscopic drop

We now turn to the consequences of the macroscopic (i.e., of $O(1)$) stress drop as well as to the properties of the shear band that formed. We will show that the contribution to the largest jump coming from sites inside the shear band is subextensive, while the one coming from sites in the bulk is the significant one. Due to the scaling of the number of events per site with the system size the total contribution is however finite in the thermodynamic limit. To get more insight on the local stress during the macroscopic avalanche we focus on its distribution, $P(\sigma_i)$. In Fig. 1.4 we display $P(\sigma_i)$ before and after the macroscopic stress drop, for sites that are inside and outside the shear band in a system with $L = 1024$ and $R = 0.10$. The first thing one notices by looking at Fig. 1.4 is that before yielding, there is no difference between the distribution of stress at sites inside and outside the incipient shear band. Indeed, the presence of the small weak region from which plastic activity will propagate has not enough weight to change the whole distribution. As a consequence, it is not a trivial task to predict where the band will form just from this measure (predicting the formation of shear band is a very difficult task in general [69]). We then look at the consequences of the macroscopic stress drop on the stress distribution of sites in the bulk, and we observe that its form remains unchanged during yielding. The only effect is a homogeneous shift that affects

the average value. This is in agreement with what we discussed before about Fig. 1.3(c), where we saw that sites far away from the activity only see a steady decrease in their stress value. Inside the shear band the distribution of stress changes radically. Before yielding it resembles very much the initial distribution. However, after the macroscopic avalanche, $P(\sigma_i)$ is almost identical to the steady state distribution. The sites inside the band have already fluidized and as a result their distribution is that of the fluidized state.

From these results we should be able to predict some properties of the maximum stress drop that we observe. We define $\Delta\sigma_{\max} = \max_\gamma(|\sigma(\gamma+\delta\gamma) - \sigma(\gamma)|)$ (notice that we left the dependence on the disorder realization implicit, but clearly $\Delta\sigma_{\max}$ changes from sample to sample). We split the average maximum stress drop $\langle\Delta\sigma_{\max}\rangle$ as $\langle\Delta\sigma_{\max}\rangle = \langle\Delta\sigma_{\rm in}\rangle + \langle\Delta\sigma_{\rm out}\rangle$, with $\langle\Delta\sigma_{\rm in}\rangle$ the contribution coming from the sites inside the band and $\langle\Delta\sigma_{\rm out}\rangle$ the one coming from the sites in the bulk. From what we just discussed we know that just before yielding, the average stress inside and outside the band are almost identical and equal to $\langle\sigma_{\max}\rangle = \langle\max_\gamma \sigma(\gamma)\rangle$. We also know that after yielding the sites inside the shear band have an average stress equal to that of the steady state, $\sigma_{\rm st}$. As a consequence we expect that, on average, $\langle\Delta\sigma_{\rm in}\rangle \approx \langle(\sigma_{\max} - \sigma_{\rm st})N_{\rm SB}/N\rangle$, where $N_{\rm SB}$ is the number of sites inside the shear band, such that $N_{\rm SB} = w_{SB}L^{d-1}$ with $w_{\rm SB}$ the shear-band width. One then has $\langle\Delta\sigma_{\rm in}\rangle \sim \langle w_{\rm SB}\rangle/L = L^{\beta-1}$, where we made the hypothesis that the width of the shear band grows with the linear system size as $\langle w_{\rm SB}\rangle \sim L^\beta$, with $\beta < 1$. The sites in the bulk receive a kick that is on average proportional to the amount of plastic activity that took place in the largest avalanche. The scaling of their contribution to the $O(1)$ stress drop cannot be inferred in a similar way to what we did for the sites inside the band. Notice that while $\langle\Delta\sigma_{\rm in}\rangle$ is proportional to the number of sites in the shear band N_B, the contribution $\langle\Delta\sigma_{\rm out}\rangle$ depends instead on the number of events. The reason why the former is subextensive, while the latter is not will be clear from our study of the shear band profile below.

In order to check this conclusion, we measured the different contributions to the stress drop for $R = 0.10$ and $R = 0.22$ in 2D and for $R = 0.15$ and $R = 0.28$ in 3D, as we vary the system size. The results are shown in Fig. 1.5. First, we confirm that the stress drop contribution from the bulk is larger than that from the shear band. Second, for the larger value of R we indeed observe a power law behavior of the stress drop inside the shear band, that by fitting gives $\beta = 0.610 \pm 0.004$ in 2D and $\beta = 0.640 \pm 0.003$ in 3D (the error bars come from the error in the fit). However, we observe a different behavior from what we expected for the smaller values of R. Both the bulk and the shear band contributions to the stress drop vary substantially with the system size. To understand this we should imagine what happens in our model in the limit $R \to 0^+$, when there is vanishing initial disorder. We call this the very low-disorder regime. In this limit, the system evolves without any plastic event until some value $\gamma = \gamma_{\max}$ for which $\sigma(\gamma_{\max}) = \sigma_{\max} = \mu\gamma_{\max}$. The total stress drop is then given by $\Delta\sigma_{\max} = \mu\gamma_{\max} - \sigma_{\rm st}$. If we now assume that the stress value after the drop does not depend on R and L (a reasonable assumption), then the dependence of $\Delta\sigma_{\max}$ on the system size is only coming from $\gamma_{\max}$. In this low-disorder limit, the value of γ at which one attains the maximum stress (which coincides with the value of γ at which yielding occurs) is just given by the strain necessary to make the most unstable site at $\gamma = 0$ yield. The distribution $P_N^{\gamma_{\max}}$ of $\gamma_{\max}$ is then related to that of the largest stress value among the blocks at $\gamma = 0$, which we call $\sigma_i^{\max} = \max_i(\sigma_i(\gamma = 0))$. The probability density $P_N^{\sigma_i^{\max}}$ of

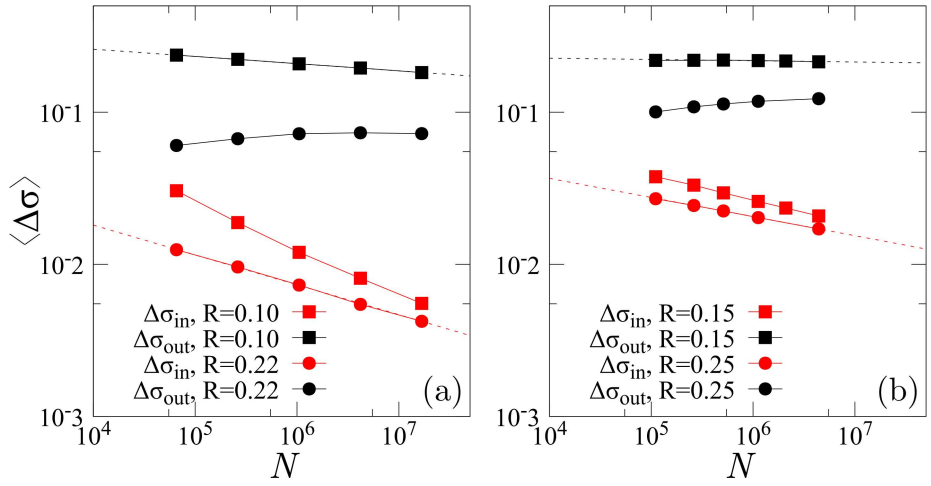

Figure 1.5: Contribution to the $O(1)$ stress drop from sites inside (red) and outside (black) the shear band, as a function of the system size. We see that the macroscopic stress drop is dominated by sites in the bulk of the material, whose contribution is barely affected by the system size. The stress variation coming from the sites inside the shear band is negligible and decreases with a power law as a function of the system size, as explained in the main text. Data for 2D (a) and 3D (b).

this quantity follows a Gumbel distribution,

$$P_N^{\gamma_{\max}}(\gamma_{\max}=\gamma,R)=P_N^{\sigma_i^{\max}}(\sigma_i^{\max}=1-\gamma,R)\approx \frac{1}{a_N}\exp\left[-\frac{(1-\gamma)-b_N}{a_N}-\exp\left(-\frac{(1-\gamma)-b_N}{a_N}\right)\right], \tag{1.12}$$

with $a_N = R/\sqrt{2\log(N)}$ and $b_N = R[\sqrt{2\log(N)} - \log(4\pi N)/(2\sqrt{2\log(N)})]$, since in the small R limit our initial distribution is almost identical to a Gaussian [164]. This means that, in the hypothesis that $\Delta\sigma_{\max}(N)$ is proportional to $1-\sigma_i^{\max}(N)$, the average value of the stress drop decreases with the system size, which explains the results in Fig. 1.5. From the form of the probability distribution in Eq. (1.12) one can see that the average of $\Delta\sigma_{\max}$ decreases with the system size, although very slowly. This effect is a consequence of the absence of plastic activity in the elastic branch for small values of R and represents an unphysical result of our model, since in MD and in real materials plastic events are observed also in the elastic part. In Section 2.3 and in Section 3.1 we discuss other effects that originate from this issue and that will affect our choice of the order parameter for the brittle-to-ductile transition. We expect that, in a large enough system, the relation between $\Delta\sigma_{\max}$ and $\sigma_i^{\max}$ does not hold anymore, and the value of the macroscopic stress drop saturates. In Section 4.1 we give an argument to support this view.

To conclude this part about the analysis of the shear band formation and its effects, we study how the profile of the plastic activity during the macroscopic stress drop changes when changing the system size. As we increase L we note that the width of the shear band also increases, as does the accumulated plastic activity at each site. This means that during the formation of the shear band, the sites that are involved tend to yield multiple times and,

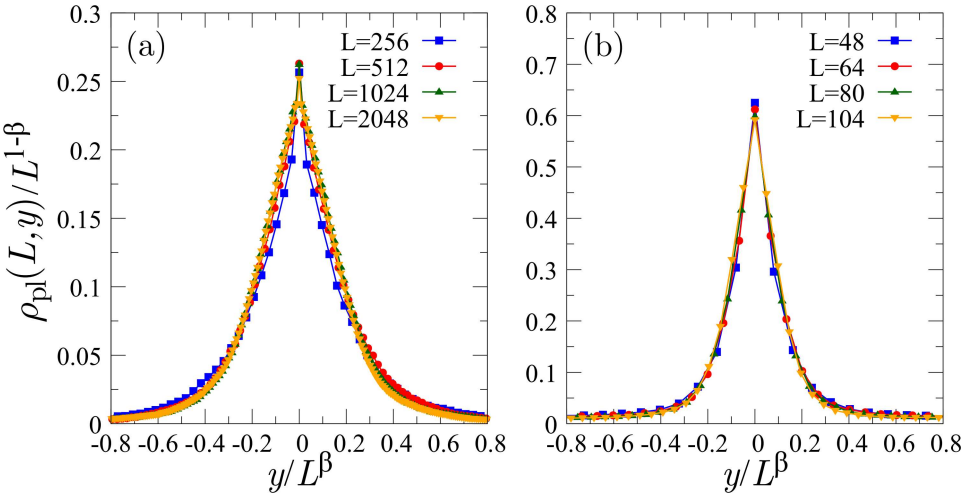

Figure 1.6: Distribution of plastic strain along the direction perpendicular to the shear band as a function of the distance from its center, for 2D (a) and 3D (b) systems, with $R = 0.22$ and $R = 0.25$ respectively. The curves show a good collapse for the choice $\beta = 0.61$ in 2D and $\beta = 0.64$ in 3D.

on average, they yield more and more times as the system size increases. The possibility of yielding multiple times appears as an important factor in explaining the macroscopic stress drop that we observe. In order to have a more quantitative measure of the variation of the plastic activity with the system size we define the quantity $\rho_{\rm pl}(L, y)$ as the average amount of plastic activity along the direction perpendicular to the shear band. We assume for example that the shear band is aligned along the x axis (one can define the same quantity for the other cases by symmetry). For each value of y we compute the average plastic activity, centering it for each sample around the value $y_{\rm SB}$ where the maximum plastic activity occurs. This gives

$$\rho_{\rm pl}(L, y) = \frac{1}{L}\Big\langle \sum_x \gamma^{\rm pl}_{x,y-y_{\rm SB}} \Big\rangle. \tag{1.13}$$

Since the stress drop is system-size independent in the low-disorder regime and is a direct consequence of the plastic activity, we have the constraint that the integral over the whole system length of $\rho_{\rm pl}(L, y)$ does not depend on L. As a consequence, we expect $\rho_{\rm pl}(L, 0) \sim L^{\beta-1}$, since the width of the shear band grows as L^{β} (see above). We plot this quantity with rescaled axis in Fig. 1.6, for $R = 0.22$ in 2D and $R = 0.25$ in 3D and for different system sizes. We observe a good collapse of the curves with exponents that are compatible with the ones obtained by fitting $\Delta\sigma_{\rm in}$. Such a collapse is not very good when instead we consider the very low disorder regime, again because of the relation between $\Delta\sigma_{\rm max}$ and $\sigma_i^{\rm max}$.

2.3 Characterizing the brittle transition

The view of the yielding transition as an out-of-equilibrium first-order transition was already proposed in [70, 71, 81]. As we did for the standard RFIM in the Introduction, we study here how the susceptibilities evolve with the strain γ when the system is prepared in the

brittle regime. In this case we define the connected and disconnected susceptibility as

$$\begin{aligned}\chi_{\text{conn}} &= \frac{\partial \langle n^{\alpha}(\gamma)\rangle}{\partial \gamma}, \\ \chi_{\text{disc}} &= N\big(\langle n^{\alpha}(\gamma)^2\rangle - \langle n^{\alpha}(\gamma)\rangle^2\big),\end{aligned} \tag{1.14}$$

for the order parameter $n(\gamma)$ (where we made the dependence on the disorder realization explicit again). The definition can be generalized to a different order parameter, for example σ, but the results are very similar. In [70, 71] the overlap between configurations was used as an order parameter in MD simulations, but such a quantity cannot be defined in the EPM. The function $n(\gamma)$ starts at 0 and then grows up to 1 when the shear band forms (if in the brittle phase) or as soon as all the sites in one row or column of the system have undergone a plastic event (if in the ductile phase). In this part we focus on the case where a macroscopic stress drop occurs and we study the susceptibilities at the yielding strain γ_{y}. Since we are now in the brittle case, the value of the order parameter $n^{\alpha}(\gamma)$ for a particular realization α of the disorder will at some point undergo a jump of order 1 for some value of the external strain $\gamma_{\text{y}}^{\alpha}$ (itself depending on disorder) when the shear band forms. Obviously this discontinuity disappears as we take the average over many realizations of the disorder, but by a careful finite-size scaling analysis we can investigate the behavior of the resulting average as the system size grows. We use the same idea as presented in Section 2.2.2 of the Introduction for the RFIM: we consider that the order parameter $n^{\alpha}(\gamma)$ evolves by simply following $n^{\alpha}(\gamma) = \theta(\gamma - \gamma_{\text{y}}^{\alpha})$ with $\theta(x)$ the Heaviside function. By averaging over disorder we obtain

$$n(\gamma) = \langle n^{\alpha}(\gamma)\rangle = \int_0^{\gamma} \rho_{\text{y}}(\gamma')d\gamma', \tag{1.15}$$

with $\rho_{\text{y}}(\gamma)$ the probability density of having a yield strain $\gamma_{\text{y}}^{\alpha} = \gamma$ for a certain sample α. The connected susceptibility is just equal in this case to the distribution of $\gamma_{\text{y}}^{\alpha}$ and it scales in the same way with the system size. We can then focus on the study of the distribution of $\gamma_{\text{y}}^{\alpha}$ instead. We assume that the value of the yielding strain fluctuates around a mean value $\gamma_{\text{y}} = \langle \gamma_{\text{y}}^{\alpha}\rangle$ that depends in general on the value of R but not on the system size. Since there are many independent sources of disorder, we would expect the distribution $\rho_{\text{y}}(\gamma)$ to follow the central limit theorem and as a result to be centered around some mean γ_{y} with a Gaussian form,

$$\rho_{\text{y}}(\gamma) \propto L^{d/2} \exp\Big(-(\gamma - \gamma_{\text{y}})^2/(\Delta L^{d/2})\Big), \tag{1.16}$$

where Δ is a constant of order one that depends on the sources of randomness. It follows that, if this is true, we expect to find $\chi_{\text{conn}} \sim L^{d/2}$, which is also the result naively expected in the RFIM (but not observed, recall Section 2.2.2) and in the mean-field approximation of the EPM (see Chapter 3). In Fig. 1.7 we show some results for the connected susceptibility of our EPM in 2D and 3D. In the panels (a) and (b) we plot χ_{conn} and the distribution of the yield strain $\rho_{\text{y}}(\gamma)$ for different values of the disorder strength R. As we expected, the crude approximation on the evolution of $n(\gamma)$ works quite well for small values of R ($R = 0.10$ in 2D and $R = 0.15$ in 3D), while it deteriorates as we go toward the critical point. From the distribution of γ_{y} in Eq. (1.16) we would expect the peak of the connected susceptibility to grow as $L^{d/2}$. We plot the scaling of $\chi_{\text{conn}}^{\text{peak}} = \chi_{\text{conn}}(\gamma_{\text{y}})$ and $\rho_{\text{y}}(\gamma_{\text{y}})$ for the same two values of R in panels (c) and (d). We see that for both values of R and both in 2D and 3D the susceptibility does not grow as $N^{1/2} = L^{d/2}$ as expected. In particular for very small

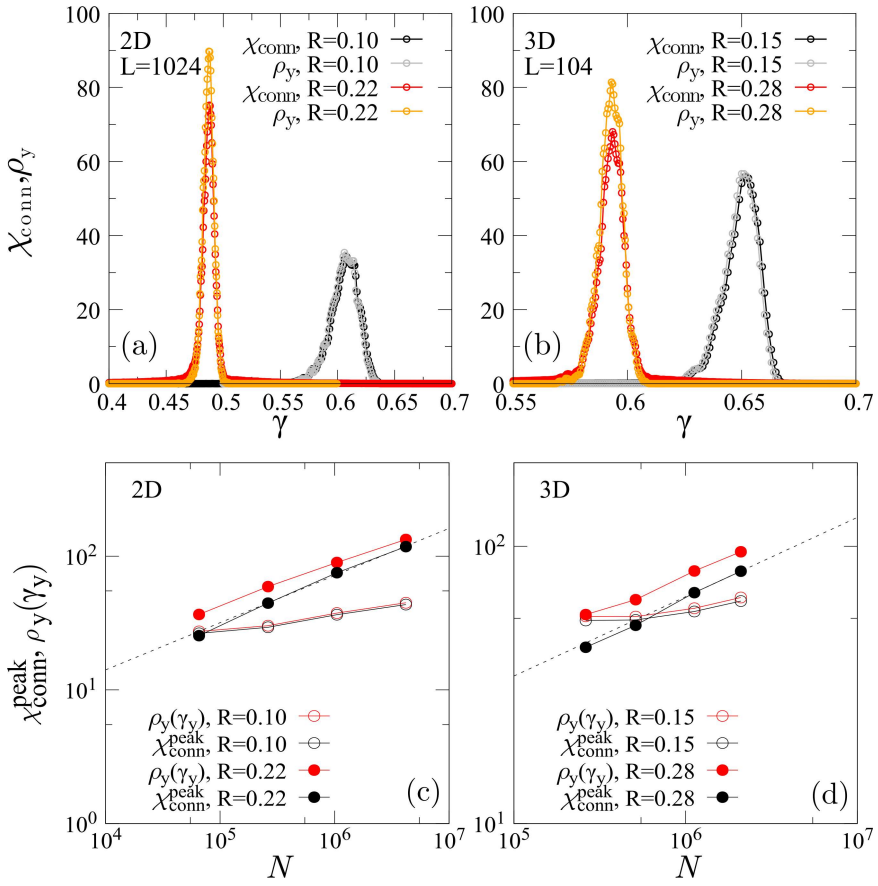

Figure 1.7: Connected susceptibility as a function of the external strain γ and distribution of the yield strain γ_y. Plotted for $L = 1024$ in 2D (a) and $L = 104$ in 3D (b). When R is small the connected susceptibility coincides with ρ_y almost perfectly, while as R gets closer to ductile regime the analogy deteriorates a bit. Scaling of the susceptibility peak $\chi^{peak}_{conn} = \chi_{conn}(\gamma_y)$ and ρ_y peaks in 2D(c) and 3D(d) for the same two values of R. The black dashed lines are fits performed using the last 3 points and give $\chi^{peak}_{conn} \sim N^{0.35}$ in 2D and $\chi^{peak}_{conn} \sim N^{0.28}$ in 3D. The curves are obtained after averaging over $8000, 6000, 5000, 1000$ samples respectively the sizes $L = 256, 512, 1024, 2048$ in 2D and $5000, 3000, 3000, 1500$ samples respectively the sizes $L = 64, 80, 104, 128$ in 3D.

R values, the peak is almost unchanged in 2D and increases slowly in 3D. For a slightly larger R we instead have a clear growth with the system size, but the exponents obtained from the fit (0.35 in 2D and 0.28 in 3D) are closer to 0.3 than to 0.5. A similar scaling is also observed in 2D MD simulations [137], while in 3D the susceptibility scales as predicted by Eq. (1.16) [4]. This issue can have two explanations. First of all it is possible that the results we obtained are influenced by the rare regions that occur only in sufficiently large samples. Because of the scarsity of plasticity before yielding in systems at low disorder and small sizes, it is possible that the first-order transition that we observe is not the "correct" one. As we discuss in Section 4.1 following the lines of [163], the addition of a weaker region prone to yield indeed alters the value of the yielding strain. Not only the average value, but

also the whole distribution of γ_y^α may be affected by the presence of such regions. And, as discussed, this distribution is intimately related to the connected susceptibility. To check this we studied a variant of the EPM in which a seed is inserted at the beginning of the dynamics (see Section 4.1). However, we cannot exclude the possibility that we are measuring the correct exponent and that the emergent effective random field is not independent for every site, but is instead correlated with correlations that decay with $r^{-(d-\rho)}$ (see [137]). The first hypothesis seems more plausible, also in view of the results obtained for the RFIM in Section 2.2.2 of the Introduction.

In the low-disorder hypothesis $n^\alpha(\gamma) = \theta(\gamma - \gamma_y^\alpha)$, the disconnected susceptibility is simply

$$\chi_{\text{disc}}(\gamma) = N\big(\langle\theta(\gamma - \gamma_y^\alpha)\rangle - \langle\theta(\gamma - \gamma_y^\alpha)\rangle^2\big), \tag{1.17}$$

whose maximum at γ_y goes like $N = L^d$. This scaling is confirmed by simulations, so that the finite-size effects that influence the scaling of the connected susceptibility do not play a role in the disconnected one. As we will see, this is due to the fact that finite-size effects act mainly in the distribution of γ_y^α, which does not affect much the disconnected susceptibility which scales as N for whatever (reasonable) ρ_y.

3 Critical point between brittle and ductile regime

In this part we describe the main result of this chapter, i.e., the numerical evidence for the presence of a finite-disorder critical point that separates brittle and ductile behavior. First we show how to characterize the properties of the critical point with two different order parameters via the finite-size scaling procedure. We however observe that the value of the critical point slowly shifts as we increase the system size, which makes one wonder whether R_c stays finite when we approach the thermodynamic limit. We then give an argument for a finite-disorder critical point even as $N \to \infty$.

3.1 Characterizing the brittle-to-ductile transition

In order to capture the change in the stress-vs-strain curve we start by using the same order parameter as in [4], the largest stress drop $\Delta\sigma_{\max}^\alpha$. This is equivalent to what we did in the Introduction, where we described the critical point of the RFIM by means of the order parameter $\Delta m_{\max}^\alpha$. As we discussed, we expect the order parameter to be of order 1 when the disorder is weak and to become small when instead R grows. The quantity $\Delta\sigma_{\max}$ seems to fit well: in systems with large disorder it goes to 0 as the system size increases, while in the brittle phase it remains finite. The mean and variance of $\Delta\sigma_{\max}$ are presented in Fig. 1.8 for both the 2D and 3D EPMs. As anticipated, the average value decreases to a very small value (vanishing in the limit $N \to \infty$) for large R. Around the onset of the growth of $\langle\Delta\sigma_{\max}\rangle$, the (disconnected) susceptibility, $N\left(\langle\Delta\sigma_{\max}^2\rangle - \langle\Delta\sigma_{\max}\rangle^2\right)$, shows a peak that grows with the system size. This is in accordance with the observations from molecular dynamics [4] and is the signature of a critical point. However, as we decrease R further, the average value decreases with the system size, as already observed in Fig. 1.5. Even more strikingly, around the same values of R, the susceptibility seems to diverge again with the system size. This unexpected behavior can be explained by considering the same simple argument from extreme value statistics that we used to explain the decreasing of $\Delta\sigma_{\max}$ with N observed

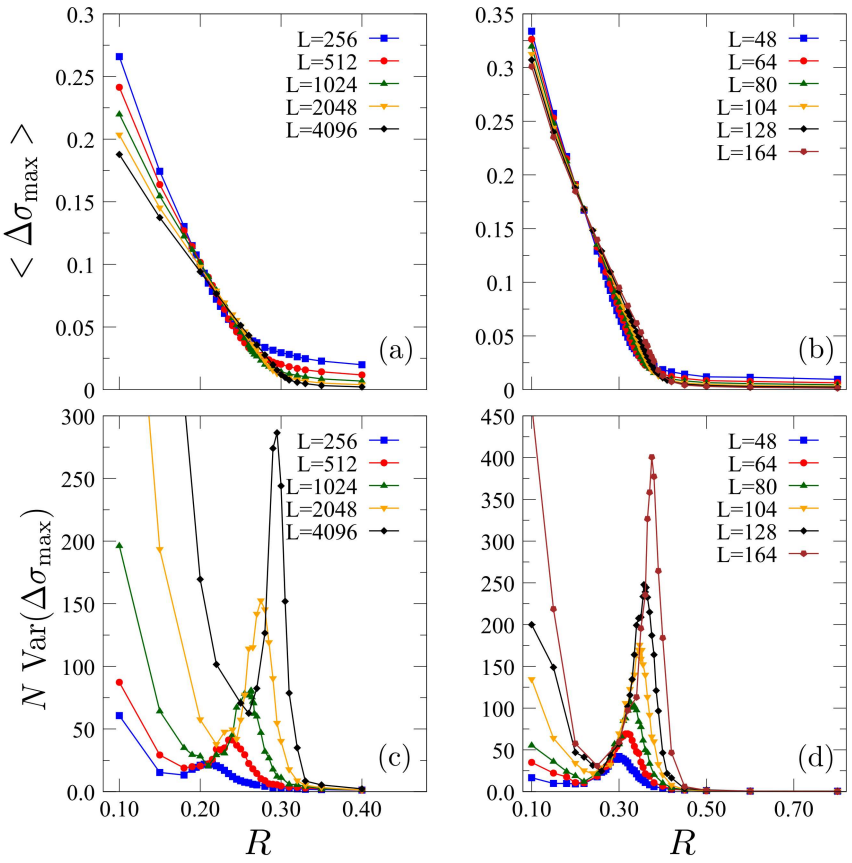

Figure 1.8: Evidence for a critical point in the 2D and 3D EPM. Upper: Disorder-averaged value of the order parameter $\langle \Delta\sigma_{\max} \rangle$ as a function of R for several system sizes in 2D (a) and 3D (b). Lower: Variance of $\Delta\sigma_{\max}$ multiplied by $N = L^d$, i.e., disconnected susceptibility, in 2D (c) and 3D (d). The susceptibility increases again when R goes to 0.

in Fig. 1.5 for very weak disorder R. From our argument we saw how the macroscopic stress drop $\Delta\sigma_{\max}$ is related to $\sigma_i^{\max}$ in this case. We used before this analogy to understand the behavior of the average of $\Delta\sigma_{\max}$ and we now use the same idea to discuss its variance. We then get that in the $R \to 0^+$ limit

$$\langle \Delta\sigma_{\max}^2 \rangle - \langle \Delta\sigma_{\max} \rangle^2 \approx \frac{\pi^2 R^2}{12 \log(N)}, \tag{1.18}$$

which explains the growth of the susceptibility at small values of R. As already pointed out, this growth would not be observed in MD simulations or in experiments, as many plastic events are present even in the elastic branch [158], destroying the relation between $\Delta\sigma_{\max}$ and $\sigma_i^{\max}$.

In order to avoid this problem we have used another order parameter, $n(\gamma)$, which we introduced before. Since the presence of a macroscopic stress drop in the brittle regime is accompanied by the abrupt formation of a shear band, one can think of characterizing yielding by looking at the number of sites that yield in each horizontal or vertical line

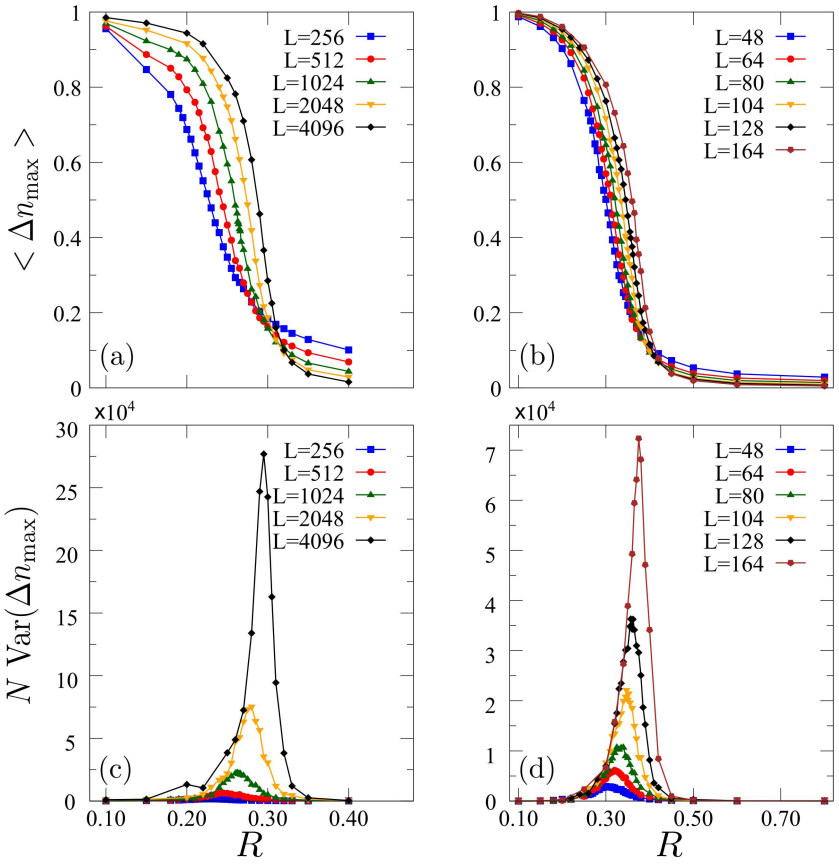

Figure 1.9: Evidence for a critical point in 2D and 3D EPMs. Upper: Average value of the order parameter $\langle \Delta n_{\max} \rangle$ as a function of R for several system sizes in 2D (a) and 3D (b). Lower: Variance of $\Delta n_{\max}$ multiplied by $N = L^d$, i.e. disconnected susceptibility, in 2D (c) and 3D (d).

(in 2D) or plane (in 3D). This is exactly what $n(\gamma)$ does. As we saw in Fig. 1.1, the discontinuous stress drop of $\sigma(\gamma)$ in the brittle regime corresponds to the discontinuous jump of $n(\gamma)$, whereas the mild continuous crossover of $\sigma(\gamma)$ in the ductile regime corresponds to a continuous increase of $n(\gamma)$. Therefore, $n(\gamma)$ essentially contains the same information as $\sigma(\gamma)$ for characterizing brittle and ductile yielding. As for the stress-drop order parameter, we compute the largest jump in this quantity, which allows us to define a new order parameter $\Delta n_{\max}$ as $\Delta n_{\max} = \max_\gamma(n(\gamma + \delta\gamma) - n(\gamma))$ appropriate for studying the critical point. We then proceed as before and compute the average value and the variance of this quantity. This is what we show in Fig. 1.9. Again, the average value of $\Delta n_{\max}$ over many samples is plotted as a function of R in 2D (left) and 3D (right) systems. Essentially the same phenomenology as with $\Delta\sigma_{\max}$ is observed, but now the jump happening at small disorder strength saturates to 1 as $R \to 0^+$ and $N \to \infty$, as expected. In the bottom panels of Fig. 1.9 we show the disconnected susceptibility of the order parameter $\Delta n_{\max}$, which shows a peak that becomes sharper and higher as the system size increases, as we already saw for $\Delta\sigma_{\max}$. This time however, the fluctuations go to zero fairly quickly both on the right-hand side and on the

left-hand side of R_c, and no increase is observed for the small values of R that we studied. The choice of this new order parameter solves the problems we faced when computing both the average and the fluctuations of $\Delta\sigma_{\max}$. Note that contrary to the definition in Eq. (1.14), the disconnected susceptibility that we use here is studied as a function of R and not γ and goes to vanishingly small values in the brittle regime.

We can then proceed by performing a finite-size scaling analysis in order to investigate the existence of the critical point and its properties. Due to the similarities that the yielding transition shows with the RFIM, we use the same scaling ansatz here, with $\chi_{\text{disc}}(r, L) \sim L^{\bar{\gamma}/\nu}\Psi(rL^{1/\nu})$, where $r = (R - R_c)/R$ is the relative distance to the critical point $R_c(L)$, $\bar{\gamma}$ and ν are critical exponents, and $\Psi(\cdot)$ is a scaling function. Obtaining an estimate of these quantities is not an easy task for systems out of equilibrium and with disorder and is sometimes difficult even when one already knows the correct solution [10]. Here we start by trying to evaluate the exponents. Following the scaling ansatz of the RFIM we expect the peak of the disconnected susceptibility to diverge as $L^{\bar{\gamma}/\nu}$ while its width should vanish as $L^{-1/\nu}$. We then plot the value of the peak as well as the full width at half-maximum (FWHM) of the disconnected susceptibility in a log-scale and we fit to a line in order to get a first estimate of the exponents. The results are shown in the top panels of Fig. 1.10. We see that the fit is good for the scaling of $\max(\chi_{\text{disc}})$, which gives $\bar{\gamma}/\nu = 1.86 \pm 0.02$ in 2D and $\bar{\gamma}/\nu = 2.66 \pm 0.04$ in 3D, with the error bars coming from the fitting procedure. On the other hand, the fit of the FWHM depicted in Fig. 1.10(b) is less precise, as the data points are more noisy. As a consequence, the error bars are larger, and the fit gives $\nu = 3.0 \pm 0.3$ in 2D and $\nu = 2.5 \pm 0.2$ in 3D. Another possibility to perform the finite-size scaling analysis is to collapse the curves obtained for different system sizes. From the relation $\chi_{\text{disc}}(r, L) \sim L^{\bar{\gamma}/\nu}\Psi(rL^{1/\nu})$, it follows that

$$\Psi(x) \sim L^{-\bar{\gamma}/\nu}\chi_{\text{disc}}(xL^{-1/\nu}, L) \tag{1.19}$$

does not depend on the system size, so that by plotting the right-hand side of the above equation all the curves should collapse on a single master curve for the right values of $\bar{\gamma}/\nu$ and ν. In Fig. 1.10(c,d) we can see that the curves collapse quite well both in 2D and in 3D, and which also provides the shape of the scaling function. This figure is obtained by adjusting the parameters $\bar{\gamma}$, ν, and $R_c(L)$ in order to get the best possible visual collapse. The curves shown in Fig. 1.10(c,d) are obtained for $\bar{\gamma}/\nu \approx 1.82$ and $\nu \approx 2.9$ in 2D, and $\bar{\gamma}/\nu \approx 2.61$ and $\nu \approx 2.2$ in 3D, values that are consistent with those determined by the fitting procedure considered above. While searching for the best values of the exponents to collapse the disconnected susceptibility curves we noticed that such a collapse is quite sensitive to a change in the value of $\bar{\gamma}/\nu$, while a satisfying result is obtained for a large spectrum of ν values. This is also reflected in the fact that the main differences between all the scaling procedures are in the value of ν rather than in that of $\bar{\gamma}/\nu$. This makes the determination of the exponent ν rather difficult. We also notice that in 2D the collapse is slightly worse for $R < R_c$ and small system sizes, but in general we are not too interested in what happens in the tails of the plot. Our main goal is to have a good collapse close to the critical point, i.e. for $r \approx 0$. Finally, we compute the values of the exponents and we give an expression for the scaling function $\Psi(x)$ in a third way, following the procedure of [165]. In order to fit the data to the scaling prediction we use the following functional form for the

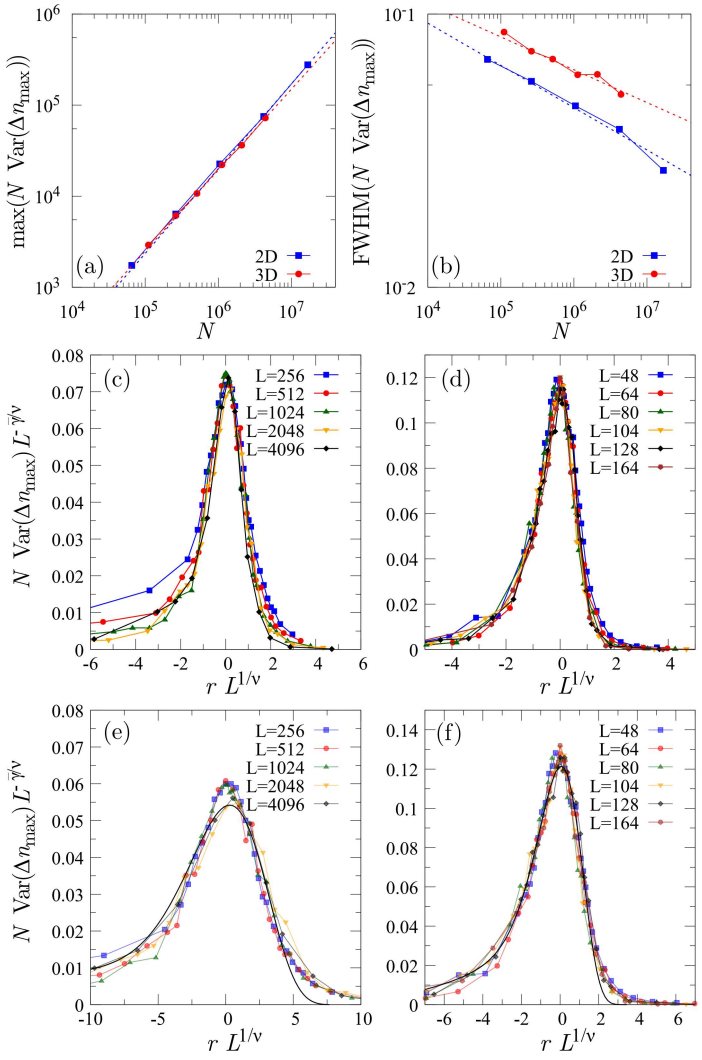

Figure 1.10: Finite size scaling analysis of the EPM close to the critical point. In (a) and (b) we plot the scaling of the maximum and of the full width at half maximum of the disconnected susceptibility, respectively. The dashed lines are obtained by fitting the points and give $\bar{\gamma}/\nu = 1.86 \pm 0.02$ and $\nu = 3.0 \pm 0.3$ in 2D and $\bar{\gamma}/\nu = 2.66 \pm 0.04$ and $\nu = 2.5 \pm 0.2$ in 3D. The error bars come from the fitting procedure. In (c,d) we collapse the disconnected susceptibility curves by hand in 2D and 3D, respectively. A good collapse is obtained with $\bar{\gamma}/\nu = 1.82$ and $\nu = 2.9$ in 2D and $\bar{\gamma}/\nu = 2.61$ and $\nu = 2.2$ in 3D. In (e,f) the collapse is obtained by fitting to a master curve the three largest system sizes for both 2D and 3D, respectively. From this procedure we have $\bar{\gamma}/\nu = 1.85$ and $\nu = 1.92$ in 2D and $\bar{\gamma}/\nu = 2.59$ and $\nu = 1.70$ in 3D.

scaling function:

$$\Psi(x) = C \exp\left[y(x) - \exp(y(x))\right] \sum_{i=0}^{i=3} a_i H_i(y(x)), \tag{1.20}$$

with $y(x) = (x - x_c)/\alpha$, $H_i(x)$ the i-th Hermite polynomial, and C, x_c, α and the a_i's are

fitting parameters. With the scaling hypothesis in Eq. (1.19) and this functional form we have fitted the curves for the three largest system sizes that we simulated. The results are shown in Fig. 1.10(e,f) for 2D and 3D respectively. This last fitting procedure gives slightly different values for the exponents, with $\bar{\gamma}/\nu \approx 1.85$ and $\nu \approx 1.92$ in 2D and $\bar{\gamma}/\nu \approx 2.59$ and $\nu \approx 1.70$ in 3D. By plotting again the curves, one can see that even if the value of ν seems to change in a significant way, the collapse is still quite good. As we already stressed, finding the precise value of ν is hard, since our procedure is not very sensitive to its change. Probably still more data would be needed to perform a more accurate finite-size scaling analysis.

3.2 Bounding the location of the critical point

The above results support the existence of a critical point that separates the brittle and ductile regimes, as proposed in [4]. However, from the bottom panels of Fig. 1.9 it seems that this critical point slowly shifts to larger values of R as L increases. A similar effect on the critical temperature was observed in MD simulations of sheared solids in [4, 137] (as well as in numerical simulations of the 2D RFIM [132]), where it was argued that the value of the critical disorder stays finite as $L \to \infty$. As we discussed, a different point of view has recently been proposed in [6, 83, 84], where it was argued that stress-vs-strain curves in which an overshoot without a macroscopic jump is observed are just a result of the small system sizes used in simulations. In this picture, the yielding transition should always be brittle and, as a consequence, $R_c^\infty \to \infty$. This means that all systems are brittle when taken in the thermodynamic limit and in the AQS setting. Understanding the fate of the critical point as L diverges is therefore a key issue. It is actually different from the persistence of a continuous overshoot in the ductile regime in the thermodynamic limit, which was the main concern of [83]. As we showed in Fig. 1.1 a clear evolution between distinct yielding patterns is observed as R is decreased, from a purely monotonic increase of the stress to a continuous overshoot and then to a discontinuous drop. The critical point that we characterized in the previous section marks the passage between the last two patterns. To try to understand the fate of the overshoot and its relation with the critical point when $N \to \infty$, we measure for different values of N the value of R at which the overshoot first appears (coming from large R) in the average stress-vs-strain curve, and we denote it by $R_o(N)$. Clearly $R_o(N)$ bounds $R_c(N)$ as in order to have a macroscopic stress drop one first needs an overshoot in the stress-vs-strain curve. In order to determine this value we average the stress-vs-strain curve over many independent samples. In Fig. 1.11(a) we show an example for the 2D EPM with $L = 2048$. We plot three averaged stress-vs-strain curves for different values of R in the vicinity of R_o, and we can clearly observe in the insets where the non-monotonicity first appears. We perform the same analysis for different values of L both in 2D and in 3D. In order to be sure that no overshoot appeared even at large values of γ, we let the code run up to $\gamma = 10$ for small system sizes and up to $\gamma = 3$ for larger ones. Due to the computational cost of these simulations we could not reach the same system size values as for R_c, but the ones we managed to study seem sufficient to conclude. In Fig. 1.11(b,c) we display $R_o(N)$, together with the critical disorder $R_c(N)$ for 2D and 3D. We plot the two quantities in log-lin scale as a function of the system size $N = L^d$. From our results we find that the value of R_o stays essentially unchanged when N varies in both cases, while R_c shows a slow increase. The values of $R_o(N)$ and $R_c(N)$ define three distinct yielding regimes in the (N, R) plane, as schematically illustrated by the insets in Fig. 1.11(b,c).

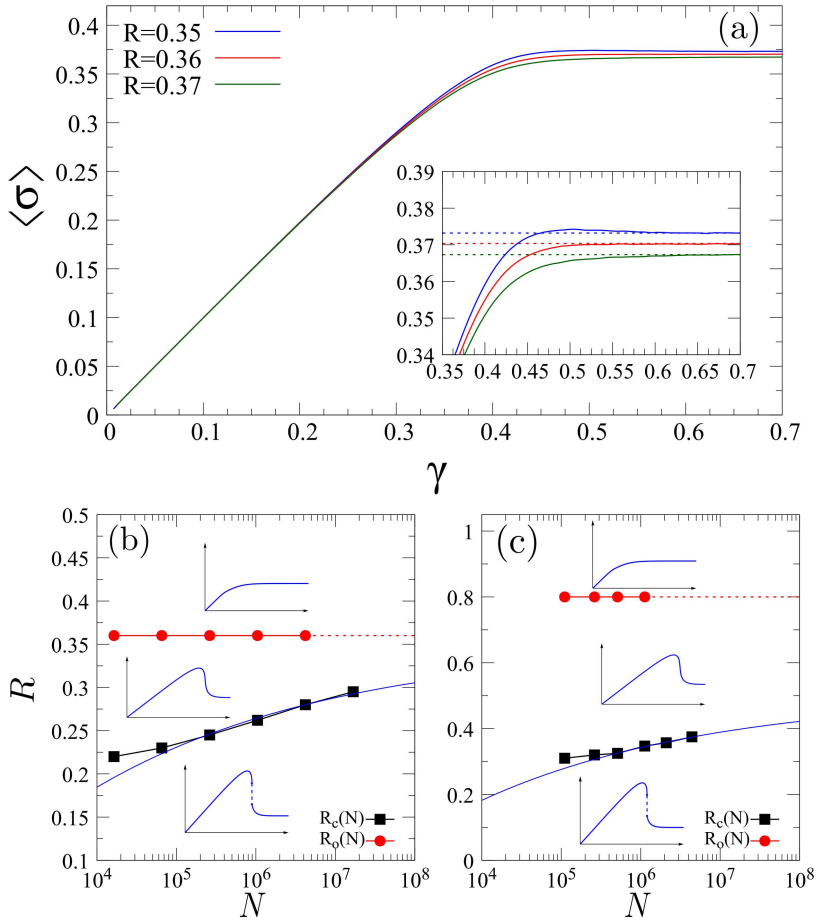

Figure 1.11: (a) Average stress-versus-strain curves for a 2D model with $L = 2048$ close to $R_o = 0.36$. Inset: zoom in on the region where the overshoot appears. The dashed horizontal lines are a guide for the eye. (b,c) Value of the disorder at which the overshoot first appears, R_o, and at the apparent critical point, R_c, as a function of the system size, $N = L^d$, in 2D (b) and in 3D (c). Blue lines are fits to $R_c^\infty - a/N^b$, with $R_c^\infty = 0.35$, $a = 0.61$, $b = 0.14$ in 2D and $R_c^\infty = 0.5$, $a = 1.29$, $b = 0.15$ in 3D. The parameter b is related to the critical exponent ν through $1/\nu = db$, so that the fits yield $\nu \approx 3.57$ in 2D and $\nu \approx 2.22$ in 3D. Insets: The corresponding schematic stress-versus-strain curves.

The upper part, where $R > R_o(N)$ corresponds to a monotonic increase of the average stress, with no overshoot (black curve in Fig. 1.1). The region $R < R_c(N)$ corresponds to a discontinuous stress drop at yielding (red curve in Fig. 1.1). Finally, the region between the two values, $R_c(N) < R < R_o(N)$, corresponds to a continuous average stress curve with a mild overshoot (blue curve in Fig. 1.1). As we discussed above, $R_c(N)$ has to remain below $R_o(N)$, which then gives an upper bound on the critical disorder. The fact that $R_o(N)$ is essentially independent of N thus provides strong evidence that $R_c(N)$ converges to a finite value for large N (bounded by $R_o^\infty = R_o(N \to \infty)$) and that a finite-disorder brittle-to-ductile critical point persists in the thermodynamic limit. Moreover, this is also evidence for the existence of a ductile phase over a finite range of disorder strength. The fate of the region

where a continuous overshoot with a ductile behavior takes place as $N \to \infty$ (which was the main concern of [83]) is less clear and depends on whether $R_c(N)$ converges to R_o^∞ or to $R_c^\infty = \lim_{N\to\infty} R_c(N) < R_o^\infty$ in the thermodynamic limit. In the former case the overshoot disappears exactly at the critical point whereas a regime of ductile yielding with an overshoot exists in the latter case. We show in Fig. 1.11(b,c) the best fits to $R_c(N) = R_c^\infty - a/N^b$ with R_c^∞, a, and b free parameters. We find that R_c^∞ is finite in 2D and 3D. In the critical scaling picture, the parameter b is related to the exponent ν through $1/\nu = db$. The fits then yield $\nu \approx 3.57$ in 2D and $\nu \approx 2.22$ in 3D, values which, given the large uncertainties, are consistent with the previous determinations given above. Strictly speaking, we cannot exclude an alternative scenario in which $R_o(N)$ would start to increase with N above some critical size N^* which is out of reach of present-day simulations and would ultimately diverge in the thermodynamic limit together with $R_c(N)$. However, in view of the absence of any observable N-dependence of $R_o(N)$ in the accessible range, which spans three decades in 2D, and of the lack of any sound theoretical argument supporting the existence of a critical size N^*, this possibility seems unlikely.

4 Variations of the model

We now discuss some variations of the model to explain the observed behavior and to check the robustness of our conclusions.

4.1 Effect of a seed

It has been shown that, as for the short-range RFIM [133], the discontinuous yielding transition of amorphous solids is controlled by rare weak regions [7, 163]. In the Introduction we discussed how the plastic deformation is a consequence of localized rearrangements of particles and how the formation of a shear band originates from the organization of multiple events in a line (plane) in 2D (3D). The structural origin of the regions that undergo a plastic rearrangement has been of interest in the last few years [69]. From these studies one can see that plasticity emerges from "weak spots", i.e., regions in which the material is locally more poorly annealed than the bulk. However, for very stable glasses, the occurrence of such weak spots is improbable. If ξ is the typical structural length in the amorphous solid, length which is known to be rather small, one expects that the probability to find a weak region of volume v is exponentially suppressed as $\exp\left(-cv/\xi^d\right)$, with c some constant of order 1, so that such regions are extremely rare [163]. The probability of finding a weak region of volume v in a system of volume $N = L^d$ is then proportional to $(L^d/v)\exp\left(-cv/\xi^d\right)$ and is of order 1 only for L exponentially large in v. The idea here is similar to the one of Griffiths phases [93], studied in the case of an Ising ferromagnet, with a certain probability of an empty site $p \in [0, 1]$. At $p = 0$ the standard Ising model is recovered, while at $p = 1$ no more sites are present. Between these values, as the value of p is decreased below p_c the first percolating clusters appear. The critical temperature $T_c(p)$ of this model decreases as p increases, from the pure Ising model one T_c^0 at $p = 0$ to $T_c = 0$ at $p = p_c$. Below this temperature the system shows a ferromagnetic orientation, while above it is paramagnetic. In [93] it is however argued that, for $p > 0$, the magnetization of the system is non-analytical in $H = 0$ even at larger temperatures than the critical ones, for $T_c < T < T_c^0$. The rare large

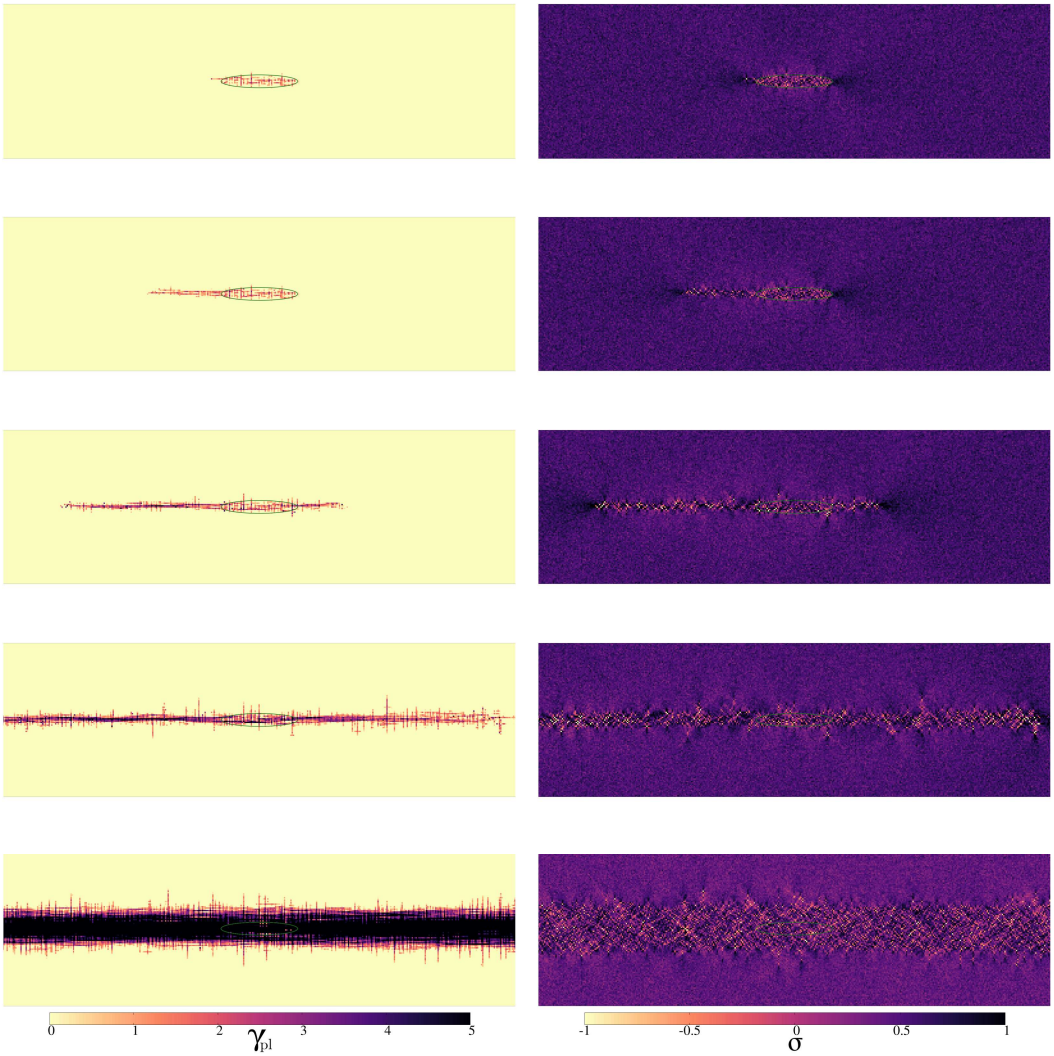

Figure 1.12: Evolution of the shear band inside the largest avalanche in an EPM with a seed. The direction is forced by the symmetry of the ellipse (in green) which has the major axis along x of semi-length $D_a = 30$ and the minor one along y of semi-length $D_b = 5$. Avalanche steps are $l/l_{max} = 0, 0.1, 0.2, 0.3$ and 1. Obtained in 2D with $L = 1024$ and $R = 0.10$. The plot is for $y \in [452, 572]$ and $x \in [256, 768]$ with the seed centered at $(512, 512)$.

clusters are responsible for this non analyticity. If a sufficiently large region of occupied sites is found when $T < T_c^0$, this will have a magnetization different from 0 that cannot be altered from thermal fluctuations. Such large regions are however exponentially rare in their size, so that their contribution will only appear as an essential singularity in the behavior of $m(H)$. As we saw in the Introduction, a similar role is played by rare weak regions in the spinodal transition of the AQS-driven RFIM in 3D [133]. In particular these rare regions alter the whole distribution of the coercive field of the RFIM, which in turn has a consequence on the scaling of the connected susceptibility.

To check the role of weak regions in the case of the EPM we use a similar method as

that described in [133] and [163]. The idea is to mimic the effect of spontaneously present weak regions in a very large sample (in the thermodynamic limit) by the introduction by hand of a weak region in a finite-size sample. We initialize our EPM as before, but with the addition of a weak region at the center of the sample. The shape of the seed can be chosen at will, since in the thermodynamic limit all shapes will be present. The ones of interest to us are those which favor the formation of a shear band and for simplicity we choose an ellipsoidal form (see Fig. 1.12). In 2D the weak region is characterized by the semi length of major and minor axes D_a and D_b, which are parallel to the x and y axes respectively. Due to the symmetry of the model the seed can be oriented with the major axis along y as well, without changing the results. In 3D the situation is slightly different, since the kernel has the quadrupolar long-range nature only in the $x-y$ plane. We then take the seed to be oriented with the short axis along y and we define the half length of the ellipse axis along z as $D_c = D_a$. The resulting shear band plane will appear perpendicular to the y axis. We choose a site-dependent stress threshold for sites inside the ellipse from a Gaussian distribution of zero mean and standard deviation $R_{\text{seed}} = 0.2$. The initial value of the stress for such sites is taken from a probability distribution similar to the one in the standard version, but adapted to consider the fact that each site has a different threshold (see Appendix B for more details). The sites in the bulk of the material have the same stress threshold $\sigma_i^{\text{th}} = 1$ as before, and they start at $\gamma = 0$ with a value chosen from the same distribution Eq. (1.7) as the standard version of the model. A similar test was performed in [7], where a weak seed was inserted in order to trigger the formation of a shear band in a very brittle system.

To start, we notice from Fig. 1.13(a) that, as in [163], the behavior of the stress inside the seed is similar to the one of a poorly annealed sample, while the total stress shows the characteristic drop of brittle materials. We point out that the seed insertion leaves the elastic regime almost unchanged, as it is clear from the full and dashed lines. However, as strain increases, all the samples with a seed yield systematically before the ones without. In order to quantify the effect of this weak region we measure the average value of the yield strain $\langle \gamma_{\text{y}} \rangle$ and we plot it for different values of R and D_a. The value of D_b is kept fixed, with $D_b = 5$ in 2D and $D_b = 3$ in 3D. The results are displayed in Fig. 1.13(b) and (c) for 2D and 3D respectively. This plot is very similar to that of [133] for the RFIM, which is shown in Fig. I.13(b). In the latter, the presence of a region prone to flip influenced the value of the coercive field H_c, while in the present case it affects γ_{y}. In both cases the effect of the seed vanishes as one approaches the critical value of the disorder strength R_c. In Fig. 1.13(d) we show how the seed size affects the stress-vs-strain curve in the brittle case. The larger the seed the sooner the systems yields, as already observed [7, 163] and depicted in panel (c). At the same time, we see that both the stress and the order-parameter curves are not affected by the presence or the size of the seed. We checked that these results are robust with respect to changes in D_b up to $D_b \approx D_a/2$. We therefore conclude that one should consider the effect of large weak regions in order to get an estimate of the value of γ_{y} in the thermodynamic limit. How large should these weak regions be? In principle one should consider the double limit $1 \ll D_a \ll L$, in which the region is very large but does not scale with the system size. Notice that in the case of the standard driven RFIM one can give an argument on the correct form of the seed that one expects to nucleate the largest avalanche at small values of R. As the system is isotropic, the limit of the depinning of a flat interface is known, and one cannot find a more efficient destabilizing process. One can assume that

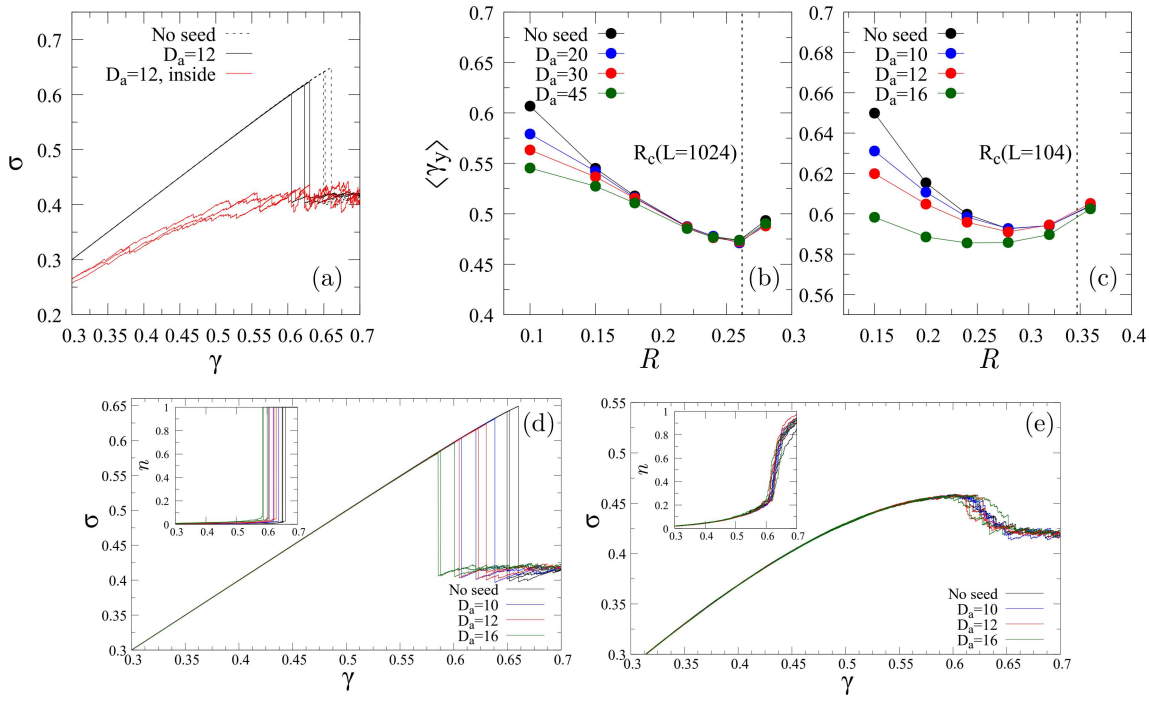

Figure 1.13: (a) Stress-vs-strain curves for three different samples with (full line) and without (dashed line) seed, obtained for a 3D EPM with $L = 104$, $R = 0.15$, and seed size $D_a = D_c = 12$, $D_b = 3$. Red lines display the stress evolution inside the seed. The figure is very similar to what was shown in [163]. (b,c) Effect of seeds for different sizes D_a on the average value of yield strain γ_y for $L = 1024$ in 2D (b) and $L = 104$ in 3D (c). The vertical dashed line marks the critical value R_c for the relative system sizes. The results are obtained with $D_b = 5$ in 2D and $D_b = 3$ in 3D. (d,e) Stress-vs-strain curves from three independent samples obtained in 3D with $L = 104$ and different seed sizes. In (d) $R = 0.15 < R_c(L = 104)$, while in (e) $R = 0.36 > R_c(L = 104)$. Inset: the effect of the seed on the n-vs-strain curve.

a spherical seed of size of the order of the depinning correlation length drives the system to the macroscopic jump in the thermodynamic limit. A similar reasoning is not possible here in the EPM, since among others it is not a priori clear which precise shape should one give to the seed. It is however clear that some seeds are unstable at a value of the external strain $\gamma_y^{\text{seed}} < \gamma_y^{\text{noseed}}$, which means that in the thermodynamic limit the yield strain is bounded from above by γ_y^{seed}.

Seed insertion affects the average value of the yielding strain. It also more generally affects the distribution of γ_y and consequently it can change the connected susceptibility and its scaling at γ_y. As we discussed before, in the case without seed and for very small values of the disorder strength, the distribution of the least stable site controls the value of the yielding strain. It follows that γ_y is drawn from a Gumbel distribution. This mechanism hides the true scaling of the connected susceptibility, due to the lack of the weak regions that are present in the thermodynamic limit. Contrary to the change of the average value of γ_y, for which we can give some tentative estimates through the addition of a seed, the effect of rare regions on its distribution remains hard to evaluate. When the seed is added, the sites

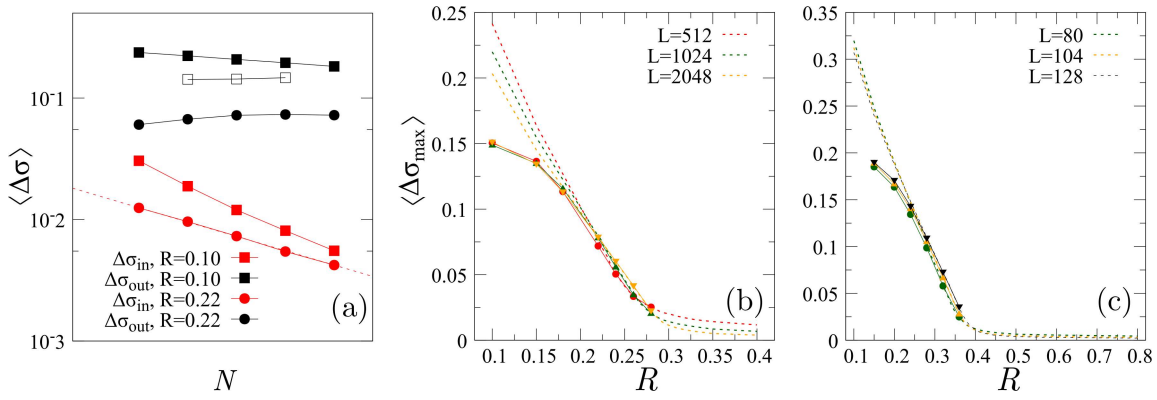

Figure 1.14: In (a) we report the same picture showing the stress drop contributions, as in Fig. 1.5(c), with the addition of the empty square symbols that are obtained in a 2D EPM with a seed of dimension $D_a = 45$, $D_b = 4$. In (b) and (c) we plot instead the average macroscopic stress drop as a function of R for different system sizes in 2D and 3D. The dashed curves are the ones of the system without seed, shown in the top panels of Fig. 1.8.

that flip first and trigger the spanning avalanche are those close to the weak region, so that the distribution of γ_y depends mainly on the number of sites close to the seed, which has no reason to lead to a Gaussian distribution as in Eq. (1.16). In the thermodynamic limit many weak regions of different sizes are present, and their distribution affects that of γ_y, and in turn the scaling of the connected susceptibility.

Before concluding we discuss how the insertion of a seed affects the macroscopic stress drop $\Delta\sigma_{\max}$. The presence of the seed introduces plastic activity that takes place in the system prior the macroscopic jump, and as a result breaks the relation between $\Delta\sigma_{\max}$ and $\sigma_i^{\max}$. The results are shown in Fig. 1.14. We first observe in panel (a) that the stress drop coming from sites outside the shear band does not decrease with the system size as observed in the case with no seed. Its value is almost constant with N. In panel (b) and (c) of the figure we plot how $\langle\Delta\sigma_{\max}\rangle$ changes with R. We see that for large enough values of the disorder strength the macroscopic stress drop is unchanged after the addition of the seed, while as R decreases we notice a stronger and stronger effect. The value of the largest stress drop decreases to a smaller value at small R with respect to the case without seed, and its value seems to saturate to a finite value in the limit $R \to 0^+$.

To conclude, we have shown that the EPM captures the effect of a weak region on the stress-vs-strain curve that was described in [163], both in 2D and in 3D. In particular, we have measured the shift of the yielding strain, while understanding the consequences of such regions on the scaling of the connected susceptibility remains a difficult task.

4.2 The Popović-de Geus-Wyart version of the EPM

To test the degree of generality of our results we have considered a different way of tuning the disorder in the EPM. We follow here the procedure described in [7] for the definition of the model. The rules are the following: we fix the initial stress distribution to be a Gaussian with zero mean and standard deviation $R = 0.45$. We let instead the stress threshold σ_i^{th}

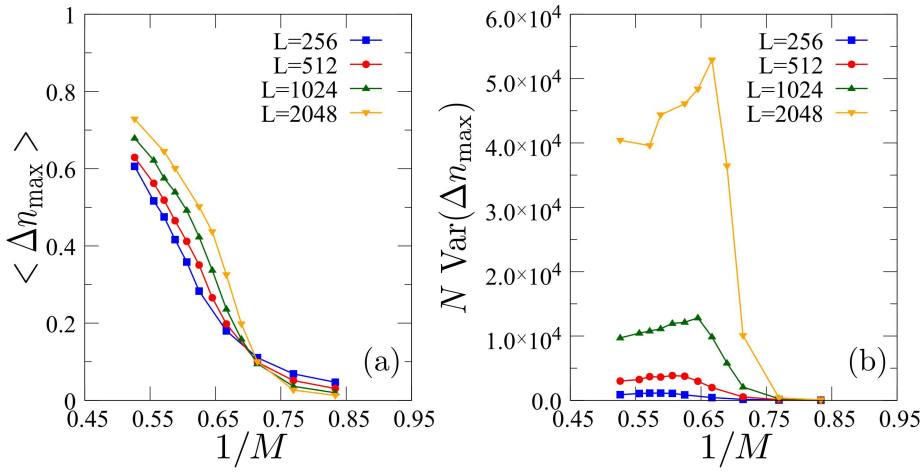

Figure 1.15: Finite-size study of the critical point for the EPM defined in [7]. (a) Average value of $\Delta n_{\max}$ and (b) associated disconnected susceptibility.

be randomly distributed: in this model, the local stress threshold at each site when $\gamma = 0$ is chosen according to a Gaussian distribution of mean M and variance 0.01. After each plastic event, σ_i^{th} is updated from a Gaussian distribution of mean 1 and variance 0.01, while the new local stress is drawn from a Gaussian distribution of mean 0 and variance 0.01. Note that in this model the system shows brittle or ductile yielding depending on the average value M of the initial σ_i^{th}, which plays now the role that R played in our version. This is what mimics the degree of stability and disorder of the amorphous solid. A large M corresponds to a stable or weakly disordered sample, whereas a small M corresponds to a less stable or highly disordered sample. We have first checked that our code reproduces the same results as that in [7], in which again the stress curves show a macroscopic jump, a continuous overshoot, or a monotonic behavior depending on M. We then proceed by studying the putative critical point. Although this model contains some ingredients that are different than those of the model we have studied before, such as the threshold distribution and its softening, the precise way to enforce force balance, etc., it essentially displays the same phenomenology. This is illustrated in Fig. 1.15 for the mean value of the order parameter $\Delta n_{\max}$ and the associated disconnected susceptibility. Contrary to the other studied model, we see here that χ_{disc} does not decrease to zero very fast as we move away from the critical point toward the brittle phase. This relates to how the disorder is inserted in the model. The limit of low disorder had some problems in our version, but it is also the case for the present variation. If M is very large, at each γ the system is going to be effectively decoupled between sites that did not yield and sites that yielded at least once. A plastic event occurring at a site that did not yield yet propagates in the system a contribution of order M, and can potentially trigger a rearrangement of sites that already yielded as well as sites that did not. On the other hand, when a site that already yielded fails again, its contribution is of order 1, and as a consequence less important for a site with threshold M. Despite this caveat, a clear peak is present in Fig. 1.15(b), which suggests that a critical value of the disorder can be defined in this case too. These numerical observations suggest that the critical point that we have identified in our version is quite robust with respect to changes in the details of the simulated elasto-plastic models.

5 Conclusion

In this chapter we have a version of elasto-plastic model in which only the minimal ingredients are included. We have shown that, depending on the initial disorder controlled by the width of the stress distribution R, the resulting stress-vs-strain curve can show different types of behavior. When the disorder is weak, a macroscopic stress drop is observed, accompanied by the localization of plastic activity in a shear band. When a stronger disorder is present, the macroscopic jump is replaced by a smooth overshoot and, eventually, by a monotonic stress curve. We have described the brittle phase by first studying qualitatively the properties of the shear band formation and of the evolution of the sites during the largest avalanche. We have then quantified the shear-band contribution to the stress drop. We have concluded this first part by showing that finite-size effects are important in the brittle regime, similarly to what is observed in the RFIM, in that they affect the value of the largest stress drop. We have highlighted that the problem lies in the absence of plastic activity in the first part of the dynamics for small enough R. This is a limitation of the EPM approach, as this regime is not observed in MD where plastic avalanches are observed in the elastic branch as well. However, we do not think that this drawback is relevant for the computation of the critical point.

We have then confirmed by a careful finite-size scaling analysis the existence of a critical point separating brittle and ductile regime in the EPM. This has been made possible by the mesoscopic nature of the model, which allowed us to simulate very large systems and to average over a large number of disorder realizations. In order to perform sample averages of the various observables we have used $1000-2000$, $400-600$, $400-600$, $200-400$, and $100-200$ samples for $L = N^{1/2} = 256, 512, 1024, 2048$, and 4096, respectively, in 2D, and $800-2000$, $800-1000$, $800-1000$, $400-1000$, $200-500$, and $100-200$ samples for $L = N^{1/3} = 48, 64, 80, 104, 128$, and 164, respectively, in 3D. These numbers are much larger than those used in molecular dynamics (MD) simulation studies. To make a comparison with previous MD results, in [137] the quantities were averaged over $800, 700, 400, 200, 200, 200, 200$, and 100 samples for $N = 1000, 2000, 4000, 8000, 16000, 32000, 64000$, and 128000, respectively, in 2D, and $800, 400, 200, 100, 100, 50$, and $25-50$ samples for $N = 1500$, 3000, 6000, 12000, 24000, 48000, and 96000, respectively, in 3D in [4]. As for comparing system size, in EPMs and in MD simulations, one can follow two distinct approaches. The first one is measuring the typical size of a shear transformation zone, which corresponds to the building block of the EPM mesoscopic description, in an MD simulation: see, for example, [152]. The second one is a quantitative calibration or mapping from MD to EPM, such that the statistical properties and the macroscopic responses in both studies match: see, for example, [156, 157]. All of this indicates that a single site in an EPM corresponds to of the order of magnitude of 100 particles (atoms) in an MD simulation. Although these studies focus on a rather ductile yielding regime, we expect that this order of magnitude does not change significantly in the brittle yielding regime. Using this conversion, 16 millions of particles in an MD simulation as in [84] (but for only very few samples) correspond to 160000 sites in EPMs. Our largest EPM in 2D ($N = L^2 = 16777216$) is thus about 100 times larger and in 3D ($N = L^3 = 4410944$) about 30 times larger than the MD counterpart in [84]. Therefore, in effect, our study accesses much larger system sizes than previous MD studies.

We have found that there are strong finite-size effects. As seen in the study of the

connected susceptibility in the brittle regime, the role of exponentially rare soft regions cannot be neglected. The effect of such weak spots (prone to yield or flip) has already been unveiled in determining the coercive field in the standard RFIM [133] and has been studied in MD simulations of amorphous solids as well [163]. While some features may be robust with respect to such finite-size effects (e.g., the process of formation of the shear band that we have discussed, the exponent of the shear-band growth, etc.) others may be affected (e.g., the scaling exponent of the connected susceptibility). How much this influences the results when R approaches the critical point is not fully understood, but it is expected that such effects are then strongly reduced when $R \geq R_c$.

In [6, 83, 84] it was argued that the observation of a critical point between brittle and ductile behavior could be a finite-size effect and that no stress overshoot associated with a continuous stress-vs-strain curve should be present in the thermodynamic limit. This conclusion was obtained in [6] by means of a linear stability analysis on an especially tailored version of the EPM. In their version, the authors divide the solid in streamlines, inside which the elasto-plastic elements evolve following a mean-field dynamics. They then proceed to decouple the system's state quantities into a homogeneous part plus a (initially) small heterogeneous perturbation. By expanding the equations of the model to first order in the amplitude of the perturbation they find that the amplitude goes as $1/\partial_\gamma \sigma(\gamma)$. They conclude that the system is unstable as soon as the stress reaches its maximum value. This argument is supported by numerical results obtained from MD simulations [84] and EPM models [83] that show how the stress-vs-strain curve becomes steeper after the maximum stress value for larger system sizes, suggesting that what is observed in [4] and in Fig. 1.1 is a finite-size effect. This argument, however, is itself questionable for two reasons: first, it is not clear that the putative instability is a long wavelength one that explains the trend of the stress-vs-strain curve to become steeper as the system size increases. Second, being limited to the consideration of the average behavior, it does not take into account the possible pinning of the propagation of the linear instability by disorder. The numerical evidence that we have provided firmly supports the persistence of a critical point when extrapolating to the thermodynamic limit. As we have discussed it is however less conclusive concerning the persistence of a smooth overshoot in the AQS protocol.

The robustness of the critical point and of the other results with respect to the specific form of the propagator has yet to be tested. In particular, recent studies showed that the quadrupole-quadrupole interaction kernel may be screened by emerging dipoles, as suggested in [166]. Whether or not the same qualitative scenario as the one just described persists or not is an important question that deserves further study.

Chapter 2

The athermally driven Eshelby Random-Field Ising model

Contents

1 Introduction 70
1.1 The Eshelby-like interactions 71
1.2 Magnetization curves 72
2 The "brittle" regime and the "shear band" formation 75
2.1 Inside the "shear band" 76
2.2 Before and after the macroscopic jump 78
2.3 Characterizing the discontinuous transition 79
3 Disorder-controlled critical point 82
3.1 Characterizing the "brittle-to-ductile" transition 82
3.2 Bounding the location of the critical point 87
4 Variations of the model 89
4.1 Effect of a seed 89
4.2 Rotated Eshelby-RFIM 92
5 Conclusion 94

1 Introduction

From the beginning of this work we have been referring frequently to the phenomenology of the athermally quasistatically driven random-field Ising model and we have underlined how it shows similarities to what one observes in the EPM and in MD simulations of sheared amorphous solids. These analogies suggest that the RFIM could be used as an effective model for yielding, which could be useful in practice. As already discussed, many techniques, both analytical and numerical, have been developed to study the random-field Ising model, which could help getting insights into the yielding transition if such an analogy between the two models holds. In particular this would overcome a fundamental limitation of the EPM, which is the absence of a Hamiltonian, due to its cellular automaton nature. The EPM is a phenomenological model, and the dynamical rules that govern its evolution are constructed ad hoc. Having a Hamiltonian description would allow for the use of field theoretical tools, including the renormalization group discussed in the Introduction.

However, apart from the apparent similarity in terms of discontinuous to continuous transition with a critical point in between, the phenomenology of the EPM and the standard ferromagnetic RFIM are quite different in finite dimensions (not so different, instead, in the mean-field limit, see Chapter 3). In particular, the shape of the largest avalanche in the low-disorder phase is rather isotropic in the standard driven RFIM with nearest neighbor ferromagnetic interactions. This is not the case for the EPM that correctly reproduces the spatial organization of plastic events in the form of shear bands as seen in sheared amorphous solids. This difference clearly comes from the different interactions that are present in the models: while in the standard RFIM they are short-ranged and ferromagnetic, in the EPM one uses the Eshelby kernel which has instead a long-ranged and anisotropic nature. Another important difference is the notion of plastic versus elastic site in the EPM which does not easily translate in the language of the RFIM. After a site yields, it goes back to the elastic state and will yield again if the strain keeps increasing. This cannot be reproduced in the RFIM, where a single spin has only two possible values, either -1 or $+1$, and essentially flips only once during the whole process. In order to devise a RFIM model which incorporates some of the specific ingredients of sheared amorphous solids we study, via computer simulations, a random-field Ising model in which the interactions between spins are mediated by the Eshelby kernel. We call this model the Eshelby-RFIM. In this chapter we show the results obtained from simulations of the model in two and three dimensions, and we discuss its phenomenology as one changes the disorder strength. We then focus on the low-disorder phase. We carry on the same careful study on the largest avalanche that we did for the EPM and we highlight the analogies and differences between the two models in this phase. We also study the properties of the first-order (discontinuous) transition. We next perform a finite-size scaling analysis around the critical point that separates the discontinuous regime from the continuous one, in the same spirit as we did in the first chapter. We show once again that the critical point is well defined and we argue that it persists at the thermodynamic limit. We extract the critical properties of the model and we compare them with those of the EPM. We conclude by showing some variants of the model and by discussing the role of rare regions.

1.1 The Eshelby-like interactions

We define the Hamiltonian of this Eshelby-RFIM as

$$\mathcal{H}(\{s_i\}) = -\frac{1}{2}\sum_{i,j} G_{ij} s_i s_j - \sum_i (h_i + H) s_i, \tag{2.1}$$

with $s_i = \pm 1$ the local spins, H the external field, and h_i the local random fields, which we choose to be drawn from a Gaussian distribution of zero mean and standard deviation R. The coupling G_{ij} is the Eshelby propagator defined in Appendix A. The effective field that governs the stability of spin i is then given by

$$h_i^{\text{eff}} = \sum_{j \neq i} G_{ij} s_j + h_i + H, \tag{2.2}$$

so that the spin is stable when $h_i^{\text{eff}} s_i > 0$. If this is not the case the spin is considered unstable and it flips as $s_i \to -s_i$. We initialize the simulation of this model with all spins pointing down and a large negative external field $H = -50$ (here and in the following we only consider the ascending branch of the magnetization curve). This ensures that each spin is stable in the -1 state as the external field dominates the sum inside the effective field for every i. The model is then driven following the AQS protocol, similarly to what we did for the EPM. At each time step t, the external field is increased by a quantity ΔH_t large enough to make the least stable spin flip, i.e., $\Delta H_t = \min_i(-h_{i,t}^{\text{eff}} | h_{i,t}^{\text{eff}} < 0)$. When the spin at site i flips, it influences the effective field at all the other sites as

$$h_{j,t}^{\text{eff}} \to h_{j,t}^{\text{eff}} + 2G_{ji}. \tag{2.3}$$

Already at this point some differences with the EPM appear. First of all, by comparing Eq. (2.3) with Eq. (1.5), we notice that in the EPM the stress contribution that a site receives after a yielding event takes place somewhere in the system is in part random, due to the random variable η inside $\delta\sigma$, and it changes at each event. This is not the case in the Eshelby-RFIM. Each spin flip affects the effective field of the rest of the system by the same quantity, given by $2|s_i| = 2$, appropriately scaled with the Eshelby propagator. Moreover, in the EPM we have implemented the Eshelby propagator in such a way that the stress redistributed by a site is removed from the site itself (i.e., $G_{ii} = -1$). In the Eshelby-RFIM we do not want the local effective field of the site to be influenced by the event. The relation between h_i^{eff} and s_i is unidirectional: the first affects the second, but not the other way around. In order to impose this relation we need to fix the value $G_{ii} = 0$. The details of the implementation of the Eshelby propagator in the RFIM are discussed in Appendix A. Following the spin flip triggered by the external field, more spins can reach the condition of instability due to Eq. (2.3), and their flipping can in turn make other sites unstable and so on. This process goes on until the stability condition $h_i^{\text{eff}} s_i > 0$ is realized for every site i. Once the system has completely relaxed the external field is increased again, so that once again the timescale of the driving is decoupled from that of the avalanches. The evolution of the local effective field for the Eshelby-RFIM can then be summarized as

$$h_{i,t+1}^{\text{eff}} = h_{i,t}^{\text{eff}} + \Delta H_t + \sum_j G_{ij}(s_{j,t+1} - s_{j,t}). \tag{2.4}$$

We then consider the time evolution of the average effective field, $h_t^{\text{eff}} = \frac{1}{N}\sum_i h_{t,i}^{\text{eff}}$, by averaging Eq. (2.4) over i:

$$h_{t+1}^{\text{eff}} = h_t^{\text{eff}} + \Delta H_t + \hat{G}_{\mathbf{q}=\mathbf{0}} \Delta m_t, \tag{2.5}$$

where $\hat{G}_{\mathbf{q}=\mathbf{0}} = \sum_i G_{ij}$, $\mathbf{q} = (q_x, q_y)$ in 2D and $\mathbf{q} = (q_x, q_y, q_z)$ in 3D denote the wave-vector, and Δm_t is the magnetization jump at step t. In this study, we set $\hat{G}_{\mathbf{q}=\mathbf{0}} = 0$.

Before discussing the results obtained with this RFIM we discuss the updating scheme used in our algorithm. When the effect of a spin flip propagates during the avalanche, it is possible that several spins become unstable at the same time. This is analogous to what we described in the EPM, where multiple blocks can simultaneously have a stress larger than the threshold during relaxation. In that case we made all the sites relax and propagate their stress together at the same time, uploading all the unstable blocks in parallel (parallel update scheme). A similar approach is also used in the simulation of the standard ferromagnetic RFIM, where the order of flipping of the spins does not change the final configuration, allowing them to be flipped all together. Unfortunately, this updating scheme cannot be used in the present model, as the system may enter an infinite loop during an avalanche. Consider for example that two spins s_i and s_j, with $G_{ij} < 0$, are the only ones unstable at the step l during an avalanche specified by the time t (or the external field H_t). In particular, we consider $h_{i,t,l}^{\text{eff}} > 0$ and $s_{i,t,l} = -1$ for site i, and $h_{j,t,l}^{\text{eff}} > 0$ and $s_{j,t,l} = -1$ for site j. When $|h_{i,t,l}^{\text{eff}}| < 2|G_{ij}|$ and $|h_{j,t,l}^{\text{eff}}| < 2|G_{ji}|$, at the next step $l+1$ we get

$$\begin{aligned} h_{i,t,l+1}^{\text{eff}} &= h_{i,t,l}^{\text{eff}} + 2G_{ij} < 0 \quad \text{and} \quad s_{i,t,l+1} = 1, \\ h_{j,t,l+1}^{\text{eff}} &= h_{j,t,l}^{\text{eff}} + 2G_{ji} < 0 \quad \text{and} \quad s_{j,t,l+1} = 1, \end{aligned} \tag{2.6}$$

which means that both spins become unstable again at $l+1$. Therefore the process will never stop, giving rise to an infinite loop. In the above example only a pair of spins were considered for simplicity, but there are many other possible combinations that lead to a similar situation in which the system is stuck in an infinite loop and cannot relax. In order to avoid this problem, we consider instead a random updating scheme: once we have the list of all the unstable sites, we choose one spin at random and flip it. If we now go back to the previous example we see that with this new updating scheme the problem is solved. At step $l+1$ of the avalanche we now get

$$\begin{aligned} h_{i,t,l+1}^{\text{eff}} &= h_{i,t,l}^{\text{eff}} > 0 \quad \text{and} \quad s_{i,t,l+1} = 1, \\ h_{j,t,l+1}^{\text{eff}} &= h_{j,t,l}^{\text{eff}} + 2G_{ji} < 0 \quad \text{and} \quad s_{j,t,l+1} = -1, \end{aligned} \tag{2.7}$$

which means that both spins are now stable. In practice, we have confirmed that the random updating scheme always converges and we have never found an infinite loop in the simulations. More details on the implementation of the Eshelby-RFIM algorithm can be found in Appendix B, where also a pseudocode for the simulation of the model is given.

1.2 Magnetization curves

In the discussion of the EPM we have introduced the quantity $n(\gamma)$, which is the maximum fraction of sites in a line (or a plane in 3D) that has yielded at least once before reaching the strain γ, with the goal of capturing the formation of the shear band. We

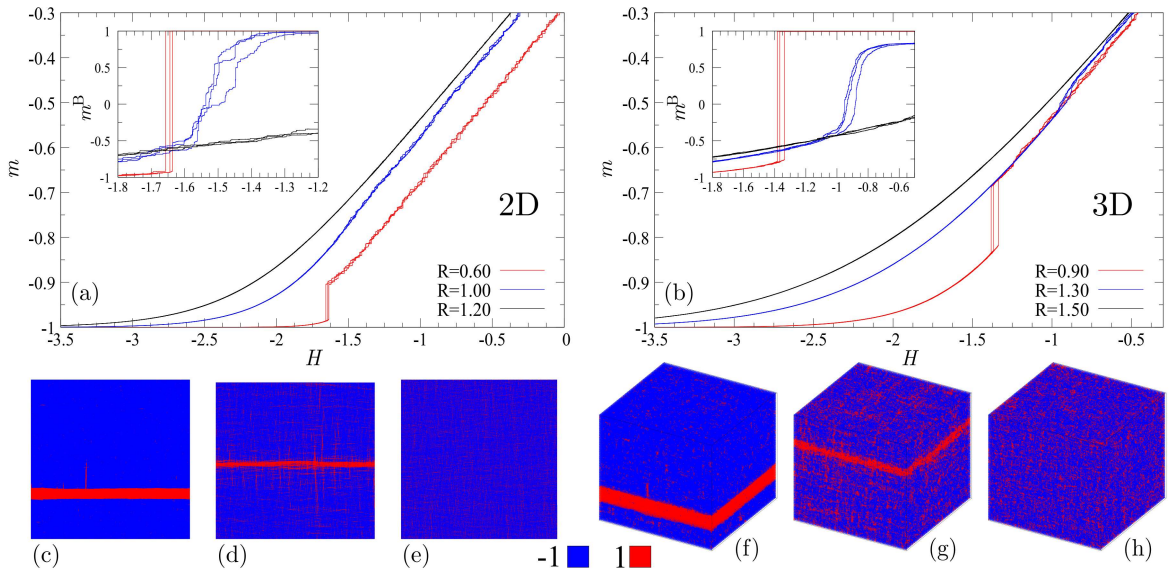

Figure 2.1: Top row: magnetization curves for the Eshelby-RFIM in 2D (a) and 3D (b), with respectively $L = 2048$ and $L = 128$, for three independent samples. Similarly to the EPM, one can see a smooth curve for large values of R, while as the disorder strength decreases a jump appears. In the inset we show the behavior of the order parameter m^B defined in the text for the same samples. Bottom row: real space configurations of the spins in the system (red for positive spins and blue for negative ones), which show how the positive magnetized spins tend to organize in a band. (c),(d), and (e) correspond to the configurations found in a 2D system for $R = 0.60, 1.00$ 1.20 respectively. Taken at $H = -1.5$ for $R = 0.60, 1.20$ and at $H = -1.3$ for $R = 0.90$. (f), (g), and (h) correspond to the configurations found in a 3D system for $R = 0.9, 1.30$ and 1.50 respectively. Taken at $H = -1.2$ for $R = 0.90, 1.50$ and $H = -0.75$ for $R = 1.30$.

proceed in a similar way for the Eshelby-RFIM. In addition to the evolution of the macroscopic magnetization $m = 1/N \sum_{x_i,y_i} s_{(x_i,y_i)}$ (in 2D), we introduce a quantity that measures "how close" the system is to form a system-spanning line (plane) in 2D (3D) of positively magnetized spins. We define the sum along rows $m^{\mathrm{x}}_{y_i}(H) = 1/L \sum_{x_i=1}^{L} s_{(x_i,y_i)}(H)$ and columns $m^{\mathrm{y}}_{x_i}(H) = 1/L \sum_{y=1}^{L} s_{(x_i,y_i)}(H)$ of the local magnetization, and choose the row or column that had the maximum number of events before reaching the field H as $m^B(H) = \max_{x_i,y_i}(m^{\mathrm{x}}_{y_i}(H), m^{\mathrm{y}}_{x_i}(H))$. By construction, $m^B(H = 0) = 0$ at the beginning of the process, while $m^B(H) = 1$ when every spin in at least one row or column has flipped to $+1$. One can generalize this quantity to 3D by checking each plane with normal vector parallel to x, y, and z and choosing the one with the larger number of positive spins. This quantity has the same role as $n(\gamma)$ in the EPM. It shows a discontinuous jump when the magnetization $m(H)$ shows a discontinuous jump, so that both capture the presence of a first-order (discontinuous) transition. However, for characterizing the critical point, $m^B(H)$ presents some advantages that will be clear in Section 3.

In Fig. 2.1(a,b) we show the magnetization curves of the Eshelby-RFIM, for different values of R. The magnetization starts at -1 when the external field is large and negative and

increases as H increases. During the initial stage of the process, the curve appears relatively smooth as the spin flips occur in a rather homogeneous and unorganized way. As H increases further, $m(H)$ enters a (transient) linear regime, characterized by $m(H) = aH + b$, until all the spins become positive at large H. In this regime, the magnetization curve is clearly serrated, which indicates that the dynamics proceeds by avalanches of various sizes. The evolution from the initial stage to the linear regime can take place in different ways depending on the disorder strength. For small values of R, the magnetization shows a jump of order 1 at a coercive field $H = H_{\rm co}$ (here and in the following, we will use the term "coercive field" to refer to the value of H at which the macroscopic jump occurs) and then keeps increasing linearly with the external field until all spins point towards the positive direction. As confirmed from the evolution of $m^B(H)$ shown in the inset of Fig. 2.1(a,b) and from the configuration snapshots in Fig. 2.1(c), the spin flips leading to the jump are collectively organized in a band, analogously to what was observed in the EPM. The resulting band of positively magnetized spins is less rough than the shear band of the EPM (see Fig. 1.1(c)). (The origin of this observation could be spurious and come from faceting effects found when the disorder strength is small for finite system sizes [135, 167, 168].) For larger disorder strength R the macroscopic jump disappears. In this case m increases from its initial value of -1 and then reaches continuously the linear regime. However, two potential patterns are still possible as illustrated by the black and the blue curves in Fig. 2.1(a,b). For a very large value of R (black curve), the magnetization m is always larger that the linear regime function $m^{\rm LR}(H) = aH + b$ (with a and b some R dependent constants in general): $m(H) \geq m^{\rm LR}(H)$, with $m(H) \to m^{\rm LR}(H)$ for sufficiently large external field. For intermediate values of R instead (blue curve), the magnetization first passes below the linear regime function. To make this difference clearer we have plotted the curves of Fig. 2.1 by now subtracting the linear regime. The outcome in Fig. 2.2(a,b) shows $\tilde{\sigma} = m(H) - aH$ as a function of the external field H. The qualitative similarity with the results obtained with the EPM is obvious, as seen by comparing for instance with Fig. 1.1. By plotting the curves in this way it becomes clear that the regime of intermediate disorder strength R corresponds in the EPM to that in which the stress-vs-strain curve displays a smooth overshoot. In the present case too, the space organization of the up-pointing spins after the "overshoot" resembles a shear band, which however does not occur in a single step as in the weak-disorder regime. The similarity between the Eshelby-RFIM and the EPM is striking when plotting the magnetization curves in this way, but we would like to be more quantitative and for this we focus on the "yielding" transition. Note that it is obvious from its definition that the RFIM cannot reach a bona fide steady state as observed in amorphous solids, as at some point the system will be completely positively magnetized and the evolution stops (see Fig. 2.2(c)). For small values of R, the linear regime of the Eshelby-RFIM corresponds to the band propagating into the rest of the system. The reason why this regime is so universal across different samples (assuming that R small enough for the band to arise in a single step) is that once the band is formed the evolution of the system is controlled only by its propagation. This is confirmed by simulations in which a band is inserted into the system from the beginning (see Section 4.1). This kind of behavior is analogous to that found in the EPM after the macroscopic stress drop, when the shear band propagates into the rest of the system. It is important to note that this portion of the dynamics of the EPM, in which the stress is nonetheless approximately constant on average, does not correspond to the true steady state, as the system retains a memory of its initial condition. The Eshelby-RFIM does not reproduce the full behavior observed in the

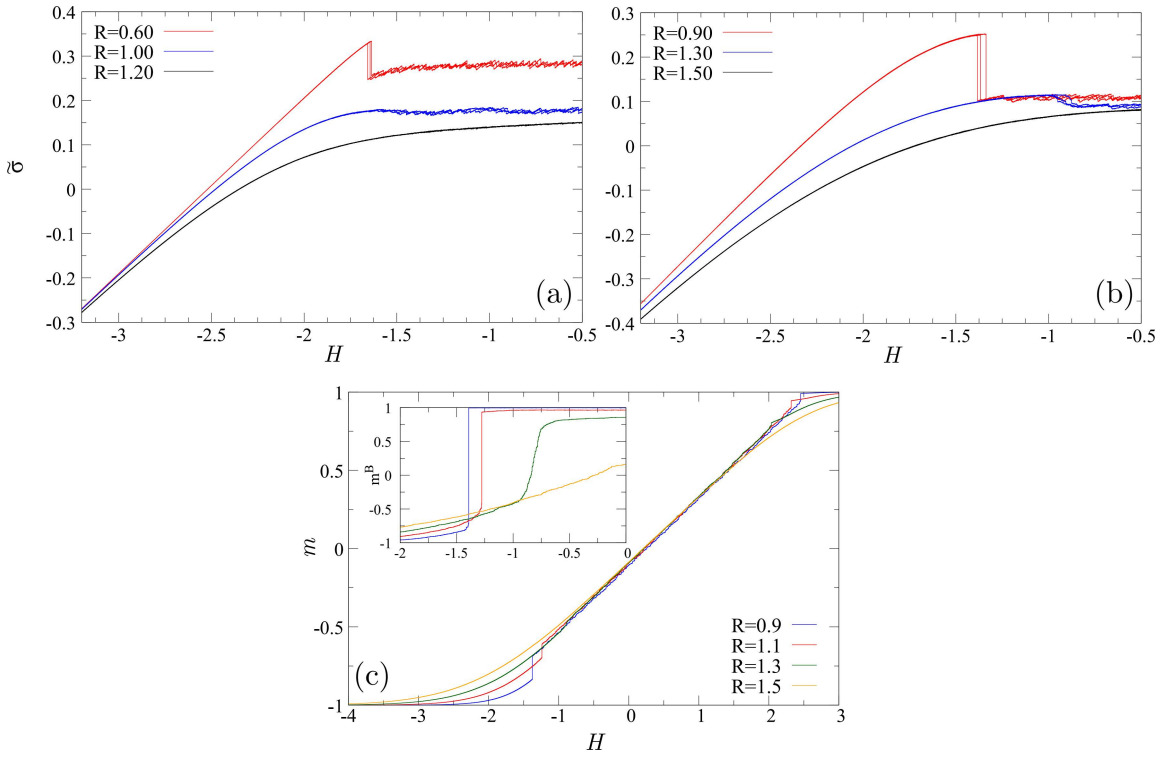

Figure 2.2: Plot of $\tilde{\sigma}(H) = m(H) - aH$ for the same 2D (a) and 3D (b) Eshelby-RFIM samples as in Fig. 2.1(a,b). The value of a is obtained by fitting the linear regime for one sample. In the plot $a = 0.39672$ in 2D and $a = 0.42372$ in 3D. In (c) the complete magnetization curve for a single disorder realization for different values of R with $L = 104$ in 3D.

sheared amorphous solids (as expected), but it qualitatively captures their behavior at and around the yielding point.

We point out that a phenomenological model based on a Hamiltonian description was proposed in [148] and was shown to be intimately related to the EPM. One can find a direct mapping between this model and an Eshelby-RFIM in which the local spins are "soft" (i.e., $s_i \in \mathbb{R}$ as opposed to $s_i = \pm 1$) and subject to a given potential $V(s_i)$. In this analogy, the local stress s_i in the Eshelby-RFIM represents the local deformation in the model from [148] and the subtraction of aH from the magnetization to obtain an analogous of the stress-vs-strain curve (as in Fig. 2.2(a,b)) arises naturally. The main difference between the two models is in the random potential V acting on the local variables, which has multiple minima in [148] but only two, at $s_i = -1$ and $s_i = 1$, in the RFIM. The model proposed in [148] could effectively work as an intermediate model between the EPM and the Eshelby-RFIM.

2 The "brittle" regime and the "shear band" formation

When the disorder strength R is small enough, the magnetization curve of the system displays a macroscopic jump (as for the EPM, we use the term "macroscopic jump" to denote a

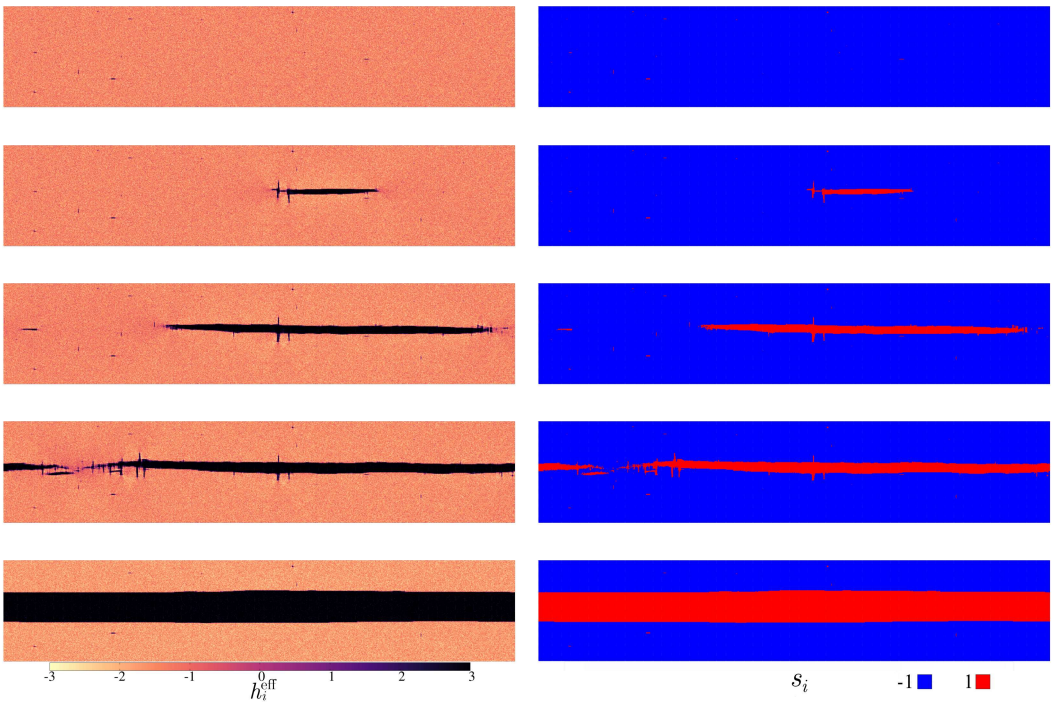

Figure 2.3: Evolution of the local effective field (left) and the local magnetization (right) during the largest event. The avalanche starts from a region in which spins are prone to flipping and picks a direction (here, horizontal) to propagate. As for the stress in Fig. 1.2, one can see that the local effective field is on average larger at the end points of the active region. Avalanche times are $l/l_{max} = 0, 0.03, 0.16, 0.28$ and 1. The plot is from $y_B - 100$ to $y_B + 100$ with y_B the location of the shear band. Obtained in 2D with $L = 1024$ and $R = 0.40$.

collective flip of a macroscopic fraction of the spins which result in a jump of order 1 in the magnetization per spin m) similar to the stress drop of brittle materials. This is also observed in the standard RFIM with short-range and ferromagnetic interactions, but the macroscopic avalanche is then rather isotropic. As shown in Fig. 2.1(c) the Eshelby-RFIM instead reproduces the band-like shape of the avalanche observed in the EPM, which justifies the introduction of Eshelby-like couplings between the spins to capture the anisotropic nature of yielding in sheared amorphous solids.

2.1 Inside the "shear band"

To start, we show in Fig. 2.3 how the local effective field and the local magnetization evolve to give rise to the positively magnetized band. The figure is obtained by taking snapshots during the largest avalanche formation, at fixed $H = H_{\text{co}}$, for $L = 1024$ and $R = 0.40$ in 2D. At the beginning, when $l = 0$ (top panels), there is no clear hint on how the band will nucleate and appear, and the few spins that are already up are scattered all over the sample. The band starts forming around one of the positive islands and chooses a preferred direction based on the effective field of the neighboring sites. The band embryo then propagates from its endpoints, growing first in length. After the band has spanned the whole system, it grows

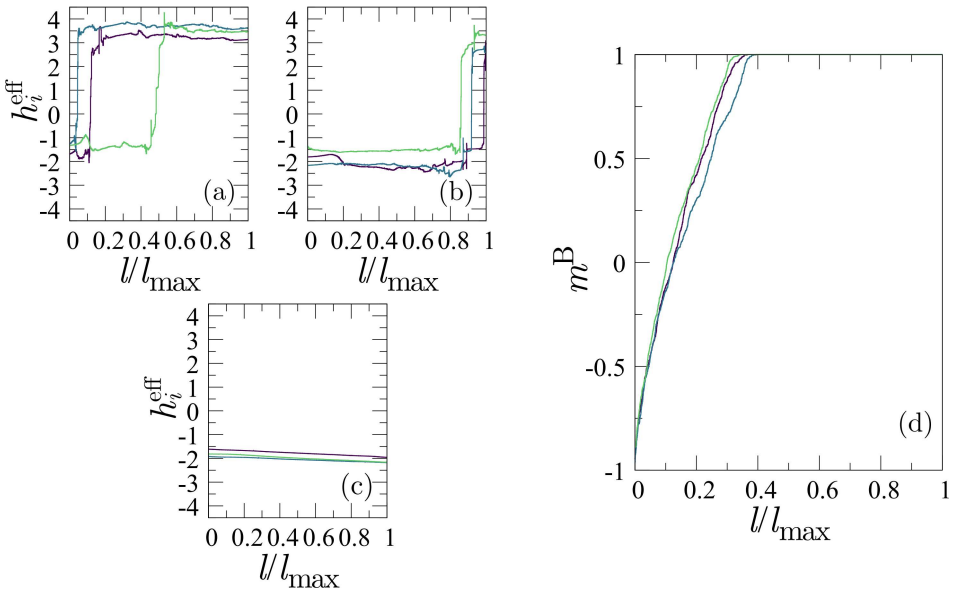

Figure 2.4: Evolution of the local effective field inside (a), on the boundary (b), and outside (c) the band during its formation. In (d) the evolution of the maximum magnetization in a line m^B is shown. We see that the main contribution to m^B comes from the first steps of the avalanche and saturates before the band spans the whole system. The plot is obtained in 2D with $L = 1024$ and $R = 0.40$, with different colors corresponding to 3 different samples.

in width and the avalanche eventually dies out, as shown in the bottom panels of the figure. As before, the growth takes place mostly at the edges of the band due to the geometry of the interactions. This qualitative behavior is almost identical to what is observed in the EPM (see Fig. 1.2 and [83]) and in MD simulations [163].

We now investigate what happens to sites inside and outside the band as the avalanche progresses. In Fig. 2.4(a,b,c) we show the evolution of the effective field of sites inside (a), on the border (b) and outside (c) the band. The local effective field h_i^{eff} starts from a negative value (we are considering spins that were negative before the jump) and, in (a) and (b) ends up in a positive value, meaning that the associated spins flipped. Spins inside the band usually flip in the first half of the evolution process, while those on the boundary tend to flip at the end, when the band thickens. The spins in the bulk of the material have their effective field that decreases steadily as the band is formed. When comparing Fig. 2.4 and Fig. 1.3 one has to be careful and remember that different update algorithms are used for the dynamics during an avalanche in the two models, and that the avalanche time l has different meanings. In the EPM, due to the parallel update scheme, the number of yielding events increases in bursts with the step l, which explains why the system-averaged stress decreases more for some values of l than for others. Here instead, to each value of l there is an associated spin flip, so that the magnetization increases essentially linearly with the value of l. With this in mind, and by looking at Fig. 2.4(d), we notice that once again the main contribution to the magnetization is not given by the first part of the dynamics in which the band extends along its length, but instead by the second part in which it thickens, just as in the EPM.

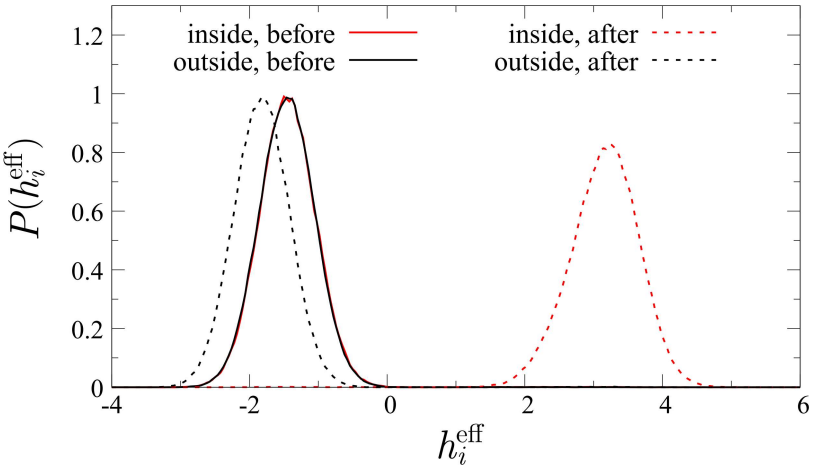

Figure 2.5: Distribution of the local effective field for sites that are inside (red) and outside (black) the band, before (full) and after (dashed) the macroscopic jump. Obtained in 2D with $L = 512$, $R = 0.40$ and averaged over 200 samples.

2.2 Before and after the macroscopic jump

We have found that the Eshelby-RFIM displays indeed a macroscopic jump for small values of the disorder strength. Moreover, the macroscopic avalanche associated to this jump has qualitatively the same band appearance than that encountered in the EPM. We continue by exploring the analogy with the brittle regime, following the same lines as in the previous chapter. In the EPM we have studied how the stress distribution inside and outside the shear band changes from just before to just after the discontinuous transition (see Fig. 1.4). In the Eshelby-RFIM it does not make sense to study the distribution of the spin values, since they are fixed to be ± 1 and their sign before and after the avalanche is trivial. However, we can perform a similar analysis by looking at the distribution of the local effective field that characterizes the sign of the spins. In order to do this we save the configuration of local effective fields along the line (in 2D) with the largest value of m^B to capture sites inside the band as well as along a parallel line at a distance $L/2$ to get sites in the bulk. We then compute the probability of having a certain value of h_i^{eff} by repeating the procedure for independent samples. The results for the probability $P(h_i^{\text{eff}})$ are shown in Fig. 2.5. As in the previous chapter, there is virtually no difference in the distribution of local effective fields at sites that are inside or outside the band before its appearance. In this case $P(h_i^{\text{eff}})$ is very similar to the Gaussian we started with and lies in the negative part of the x-axis, which is expected since the majority of spins are still pointing in the negative direction. After the jump the distribution changes drastically between sites inside or outside. For the former case, $P(h_i^{\text{eff}})$ is now larger than 0 in the positive half of the h_i^{eff} axis, since the spins have all flipped to $+1$. The distribution is slightly wider than the initial one, but its form is almost unchanged with respect to the starting Gaussian. This is quite different from the EPM case, in which the distribution of sites inside the band was completely transformed by the jump and ended up being essentially the same as the steady-state distribution. Since in the Eshelby-RFIM there is no true steady state we cannot compare $P(h_i^{\text{eff}})$ for sites in

the band after the jump with a steady-state distribution. For the spins in the bulk of the material $P(h_i^{\text{eff}})$ is just slightly shifted to the negative side due to the formation of the band, similarly to the EPM case.

In Section 2 of the previous chapter we have proposed an argument to predict the scaling of the contributions to the stress drop. We found that the blocks that give the dominant contribution to the $O(1)$ stress jump are those in the bulk of the material, as opposed to the ones inside the shear band that were in subextensive number. This was associated to the property that sites in the shear band may yield many times and that the bulk can also respond elastically. This is different in the RFIM: since the jump that we observe is in the magnetization, only the spins that flip to a positive value, i.e., essentially those inside the band, give a contribution. In a given sample the largest magnetization jump defined as $\Delta m_{\max} = \max_H(m(H+\delta H) - m(H))$ is then given by $\Delta m_{\max} \approx 2N_B/N$, with N_B the number of sites inside the band. The relation is only approximate because there may for instance be spins that were pointing in the positive direction before the jump and are flipped to -1 by the band formation. Their contribution is however very small and is neglected in the following. We can then write the average over samples of the largest magnetization jump as $\langle \Delta m_{\max} \rangle \approx \langle w_B \rangle / L = L^{\beta-1}$, where we have defined the band width $w_B = N_B/L^{d-1}$ and used the same hypothesis as in the previous chapter, $\langle w_B \rangle \sim L^\beta$ with $\beta \leq 1$. In order for $\langle \Delta m_{\max} \rangle$ to remain finite in the thermodynamic limit we clearly need $\beta = 1$ in this case. (Note that in this chapter, as in the previous one, we use brackets $\langle \cdot \rangle$ to denote an average over samples, contrary to the Introduction and Chapter 3 where one has to be more specific and use an overline $\overline{(\cdot)}$ to distinguish it from other types of averages.)

We conclude the study of the band formation process by looking at the band profile, as we did in the EPM case, and comparing the outcome with the prediction $\beta = 1$. In order to do so we define the quantity $\rho_{\text{band}}(L, y)$ which measures the magnetization along the direction perpendicular to the shear band at position y:

$$\rho_{\text{band}}(L, y) = \frac{1}{L} \Big\langle \sum_x s_{x, y - y_{\text{B}}} \Big\rangle, \tag{2.8}$$

where we have centered each line around the value y_B where the band takes place. Notice that, differently from the previous chapter, the amplitude of this quantity is limited by 2, since it is the maximum value of the variation of the magnetization along a line. In the EPM there is instead a number of plastic events that grows with the system size, thereby increasing the plastic strain: Then, one may have $\rho_{\text{pl}}(L, y)$ such that $\rho_{\text{pl}}(L, y) \sim \tilde{\rho}_{\text{pl}}(y/L^\beta) L^{\beta-1}$, with $\beta < 1$. In the Eshelby-RFIM we have instead $\rho_{\text{band}}(L, y) \sim \tilde{\rho}_{\text{band}}(y/L)$, equivalent to $\beta = 1$. The results are shown in Fig. 2.6 for both the 2D and 3D Eshelby-RFIM. The curves show a very good collapse in 3D, not as good in the 2D case. As we will see below, this is because the largest magnetization jump in this case seems to slightly decrease with the system size.

2.3 Characterizing the discontinuous transition

We have found evidence that the Eshelby-RFIM displays a first-order (discontinuous) transition for some value $H = H_{\text{co}}$, analogously to the EPM and to the standard RFIM. In the Introduction we discussed how, in athermally driven systems in which the disorder enters in the form of random fields, the disconnected susceptibility diverges with system size more strongly than the connected one. Under some generic assumption concerning the Gaussian

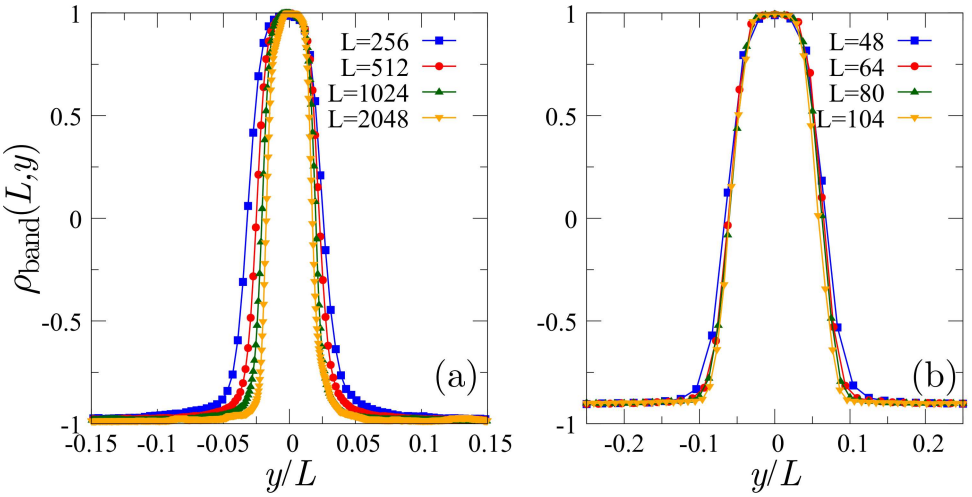

Figure 2.6: Distribution of magnetization along the direction perpendicular to the band as a function of the distance from the center of it, for 2D (a) and 3D (b) systems, with $R = 0.60$ and $R = 0.90$ respectively.

distribution of the sample-dependent coercive field, the former scales as the square of the latter. We have therefore studied the behavior of

$$\begin{aligned} \chi_{\text{conn}} &= \frac{\partial \langle m^{B,\alpha}(H) \rangle}{\partial H}, \\ \chi_{\text{disc}} &= N(\langle m^{B,\alpha}(H)^2 \rangle - \langle m^{B,\alpha}(H) \rangle^2), \end{aligned} \tag{2.9}$$

as a function of the external field H, when the disorder strength R is small enough to have a macroscopic jump in the magnetization. One can also consider the equivalent quantities for the magnetization $m^{\alpha}(H)$, but the choice of m^B more directly captures the anisotropic nature of the phenomenon and leads to crisper results (see Section 3). The jump in m^B is observed in every sample for small values of R but is smeared out as one takes the average over many samples, due to the fact that the value of H at which the jump occurs, H_{co}, changes from one disorder realization to the other. In the thermodynamic limit, if the transition is indeed discontinuous, one should recover a sharp jump. Due to the presence of the jump, the evolution of the order parameter m^B can be again schematized as $m^{B,\alpha}(H) = -1 + 2\theta(H - H^{\alpha}_{\text{co}})$ with $\theta(x)$ the Heaviside function. Averaging over disorder, we then find

$$m^B(H) = \langle m^{B,\alpha}(H) \rangle = -1 + 2 \int_{-\infty}^{H} \rho_{\text{co}}(H')dH', \tag{2.10}$$

with $\rho_{\text{co}}(H)$ the distribution of coercive fields for different realizations of the disorder. To compute the connected susceptibility it is sufficient to perform a derivative with respect to H of the formula above, which gives the relation $\chi_{\text{conn}}(H) = 2\rho_{\text{co}}(H)$ for small enough R. We have checked this relation numerically by computing both quantities for different values of R and for different system sizes. Results are shown in Fig. 2.7. In panels (a) and (b) we display the evolution of the connected susceptibility with the external field H for 2D and 3D respectively, which has a peak centered around the average coercive field H_{co}. For the smaller value of R the relation $\chi_{\text{conn}}(H) = 2\rho_{\text{co}}(H)$ is followed almost perfectly both in 2D

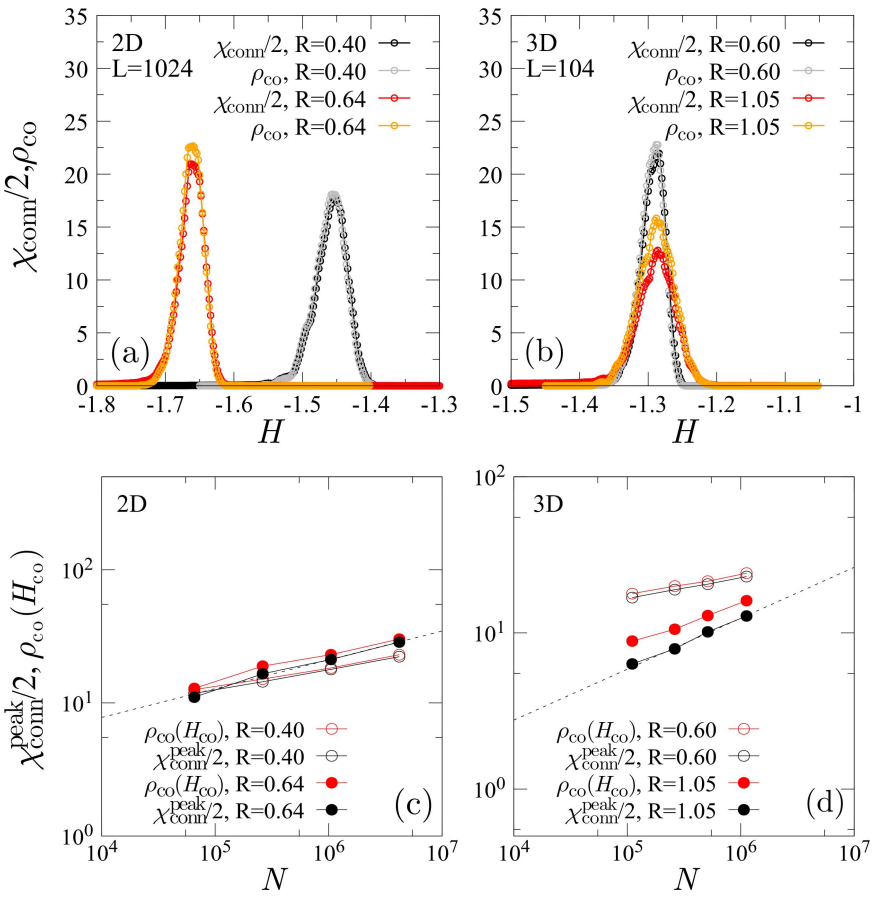

Figure 2.7: Connected susceptibility (divided by 2) as a function of the external field H and distribution of the coercive field H_{co}. Plotted for $L = 1024$ in 2D (a) and $L = 104$ in 3D (b) for two different values of R in the brittle regime. When R is small the connected susceptibility coincides with ρ_{co} almost perfectly, while as R gets larger the analogy deteriorates a bit. Scaling of the susceptibility peak $\chi^{peak}_{conn} = \chi_{conn}(H_{co})$ and $\rho_{co}(H_{co})$ peaks in 2D(c) and 3D(d) for the same two values of R. The black dashed lines are fits performed using the last 3 points and give $\chi^{peak}_{conn} \sim N^{0.21}$ in 2D and $\chi^{peak}_{conn} \sim N^{0.32}$ in 3D. The curves are obtained after averaging over $8000, 6000, 5000, 2000$ samples respectively the sizes $L = 256, 512, 1024, 2048$ in 2D and $8000, 6000, 5000, 3000$ samples respectively the sizes $L = 48, 64, 80, 104$ in 3D.

and in 3D. It is not as good for the larger value of R, which is closer to the critical point, which will be discussed in the next section. With the argument based on the central limit theorem that lead to Eq. (1.16) one would again expect the susceptibility peak to grow as $N^{0.5}$ and fulfill the predicted relation $\chi_{disc} \sim \chi^2_{conn}$. In panels (c) and (d) we plot the scaling of the connected susceptibility peak as a function of the system size N both in 2D and in 3D, for the two values of R. We also show the variation of the peak of the distribution of the coercive field. From the plot we see here too that the scaling exponent is different from 0.5, being closer to 0.3 or 0.2. At odd with the analogous plot in the EPM (see Fig. 1.7), the scaling seems less affected by the value of R, but the data obtained with smaller values of R is still following a power law with a smaller exponent. As in the EPM, we cannot say if

this exponent really represents the system in the thermodynamic limit or if it is affected by strong finite-size effects. We expect that, also in the present case, the absence of statistically rare regions in which the random field is unusually large for some spins plays an important role. We discuss this idea in more detail in Section 4.1. Finally, we have measured the system-size dependence of the disconnected susceptibility at $H_{\rm co}$ and found that it scales as $N = L^d$ as in the EPM. Once again, this quantity seems to be immune to strong finite-size effects.

3 Disorder-controlled critical point

We now focus on the characterization of the critical point that separates a regime in which a macroscopic jump in the magnetization takes place and one in which the magnetization increases smoothly (for large enough samples in which the effects of subextensive avalanches are smeared out). In the previous section we showed that the Eshelby-RFIM is quite good at reproducing some basic qualitative aspects of the dynamics of amorphous solids under shear. Beyond the qualitative agreement found so far between the Eshelby-RFIM and the EPM, we want to directly check if the former is a proper effective theory of the yielding transition in the vicinity of the critical point. In particular, one should investigate whether or not the critical behavior is compatible with the universality class of the yielding transition, as studied in the previous chapter. We do so by means of the finite-size scaling analysis of the disconnected susceptibility defined with the appropriate order parameter.

3.1 Characterizing the "brittle-to-ductile" transition

In order to characterize the properties of the critical point in this model it is necessary to define an appropriate order parameter that distinguishes between the "ductile" regime with a smooth magnetization curve (in the thermodynamic limit) and the "brittle" regime with a jump of order 1 in the magnetization. As for the standard RFIM, we start with the quantity $\Delta m_{\rm max} = \max_H(m(H+\delta H) - m(H))$, which represents the largest jump in the magnetization curve in a given sample. The idea is the same as for the short-range case, where we found that for small values of the disorder strength R the average $\Delta m_{\rm max}$ is finite, while as R increases it tends to zero. The results are plotted in Fig. 2.8. On the top two panels we show how the average over disorder realizations of the order parameter $\Delta m_{\rm max}$ decreases with the increase of R. In 3D (panel (b)) the results display a clear line-crossing around a common point, which gives a good estimate of the location of the critical point. In 2D (panel (a)) instead, the average maximum magnetization jump seems to decrease with the system size for almost every value of R, except for a region of values in which it seems more or less constant, in agreement with the results on the band profile described above. In the bottom panels we see the associated disconnected susceptibility. As anticipated $\chi_{\rm disc}$ is very small for large values of R, and it increases reaching a peak as R approaches the critical point. We notice that the peak value increases as we increase the system size, as we would expect for a system at the critical point. However, as in the case of the EPM, $\chi_{\rm disc}$ increases again at lower values of R. This may seem surprising at a first glance, as our explanation for this behavior in the EPM was based on the presence of a steady state. However, no true steady state exists for the Eshelby-RFIM. Consider nonetheless the limit $R \to 0^+$, so that the system does not undergo any spin flip before the macroscopic avalanche at the coercive

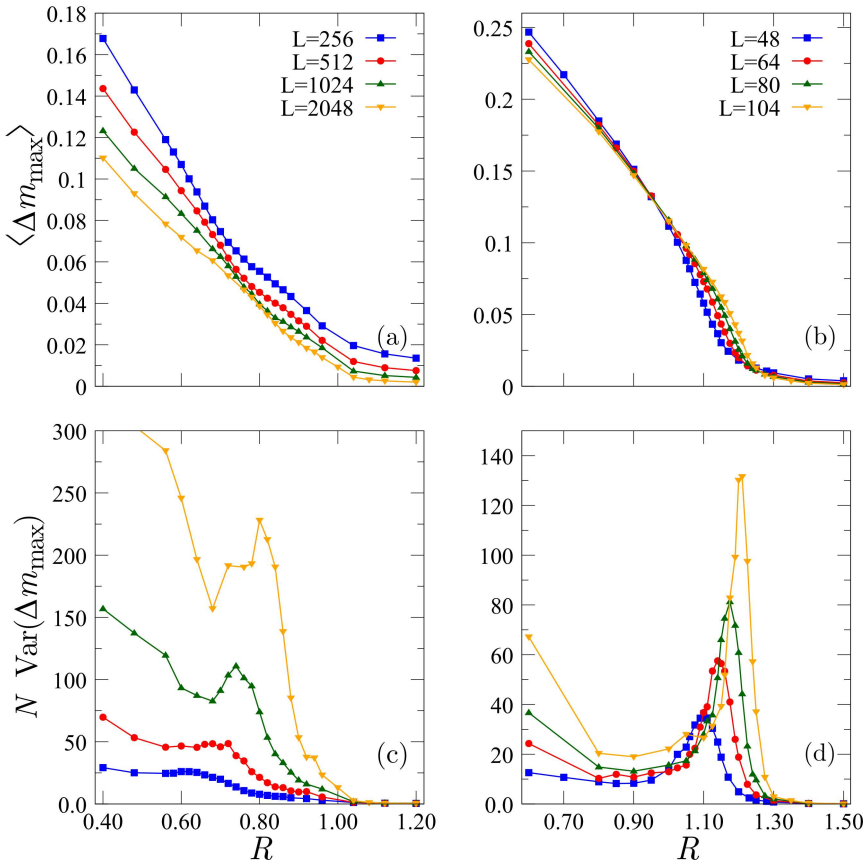

Figure 2.8: Evidence for a critical point in the 2D and 3D Eshelby-RFIM. Upper: Disorder-averaged value of the order parameter $\langle \Delta m_{\max} \rangle$ as a function of R for several system sizes in 2D (a) and 3D (b). Lower: Variance of $\Delta m_{\max}$ multiplied by $N = L^d$, i.e., disconnected susceptibility, in 2D (c) and 3D (d). The susceptibility increases when R goes to 0, which in 2D obscures the peak associated with the critical point.

field. At $H^{\alpha}_{\rm co}$, a single site i^* with the largest random field initiates the macroscopic jump. We thus define the maximum random field by $h^{\alpha}_{\max} = h_{i^*} = \max_i\{h^{\alpha}_i\}$. To find how this value is related to the coercive field we should remember that the condition for spin i^* to flip is that its effective field changes sign. As in the initial condition all the spins are pointing down, the effective field at the site i^* with the maximum local random field is given by

$$h^{\rm eff}_{i^*} = -\sum_{j\neq i^*} G_{i^*j} + h_{i^*} + H. \tag{2.11}$$

Since the model is defined with $\hat{G}_{\mathbf{q}=0} = 0$ and $G_{ii} = 0$, we then get the condition $H^{\alpha}_{\rm co} = -h^{\alpha}_{\max}$. As we have seen in the preceding section, the magnetization in this regime increases first, then undergoes a macroscopic jump, and finally follows a linear growth with H until all spins are positive. In the low-disorder regime we schematically describe the evolution of the magnetization (as we did for m^B) as

$$m^{\alpha}(H) = -1 + \theta(H - H^{\alpha}_{\rm co})(aH + b). \tag{2.12}$$

From this expression it follows that

$$\Delta m_{\max} = m(H \to H_{\rm co}^{\alpha,+}) + 1 = aH_{\rm co}^{\alpha} + b + 1. \tag{2.13}$$

Once again, the distribution of the maximum local random field affects the results of the largest magnetization jump as

$$\langle \Delta m_{\max}^2 \rangle - \langle \Delta m_{\max} \rangle^2 = a^2(\langle h_{\max}^2 \rangle - \langle h_{\max} \rangle^2), \tag{2.14}$$

where $h_{\max}$ is distributed according to a Gumbel distribution. It follows that, in the limit $R \to 0^+$, the variance of $\Delta m_{\max}$ should be proportional to $R^2/\log(N)$. This explains the curves in Fig. 2.8(c,d). It follows that the same spurious behavior at small disorder which was present in the EPM is also affecting the Eshelby-RFIM. From the figures we see in particular that this effect is much stronger in 2D than in 3D, where some spin flips occur before the jump even for small values of R.

We therefore turn to the other order parameter that we proposed, m^B. As for the EPM, using an order parameter that saturates to 1 when the system displays the instantaneous nucleation of a full band eliminates the spurious effect and enables us to better access the critical exponents of the system. The quantity $m^B(H)$ works as well as the magnetization $m(H)$ to signal the change from discontinuous to continuous regimes. In analogy to what was done for $m(H)$ we measure the largest jump of m^B in a given sample, defined as $\Delta m^B_{\max} = \max_H(m^B(H + \delta H) - m^B(H))$. We then study and plot the same quantities as in Fig. 2.8. The results are shown in Fig. 2.9. In the top panels we observe the expected behavior, with the average value of the order parameter that passes from a finite value very close to 2 for small values of R to almost 0 as R increases. The larger the system, the sharper the transition. In the bottom panels we see that the disconnected susceptibility peaks at the critical point, and that the peak becomes higher and sharper as the system size increases, as expected for a critical point. The phenomenology is the same as that observed with $\Delta m_{\max}$, but with this new order parameter the disconnected susceptibility no longer increases again when $R \to 0^+$. This is a consequence of the fact that m^B saturates to 2 for every sample for a sufficient small value of R, which corresponds to an instantaneous nucleation of a spanning band or plane of positive spins.

We now proceed to a finite-size scaling analysis. We consider the scaling ansatz of the standard RFIM, with $\chi_{\rm disc}(r, L) \sim L^{\bar{\gamma}/\nu}\Psi(rL^{1/\nu})$, where $r = (R - R_{\rm c})/R$ is the relative distance to the critical point $R_{\rm c}(L)$, $\bar{\gamma}$ and ν are the critical exponents, $\Psi(\cdot)$ is the scaling function. We start by analyzing how the peak and the full width at half maximum (FWHM) of the disconnected susceptibility scale with the system size. From the scaling ansatz above we expect that the maximum diverges as $L^{\bar{\gamma}/\nu}$, while the width of the peak decreases as $L^{-1/\nu}$. The results of this first analysis are shown in the top panels of Fig. 2.10 and give a first estimate of the critical exponents. We find $\bar{\gamma}/\nu \approx 2.06 \pm 0.001$ and $\nu \approx 2.73 \pm 0.08$ in 2D, while $\bar{\gamma}/\nu \approx 2.90 \pm 0.09$ and $\nu \approx 1.36 \pm 0.04$ in 3D, with the error bars coming from the fit. With respect to the EPM case, the fit appears more precise here, which leads to smaller error bars, but note that the range of linear system sizes is somewhat smaller. We then try to collapse the disconnected susceptibility curves onto a single master curve by adjusting the critical exponents by hand. We choose the values of $\bar{\gamma}/\nu$ and ν that give the best visual collapse of the curves, and we obtain $\bar{\gamma}/\nu \approx 2.05$ and $\nu = 2.8$ in 2D, while $\bar{\gamma}/\nu \approx 2.81$ and $\nu = 2.5$ in 3D.

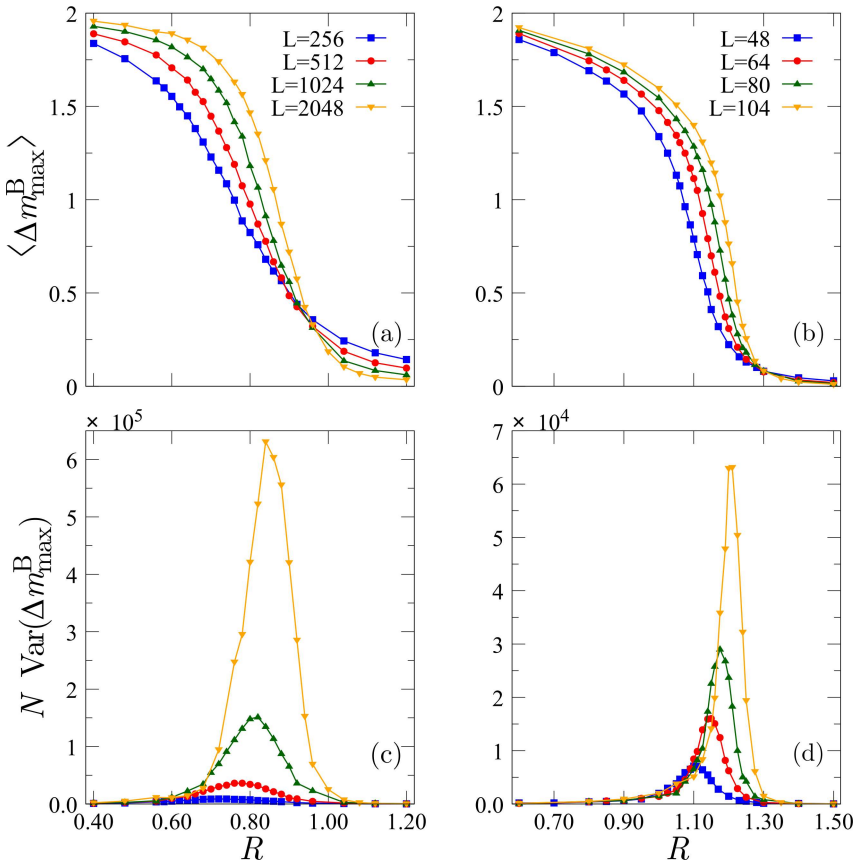

Figure 2.9: Evidence for a critical point in 2D and 3D Eshelby-RFIMs. Upper: Average value of the order parameter $\langle \Delta m^B_{\mathrm{max}} \rangle$ as a function of R for several system sizes in 2D (a) and 3D (b). Lower: Variance of $\Delta m^B_{\mathrm{max}}$ multiplied by $N = L^d$, i.e. disconnected susceptibility, in 2D (c) and 3D (d).

During this procedure, we have tested several values of the exponents and we have observed that the collapse is highly sensitive to the value of $\bar{\gamma}/\nu$, while the choice of ν has little effect on the results for a rather large range of values. This is also reflected in the comparison with the values of the exponents found with the fit of the maximum and the FWHM, which are in good agreement for the prediction of $\bar{\gamma}/\nu$, while a worse agreement is observed for ν. We conclude the finite-size scaling analysis of the model by fitting the disconnected susceptibility with a precise analytical form for the scaling function. As for the EPM, we define

$$\Psi(x) = C \exp\left[y(x) - \exp(y(x))\right] \sum_{i=0}^{i=3} a_i H_i(y(x)) \sim L^{-\bar{\gamma}/\nu} \chi_{\mathrm{disc}}(xL^{1/\nu}, L), \tag{2.15}$$

where $y(x) = (x - x_c)/\alpha$, $H_i(x)$ is the i-th Hermite polynomial, and C, x_c, α and a_i are adjustable parameters. The advantage of this method is that it provides not only an estimate of the critical exponents, but also the form of the scaling function. We fit χ_{disc} for the two largest system sizes both in 2D and 3D with this function and we obtain the results displayed

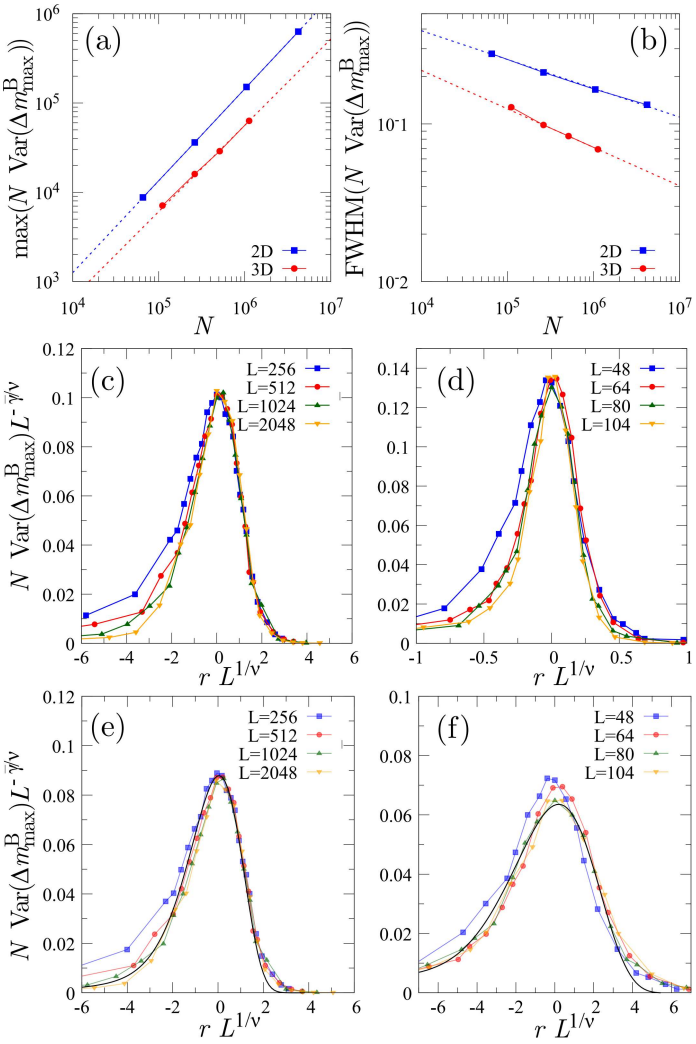

Figure 2.10: Results from the finite-size scaling analysis of the Eshelby-RFIM close to the critical point. Scaling of the peak (a) and of the full width at half maximum (b) of the disconnected susceptibility with N. The fits in (a) give $\bar{\gamma}/\nu \approx 2.06 \pm 0.001$ in 2D $\bar{\gamma}/\nu \approx 2.90 \pm 0.09$ in 3D, while from the ones in (b) $\nu \approx 2.73 \pm 0.08$ in 2D and $\nu \approx 1.36 \pm 0.04$ in 3D. In all cases the errorbars come from the fit. (c,d) collapse by hand of the disconnected susceptibility data for the 2D and the 3D case respectively. In this case $\bar{\gamma}/\nu \approx 2.05$ and $\nu = 2.8$ in 2D, while $\bar{\gamma}/\nu \approx 2.81$ and $\nu = 2.5$ in 3D. (e,f) fit with a master curve, which gives $\bar{\gamma}/\nu \approx 2.07$ and $\nu = 2.68$ in 2D, and $\bar{\gamma}/\nu \approx 2.97$ and $\nu = 1.03$ in 3D.

in Fig. 2.10(e,f). We see that the scaling function based on the product between a Gumbel distribution and a polynomial reproduces reasonably well the shape of the disconnected susceptibility (with deviations for the smallest system sizes). The critical exponents obtained in this way are $\bar{\gamma}/\nu \approx 2.07$ and $\nu = 2.68$ in 2D, and $\bar{\gamma}/\nu \approx 2.97$ and $\nu = 1.03$ in 3D, which are compatible, even though slightly different, with the ones obtained with the other methods.

As our goal was to investigate whether the critical behavior of the EPM and the Eshelby-

RFIM are in the same universality class, we need to compare the estimate for the critical exponents. As already stressed, the breadth of values obtained for the correlation exponent ν is very large compared to that of $\bar{\gamma}/\nu$. Considering the three methods that we have used, we find in 2D

$$\begin{cases} \bar{\gamma}/\nu = 1.82\text{–}1.88 \\ \nu = 1.92\text{–}3.03 \end{cases} \text{for the EPM,} \qquad \begin{cases} \bar{\gamma}/\nu = 2.05\text{–}2.07 \\ \nu = 2.65\text{–}2.81 \end{cases} \text{for the Eshelby-RFIM} \tag{2.16}$$

and in 3D

$$\begin{cases} \bar{\gamma}/\nu = 2.59\text{–}2.7 \\ \nu = 1.7\text{–}2.52 \end{cases} \text{for the EPM,} \qquad \begin{cases} \bar{\gamma}/\nu = 2.8\text{–}2.99 \\ \nu = 1.03\text{–}2.5 \end{cases} \text{for the Eshelby-RFIM.} \tag{2.17}$$

Taken at face value, these results seem to indicate that the two systems are not in the same universality class, the critical exponents of the EPM being systematically smaller than those of the RFIM. However, the difference found for $\bar{\gamma}/\nu$ is not very large, of the order of 10 %, and may not be sufficient to reach a definite conclusion, considering the difficulty to reliably extract exponent values. (As mentioned before, this is already true for scaling analyses of simpler random-field models [131].) Even larger system sizes with then more sophisticated scaling analyses would be necessary to settle the issue. [1]

3.2 Bounding the location of the critical point

From the plots in Fig. 2.9 we observe that the peak of the disconnected susceptibility slowly shifts as the system size increases. From the considerations in Chapter 1 we are now familiar with this situation and we know how to face this issue. This case is a priori more complicate, as a definition of the overshoot is not as obvious as in the EPM. However, we have proposed in Section 1 a way to plot the magnetization curves that makes the analogy with the EPM clearer. We then transform the magnetization curves from $m(H)$ to $\tilde{\sigma}(H)$ and we study their average in 2D and 3D. Some of the results are plotted in Fig. 2.11(a) for a 2D system with $L = 2048$. From these plots we can as before identify the value of the disorder strength R at which an overshoot first appears, i.e. $R_o(N)$. By construction, the value of $R_o(N)$ is always larger than the critical-point disorder $R_c(N)$, so that it bounds the critical point. We thus study the size dependence of R_o. In Fig. 2.11(b,c) we plot R_o and R_c as a function of $N = L^d$ in 2D and 3D respectively. We notice that in both cases, R_o saturates to what appears to be a constant value as N increases, suggesting that $R_o^\infty = \lim_{N\to\infty} R_o(N)$ has a finite value. Whether the observed behavior changes after some very large threshold value N^* is of course possible but as for the EPM we see no reason why this should occur. The fact that R_o converges to a constant value for large N provides an upper bound on the value of the critical disorder, with $R_c^\infty = \lim_{N\to\infty} R_c(N) < R_o^\infty$ and ensures that this is finite. We

[1] It is worth noting that the trend of the exponents with dimension d are as expected. Fluctuations are larger in 2D than in 3D so that ν is larger in 2D. On the other hand, $\bar{\gamma}/\nu$ is equal to $4 - \bar{\eta}$, with $\bar{\eta}$ an anomalous dimension (see Introduction) that increases as d decreases: $\bar{\gamma}/\nu$ is thus expected to be less in 2D than in 3D.

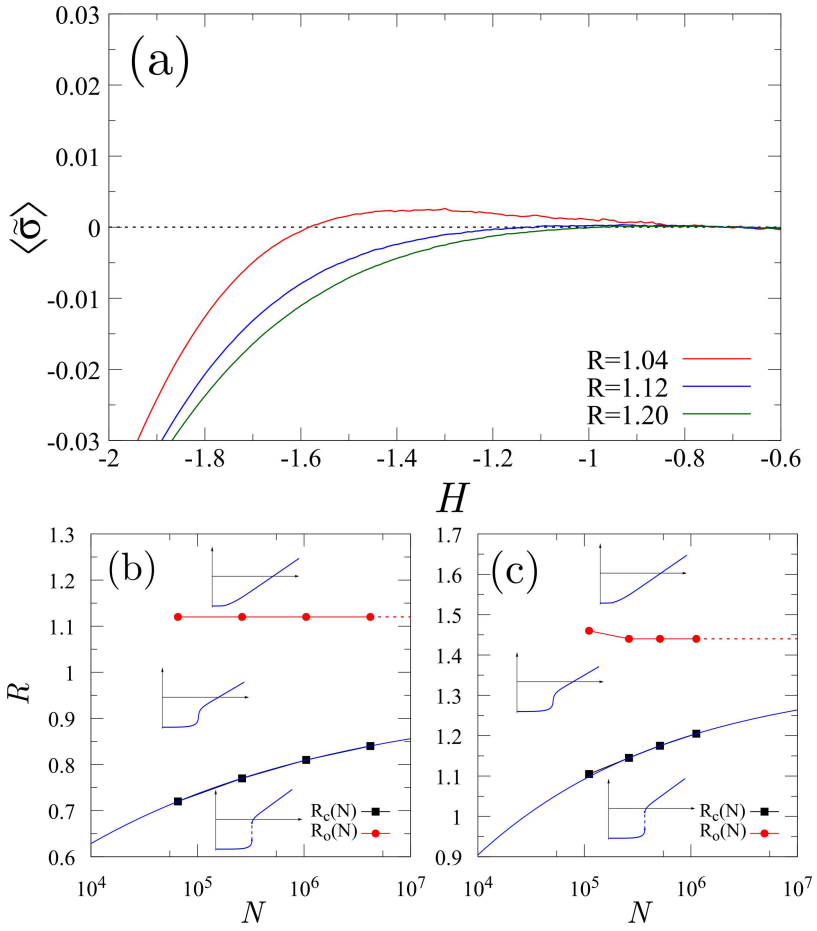

Figure 2.11: (a) Average $\langle\tilde{\sigma}(H)\rangle = \langle m(H)\rangle - aH$ curves for a 2D model with $L = 2048$ close to $R_o = 1.12$. The curves are shifted in order to converge to the same value, so that the comparison between them is easier. (b,c) The critical point $R_c(N)$ together with the value of the disorder at which the overshoot first appears, R_o, as a function of the system size, $N = L^d$, in 2D (b) and in 3D (c). Blue lines are fits to $R_c^\infty - a/N^b$, with $R_c^\infty = 0.95$, $a = 1.65$, $b = 0.178$ in 2D and $R_c^\infty = 1.35$, $a = 3.97$, $b = 0.237$ in 3D. Insets: The corresponding schematic magnetization curves.

then fit the size dependence of R_c to the relation $R_c^\infty - R_c(N) = aN^{-b}$. The results of the fit are given by the blue curves in Fig. 2.11(b,c), from which we obtain $R_c^\infty = 0.95$, $a = 1.65$, $b = 0.178$ in 2D and $R_c^\infty = 1.35$, $a = 3.97$, $b = 0.237$ in 3D. The fit supports the fact that R_c^∞ is finite. Moreover, it suggests that the region between the black and the red points (which corresponds to the stress overshoot in the EPM) does not disappear in the thermodynamic limit. The parameter b is related to the critical exponent ν through $1/\nu = db$. With the fitted values of b this gives $\nu \approx 2.80$ in 2D and $\nu \approx 1.41$ in 3D, which are not far from the values obtained by mean of the finite-size scaling analysis in Fig. 2.10.

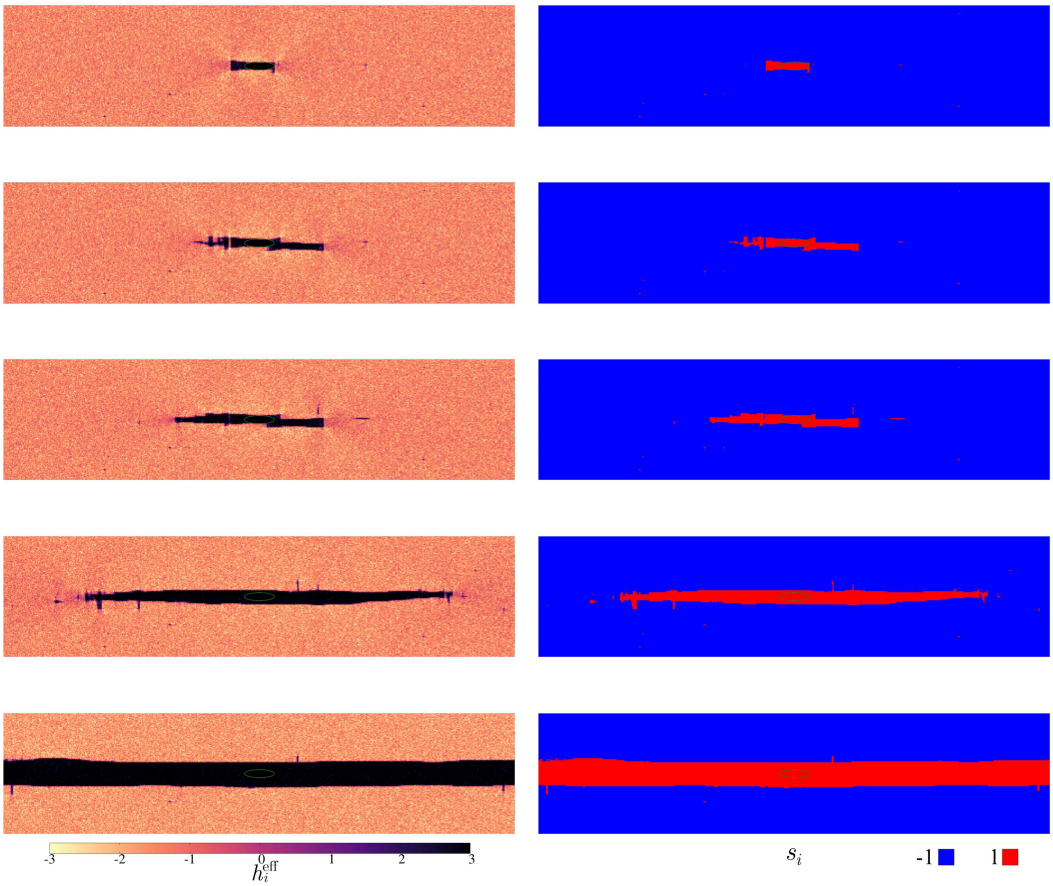

Figure 2.12: Evolution of the local effective field (left) and the local magnetization (right) during the largest event in an Eshelby-RFIM with a seed. The direction is forced by the symmetry of the ellipsoidal seed (in green) which has the major axis along x of semi-length $D_a = 15$ and the minor one along y of semi-length $D_b = 4$. Avalanche steps are $l/l_{max} = 0, 0.04, 0.07, 0.28$ and 1. Obtained in 2D with $L = 512$ and $R = 0.40$. The plot is for $y \in [196, 316]$ and the full x-axis, with the seed centered at $(256, 256)$.

4 Variations of the model

We now discuss some variations of the Eshelby-RFIM, as we did for the EPM in the previous section.

4.1 Effect of a seed

As already done for the standard RFIM in the Introduction and for the EPM in Chapter 1, we study the effect that a "seed" composed of positive spins has on the evolution of the Eshelby-RFIM and in particular on the value of the coercive field when $R < R_c$. The idea is to assess the role that rare regions, which are only present at the thermodynamic limit, have on the system. The method used in this case is the same as the one described for the standard RFIM: inside a given region of the sample we choose the spins to start with the value $+1$ and we associate to them a very large positive local field h_i, so that they cannot

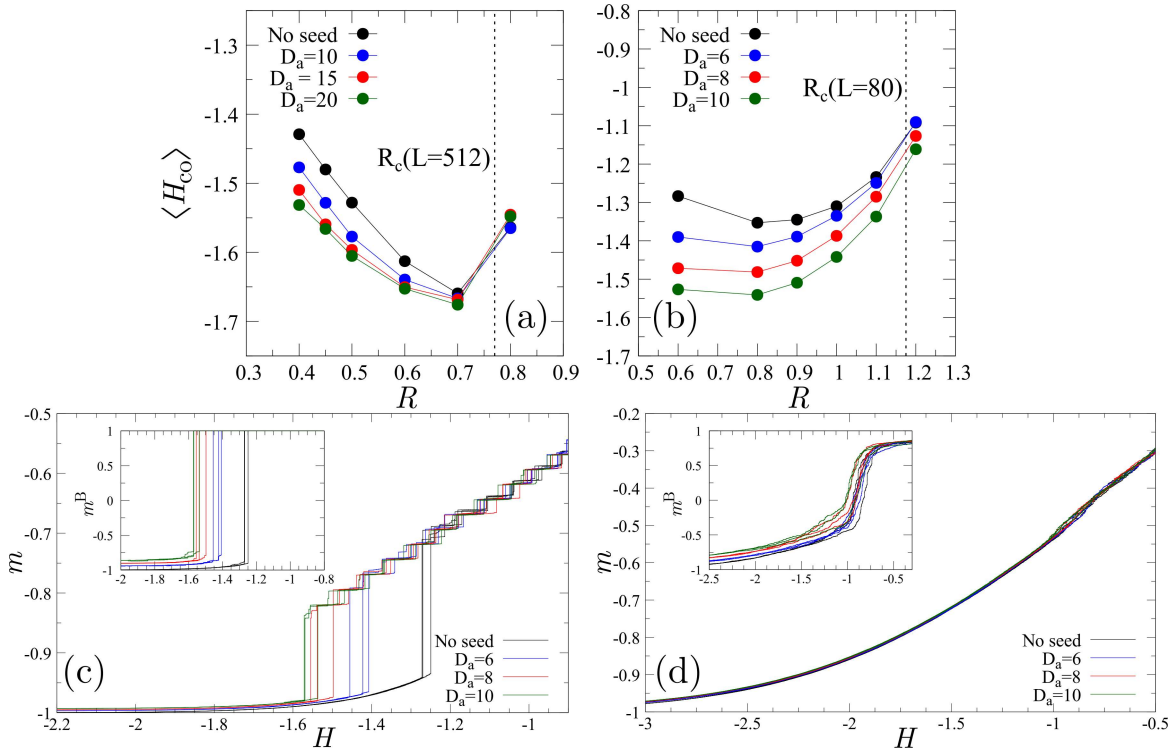

Figure 2.13: Effect of seeds for different sizes D_a on the average value of the coercive field $H_{\rm co}$ for $L = 512$ in 2D (a) and $L = 80$ in 3D (b). The vertical dashed line marks the critical value R_c for the relative system sizes. The results are obtained with $D_b = 4$ in 2D and $D_b = 3$ in 3D. (c,d) Magnetization curves from three independent samples obtained in 3D with $L = 80$ and different seed sizes. In (c) $R = 0.60 < R_c(L = 80)$, while in (e) $R = 1.30 > R_c(L = 80)$. Inset: the effect of the seed on the m^B-vs-H curve.

flip back. Since the interactions are the same as in the EPM, we also consider in this case an ellipsoidal seed, which favors the formation of a band along its major axis (see Fig. 2.12). We define D_a and D_b as the half length of the major and minor axes of the ellipse, which is aligned with the x-axis in 2D. In 3D we take the additional semi-axis $D_c = D_a$ along z. More details on the code to simulate such a situation are given in Appendix B. The evolution of the spin configuration during the largest avalanche is displayed in Fig. 2.12. As the external field increases from $-\infty$, the first spins to flip are those close to the seed, and in particular those aligned along the major axis. The system then develops a band, but the associated transition takes place for a smaller value of H than in the case without seed. The results for this setup are shown in Fig. 2.13. In the top panels we plot the average value of the coercive field as a function of the disorder strength R for different sizes of the seed in 2D and 3D. The general behavior is similar to that observed in Fig. 1.13: for small values of R the effect of the seed is strong, while as R grows closer to R_c it gets less and less important. This effect is more pronounced for larger seeds, which seem to also have consequences on the points obtained for $R > R_c$ in 3D (although much smaller ones). In the bottom panels of the figure we show the magnetization curves obtained upon the insertion of the seed. While in the EPM we saw that the seed did not affect the elastic branch, the situation is slightly

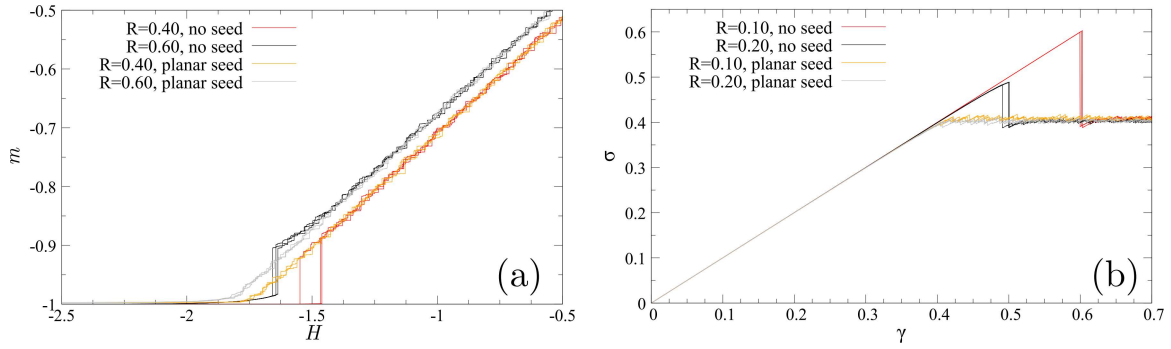

Figure 2.14: (a) Magnetization curves for three independent samples obtained with the Eshelby-RFIM for $L = 2048$ and two different values of $R < R_c$, compared with the curves obtained in the same conditions but with the addition of a line of up spins at the beginning of the dynamics. (b) Same comparison for the stress-vs-strain curves obtained from an EPM with $L = 2048$ and two values of $R < R_c$. The weak linear region is inserted as described in the previous chapter.

different for the initial part of the dynamics in the Eshelby-RFIM. The presence of the seed clearly changes the initial value of the magnetization and of m^B, which are not exactly -1 anymore. Apart from this effect, which is negligible in the thermodynamic limit, the general evolution remains unchanged in this first part. The last part of the evolution is also not affected by the presence of the seed. The linear regime is indeed the same for all seed sizes and for all samples. The passage from one regime to the other is however influenced by the rare region. For $R < R_c$ the value of H at which a macroscopic jump occurs both in m and in m^B decreases with the size of the seed, as already seen in the top panels. In panel (d) we can also observe that, for large enough D_a, the seed slightly changes the value of H at which the curve m^B is steepest, but without creating a macroscopic jump in the system.

Before concluding this part we comment on the linear regime observed in the magnetization curve of the Eshelby-RFIM. This regime stems from the propagation of the band within the system, until all the spins point in the positive direction. In order to understand the wide generality of this linear regime across different samples, we consider an Eshelby-RFIM in which a band is inserted from the beginning of the dynamics. This situation would not be physical in an EPM, as it would correspond to a solid which has already yielded. However we discuss this case here to show the origin of the linear regime and to explain the behavior of $\Delta m_{\max}$. The only difference with what we just did is that the seed is not an ellipsoid but a whole horizontal line (for simplicity we only consider the 2D case) of positive spins. We choose the band to have some thickness in order to avoid perpendicular bands, which amounts to fix $s_{x,y} = 1$ for all x and for $L/2 - 3 < y < L/2 + 3$ at the beginning of the dynamics. The results are shown in Fig. 2.14. We see that the values of R that we studied, the presence of the planar seed completely eliminates the macroscopic jump in $m(H)$, as well as the bump. The magnetization curve starts from a negative value close to -1 and it increases slightly with H as some spins flip independently. At some value of the external field $H = H_{\text{co}}^{\text{plane}}$ the curve enters continuously the linear regime. The behavior $m_{\text{LR}}(H) = aH + b$ that is followed for $H > H_{\text{co}}^{\text{plane}}$ is the same as the system without seed follows for $H > H_{\text{co}}$. The value of a seems to be independent of the sample, of the insertion of the seed and also

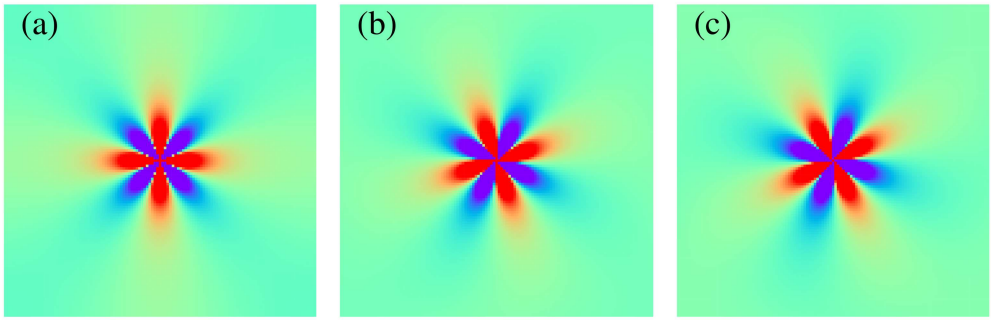

Figure 2.15: The rotated Eshelby kernels in the real space, with the angle $\psi = 0$ (a), $\psi = 0.32175$ (b), and $\psi = 0.46365$ (c). Red stands for positive interactions, while purple for negative ones (and green for 0).

of the chosen R, which instead affects b. We also show that the same behavior takes place in an EPM in which the inserted weak region is a plane as described here. Not only the macroscopic jump, but also the stress overshoot (which is still associated to the formation of a band) disappears, as the stress curves pass from the elastic branch directly to the plastic one. This is not surprising since, as already mentioned, this case would correspond to a solid that has already yielded and cannot sustain more stress than its steady-state value. It is however interesting that the Eshelby-RFIM reproduces the same behavior.

4.2 Rotated Eshelby-RFIM

It has been reported that the short-ranged ferromagnetic version of the RFIM in 2D is sensitive to faceting effects associated with the choice of the lattice [8], which can alter the properties of the system. In the model described, we have chosen the Eshelby propagators that mediate the interactions to be aligned with the positive part along the x and y axes, which represent special directions in the square lattice. In order to assess the effects of this choice we consider here a different case, in which the Eshelby kernels are rotated by an angle with respect to the horizontal one. This amounts to rotating the lattice by the same angle. We are in particular interested in how this rotation affects the possibility for the system to form a band and the presence of a critical point. Notice that by rotating the lattice one still conserves all the symmetries therein, which can still not fully eliminate faceting. A more drastic treatment would be to choose a random lattice, for example by diluting a square lattice or by choosing the sites to be positioned in a Voronoi lattice as in [8]. (Unfortunately, due to the long-range and anisotropic character of the interactions, this source of randomness dominates over the one introduced by random fields and as a consequence one loses the ability to change the behavior of the system by tuning R: the observed system is then always in the continuous-magnetization phase, and the formation of a band does not occur as spins flip almost independently.) Going back to our rotated-Eshelby model, we define the propagator as

$$G^{\psi}(\mathbf{r}) = \frac{\cos(4(\theta - \psi))}{\pi r^2}. \tag{2.18}$$

For the rotated Eshelby of this kind, we need more accuracy in the computation of the inverse Fourier transform. To overcome this issue we have performed such computation in a lattice

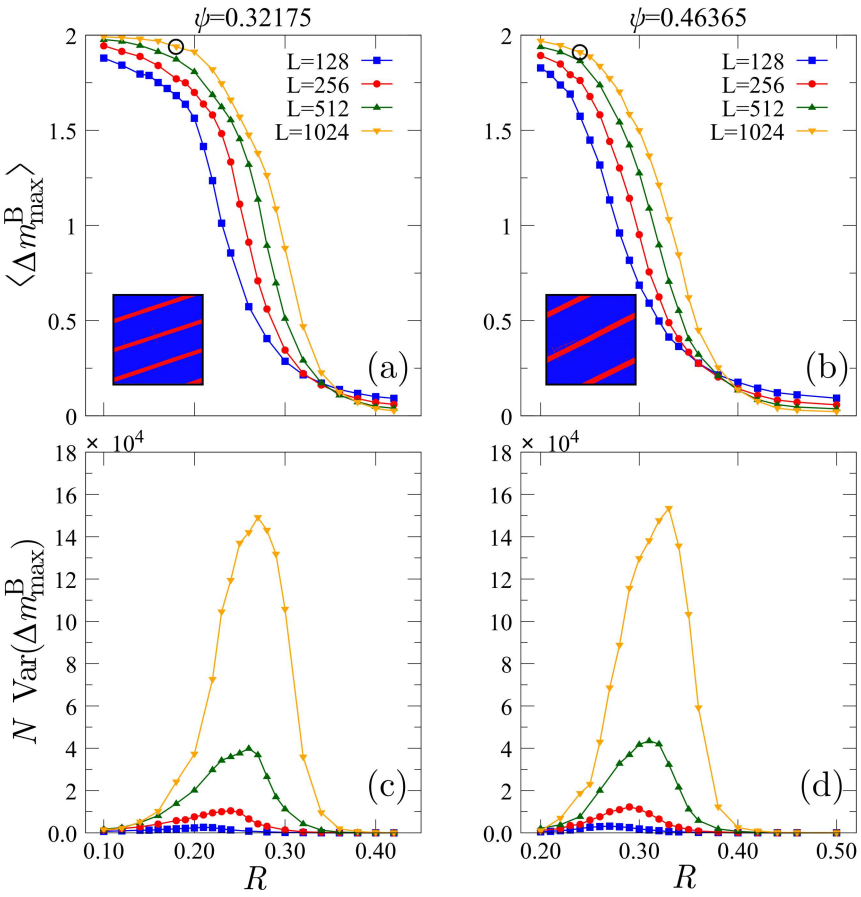

Figure 2.16: Evidence for a critical point in rotated Eshelby-RFIMs in 2D. Upper: Average value of the order parameter $\langle \Delta m_{\max} \rangle$ as a function of R for several system sizes and $\psi = 0.32175$ (a) and $\psi = 0.46365$ (b). Lower: Variance of $\Delta m_{\max}$ multiplied by $N = L^d$, i.e., disconnected susceptibility, for $\psi = 0.32175$ (c) and $\psi = 0.46365$ (d). Insets: spin configurations after the macroscopic jump for $L = 1024$ and $R = 0.18$ in (a), while $R = 0.24$ in (b).

with a finer grid, as described in [169]. Due to the periodic boundary conditions, a system spanning band must be able to close on itself, which restricts the choice to only some values of ψ. In particular we consider here two possibilities, $\psi = 0.32175$ and $\psi = 0.46365$, which correspond to the angles such that $\cos(\psi) = 3\sin(\psi)$ and $\cos(\psi) = 2\sin(\psi)$, respectively (see Fig. 2.15).

Our simulations show that the same phenomenology as in the case $\psi = 0$ is obtained: when R is large the spin flips have a homogeneous character and occur almost independently, whereas when R is small the magnetization curve displays a macroscopic jump and the system shows the formation of a system-spanning band along the direction imposed by ψ (see insets of Fig. 2.16). After the jump the system enters a linear regime in which the magnetization increases proportionally to the external field, just as in the $\psi = 0$ case. In Fig. 2.16 we show the properties of these systems as they approach the critical point. In order to do so, the order parameter $m^B(H)$ has been modified accordingly to capture the formation of the

tilted shear band, while considering periodic boundary conditions. We observe in the top panels that the mean value of $\Delta m^B_{\max}$ increases from 0 to 2 as R decreases, and it does so in a smaller region of R as the system size increases. This is associated with a peak in the related disconnected susceptibility, which once again increases and gets sharper as the system size increases. Due to the smaller system sizes and the few samples, the characterization of the critical exponents is more difficult in the tilted Eshelby-RFIM. Preliminary results give $\bar{\gamma}/\nu \approx 1.9$ and $\nu \approx 3.0$ for both models, but the collapse from which these values are obtained is not very clean. More samples and larger system sizes are needed to capture a precise value for the critical exponents in this case.

5 Conclusion

In this chapter we have taken one more step to simplify the description of the yielding transition of sheared amorphous solids and considered an athermal quasistatically driven RFIM. In order to reproduce the anisotropic nature of shear bands we have replaced the short-range ferromagnetic interactions of the standard RFIM by the Eshelby kernel, which is long-ranged and has a quadrupolar symmetry. We have then studied the evolution of the magnetization, starting from a negatively magnetized state and then increasing the external field quasistatically and at $T = 0$. The magnetization curve depends strongly on the variance R^2 of the local random fields. When R is small a macroscopic jump is observed in its evolution, while for larger values the resulting curve is essentially smooth (barring the presence of subextensive avalanches of spin flips). We then passed to the study of the weak-disorder phase, in which the magnetization jumps at some value $H_{\rm co}$ of the external field, the macroscopic avalanche is organized in a band, analogous to the shear band observed in the EPM. We have studied how the band forms and how the spins in the system evolve during its formation, highlighting similarities and differences with the EPM. We have then analyzed the critical point that separates continuous and discontinuous regimes. We have studied the system at and near criticality by looking at the disconnected susceptibility, computed with two order parameters m and m^B. From the results obtained with m^B, which more directly probes the appearance of a band, we have given evidence for the presence of a critical point and we have provided an estimate of the critical exponents by means of a finite-size scaling analysis. In order to perform sample averages of the various observables we have used $1000-3000$, $500-1500$, $240-1000$, and $100-500$ samples for $L = N^{1/2} = 256, 512, 1024,$ and 2048, respectively, in 2D, and $500-2000$, $500-2000$, $200-1000$, and $200-500$ samples for $L = N^{1/3} = 48, 64, 80,$ and 104, respectively, in 3D. In addition we have investigated the effect of a seed of positive spins, mimicking the presence of statistically rare regions in a macroscopic sample, on the value of the coercive field and its distribution in the low-disorder regime. Finally we have shown that the critical point is robust with respect to a change in the lattice which we introduced by rotating the orientation of the Eshelby kernels. In this work we have not focused on the properties of the avalanches. They have been studied in depth by many others in the case of sheared amorphous solids, both in MD simulations and with the help of the EPM [50, 147], and in the case of the RFIM [131, 170, 171]. At least in the steady state, it has been shown unambiguously that the distribution of avalanche sizes $P(S)$ follows a power law of the type $P(S) \sim S^{-\tau}$ with a cutoff S_c that depends on the system size. The scale-free property of the avalanches makes the system "self-organized critical"

or "marginal". The criticality arises with no need to tune any external parameter. This is different with what is observed in the study of the driven ferromagnetic RFIM, for which the integrated avalanche distribution rigorously shows a scale-free behavior only at the critical point $R = R_c$. One may then wonder what happens in the case of the Eshelby-RFIM. We have studied the distribution of avalanches in the linear regime of the magnetization curve (we stress once again that this regime does not correspond to a bona fide steady state). The avalanche distribution seems indeed to follow a power-law scaling, with an exponent τ which is similar to that of the EPM (we get $\tau \approx 1.25$) in 2D and slightly different in 3D. It is however difficult to assess if the large cutoff to the power law truly diverges with system size. Avalanches are discussed in more detail in Appendix D.

Chapter 3

Mean-field results: Emergence of a random field in an EPM

Contents

1 Introduction 98
1.1 Mean-field limit of the EPM 98
1.1.1 Relevance of the mean-field EPM for yielding of amorphous solids and the depinning of an interface 102
1.2 Mean-field limit of the RFIM 104
1.3 Contrasting EPM and RFIM 106
2 Sample-to-sample fluctuations and strength of the effective random field 108
2.1 Illustration for the RFIM 108
2.2 Susceptibilities in the mean-field EPM 110
3 Results for the mean-field EPM 113
3.1 Stress-vs-strain curves and the role of various types of disorder . . . 113
3.2 Connected and disconnected susceptibilities 115
3.3 Strength of the effective random field 118
4 Conclusion 123

1 Introduction

In the previous parts of this work we saw how the EPM, a mesoscopic phenomenological model, is able to reproduce the physics of amorphous solids under deformation. We showed that a critical point separates brittle and ductile behavior and that, in the former case, a macroscopic stress drop occurs with the formation of a shear band. Due to the qualitative analogy between these results and those of the AQS driven RFIM, we came up with a modified version of the random-field Ising model incorporating the anisotropic nature of the Eshelby interactions used in the EPM with the goal of finding an effective theory for the yielding transition. In this last chapter we try to get a detailed understanding of the similarities and differences between EPM and driven RFIM, but we do it in a different framework. We leave aside the finite dimensional approach, where analytical computations are too difficult, to focus on the mean-field limit of EPM and RFIM. The positive side of this approximation is that we are able to compute the sample-to-sample fluctuations analytically in the two models. The effects of different sources of disorder, especially in the EPM, can then be studied, as well as their role in the definition of an effective random field. The down side of our mean-field approach is that the geometry of space is lost and we do not account for the anisotropy of the interactions neither in the EPM nor in the RFIM. The content of this chapter has been published in a paper [172].

1.1 Mean-field limit of the EPM

The EPM has the same general rules as that simulated in finite dimensions in Chapter 1. We choose the local stress thresholds to be homogeneous and equal to 1, and we add disorder to the system by choosing an initial configuration of stress from a probability distribution $\mathcal{P}_{\gamma=0}(\{\sigma_i\}) = \prod_i P_{\gamma=0}(\sigma_i)$. The stress drop $\delta\sigma_i$ after a site fails is also chosen from a distribution $\mathcal{G}(\{\delta\sigma_i\}) = \prod_i g(\delta\sigma_i)$. A mean-field approximation can be derived by replacing the original d-dimensional lattice by a fully-connected one (equivalent to the $d \to \infty$ limit). In this limit each local variable (in this case the stress σ_i) interacts with all the others. However, taking this limit is not trivial in the EPM due to the presence of anisotropic interactions associated with the Eshelby kernel (see Appendix A). To overcome this issue one can take two possible directions. The simplest one is to assume that after an event each site redistributes part of its stress uniformly to the rest of the system. The resulting kick felt anywhere in the system is then of order $1/N$. The drawback is that the anisotropic nature of the Eshelby kernel is neglected, as the contributions coming from yielding sites are always making the rest of the system a bit more unstable. A more refined description [9] is to introduce another source of quenched disorder: each site receives a random kick due to all the plastic events that occur in the system. Due to the $1/r^d$ decay one finds that a correct distribution of kicks should be broadly distributed and random in sign, so that each site that receives a kick can be pushed either further or closer to its instability. In particular one finds that it should decrease as $g(\delta\sigma) \sim |\delta\sigma|^{-2}$ [173]. This refined model is necessary if one is interested in capturing some features of amorphous solids, such as marginal stability. However, the yielding transition and its dependence on the initial disorder are very similar in both mean-field models [9]. Since we want to analytically compute the sample-to-sample fluctuations near yielding, which appears hardly tractable in the model with random kicks, we restrict ourselves to the simpler model in which the redistribution is uniform and positive.

Let us now describe the AQS evolution of this system under strain. To this end it turns out to be more convenient to work with the local stability (distance to threshold) $x_i = 1 - \sigma_i \geq 0$ rather than with the stress itself. As the external strain increases from γ to $\gamma + d\gamma$, the local stress grows linearly with $d\gamma$ with a factor equal to twice the shear modulus, so that $x_i \to x_i - 2\mu_2 d\gamma$ (in this chapter we defined $\gamma = \varepsilon_{xy}$ so we need a factor 2 in front of the shear modulus μ_2). Following this increase, plastic events occur at sites that reached the threshold, where the stress drops. The distance to instability then goes from 0 (since they where unstable) to a random amount $\hat{x}$ chosen from the distribution $g(\hat{x})$. The same amount $\hat{x}$ is then redistributed to all the other sites, which get closer to instability by an amount $[\mu_2/(\mu_1 + \mu_2)]\hat{x}/N$, where $\mu_2/(\mu_1 + \mu_2)$ (with $\mu_1 > 0$) is the strength of the interaction kernel. As in the finite-dimensional case, also here this stress redistribution may make some sites unstable, which in turn distribute their stress and repeat the process, until the whole system is stable again (meaning that the condition $x_i > 0$ is recovered for all sites i). A key quantity needed to make progress is the total stress increment per site that did not yield during the change from γ to $\gamma + d\gamma$, which we denote by dy. Due to the fully connected nature of the lattice, all sites can be considered as statistically equivalent. However, the increment dy depends on both the sample, i.e., the initial configuration which is denoted by α, and the sequence of stress drops, or equivalently, of random variables $\{\hat{x}_i^1, \cdots, \hat{x}_i^M\}$ with $\gamma = M d\gamma$. Here, in contrast to what we did in Chapter 1, we split the dependence on the initial disorder realization (α) form the one on the random jumps ($\{\hat{x}_i^1, \cdots, \hat{x}_i^M\}$). This split does not make sense in a real system or in molecular dynamics simulations, since the kicks observed in a single realization are obviously a consequence of the initial arrangement of particles. However, as we will see, it is useful in this mean-field context as it allows to investigate separately the role of the two sources of randomness. Note that, since the stress drop on each site i is independently drawn for each plastic event from the same distribution, it is convenient to define a sequence of random drops for site i that assigns a drop for each infinitesimal step $d\gamma$ even if the site does not actually yield at this step: many random variables in the sequence $\{\hat{x}_i^1, \cdots, \hat{x}_i^M\}$ then do not appear in the evolution equations and will be averaged away in the final quantities.

The total stress increment (for sites that did not yield) $dy^{\alpha,[\hat{x}]_{M+1}}$ then reads

$$dy^{\alpha,[\hat{x}]_{M+1}} = 2\mu_2 d\gamma + \frac{\mu_2}{N(\mu_1 + \mu_2)} \sum_{i=1}^{N} \theta(dy^{\alpha,[\hat{x}]_{M+1}} - x_i^{\alpha,[\hat{x}]_M}(\gamma))\hat{x}_i^{M+1}, \tag{3.1}$$

where $[\hat{x}]_M \equiv \{\hat{x}_i^1, \cdots, \hat{x}_i^M\}$ for all sites (but keep in mind that the random jumps on each site are independent) and $\theta(x)$ is the Heaviside step function. The first term of the right-hand side corresponds to the linear elastic change while the second is the contribution coming from plastic events. (Note that $dy^{\alpha,[\hat{x}]_{M+1}}$ is infinitesimal for an infinitesimal $d\gamma$ except when there is a macroscopic avalanche of unstable sites, which as we will see only occurs at the spinodal point associated with brittle yielding; in the mean-field setting one can nonetheless constrain the cumulative parameter y to be continuous, provided one carefully accounts for the presence of a spinodal as a function of γ.)

Due to the positivity of the interaction, one may invert the above expression and relate

a now sample- and history-dependent strain increase $d\gamma$ to a fixed dy:

$$d\gamma^{\alpha,[\hat{x}]_{M+1}} = \frac{1}{2\mu_2}\left[dy - \frac{\mu_2}{(\mu_2+\mu_1)N}\sum_{i=1}^{N}\theta(dy - x_i^{\alpha,[\hat{x}]_M}(y))\hat{x}_i^{M+1}\right]. \tag{3.2}$$

With either control parameter, the initial condition is $\gamma = y = 0$. Considering the evolution of the system as a function of the control parameter y will prove much more convenient than as a function of γ because the evolution at each site is then independent of what happens at the others and follows the simple rule

$$x_i^{\alpha,[\hat{x}]_{M+1}}(y+dy) = \begin{cases} x_i^{\alpha,[\hat{x}]_M}(y) - dy & \text{if } x_i^{\alpha,[\hat{x}]_M}(y) > dy \\ \hat{x}_i^{M+1} & \text{otherwise.} \end{cases} \tag{3.3}$$

In the end, one will of course have to switch back to the physical control parameter γ by using the above expressions. The dynamics of the system when changing from y to $y+dy$ (where as an intermediate stage we discretize y in M steps dy) can be summarized by the following equation that describes the evolution of the stability at site i:

$$\begin{aligned} &\theta(x - x_i^{\alpha,[\hat{x}]_{M+1}}(y+dy)) = \\ &\theta(x - (x_i^{\alpha,[\hat{x}]_M}(y) - dy))\theta(x_i^{\alpha,[\hat{x}]_M}(y) - dy) + \theta(x - \hat{x}_i^{M+1})\theta(dy - x_i^{\alpha,[\hat{x}]_M}(y)). \end{aligned} \tag{3.4}$$

It expresses that the block i can either move elastically if it is far enough from its instability threshold or jump by a random amount $\hat{x}_i^{M+1}$ if it reaches its threshold. After rearranging the Heaviside functions by using the fact that $x \geq 0$, one can recast the equation as

$$\theta(x - x_i^{\alpha,[\hat{x}]_{M+1}}(y+dy)) = \theta(x + dy - x_i^{\alpha,[\hat{x}]_M}(y)) - \theta(\hat{x}_i^{M+1} - x)\theta(dy - x_i^{\alpha,[\hat{x}]_M}(y)). \tag{3.5}$$

From the above equation, one can for instance derive the evolution with y of the fraction of sites that have a stability less than x, $F_y^{\alpha,[\hat{x}]_M}(x) = (1/N)\sum_{i=1}^{N}\theta(x - x_i^{\alpha,[\hat{x}]_M}(y))$. It reads

$$F_{y+dy}^{\alpha,[\hat{x}]_{M+1}}(x) = F_y^{\alpha,[\hat{x}]_M}(x+dy) - \frac{1}{N}\sum_{i=1}^{N}\theta(dy - x_i^{\alpha,[\hat{x}]_M}(y))\theta(\hat{x}_i^{M+1} - x). \tag{3.6}$$

We first consider the average evolution of the system. Fluctuations will be studied and discussed later on. Since there are two (independent) sources of randomness in the present model, one should distinguish two types of averages. For a generic quantity $A^{\alpha,[\hat{x}]_M}$, one defines an average over samples α and an average over sequences of random stress drops $[\hat{x}]_M$,

$$\overline{A^{\alpha,[\hat{x}]_M}} = \int_0^\infty \left(\prod_{i=1}^{N} \mathrm{d}x_i\, P_0(x_i)\right) A^{\alpha,[\hat{x}]_M}, \tag{3.7}$$

$$\left\langle A^{\alpha,[\hat{x}]_M}\right\rangle_{[\hat{x}]_M} = \int_0^\infty \left(\prod_{n=1}^{M}\prod_{i=1}^{N} \mathrm{d}\hat{x}_i^n\, g(\hat{x}_i^n)\right) A^{\alpha,[\hat{x}]_M}, \tag{3.8}$$

as well as a full average,

$$A = \overline{\left\langle A^{\alpha,[\hat{x}]_M}\right\rangle}_{[\hat{x}]_M}. \tag{3.9}$$

In the above expressions, $A^{\alpha,[\hat{x}]_M}$ may be either taken as a function of γ (then, $\gamma = Md\gamma$) or of y (and $y = Mdy$). Note that $P_0(x) = P_{\gamma=0}(x) = P_{y=0}(x)$. Fully averaging Eq. (3.6) and using the fact that the random jumps are independent from site to site and from event to event (see Eq. (3.8)) provide an equation for the cumulative probability $F_y(x)$ for a site to have a stability less than x. Deriving it with respect to x gives an equation for the probability $P_y(x) = (1/N) < \sum_{i=1}^{N} \delta(x - x_i^{\alpha,[\hat{x}]_M}(y)) >$,

$$\partial_y P_y(x) = \partial_x P_y(x) + g(x) P_y(0), \tag{3.10}$$

which can be formally solved in the form

$$P_y(x) = P_0(x+y) + \int_x^{x+y} d\hat{x}\, g(\hat{x}) P_{x+y-\hat{x}}(0). \tag{3.11}$$

This result has already been given in [4], together with its solution for an exponential distribution of random jumps $g(\hat{x})$. For a general distribution $g(\hat{x})$ it can be recast as

$$P_y(x) = P_0(x+y) + g(x)F_0(y) + \int_0^y dy' F_0(y') R_{y-y'}(x), \tag{3.12}$$

with $F_0(x) = \int_0^x dx' P_0(x')$ and

$$R_y(x) = g'(x+y) + g(y)g(x) + \int_0^y dy' g(y') R_{y-y'}(x), \tag{3.13}$$

where a prime on a function indicates a derivative with respect to its explicit argument. For a simple exponential distribution, $R_y(x) = 0$ for every y and x, which gives back the solution of [4], and for a more general distribution $g(\hat{x})$ the above equations can be solved by a Laplace transform.

We define the volume-averaged local stability as

$$m^{\alpha,[\hat{x}]_M} = \frac{1}{N} \sum_i x_i^{\alpha,[\hat{x}]_M} = \int_0^\infty dx\, x P_y^{\alpha,[\hat{x}]_M}(x), \tag{3.14}$$

where $P_y^{\alpha,[\hat{x}]_M}(x) = \partial F_y^{\alpha,[\hat{x}]_M}(x)/\partial x = \frac{1}{N} \sum_{i=1}^{N} \delta(x - x_i^{\alpha,[\hat{x}]_M}(y))$. Averaging over the samples and the random jumps then leads to

$$m(y) = \int_0^\infty dx\, x P_y(x), \tag{3.15}$$

where $P_y(x)$ is given by Eqs. (3.12) and (3.13). The notation m anticipates the analogy with the magnetization in the RFIM. To go back to the strain γ as the control parameter, one has to take the average of Eq. (3.2). This is done by first averaging $d\gamma^{\alpha,[\hat{x}]_{M+1}}$ over $\hat{x}_i^{M+1}$, which, by using the independence of the variables at each step, simply brings a factor $< \hat{x} >$ $\forall i$ in the second term. Full averaging then further gives

$$d\gamma = \frac{1}{2\mu_2}[dy - \frac{\mu_2}{(\mu_2+\mu_1)} F_y(dy) < \hat{x} >] = \frac{dy}{2\mu_2}[1 - \frac{\mu_2}{(\mu_2+\mu_1)} P_y(0) < \hat{x} >], \tag{3.16}$$

from which one directly obtains an expression for the derivative $\gamma'(y)$ and, through an integration starting from $\gamma = 0$ at $y = 0$,

$$\gamma(y) = \frac{1}{2\mu_2}[y - x_c \int_0^y dy' P_{y'}(0)] \tag{3.17}$$

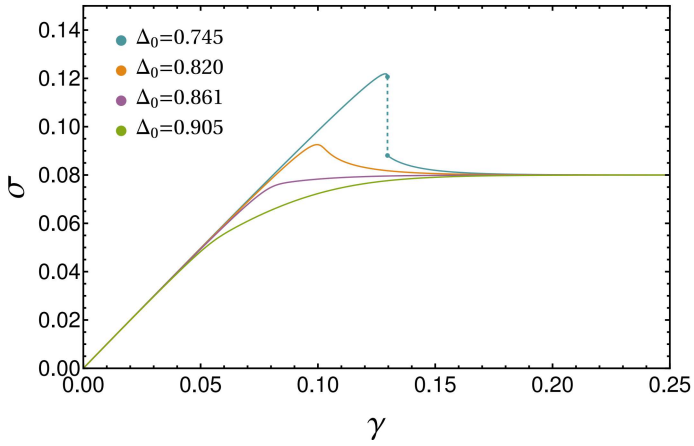

Figure 3.1: Average stress σ versus applied strain γ for the mean-field EPM with a distribution of random jumps chosen as an exponential and that of the initial local stress (or stability) as a linear combination of two exponentials [4]. As the strength Δ_0 of the disorder increases (for fixed parameters of the random jump distribution), one passes from a regime with a discontinuous stress jump to a continuous behavior with a stress overshoot to finally a monotonically increasing regime. The discontinuous and continuous regimes are separated by a critical point.

where we have defined

$$x_c =< \hat{x} > \frac{\mu_2}{(\mu_2 + \mu_1)}. \tag{3.18}$$

The loading curve, i.e., the average stress versus applied strain $\sigma(\gamma)$, is then obtained by combining Eqs. (3.12), (3.13), (3.15) and (3.17) with the relation

$$\sigma(y) = 1 - m(y) = \int_0^\infty dx(1-x)P_y(x). \tag{3.19}$$

The resulting curve is illustrated in Fig. 3.1 when the distribution of random jumps $g(\hat{x})$ is an exponential and the initial distribution $P_0(x)$ is the same linear combination of two exponentials as in [4]. More details are given in Appendix C, where other distributions are considered as well. The generic behavior is as follows: As the initial stability of the amorphous solid, which goes inversely with the variance of the initial stress distribution $\Delta_0 = \int_0^\infty dx P_0(x)x^2 - (\int_0^\infty dx P_0(x)x)^2$, decreases, yielding of the material changes from brittle-like with a discontinuous jump of the average stress to ductile-like with a continuous evolution, the two regimes being separated by a critical point for a specific value of the initial disorder strength. In this sense the value of Δ_0 plays in this case a similar role to the one played by R in the finite-dimensional version that we studied in Chapter 1.

1.1.1 Relevance of the mean-field EPM for yielding of amorphous solids and the depinning of an interface

As already stressed in the preceding subsection, the mean-field version that we study here overlooks the anisotropic character of the interactions associated with stress redistribution

after plastic events. Nonetheless, this shortcoming is not central for describing the yielding transition at the mean-field level since the improved model in which sites receive small random kicks of both signs from plastic events taking place in the whole sample yields the same qualitative description of the yielding transition as a function of the material's initial degree of stability [7]. What may be more troublesome for applications to finite-dimensional systems is the fact that the mean-field EPMs are predicted to encounter a linear instability leading to a discontinuous stress drop whenever an overshoot (i.e., a local maximum) appears in the average stress-strain curve [6]. As we stressed in Chapter 1, the outcome of this instability in real materials is still debated [163] as it is not clear whether or not it can be pinned (and the average stress still be a continuous function of the strain) by the disorder associated with the nonuniform structure of amorphous solids.

The mean-field EPM with a uniform (ferromagnetic-like) redistribution of stress has a more direct connection to the problem of the depinning of an elastic interface in a random environment, which was briefly introduced in Section 2.2.1 of the Introduction. At the mean-field (fully connected lattice) level, the evolution of the height h_i of the interface at base site i is given by [148, 159, 174]

$$\partial_t h_i(t) = k(\frac{1}{N}\sum_j h_j - h_i) + m^2(w - h_i) - \frac{\partial \mathcal{V}_i(h_i)}{\partial h_i} \tag{3.20}$$

where the first term of the right-hand side corresponds to the elastic interaction, the second to the drive and the last one to the pinning potential which is statistically translation-invariant along each coordinate h_i. When the potential $\mathcal{V}_i(h_i)$ is modeled as a collection of narrow pinning wells separated by random intervals z taken from a given distribution $g(z)$, the height at site i is pinned until the driving force exceeds a local threshold f_i^{th} associated with the well depth. The evolution equation can then be reformulated in a way similar to that of the mean-field EPM by introducing the stability of site i as $x_i = f_i^{th} - m^2(w - h_i) - k(\frac{1}{N}\sum_j h_j - h_i)$ [159]. A local depinning event is like a plastic event, the jump z_i to a new well controlled by the distribution $g(z)$ being analogous to the local stress jump $\hat{x}_i$ controlled by $g(\hat{x})$ and each site $\neq i$ getting a (negative) kick in its stability of kz_i/N equivalent to the kick of $[\mu_2/(\mu_1 + \mu_2)]\hat{x}_i/N$ in the EPM. The equivalence between depinning-like models and EPMs has been stressed for instance in [139, 144, 148, 159, 174–176] and exploited mostly for studying the properties of the stationary state in both models. However, one has to be more careful when considering the transient behavior and the yielding transition that may then take place. Indeed, one knows from Middleton's theorem [177] that when starting from $w \to -\infty$ with a flat interface the approach to the steady state must be monotonic (in the thermodynamic limit) and no overshoot in the average "stress", $\sigma(w) = m^2(w - \overline{h})$, is possible when the disorder is (statistically) translationally invariant. To observe an overshoot and the equivalent of a discontinuous or a critical yielding transition, one must therefore start, say, at $w = 0$, with a very special initial condition $\{h_i(0)\}$: the $h_i(0)$ must be such that $(1/N)\sum_i h_i(0) = 0$ (implying that each sample starts with a volume-averaged stress equal to 0) and such that $\sigma_i(0) = -(k + m^2)h_i(0) < f_i^{th}$ (stability requirement on each site when $\overline{h} = w = 0$). In the case of the EPMs these conditions are easily satisfied with an appropriate distribution $P_0(x)$. However, for an interface the $h_i(0)$'s must correspond to locations of pinning wells, which for each base site are randomly distributed from $-\infty$ to $+\infty$, leading to a statistical translational invariance. This puts strong constraints on the

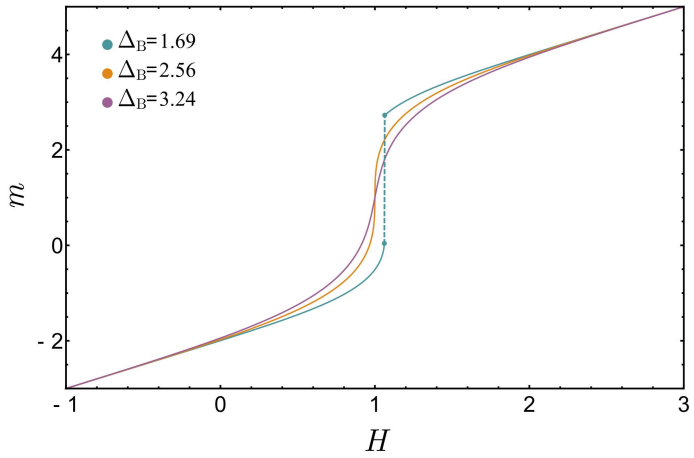

Figure 3.2: Quasi-statically driven mean-field RFIM (described by Eq. (3.22)) at zero temperature: average magnetization $m = \overline{m}$ versus applied field H for the ascending branch of the hysteresis loop and for different values of the disorder strength Δ_B. For these curves, $k = 2$ and $J = 1$.

allowed initial configurations which then correspond to rare and not typical samples. Note that, again because of Middleton's theorem, the stress of an interface starting from $w = -\infty$ is always larger than that of an interface starting at $w = w_0$ finite. Since the former is already in its steady state, the presence of an overshoot when starting from w_0 just corresponds to a particularly large avalanche in the stationary evolution, and, being untypical, it would vanish after taking the average over samples. [2]

1.2 Mean-field limit of the RFIM

We now consider the mean-field version of the random-field Ising model. In order to obtain the mean-field limit of the Eshelby-RFIM defined in Chapter 2, one should consider the anisotropic nature of the Eshelby-like interactions. As for the EPM, we focus for simplicity on the case in which the interactions are uniform and ferromagnetic and the mean-field limit corresponds to that of the standard RFIM defined in Section 2.2.2 of the Introduction. The mean-field version of the short-range ferromagnetic RFIM has been already introduced and studied in [10] and is described by the mean-field Hamiltonian

$$\mathcal{H}(\{s_i\}) = \sum_i (Jm(H) + H + h_i)s_i, \tag{3.21}$$

where $J > 0$ is the ferromagnetic interaction constant, H is the external field, $m(H) = 1/N \sum_i s_i$ is the total magnetization of the system and h_i are random fields which are independent from site to site and are drawn from the same distribution $\rho(h)$ with $\overline{h} = 0$ and $\overline{h^2} = \Delta_B$. When the system is driven quasistatically at $T = 0$, one observes the expected phenomenology also in the mean-field approximation: when the strength of the disorder associated to random fields is small, the magnetization curve shows a jump of order 1, while as

[2] A possible solution to observe an overshoot in the depinning problem is to take a disorder that breaks the statistical translational invariance, for instance by modifying the distribution of the position of the wells so that it varies as the interface progresses: Middleton's theorem no longer applies in this case.

Δ_B gets larger the jump disappears and $m(H)$ is smooth. The two behaviors are separated by a critical point Δ_B^c that can be characterized at the mean-field level. In the model defined by Eq. (3.21) the magnetization curve does not show an hysteresis loop for $\Delta_B > \Delta_B^c$ [10]. The m-vs-H curve follows the same pattern as the external field increases from $-\infty$ to ∞ and back, passing from the point $m(H = 0) = 0$. This is only an artifact of this simple mean-field version of the model, as in numerical simulations in finite dimensions the hysteresis loop is observed for every value of Δ_B [132, 170]. One can then define a coarse-grained version of the standard RFIM in which the local variables are "soft" spins that take value $s_i \in \mathbb{R}$, as opposed to the "hard" spin version $s_i = \pm 1$. The athermal evolution of the RFIM when quasistatically driven by an applied magnetic field in its soft-spin version is described by the following Hamiltonian:

$$\mathcal{H}[\{s_i\}] = -J \sum_{\langle i,j \rangle} s_i s_j + \sum_{i=1}^{N} V(s_i) - \sum_{i=1}^{N} h_i s_i, \tag{3.22}$$

where the N spins are placed on the vertices of a d-dimensional lattice, $< i, j >$ indicates nearest-neighbor sites in the lattice, $V(s)$ is a generic symmetric double-well potential with minima in $s = \pm 1$, and the h_i's are local random fields that are independent from site to site and are drawn from $\rho(h)$ with $\overline{h} = 0$ and $\overline{h^2} = \Delta_B$. (Here and below the overline denotes an average over the quenched disorder.)

When quasi-statically driven at zero temperature by an applied magnetic field H, the system evolves out of equilibrium by following a sequence of dynamically accessible metastable states which is described by the following equation of evolution:

$$\partial_t s_i(t) = J \sum_{j/i} s_j - V'(s_i) + h_i + H(t), \tag{3.23}$$

where the magnetic field $H(t)$ is infinitely slowly ramped up or down (so that the configuration of spins has time to settle in a metastable state before the field is changed again) and the sum denoted j/i is over the nearest neighbors of site i in the lattice.

In order to continue with the calculations one has to decide which potential to apply to the soft spins. An easily tractable mean-field limit is obtained by considering a fully connected lattice and a double-well potential in the form of two joining pieces of parabola,

$$V(s_i) = \begin{cases} \frac{k}{2}(s_i + 1)^2 & s_i < 0, \\ \frac{k}{2}(s_i - 1)^2 & s_i > 0, \end{cases} \tag{3.24}$$

with $k > J > 0$. This model was first introduced in [10] and further studied in [178–180]. (A similar model, with an asymmetric potential, has been used to study fracture in amorphous solids [181, 182].) It displays a rich phenomenology with history-dependent hysteresis effects for all values of Δ_B, avalanches in the evolution of the magnetization, and a sequence of qualitatively different behavior separated by an out-of-equilibrium critical point as a function of the disorder strength. In what follows we consider the protocol in which the magnetic field is ramped up, i.e., changes according to $H(t) = H + \Omega t$ with $\Omega \to 0^+$; this corresponds to the ascending branch of the hysteresis loop in the magnetization versus applied field diagram.

This mean-field model can be solved analytically [10]. On the ascending branch of the hysteresis loop, starting for instance from a negatively polarized configuration at large negative field, one finds that the solution of Eq. (3.23) when $\Omega \to 0^+$ is given by

$$s_i^\alpha(H) = \begin{cases} \frac{H+h_i+Jm^\alpha(H)}{k} + 1, & h_i > -Jm^\alpha(H) - H + k, \\ \frac{H+h_i+Jm^\alpha(H)}{k} - 1, & h_i < -Jm^\alpha(H) - H + k, \end{cases} \tag{3.25}$$

where, as in the previous chapters, the superscript α indicates that the quantities depend on the sample α, i.e., on the realization of the random fields $\{h_i^\alpha\}$, and $m^\alpha(H) = (1/N)\sum_i s_i^\alpha(H)$ is the volume-averaged magnetization which is given by the self-consistent equation

$$m^\alpha(H) = -1 + \frac{H + Jm^\alpha(H)}{k} + \frac{1}{N}\sum_{i=1}^{N}\left[\frac{h_i}{k} + 2\theta(h_i + H + Jm^\alpha(H) - k)\right]. \tag{3.26}$$

Details on the calculations are given in Appendix C. For illustration we display in Fig. 3.2 the disorder-averaged magnetization, which is obtained from

$$m(H) = \overline{m^\alpha}(H) = \left(\frac{k}{k-J}\right)\left[-1 + \frac{H}{k} + 2\int_{-(H+Jm(H)-k)}^{\infty} dh\rho(h)\right], \tag{3.27}$$

as a function of the applied field H on the ascending branch of the hysteresis curve for several values of the bare variance of the random field Δ_B. We have chosen a Gaussian for the random-field distribution. As first shown in [10] the curve has a discontinuity, i.e., a magnetization jump, at low disorder, is continuous at large disorder and for a specific value $\Delta_{B,c} = \sqrt{2/\pi}\, kJ/(k-J)$ goes through a critical point at which the slope is infinite.

1.3 Contrasting EPM and RFIM

As we will elaborate more, the comparison between the EPM and the RFIM is meaningful, at least for the mean-field models, in the region of the average stress-strain curve between the overshoot, if present, and the steady state. What has been shown [4] is that the yielding transition which takes place in this region is in the same universality class as the transition of the driven athermal RFIM.

It is instructive to make a direct comparison between the equations for the AQS evolution of the EPM and of the RFIM. They are indeed rather similar when starting from an initial condition at some intermediate strain γ_0 or magnetic field H_0. Consider the mean-field models introduced above. For simplicity we choose the EPM without randomness in the thresholds and the jumps, so that disorder only comes from the initial condition, but this does not affect the conclusions. The equations for the local stability in a given sample α starting from $x_i^\alpha(\gamma_0)$ can then be written

$$x_i^\alpha(\gamma) = \begin{cases} x_i^\alpha(\gamma_0) - 2\mu_2(\gamma - \gamma_0) - x_c\, n^\alpha(\gamma_0, \gamma), & \text{if } \gamma < \gamma_*^\alpha, \\ x_i^\alpha(\gamma_0) - 2\mu_2(\gamma - \gamma_0) - x_c\, n^\alpha(\gamma_0, \gamma) + < \hat{x} >, & \text{if } \gamma > \gamma_*^\alpha, \end{cases} \tag{3.28}$$

where $n^\alpha(\gamma_0, \gamma)$ is the fraction of sites that have yielded between γ_0 and γ, and γ_*^α is defined by $x_i^\alpha(\gamma_0) - 2\mu_2(\gamma_*^\alpha - \gamma_0) - x_c\, n^\alpha(\gamma_0, \gamma_*^\alpha) = 0$. We implicitly assume here that within the chosen interval of strain the sites yield only once; this will be further discussed and checked below.

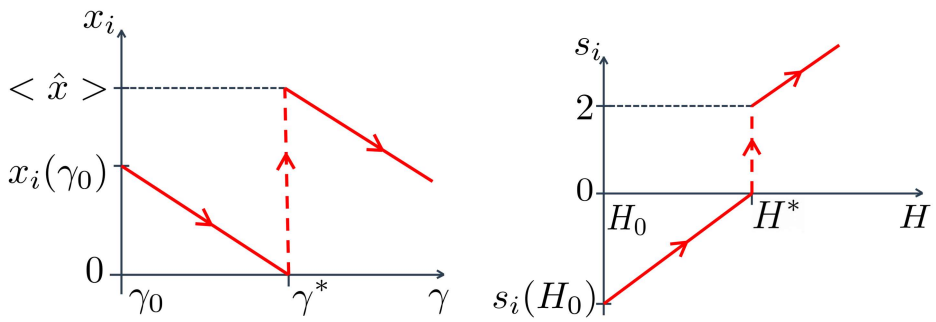

Figure 3.3: Sketch of the difference between the evolution of the local stability $x_i = 1 - \sigma_i$ versus applied strain γ in an EPM (left) and that of the local magnetization s_i versus applied magnetic field H in an RFIM (right). In both cases the evolution starts from some initial value of the drive, γ_0 or H_0.

On the other hand, the equations for the driven RFIM starting from an initial spin value $s_i(0) < 0$ can be cast as

$$s_i^\alpha(H) = \begin{cases} s_i^\alpha(H_0) + (H - H_0) + J[m^\alpha(H) - m^\alpha(H_0)], & \text{if } H < H_*^\alpha, \\ s_i^\alpha(H_0) + (H - H_0) + J[m^\alpha(H) - m^\alpha(H_0)] + 2, & \text{if } H > H_*^\alpha, \end{cases} \tag{3.29}$$

where m^α is as before the volume-averaged magnetization in sample α and H_*^α is defined by $s_i^\alpha(H_0) + (H_*^\alpha - H_0) + J[m^\alpha(H_*^\alpha) - m^\alpha(H_0)] = 0$. Eq. (3.28) and Eq. (3.29) have a similar form, except for the sign of the linear drive and for the fact that $n^\alpha(\gamma_0, \gamma)$ is not quite the difference $[m^\alpha(\gamma) - m^\alpha(\gamma_0)]$. The evolutions corresponding to the above equations are sketched in Fig. 3.3. They both correspond to continuous (linear) segments as the control parameter, either γ or H, is increased which are interrupted by a discontinuous jump associated with a local plastic event (jump of size $< \hat{x} >$) or a local spin flip (of size 2). One however notes that the relative sign of the jumps and the linear evolutions are opposite in the EPM and the RFIM. In a sense, the RFIM has a negative elasticity and, as a result, the spins can only flip once, whereas a site in an EPM will yield many times if one continues to increase the strain (not shown in the sketch), allowing the system to reach a stationary state controlled by the competition between linear elastic increases and plastic stress drops, as discussed in previous Chapters.

The difference just outlined precludes a direct mapping between the EPM and the RFIM at the level of individual dynamical realizations. Nonetheless, provided one stays in a restricted region of strain where most sites yield only once, the mapping between the mean-field EPM and the mean-field RFIM can be further pushed at the level of correlation functions: see Appendix C. As we show, a direct mapping is possible at the averaged level, e.g., the average stress-versus-strain curve, but is more demanding for sample-to-sample fluctuations. We also show that the assumption of a single plastic event per site is very good up to yielding but deteriorates beyond, although this somewhat depends on the random-jump distribution.

In the following we rather focus on the sample-to-sample fluctuations and investigate the emergence and the properties of an effective random field in the vicinity of the yielding transition.

2 Sample-to-sample fluctuations and strength of the effective random field

Now that the mean-field framework has been described for both models we can move to the central point of this chapter. Our purpose is to derive a workable expression for estimating the strength of the effective random field (if present) in an athermally driven disordered system in terms of quantities that characterize the spatial fluctuations present in the system, i.e., susceptibilities. In order to obtain such an expression, we use the procedure described in Section 2.2 of the Introduction, based on the MSRJD formalism. In particular, from Eq. (I.33), we obtained an equation for the strength of the renormalized random field, which can be used in the mean-field approximation we just introduced. Notice that this expression is more general and can in principle used also in finite dimensions. In the two previous Chapters, we did not compute the effective disorder in this way due to the strong finite-size effects that cloud the computation of the connected susceptibility, as we saw in Section 2.3 of Chapter 1 and in Section 2.3 of Chapter 2. As we already stressed when we presented Eq. (I.33), this result allows us to quantify the effective random field strength even in a system in which the latter is not present explicitly. For example, in the simple EPM description, the quenched disorder that is initially present as a result of the amorphous nature of the material does not a priori take the form of a random field coupled, say, to the local stress. Besides Eq. (I.33) and the ensuing necessary condition that there exists a nonzero disconnected susceptibility on top of the usual connected one, there are additional requirements to be satisfied before concluding to the presence of a random field:

- First, once a local order parameter is identified, the associated connected susceptibility which quantifies the linear response of this order parameter to an applied field must be strictly positive. The quantities appearing in the numerator and the denominator of Eq. (I.33) should indeed be describable as the variance of the local order parameter and the response of the average order parameter to a uniform field.
- Second, as will be illustrated below in the case of the AQS driven RFIM, the variation of $\Delta_{\text{eff}}(H)$ should be limited (at least away from the critical point) for the random-field description to be of any use.

In this section we perform the calculations to obtain an expression of the connected and disconnected susceptibilities. We start with the case of the RFIM, which is definitely simpler, and we briefly discuss the evolution of the effective disorder in this case. We then move to the EPM case, where more care is required. By changing the control parameter from γ to y and back we obtain an expression for the susceptibilities and, hence, for the effective disorder for this model as well.

2.1 Illustration for the RFIM

We first illustrate the outcome of Eq. (I.33) in the case of the AQS driven mean-field RFIM introduced in Section 1.2. To do so we have to compute the connected and the disconnected (magnetic) susceptibilities. The connected susceptibility can be simply expressed as the derivative of the average magnetization $m = \overline{m^\alpha}$ with respect to the applied field H. With

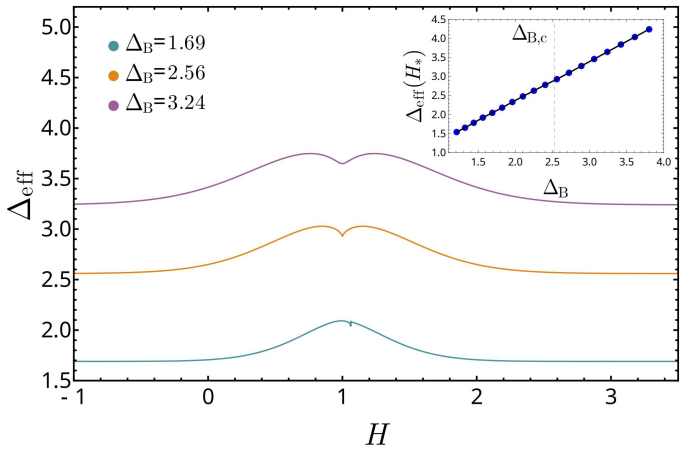

Figure 3.4: Variance of the renormalized random field $\Delta_{\rm eff}$ vs H for the mean-field AQS RFIM for different values of the bare variance Δ_B. Inset: $\Delta_{\rm eff}(H_*)$ vs Δ_B, where H_* is the location of the transition (critical or spinodal point) or of the maximum of the susceptibilities.

the help of 3.27, this leads to

$$\chi_{\rm conn}(H) = \frac{dm(H)}{dH} = \frac{1 + 2k\rho(H + Jm(H) - k)}{k - J - 2kJ\rho(H + Jm(H) - k)}, \tag{3.30}$$

where we choose for the random-field distribution $\rho(h)$ a Gaussian (centered on 0 and of variance Δ_B). We next compute the disconnected susceptibility, which requires a description of the sample-to-sample fluctuations and has not been calculated before. The disconnected susceptibility is defined by

$$\chi_{\rm disc}(H) = N\big[\overline{m^\alpha(H)^2} - \overline{m^\alpha(H)}^2\big], \tag{3.31}$$

which corresponds to Eq. (I.28) in the case of the mean-field RFIM. As standard for mean-field models, the calculation of all averaged quantities such as the mean magnetization and the connected susceptibility can be reduced to a saddle-point approximation in the thermodynamic limit where $N \to \infty$. To access the fluctuations,

$$\delta\widehat{m}^\alpha(H) = \sqrt{N}[m^\alpha(H) - m(H)], \tag{3.32}$$

one needs to consider terms beyond the saddle-point approximation. As detailed in Appendix C, this is easily performed, and one ends up with the following result for the disconnected susceptibility,

$$\chi_{\rm disc}(H) = \overline{\delta\widehat{m}^\alpha(H)^2} = \frac{\Big[\Delta_B + 4k^2 \int_{-H-Jm(H)+k}^{+\infty} dh\rho(h) \int_{-\infty}^{-H-Jm(H)+k} dh\rho(h) + 4k \int_{-H-Jm(H)+k}^{+\infty} dhh\rho(h)\Big]}{[k - J - 2kJ\rho(H + Jm(H) - k)]^2}. \tag{3.33}$$

From Eqs. (I.33), (3.30) and (3.33) one then obtains the variance of the renormalized

random field as

$$\Delta_{\text{eff}}(H) = \frac{\left[\Delta_B + 4k^2 \int_{-H-Jm(H)+k}^{+\infty} dh\rho(h) \int_{-\infty}^{-H-Jm(H)+k} dh\rho(h) + 4k \int_{-H-Jm(H)+k}^{+\infty} dhh\rho(h)\right]}{\left[1 + 2k\rho(H + Jm(H) - k)\right]^2}. \tag{3.34}$$

We plot the outcome of Eq. (3.34) in Fig. 3.4 for a range of values of Δ_B. The deterministic AQS dynamics clearly renormalizes the random field, whose variance is equal to the bare one only in the limits where $H \to \pm\infty$ and is otherwise larger than Δ_B. However, this renormalization is quantitatively very limited. The relative difference between $\Delta_{\text{eff}}(H)$ and Δ_B is indeed always less than 30%.

2.2 Susceptibilities in the mean-field EPM

The connected susceptibility, which is equal to the derivative of the averaged local stability (average distance to the local yield stress threshold) $m(\gamma) = \overline{\langle m^{\alpha,[\hat{x}]_M}(\gamma)\rangle_{[\hat{x}]_M}}$ with respect to the applied strain γ, is easily obtained from the results of Section 1.1 and [4]. It reads

$$\chi_{\text{con}}(\gamma) = m'(y(\gamma))y'(\gamma) = \frac{2\mu_2[-1+ < \hat{x} > P_{y(\gamma)}(0)]}{[1 - x_c P_{y(\gamma)}(0)]} \tag{3.35}$$

where $y(\gamma)$ is obtained by inverting Eq. (3.17) and we recall that a prime denotes a derivative with respect to the argument of the function. Note that we have defined the susceptibility such that it is negative when the derivative of the average stress-strain curve $\sigma'(\gamma)$ is positive (because $m = (1/N)\sum_i x_i = 1 - (1/N)\sum_i \sigma_i$). We now need to compute the disconnected susceptibility, which is associated with the sample-to-sample fluctuations,

$$\chi_{\text{dis}}(\gamma) = N\overline{\left\langle \left[m^{\alpha,[\hat{x}]_M}(\gamma) - m(\gamma)\right]^2 \right\rangle}_{[\hat{x}]_M}, \tag{3.36}$$

and is the central focus of the present chapter.

As already discussed, it is more convenient to first consider the quantity $m^{\alpha,[\hat{x}]_M}$ as a function of the control parameter y. However, we are interested in the fluctuations at fixed applied strain γ, and we therefore need to properly switch from the situation at fixed y to that at fixed γ. In the present mean-field model, we can introduce fluctuations as

$$\begin{aligned}
m^{\alpha,[\hat{x}]_M}(\gamma) &= m(\gamma) + \frac{1}{\sqrt{N}}\delta\widehat{m}^{\alpha,[\hat{x}]_M}(\gamma) \\
\widetilde{m}^{\alpha,[\hat{x}]_M}(y) &= \widetilde{m}(y) + \frac{1}{\sqrt{N}}\delta\widehat{\widetilde{m}}^{\alpha,[\hat{x}]_M}(y) \\
y^{\alpha,[\hat{x}]_M}(\gamma) &= y(\gamma) + \frac{1}{\sqrt{N}}\delta\widehat{y}^{\alpha,[\hat{x}]_M}(\gamma) \\
\gamma^{\alpha,[\hat{x}]_M}(y) &= \gamma(y) + \frac{1}{\sqrt{N}}\delta\widehat{\gamma}^{\alpha,[\hat{x}]_M}(y),
\end{aligned} \tag{3.37}$$

where we have momentarily added a tilde on the volume-averaged local stability m evaluated at fixed y. From the identity $m^\alpha(\gamma) = \widetilde{m}^\alpha(y^\alpha(\gamma))$, where to alleviate the notation we have

subsumed all of the disorder characterization $\alpha, [\hat{x}]_M$ in the single subscript α, we obtain the following relation:

$$\delta\widehat{m}^{\alpha}(\gamma) = \sqrt{N}\,[\widetilde{m}(y(\gamma) + \frac{1}{\sqrt{N}}\delta\widehat{y}^{\alpha}(\gamma)) - \widetilde{m}(y(\gamma))] + \delta\widehat{\widetilde{m}}^{\alpha}(y(\gamma) + \frac{1}{\sqrt{N}}\delta\widehat{y}^{\alpha}(\gamma)) = \widetilde{m}'(y(\gamma))\delta\widehat{y}^{\alpha}(\gamma) + \delta\widehat{\widetilde{m}}^{\alpha}(y(\gamma)) + \epsilon(1/N), \tag{3.38}$$

where $\epsilon(1/N) \to 0$ when $N \to \infty$. By applying the same procedure to the identities $y = y^{\alpha}(\gamma^{\alpha}(y))$ and $\gamma = \gamma^{\alpha}(y^{\alpha}(\gamma))$, we also find relations between the fluctuations of the two control parameters,

$$\begin{aligned} \gamma'(y(\gamma))\delta\widehat{y}^{\alpha}(\gamma) &= -\delta\widehat{\gamma}^{\alpha}(y(\gamma)) \\ y'(\gamma(y))\delta\widehat{\gamma}^{\alpha}(y) &= -\delta\widehat{y}^{\alpha}(\gamma(y)), \end{aligned} \tag{3.39}$$

in the limit where $N \to \infty$. We next consider the evolution with y of the volume-averaged local stability $\widetilde{m}^{\alpha,[\hat{x}]_M}(y)$, where we reinstall the full explicit dependence on the disorder (sample and history of random jumps). The infinitesimal variation between y and $y + dy$ is given by

$$d\widetilde{m}^{\alpha,[\hat{x}]_M}(y) = \frac{1}{N}\sum_{i=1}^{N}\Big[-dy\,[1-\theta(dy - x_i^{\alpha,[\hat{x}]_M}(y))] + [\hat{x}_i^{M+1} - x_i^{\alpha,[\hat{x}]_M}(y)]\,\theta(dy - x_i^{\alpha,[\hat{x}]_M}(y))\Big], \tag{3.40}$$

where the first term in the parentheses is the elastic contribution which decreases the local stabilities of the sites that do not yield by $-dy$ and the second is the plastic contribution that gives a jump $\hat{x}_i^{M+1}$ to each site i that becomes unstable. At order dy, the above equation gives

$$d\widetilde{m}^{\alpha,[\hat{x}]_M}(y) = -dy + \frac{1}{N}\sum_{i=1}^{N}\hat{x}_i^{M+1}\,\theta(dy - x_i^{\alpha,[\hat{x}]_M}(y)) = \frac{\mu_1}{\mu_2}dy - 2(\mu_1+\mu_2)d\gamma^{\alpha,[\hat{x}]_{M+1}}(y), \tag{3.41}$$

where the second line is obtained with the help of Eq. (3.2). After integrating from $y = 0$, this leads to

$$\widetilde{m}^{\alpha,[\hat{x}]_M}(y) = m^{\alpha}(0) + \frac{\mu_1}{\mu_2}y - 2(\mu_1+\mu_2)\gamma^{\alpha,[\hat{x}]_M}(y). \tag{3.42}$$

where the initial condition, $m^{\alpha}(0) = (1/N)\sum_i x_i^{\alpha}(0)$, only depends on the sample (and since $\sigma(0) = 0$, $m(0) = 1$). By combining Eqs. (3.37) and (3.38), and Eq. (3.42), one then obtains

$$\delta\widehat{m}^{\alpha,[\hat{x}]_M}(\gamma) = \delta\widehat{m}^{\alpha}(0) + \frac{\mu_1}{\mu_2}\delta\widehat{y}^{\alpha,[\hat{x}]_M}(\gamma), \tag{3.43}$$

so that the disconnected susceptibility can be cast as the sum of three terms,

$$\chi_{\rm dis}(\gamma) = \overline{< \delta\widehat{m}^{\alpha,[\hat{x}]_M}(\gamma)^2 >}_{[\hat{x}]_M} = \Delta_0 + \left(\frac{\mu_1}{\mu_2}\right)^2\overline{\langle\delta\widehat{y}^{\alpha,[\hat{x}]_M}(\gamma)^2\rangle}_{[\hat{x}]_M} + 2\left(\frac{\mu_1}{\mu_2}\right)\overline{\langle\delta\widehat{y}^{\alpha,[\hat{x}]_M}(\gamma)\delta\widehat{m}^{\alpha}(0)\rangle}_{[\hat{x}]_M}, \tag{3.44}$$

where

$$\Delta_0 = \overline{\delta\widehat{m}^{\alpha}(0)^2} = \overline{[x_i^{\alpha}(0)-1]^2} = \int_0^{\infty}dx(x-1)^2P_0(x) = \overline{[\sigma_i^{\alpha}(0)]^2} \tag{3.45}$$

is the variance of the initial sample-to-sample distribution of the local stability (and of the local stress as well) and we have used the fact that initially there are no correlations from site to site.

The calculations of the two nontrivial terms in Eq. (3.44) are rather unwieldy and are detailed in Appendix C. The final expressions read

$$\begin{aligned}
&\left(\frac{\mu_1}{\mu_2}\right)^2 \overline{\langle \delta\widehat{y}^{\alpha,[\hat{x}]_M}(\gamma)^2\rangle}_{[\hat{x}]_M} = \\
&\left(\frac{\mu_1}{2\mu_2(\mu_1+\mu_2)\gamma'(y(\gamma))}\right)^2 \Big(< \hat{x}^2 > \int_0^{y(\gamma)} dy' P_{y'}(0) - < \hat{x} >^2 \left(\int_0^{y(\gamma)} dy' P_{y'}(0)\right)^2 \\
&+ 2 < \hat{x} > \int_0^{y(\gamma)} dy' P_{y'}(0) \int_{y'}^{y(\gamma)} dy'' \Big[g(0)[< \hat{x} > -T(y''-y')] - T'(y''-y') \\
&+ \int_0^{y''-y'} d\widehat{y}[< \hat{x} > -T(\widehat{y})] R_{y''-y'-\widehat{y}}(0)\Big]\Big)
\end{aligned} \tag{3.46}$$

where $T(x) = \int_x^\infty d\hat{x}\hat{x}g(\hat{x})$, and

$$\begin{aligned}
&2\left(\frac{\mu_1}{\mu_2}\right) \overline{\langle \delta\widehat{y}^{\alpha,[\hat{x}]_M}(\gamma)\delta\widehat{m}^{\alpha}(0)\rangle}_{[\hat{x}]_M} = \frac{\mu_1 < \hat{x} >}{\mu_2(\mu_1+\mu_2)\gamma'(y(\gamma))} \int_0^{y(\gamma)} dy' \Big[(y'-1)P_0(y') \\
&+ g(0)\int_0^{y'} dy''(y''-1)P_0(y'') + \int_0^{y'} dy''\, R_{y'-y''}(0) \int_0^{y''} d\widehat{y}(\widehat{y}-1)P_0(\widehat{y})\Big],
\end{aligned} \tag{3.47}$$

where $P_y(x)$ and $R_y(x)$ are solutions of Eqs. (3.12) and (3.13). By putting all of the above equations together we obtain the expression for the disconnected susceptibility that we were looking for.

One can check that for $\gamma = 0$, the terms in Eq. (3.46) and Eq. (3.47) go to 0 (as $y(\gamma = 0) = 0$), so that, as expected, the disconnected susceptibility at the beginning of the deformation reduces to the fluctuations associated with the initial distribution of local stresses, $\chi_{\text{disc}}(0) = \Delta_0$. It is also instructive to study the limiting form of the disconnected susceptibility when $\gamma, y \to \infty$, which corresponds to the stationary state. Then, from Eqs. (3.12) and (3.13), one finds that $R_\infty(x) = 0$ and $P_\infty(x) = 1/ < \hat{x} > \int_x^\infty g(x')dx'$. After some lengthy algebra, the disconnected susceptibility in the stationary state can be simply expressed as

$$\begin{aligned}
\chi_{\text{dis}}(\gamma \to \infty) &= < x^2 >_\infty - < x >_\infty^2 \\
&= \frac{< \hat{x}^3 >}{3 < \hat{x} >} - \frac{< \hat{x}^2 >^2}{4 < \hat{x} >^2},
\end{aligned} \tag{3.48}$$

where we have defined $< x^n >_\infty = \int_0^\infty dx P_\infty(x) x^n$. As expected, this expression does not depend on the initial condition. Both the connected and the disconnected susceptibilities diverge at the yielding transition, corresponding either to a mean-field spinodal point or a critical point (see below). For a range of continuous, ductile, behavior the susceptibilities go through a local maximum at a finite, nonzero value of the strain γ. One can easily check that the locations of the maxima are not exactly the same for the two susceptibilities but asymptotically converge to the same value when the connected susceptibility becomes very large.

3 Results for the mean-field EPM

As we emphasized when introducing them, EPMs account for the disorder associated with the structure of the amorphous solid at the beginning of the deformation process through a distribution of initial local stresses (or stabilities), which we call $P_0(x)$, a distribution of local thresholds, which we take here as a delta-function $\delta(\sigma^{th}-1)$, and a distribution of stress jumps after local yielding, which we have introduced here as $g(\hat{x})$. Much more complicated schemes can be envisaged in order to reproduce more realistic details of the deformation of amorphous solids. For example, the distributions of local thresholds and of stress jumps after a plastic event could evolve during the dynamics, mimicking the softening observed in MD simulations [156]. We stress once again that, while in the EPM we describe these sources of noise as different and unrelated, in the more realistic MD simulations they all originate from the initial configuration of the glass. In this section we discuss what is the role of these various types of disorder and how do they conspire to generate an emergent random field. We start by showing how the different sources of disorder affect the resulting average stress-vs-strain curve. We check that not only the initial disorder, but also the one related to the stress jumps can change the behavior from brittle to ductile.

3.1 Stress-vs-strain curves and the role of various types of disorder

We first address the role of the various types of disorder (mainly, random initial stresses and random stress jumps) on the averaged stress-strain curves for the mean-field EPM that we have analyzed in the previous sections. We consider three different distributions of the local random jumps,

$$\begin{aligned} g(\hat{x}) &= \frac{e^{-\frac{x}{<\hat{x}>}}}{<\hat{x}>}, \\ g(\hat{x}) &= \frac{e^{-\frac{x}{t}}-e^{-\frac{x}{<\hat{x}>-t}}}{2t-<\hat{x}>}, \text{ with } t\in]\frac{<\hat{x}>}{2},<\hat{x}>[, \\ g(\hat{x}) &= \delta(x-<\hat{x}>), \end{aligned} \tag{3.49}$$

all with the same average value $<\hat{x}>$. In addition we consider two different distributions of the initial local stresses or stabilities,

$$\begin{aligned} P_0(x) &= \frac{e^{-\frac{x}{A}}-e^{-\frac{x}{1-A}}}{2A-1}, \text{ with } A\in]\frac{1}{2},1[, \\ P_0(x) &= \frac{1}{\sqrt{2\pi\Delta_0}}e^{-\frac{(x-1)^2}{2\Delta_0}}. \end{aligned} \tag{3.50}$$

They both satisfy $<x>_0=1$, implying $<\sigma>_0=0$, as well as the requirement of plastic stability, $P_0(0)=0$. (In the case of the Gaussian the latter requirement is only approximately satisfied but, since we use small values of Δ_0, $P_0(0)$ is then negligible; we also tried a truncated Gaussian which exactly enforces the condition in $x=0$ but we found virtually no difference with the results obtained with the full Gaussian.) The initial variance is given by $<x^2>_0-<x>_0^2=\Delta_0$. For the combination of two exponentials, $\Delta_0=1-2A(1-A)$ with $1/2<A<1$. For all of the above cases deriving the analytical formulas for $\sigma(\gamma)$ is quite involved and the details are given in Appendix C.

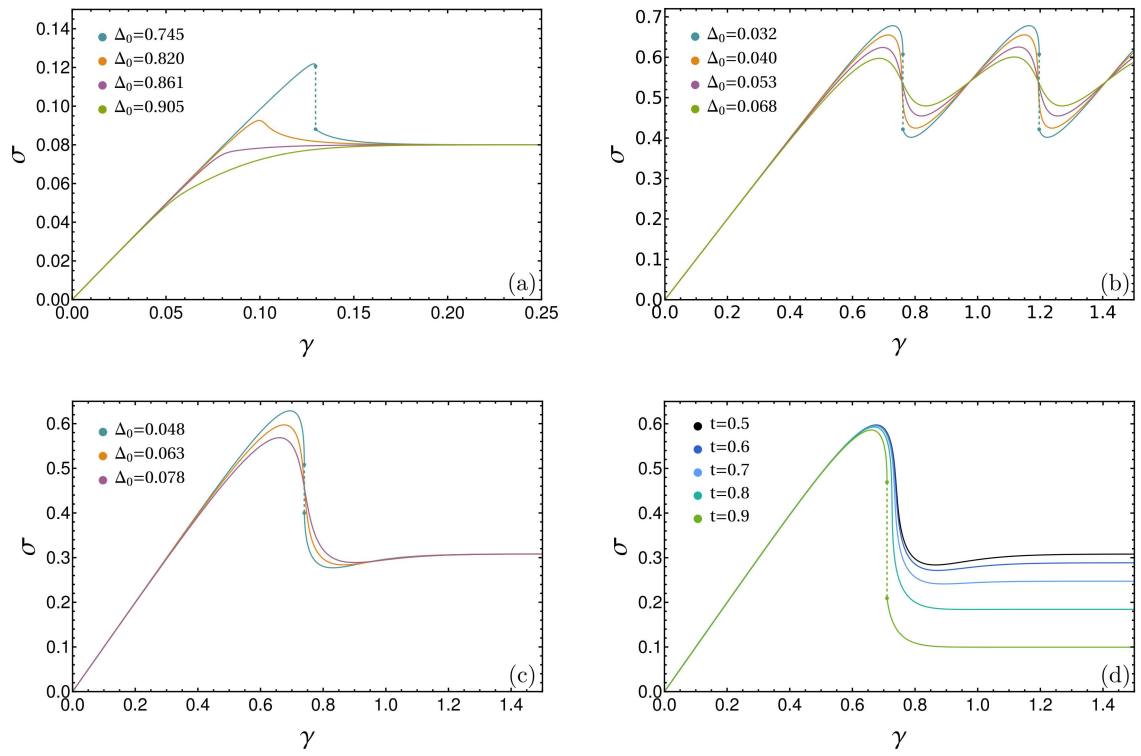

Figure 3.5: Average stress σ versus strain γ for the MF-EPM with different distributions of the local random jumps $g(\hat{x})$ (see Eq. (3.49)) and different distributions of the initial local stresses $P_0(x)$ (see Eq. (3.50)). (a): $P_0(x)$ is a 2-exponential combination and $g(\hat{x})$ is a single exponential; curves are shown for several values of the initial disorder variance Δ_0. (b-d): $P_0(x)$ is a Gaussian and $g(\hat{x})$ is either a delta function (no randomness) in (b), a 2-exponential combination at fixed $t = 0.5$ and several values of Δ_0 in (c), or a 2-exponential combination at fixed $\Delta_0 = 0.25$ and several values of t in (d). In all cases, $2\mu_2 = 1$ and $< \hat{x} >= 0.92$. When $P_0(x)$ is the combination of 2 exponentials, $\mu_1 = 0.0222\mu_2$, while in the Gaussian case we chose $\mu_1 = 0.9\mu_2$ in order to see both ductile and brittle behavior.

In Fig. 3.5 we display the averaged stress-strain curve for several combinations of the above cases and for several values of the initial variance Δ_0. As we did for the finite dimensional case, we look at the curves by considering three different domains of deformation: (i) small deformation, $\gamma \ll 1$, (ii) stationary state, $\gamma \gg 1$, which should physically correspond to the "flowing state" of the sheared material when the average stress stays constant and equal to the macroscopic yield stress, and (iii) the region of the overshoot and of the yielding transition, when present. In region (i) at very small deformation, the response is purely elastic and $\sigma(\gamma) \approx 2\mu_2\gamma$, irrespective of the disorder type and strength. Region (ii) is obviously very different when there is randomness in the local jumps and where there is none (as in panel (b)). In the former case, a bona fide steady state with an essentially constant stress is reached, with

$$\sigma(\gamma \to \infty) = 1 - \frac{< \hat{x}^2 >}{2 < \hat{x} >}. \tag{3.51}$$

This expression is independent of the initial distribution $P_0(x)$, as it should. Notice that in this case we do not need to discuss force balance issues, which could affect the steady-state value in the finite-dimensional case. For a single exponential, the asymptotic value $\sigma(\gamma \to \infty)$ is simply equal to $1- < \hat{x} >$, but for a combination of two exponentials, $< \hat{x}^2 >$ is in general different from $2 < \hat{x} >^2$ and one can change the steady-state stress for a given $< \hat{x} >$ by varying the parameter t, as illustrated in Fig. 3.5(d). On the other hand, in the absence of randomness in the jumps, $\sigma(\gamma)$ is a periodic function at large deformation (of period $\hat{x}\mu_1/[(2\mu_2)(\mu_1 + \mu_2)]$ when $y \gg 1$, as shown in Appendix C) and it does not reach a physically acceptable steady state (see Fig. 3.5(b)). Region (iii) is the one of most interest for our present purpose of investigating an emergent potential random field. One can see from Fig. 3.5 (and confirm by a direct analysis of the expressions in Appendix C) that the same sequence of behavior is observed for all distributions. As Δ_0 decreases the behavior passes through a regime with an overshoot and a continuous evolution to finally reach a "brittle" regime with a discontinuity in the stress. The brittle and the continuous regimes are separated by a critical point [4]. Of course, the quantitative details vary from one distribution to another but the pattern is the same.

We illustrate the quantitative differences in Fig. 3.6 by plotting the location at which the stress is maximum, denoted by $\gamma_{\max}$, and that at which the slope of the stress-strain curve (i.e., the connected susceptibility) is negative and maximum, γ_y, for several models. The latter corresponds to either a spinodal point or the critical point when the slope is infinite. (When the slope is not infinite but a local maximum still exists in the susceptibilities, we keep the notation γ_y for the maximum of the connected susceptibility; the maximum of the disconnected susceptibility $\gamma_y^{\rm dis}$ slightly deviates from γ_y as one moves away from the critical point in the ductile region, as seen from the insets in Fig. 3.6.) Note that the maximum stress (overshoot) and the maximum negative slope disappear for a large initial disorder Δ_0 when the stress-strain curve is monotonic.

We also display in Fig. 3.7 the variation of the critical value of the initial variance, $\Delta_{0,c}$, as a function of the parameter t in the 2-exponential distribution of random jumps (see Eq. (3.49)). Region (iii) is where the analogy with an AQS driven RFIM may hold. It is clear however that the quantitative aspects and, as we will see below, the strength of the effective random field depend on the details of the disorder distributions. Before delving more into this issue, we consider the effect of the disorder distributions on the connected and disconnected susceptibilities computed in Section 2.2.

3.2 Connected and disconnected susceptibilities

We now discuss the results for the connected and disconnected susceptibilities in the mean-field EPM. Their expressions have been given above and are more explicitly derived in C. We again illustrate the results for the three different distributions of the local random jumps and the two distributions of initial local stresses considered above. The connected susceptibility $\chi_{\rm conn}(\gamma)$ is shown in Fig. 3.8 and the disconnected susceptibility in Fig. 3.9, both for several values of the initial disorder variance Δ_0. Because it is defined as the opposite of the derivative of the stress-strain curve $\sigma(\gamma)$ (see above), the connected susceptibility is negative and equal to $-2\mu_2$ at small strain, goes through 0 when there is an overshoot, is maximum in region (iii) previously defined, and goes to zero at large strain; it then approaches zero either from above or, when there is a local minimum in the stress-strain curve, from below

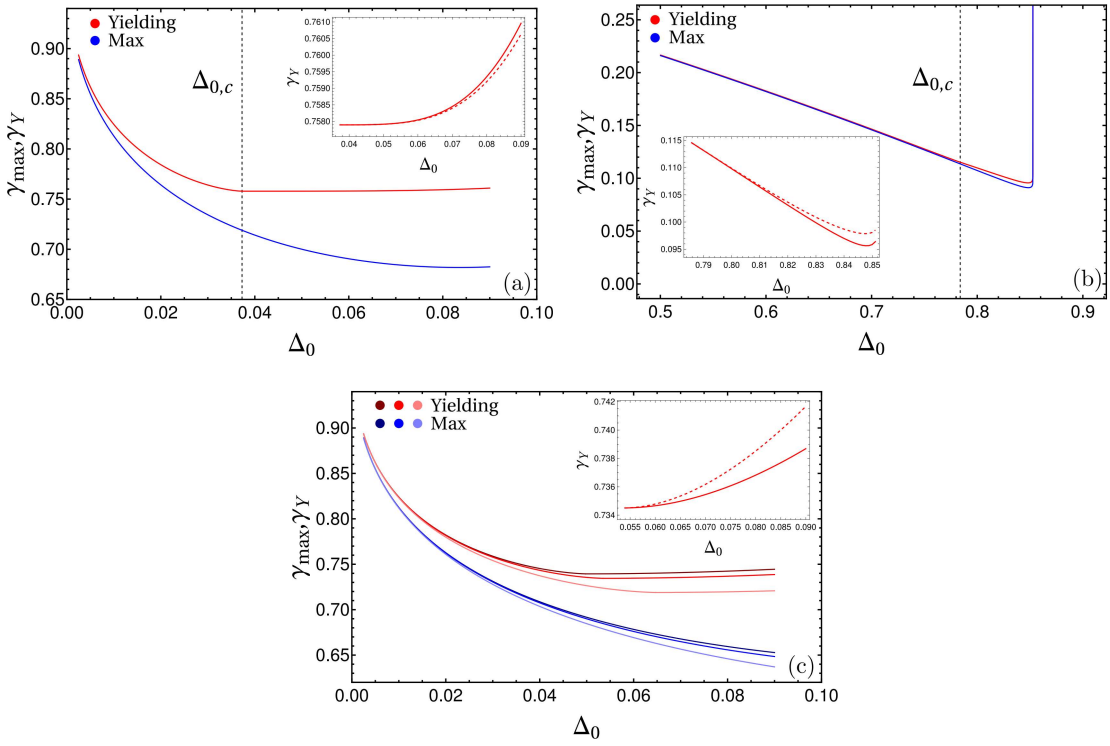

Figure 3.6: (a): Location of the overshoot $\gamma_{\max}$ and of the yielding transition and/or the local maximum of the connected susceptibility $\gamma_{\rm y}$ versus the initial disorder variance Δ_0 for the mean-field EPM. (a) Gaussian initial distribution of the initial local stresses and no random jumps. (b): Combination of two exponentials for the initial local stresses and single-exponential distribution of random jumps. In both cases the vertical dashed line marks the critical value of the bare disorder. (c): Dependence on the parameter t when the distribution of random jumps is the 2-exponential combination and the initial distribution $P_0(x)$ is a Gaussian; from top to bottom: $t = 0.5, 0.7, 0.85$. Insets: Comparison of the location of the maxima of the connected susceptibility $\gamma_{\rm y}$ (full line) and the disconnected susceptibility $\gamma_{\rm y}^{\rm dis}$ (dashed line). In (c), $t = 0.7$. One can show that the divergence of $\gamma_{\max}$ in (b) goes as $\gamma_{\max} \sim \log(1/(< \hat{x} > -A))$.

after passing first through 0 at a finite strain (see Fig. 3.8(c,d)). In the case where there is no randomness in the jumps Fig. 3.8(b)), the curve is periodic and the steady state is not physical.

The disconnected susceptibility is always positive. It starts from Δ_0 at small strain, is maximum in region (iii), and goes to a positive value equal to the variance of the random jumps $< \hat{x}^2 > - < \hat{x} >^2$, either from above or from below. Again, in the case where there is no randomness in the jumps Fig. 3.9(b)), the curve is periodic.

When there is a bona fide yielding transition, either discontinuous or critical, the two susceptibilities diverge. The divergence at the spinodal, which is the onset of the discontinuous jump in the average stress, is a consequence of the mean-field character of the model

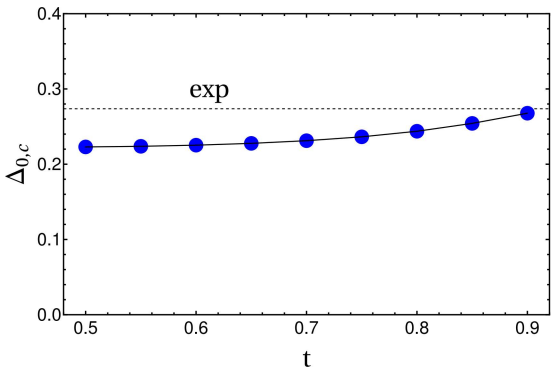

Figure 3.7: Critical value of the initial variance of the local stresses, $\Delta_{0,c}$, as a function of the parameter t that appears in the distribution of random jumps (see Eq. (3.49)). The initial distribution $P_0(x)$ is a Gaussian. The dashed line is the value $\Delta_{0,c} = 0.273677$ obtained for the case of a single-exponential distribution of random jumps: it is reached when $t =< \hat{x} >= 0.92$.

and can be expressed, e.g., as a function of the initial disorder variance Δ_0, as

$$\begin{aligned} \chi_{\rm conn}(\gamma;\Delta_0) &\sim (\gamma_{\rm y,c}-\gamma)^{-\frac{1}{2}}, \\ \chi_{\rm disc}(\gamma;\Delta_0) &\sim (\gamma_{\rm y,c}-\gamma)^{-1}, \end{aligned} \tag{3.52}$$

when $\gamma \to \gamma_{\rm y,c}^-$ for $\Delta_0 < \Delta_{0,c}$. In the vicinity of the critical point at $\Delta_0 = \Delta_{0,c}$, the susceptibilities can be described by scaling forms,

$$\begin{aligned} \chi_{\rm conn}(\gamma;\Delta_0) &= |r|^{-(\beta\delta-\beta)}\mathcal{F}_{\rm conn,\pm}(\frac{h}{|r|^{\beta\delta}}), \\ \chi_{\rm disc}(\gamma;\Delta_0) &= |r|^{-2(\beta\delta-\beta)}\mathcal{F}_{\rm disc,\pm}(\frac{h}{|r|^{\beta\delta}}) \end{aligned} \tag{3.53}$$

where $r = (\Delta_0 - \Delta_{0,c})/\Delta_{0,c}$ and $h = (\gamma - \gamma_{\rm y,c})/\gamma_{\rm y,c}$, and the exponents have their classical values, $\beta = 1/2$ and $\delta = 3$, hence $\beta\delta - \beta = 1$. The scaling functions are different above and below the critical strain $\gamma_{\rm y}$ and are simply given by the smallest real root of cubic equations, just as in the mean-field RFIM [10]. These scaling forms are illustrated in Fig. 3.10. The fact that the exponent of the divergence of the disconnected susceptibility is twice that of the divergence of the connected susceptibility, either at the mean-field spinodal or at criticality, is a property that is characteristic of the mean-field RFIM and indicates the presence of an emerging random field at yielding. An additional signature of RFIM physics, also found in sample-to-sample fluctuations, is provided by the study of the size distribution of the avalanches (i.e., stress drops) present in the mean-field EPM. As shown in [4, 159], the distributions both at the critical and the spinodal points coincide with those of the mean-field RFIM [10].

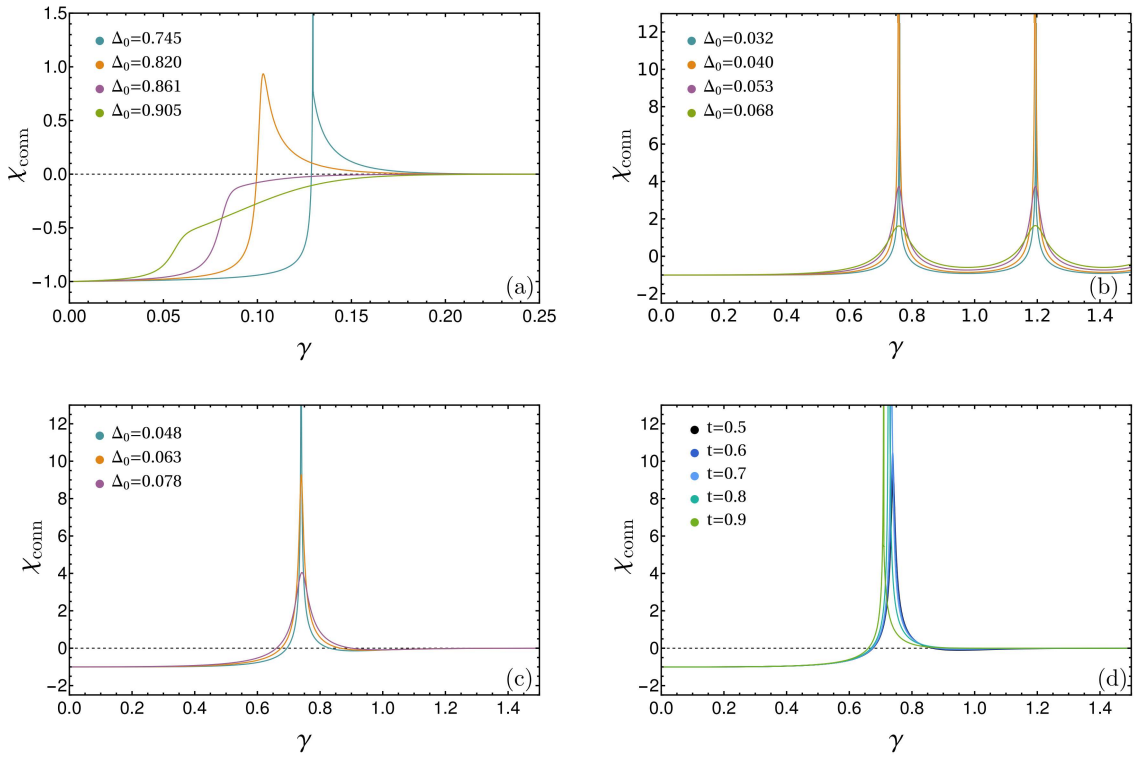

Figure 3.8: Connected susceptibility $\chi_{\rm conn}(\gamma)$ for the MF-EPM with different distributions of the local random jumps $g(\hat{x})$ (see Eq. (3.49)) and different distributions of the initial local stresses $P_0(x)$ (see Eq. (3.50)). (a): $P_0(x)$ is a 2-exponential combination and $g(\hat{x})$ is a single exponential; curves are shown for several values of the initial disorder variance Δ_0. (b-d): $P_0(x)$ is a Gaussian and $g(\hat{x})$ is either a delta function (no randomness) in (b), a 2-exponential combination at fixed $t = 0.5$ and several values of Δ_0 in (c), or a 2-exponential combination at fixed $\Delta_0 = 0.25$ and several values of t in (d). In all cases, $2\mu_2 = 1$ and $< \hat{x} >= 0.92$. When $P_0(x)$ is the combination of 2 exponentials, $\mu_1 = 0.0222\mu_2$, while in the Gaussian case we chose $\mu_1 = 0.9\mu_2$ in order to see both ductile and brittle behavior.

3.3 Strength of the effective random field

Having computed the connected and disconnected susceptibilities for the mean-field EPM we can obtain the strength of the effective random field from I.33, which here reads

$$\Delta_{\rm eff}(\gamma) = \frac{\chi_{\rm disc}(\gamma)}{\chi_{\rm conn}(\gamma)^2}\,. \tag{3.54}$$

We have already stressed that for the mean-field EPM, it is the yielding transition which is in the universality class of the (mean-field) RFIM. As a result, one expects the above expression to be valid only in the region where yielding takes place, i.e., in a region where the connected susceptibility is positive and is large. Actually, Eq. (3.54) predicts that $\Delta_{\rm eff}$ diverges at a local maximum (overshoot) or minimum of the stress-strain curve, which has no physical meaning. The random field is an emergent property that results from the disorder present in the system (random initial local stresses, random local thresholds, random local

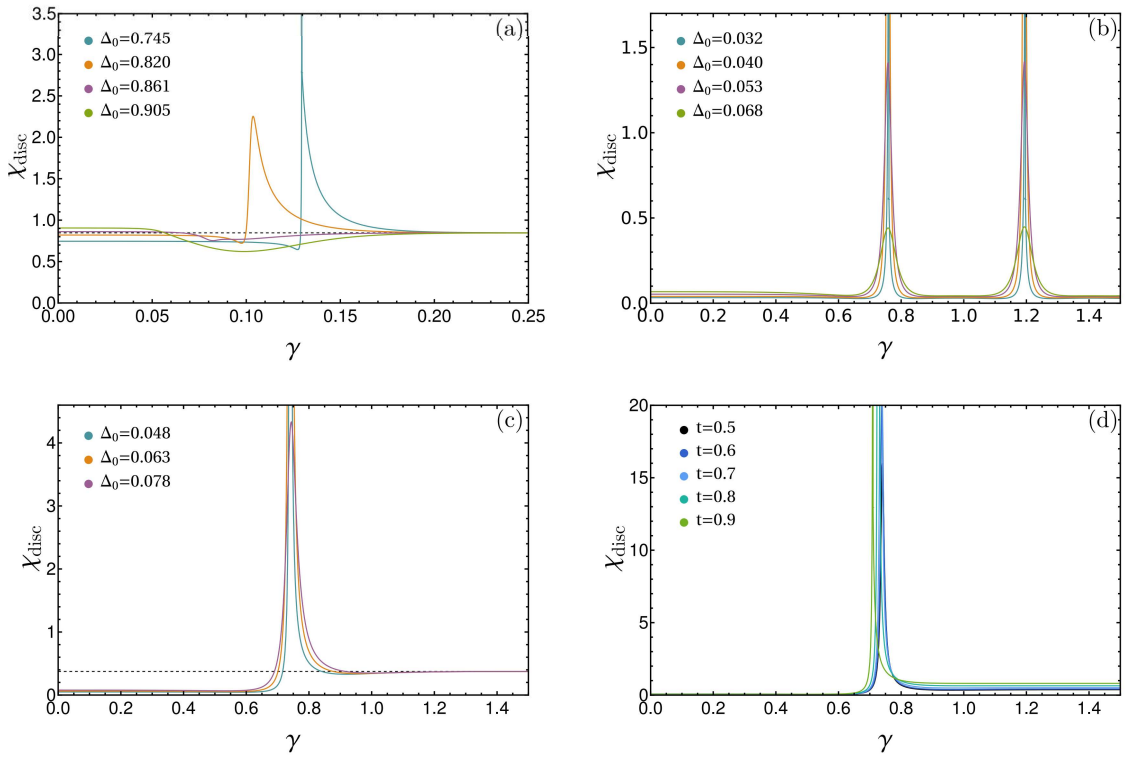

Figure 3.9: Disconnected susceptibility $\chi_{\rm dis}(\gamma)$ for the MF-EPM with different distributions of the local random jumps $g(\hat{x})$ (see Eq. (3.49)) and different distributions of the initial local stresses $P_0(x)$ (see Eq. (3.50)). (a): $P_0(x)$ is a 2-exponential combination and $g(\hat{x})$ is a single exponential; curves are shown for several values of the initial disorder variance Δ_0. (b-d): $P_0(x)$ is a Gaussian and $g(\hat{x})$ is either a delta function (no randomness) in (b), a 2-exponential combination at fixed $t = 0.5$ and several values of Δ_0 in (c), or a 2-exponential combination at fixed $\Delta_0 = 0.25$ and several values of t in (d). In all cases, $2\mu_2 = 1$ and $< \hat{x} >= 0.92$. When $P_0(x)$ is the combination of 2 exponentials, $\mu_1 = 0.0222\mu_2$, while in the Gaussian case we chose $\mu_1 = 0.9\mu_2$ in order to see both ductile and brittle behavior.

jumps) but only appears in the region of deformation around yielding. From Eqs. (3.35), (3.44) and (3.46) we obtain that when $\chi_{\rm conn}(\gamma), \chi_{\rm disc}(\gamma) \gg 1$,

$$\Delta_{\rm eff}(\gamma) \approx \left(\frac{\mu_1}{2\mu_2(\mu_1+\mu_2)[1- < \hat{x} > P_{y(\gamma)}(0)]} \right)^2 \Big(\mathcal{A}_1(y(\gamma)) + \mathcal{A}_2(y(\gamma)) + \mathcal{A}_3(y(\gamma)) \Big), \quad (3.55)$$

with

$$\begin{aligned} \mathcal{A}_1(y) &= < \hat{x}^2 > \int_0^y dy' P_{y'}(0) - < \hat{x} >^2 \left(\int_0^y dy' P_{y'}(0) \right)^2, \\ \mathcal{A}_2(y) &= 2 < \hat{x} > \int_0^y dy' P_{y'}(0) \int_{y'}^y dy'' g(0)(< \hat{x} > -T(y''-y')) - T'(y''-y'), \\ \mathcal{A}_3(y) &= 2 < \hat{x} > \int_0^y dy' P_{y'}(0) \int_{y'}^y dy'' \int_0^{y''-y'} d\hat{y}(< \hat{x} > -T(\hat{y})) R'_{y''-y'-\hat{y}}(0), \end{aligned} \quad (3.56)$$

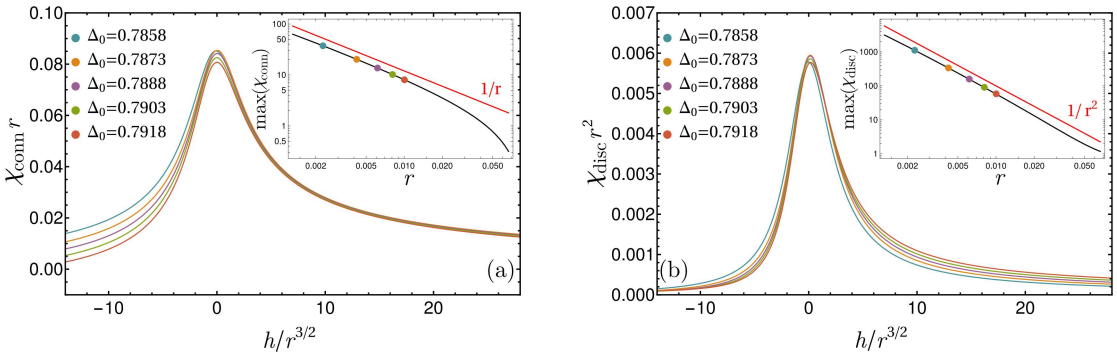

Figure 3.10: Collapse of the rescaled connected susceptibility $\chi_{\rm conn}(\gamma;\Delta_0)r$ (a) and rescaled disconnected susceptibility $\chi_{\rm disc}(\gamma;\Delta_0)r^2$ (b) versus $h/r^{3/2}$, with $r=[(\Delta_0-\Delta_{0,c})/\Delta_{0,c}]$ and $h=(\gamma-\gamma_{\rm y})/\gamma_{\rm y}$, for the MF-EPM in the vicinity of the critical yielding transition at $\Delta_{0,c}$. (Here, $\gamma_{\rm y}$ is taken as the maximum of the connected (a) or disconnected (b) susceptibility, but the two maxima are extremely close to $\gamma_{\rm y,c}$ in the vicinity of the critical point.). The insets show the scaling of the maxima of the susceptibilities with r as $r\to 0$. The distribution of the local random stresses is the linear combination of two exponentials and that of the random jumps is the single-exponential one (then, $\Delta_{0,c}=0.78388$). Note that the collapse is not perfect but, as suggested in [131] for the mean-field RFIM, could likely be improved by using a rotated scaling variable of the form $h'=h+br$.

and where, as defined before, $T(x)=\int_x^\infty d\hat{x}\hat{x}g(\hat{x})$, and the functions $P_y(0)$ and $R_y(0)$ have been introduced in Section 1.1.

We illustrate in Fig. 3.11 the behavior of $\Delta_{\rm eff}(\gamma)$ in the yielding region (region (iii)) for the three choices of random-jump distribution and the two choices of initial local-stress distribution, for several values of the initial disorder variance Δ_0. We see that the effective variance increases very rapidly for a given value of the initial disorder Δ_0 when one moves away from $\gamma_{\rm y}$ (which is either the location of the yielding transition when the susceptibilities diverges or the location of the local maximum of the connected susceptibility when the susceptibilities do not diverge). The region of interest where $\Delta_{\rm eff}$ changes by less than a factor of, say, 2 is very narrow around $\gamma_{\rm y}$. This results from the emergent character of the random field near yielding, for which the underlying random-field strength that incorporates the whole history of the system depends on the deformation. It is quite different than the behavior of the RFIM shown in Fig. 3.4 in which the effective random-field strength does not vary much.

We plot in Fig. 3.12(a-c) the effective random-field variance as a function of the initial disorder variance Δ_0 for both $\gamma=\gamma_{\rm y}$, the maximum of the connected susceptibility, and $\gamma=\gamma_{\rm y}^{\Delta}$, the extremum (minimum) of $\Delta_{\rm eff}(\gamma)$. Note first that the two locations $\gamma_{\rm y}^{\Delta}$ and $\gamma_{\rm y}$ are identical when there is a bona fide yielding transition and are otherwise very close, as a result of the proximity of the maxima of the connected and disconnected susceptibilities (insets of Fig. 3.6): in consequence, there is virtually no difference in the values of the effective random-field strength evaluated at the two locations. We observe that $\Delta_{\rm eff}(\gamma_{\rm y}$ or $\gamma_{\rm y}^{\Delta})$ monotonically increases with Δ_0. As physically expected, it also increases as yielding changes

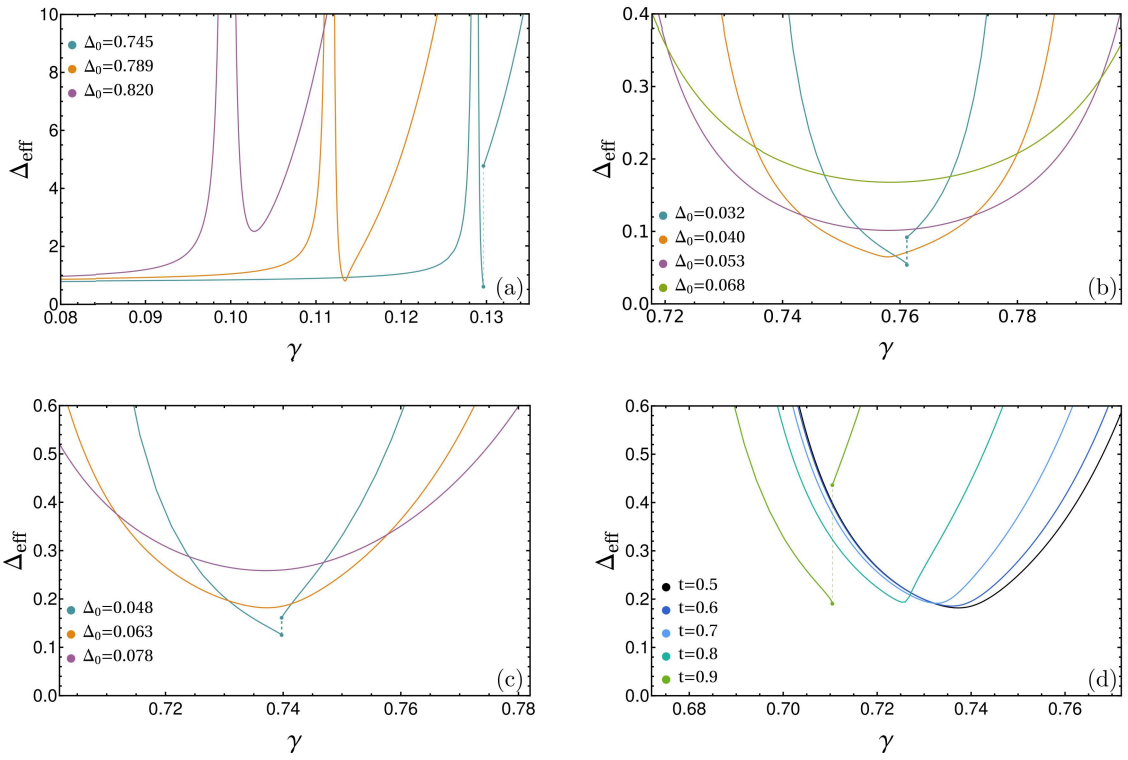

Figure 3.11: Effective random-field strength $\Delta_{\text{eff}}(\gamma)$ for the MF-EPM in the region of the yielding transition where the connected susceptibility $\chi_{\text{con}}(\gamma) \gg 1$. As in previous figures, different distributions of the local random jumps $g(\hat{x})$ (see Eq. (3.49)) and different distributions of the initial local stresses $P_0(x)$ (see Eq. (3.50)) are considered. (a): $P_0(x)$ is a 2-exponential combination and $g(\hat{x})$ is a single exponential; curves are shown for several values of the initial disorder variance Δ_0. (b-d): $P_0(x)$ is a Gaussian and $g(\hat{x})$ is either a delta function (no randomness) in (b), a 2-exponential combination at fixed $t = 0.5$ and several values of Δ_0 in (c), or a 2-exponential combination at fixed $\Delta_0 = 0.25$ and several values of t in (d). In all cases, $2\mu_2 = 1$ and $< \hat{x} >= 0.92$. When $P_0(x)$ is the combination of 2 exponentials, $\mu_1 = 0.0222\mu_2$, while in the Gaussian case we chose $\mu_1 = 0.9\mu_2$ in order to see both ductile and brittle behavior.

from discontinuous to continuous, a discontinuous transition requiring a smaller effective random-field strength, just like in the RFIM. One can also see that $\Delta_{\text{eff}}(\gamma_{\text{y}}$ or $\gamma_{\text{y}}^{\Delta})$ is not a unique function of Δ_0 and is sensitive to the various kinds of disorder present in the EPM: although qualitatively similar, the curves in (a), (b) and (c) are quantitatively different. In addition, Fig. 3.12(d) illustrates the variation of $\Delta_{\text{eff}}(\gamma_{\text{y}}$ or $\gamma_{\text{y}}^{\Delta})$ with the parameter t of the random jump distribution for the same given value of Δ_0. The parameter t has a small but noticeable effect on the effective random-field strength. (At the same time, changing t has a strong influence on the steady state, as can be seen from Fig. 3.5(d).) Note that the variation with t is nonmonotonic but, in the immediate vicinity of the critical point t_c, one again finds that the brittle side of yielding ($t > t_c$) corresponds to smaller values of $\Delta_{\text{eff}}(\gamma_{\text{y}}$ or $\gamma_{\text{y}}^{\Delta})$ than the ductile side ($t < t_c$).

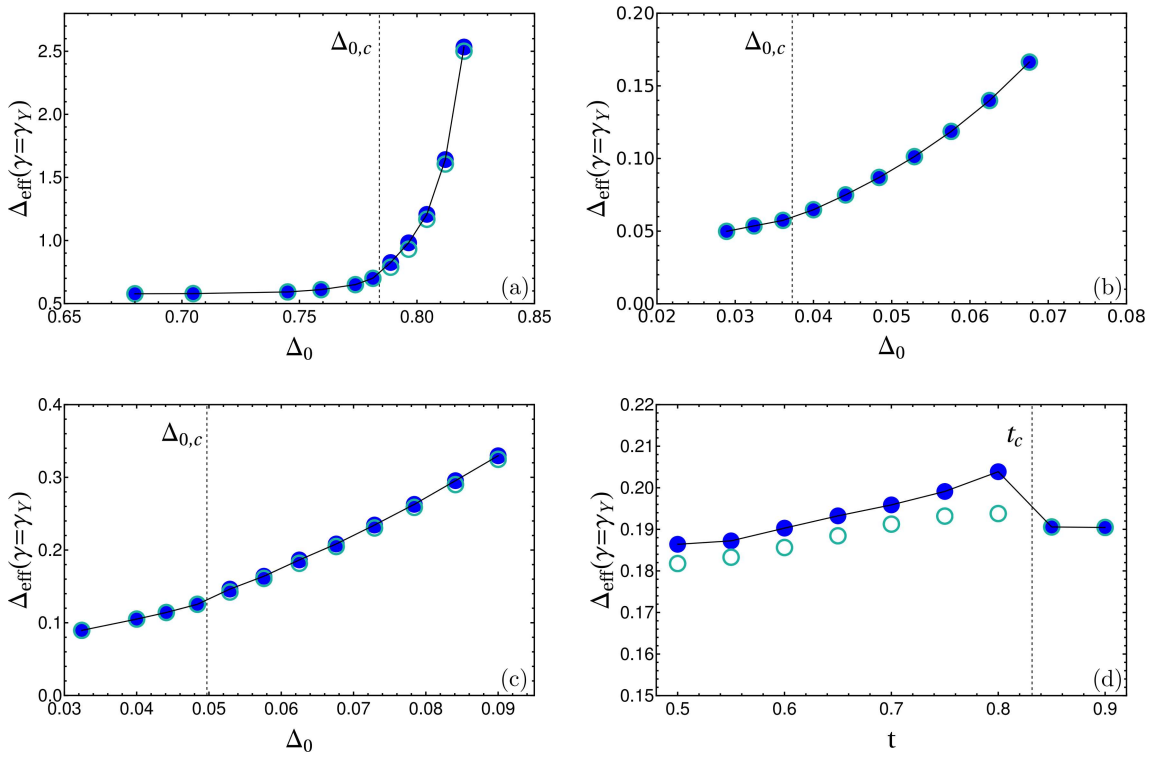

Figure 3.12: Variation of the effective random-field variance $\Delta_{\rm eff}(\gamma)$ for $\gamma = \gamma_{\rm y}$ (filled symbols and full line), at which the connected susceptibility diverges or/and is maximum, and for $\gamma = \gamma_{\rm y}^{\Delta}$ (open symbols), the value at which $\Delta_{\rm eff}(\gamma)$ is minimum. We consider the same distributions of the local random jumps $g(\hat{x})$ and of the initial local stresses $P_0(x)$ as in the previous figures. (a): $P_0(x)$ is a 2-exponential combination and $g(\hat{x})$ is a single exponential; curves are shown for several values of the initial disorder variance Δ_0. (b-d): $P_0(x)$ is a Gaussian and $g(\hat{x})$ is either a delta function (no randomness) in (b), a 2-exponential combination at fixed $t = 0.5$ and several values of Δ_0 in (c), or a 2-exponential combination at fixed $\Delta_0 = 0.25$ and several values of t in (d). In (b) the evolution is periodic and we only consider the first yielding region. In this case $\gamma_{\rm y}^{\Delta} = \gamma_{\rm y}$ over the range shown in the plot and the filled and open symbols exactly coincide. In (a-c) the vertical dashed line marks the critical value of the bare disorder.

To further evince the fact that the emerging random field is not fixed once for all in the initial distribution but also arises from the history of the deformation, e.g., through the sequence of random jumps associated with local plastic events, we consider two different ways of computing $\Delta_{\rm eff}(\gamma)$: one in which the sample-to-sample fluctuations are calculated via a "quenched" average over the random jumps (this is the calculation done up to now) and one in which we perform an "annealed" average over the random jumps, i.e.,

$$\chi_{\rm disc}^{\rm ann}(\gamma) = N\overline{\left[\left\langle m^{\alpha,[\hat{x}]_M}(\gamma)\right\rangle_{[\hat{x}]_M} - \overline{\left\langle m^{\alpha,[\hat{x}]_M}(\gamma)\right\rangle_{[\hat{x}]_M}}\right]^2}. \tag{3.57}$$

Note that by construction the connected susceptibility is not affected by the change of

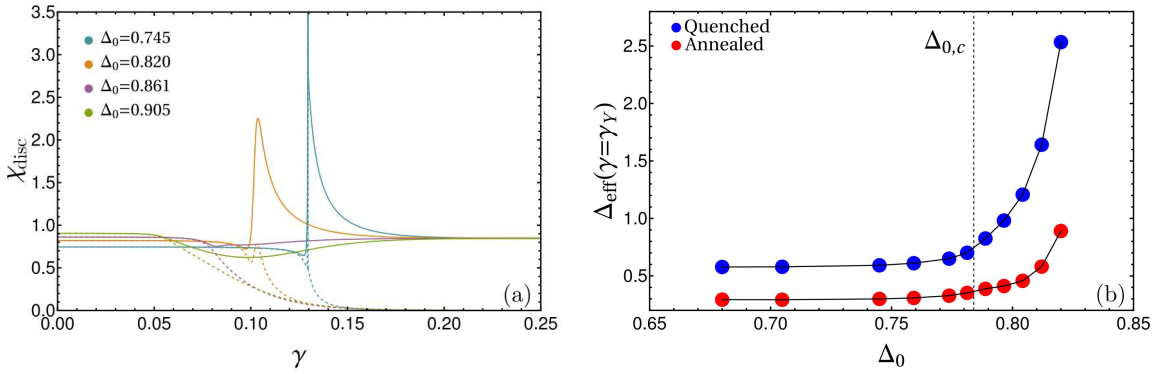

Figure 3.13: Comparison between the quenched and the annealed average over the random jumps: (a) Disconnected susceptibility $\chi_{\rm disc}(\gamma)$ for several values of the initial disorder variance Δ_0 and (b) variation with Δ_0 of the effective random-field variance at yielding $\Delta_{\rm eff}(\gamma_{\rm y})$ (note that $\gamma_{\rm y}$ is identical for the quenched and the annealed computations and so is the critical value of the bare disorder $\Delta_{0,c}$ which is indicated by the vertical line). The distribution $P_0(x)$ is a 2-exponential combination and $g(\hat{x})$ is a single exponential.

averaging. We illustrate the comparison between the quenched and annealed computations over the random jumps for the disconnected susceptibility and for the effective random-field variance at yielding, $\Delta_{\rm eff}(\gamma_{\rm y})$, in Fig. 3.13. One observes that the way the average over the history of random jumps is done influences the sample-to-sample quantities and in particular the strength of the effective random field. The latter is slightly smaller with the annealed average.

4 Conclusion

In this chapter we have analytically characterized the sample-to-sample fluctuations in a mean-field elasto-plastic model (EPM) describing the AQS evolution of a disordered system under simple shear. We have shown that the vicinity of the yielding transition can be described as an effective AQS driven (mean-field) RFIM in which the applied magnetic field plays the role of the applied strain. We have emphasized that the effective random field that linearly couples to the local stability (i.e., the distance to the local yield stress playing the role of the local order parameter akin to the local magnetization in the RFIM) is an emergent property: it is not present at the "bare" level in the system prior to deformation and rather arises at a later stage from a combination of the initial conditions and the history of deformation involving a sequence of local plastic events. We have then investigated the influence of the various types of disorder introduced in the EPM to mimic the effect of the local structural inhomogeneity of an amorphous solid (random initial local stresses, random local stress jumps, ...) on the strength of the effective random field, showing that they all contribute. As expected from the analogy with the RFIM, we find that for a decreasing strength of the random field yielding passes from a continuous crossover to a discontinuous transition, the two regimes being separated by a critical point.

Although the framework and some general considerations are valid for finite-dimensional systems as well, our study of the effective random field is restricted to mean-field models.

The advantage is that we are able to obtain an exact analytical solution but one may wonder which of the conclusions hold beyond mean-field. The main issue which we have stressed several times is the description of the stress redistribution after a local plastic event and therefore the nature of the effective interactions between site variables in the EPM. A proper description should account for the anisotropic, quadrupolar-like character of the Eshelby kernel [5, 28, 143]. As seen in the previous chapter, this has a dramatic influence on the shape of the large avalanches that take the form of bands. Improving the mean-field description to capture at least part of this phenomenology would be an important step toward an effective theory of yielding.

Conclusions and perspectives

We have focused on sheared amorphous solids and in particular on the yielding transition. The response of these materials to deformation can vary greatly: hard amorphous solids such as silicate glasses catastrophically fail at a given value of the applied strain γ, while soft ones such as mayonnaise can flow plastically for large values of γ. Due to the different response of hard and soft amorphous solids to deformation, the two have been studied within largely different frameworks for a long time. In spite of their differences, amorphous materials display common behavior when subjected to an external load, such as the localized nature of the elementary plastic events and their organization in shear bands. The preparation protocol can modify the response of an amorphous solid, but it has so far been difficult to experimentally observe a drastic change of behavior, from a brittle (discontinuous) regime to a ductile (continuous) regime of deformation. Such a change on the other hand has been observed in molecular dynamics simulations [4]: by only varying the so-called fictive temperature at which the liquid falls out of equilibrium to form a glass, the same material under simple shear can be brittle or ductile. It has been proposed that a critical point for a specific value of the fictive temperature separates the two regimes. These results give a new perspective on the long-standing problem of the yielding transition of amorphous solids, which was previously argued to always correspond to a spinodal point. (Note that there are amorphous solids such as glass made of nanocolloids [183] that can now be prepared over a large range of annealing, i.e., of stability, and could allow an experimental investigation of the proposed brittle-to-ductile critical point.)

In the present work we attempted to build an effective theory for the yielding transition of amorphous solids, i.e., a theory able to capture the physics of the system at long length scales while only retaining a few salient ingredients. One usually builds an effective theory by starting from a microscopic description and integrating out the effect of the small scales. Proceeding systematically along this line is not straightforward for the yielding transition, due to the absence of a microscopic theory able to describe the relevant physics and because of the out-of-equilibrium nature of the process. A first phenomenological step is the derivation of elasto-plastic models (EPMs) which are cellular automata that are devised to mimic at a mesoscopic level the response of amorphous solids under deformation. This comes at the expense of debatable assumptions and some arbitrariness in the choice of the rules. Furthermore, they do not correspond to a Hamiltonian description. Provided one keeps only a few basic ingredients of the EPMs without putting much emphasis on their ability to reproduce the microscopic details of realistic materials, these models nonetheless provide a mesoscopic description that may allow one to capture the long-distance physics associated with the yielding transition and the brittle-to-ductile critical point. A further step is to drop

even more details in an attempt to simplify the description of this physics: as suggested in [4] we therefore explore the possibility to describe the yielding transition by means of an out-of-equilibrium, athermally driven random-field Ising model.

Our purpose in Chapter 1 was to assess the existence of the critical point that separates the brittle from the ductile regime and to characterize its properties. This implies studying large system sizes and a large number of samples, which is difficult in MD simulations due to the computational cost. Moreover, the presence of the critical point has been challenged [6, 83, 84] and it has been suggested that strong finite-size effects are at play. To bypass these issues we considered an EPM. Its mesoscopic nature allowed us to explore large system sizes and to collect data for a large number of samples, from which a finite-size scaling analysis was possible. To allow for a crisp definition of transitions, avalanches, spinodals, etc., we studied the simple shear deformation at zero temperature under a quasistatic drive. We showed that the model reproduces the pattern of brittle-to-ductile stress-vs-strain curves when the amplitude of the initial disorder is changed, as observed in [4]. We first focused on the brittle regime showing that the largest contribution to the $O(1)$ stress drop comes from the sites outside the shear band. We found that the width of the shear band grows subextensively with system size, while the total number of plastic events in the largest avalanche is proportional to $N = L^d$, due to the fact that sites within the shear band yield a large number of times (a number of times that grows with L). We found the clear signature of a critical point in the model by studying the sample-to-sample fluctuations of an appropriate order parameter. We then gave a first estimate of the critical exponents via a careful finite-size scaling analysis. In addition we gave strong arguments supporting the view that the value of the disorder strength R at which the critical point takes place persists at finite disorder in the thermodynamic limit. In [4] it was proposed that it is possible for the average stress-vs-strain curve to display a continuous overshoot (with no discontinuous jump) before converging to the steady state. This possibility has since been questioned by theoretical arguments [6] and by numerical simulations [84]. This issue is different from the presence of a critical point for a finite value of R when $N \to \infty$ and, although we simulated large systems with the EPM, we were unable to conclude on this. Progress is needed on the theoretical side (see below). Finally, we assessed the role of statistically rare weak regions on the yielding transition in the brittle regime of the EPM. This was done by artificially introducing such a region in the system and studying its influence. These rare weak regions not only change the average value of the sample-dependent yielding strain γ_y but modify its distribution as well, which in turn affects the scaling of the connected susceptibility at yielding.

In Chapter 2 we investigated the possibility of building an effective theory for the yielding transition based on the random-field Ising model. To mimic the quadrupolar plastic events and their interaction leading to the appearance of a shear band we replaced the nearest-neighbor ferromagnetic interactions of the standard RFIM by the Eshelby propagator. We then studied the dynamics of this new model under an AQS driving protocol. The resulting magnetization-vs-field curves show some similarities with the stress-vs-strain curves in the EPM, displaying a jump of order 1 for small values of the variance of random field R, jump which is associated with the organization of spin flips in a band. For larger values of R the magnetization increases smoothly (in the thermodynamic limit) with the external field and the spins flip homogeneously in the whole sample. We found that a critical point at

$R = R_c$ separates these two types of behavior. This is qualitatively very similar to the EPM, but by looking carefully at the evolution in the weak disorder case we noticed an important difference: The possibility for a site in the EPM to yield multiple times is absent in the Eshelby-RFIM and has consequences on the scaling of the resulting band width with the system size. We then studied the critical point by computing the sample-to-sample fluctuations of an order parameter able to capture the formation of a band of positively magnetized spins, analogous to the one defined in the EPM. The large system sizes and the large amount of samples allowed for a finite-size scaling analysis of the model around the critical point situated at R_c. Yet, the uncertainty on the critical exponents remains large and corrections to scaling may be important. The values of the extracted exponents are systematically smaller than those of the EPM, but it does not seem sufficient to safely conclude that the two models are in different universality classes. Similarly to the EPM, the critical disorder R_c in the Eshelby-RFIM slowly shifts to larger values as the system size is increased. By employing the same method we managed to give a convincing argument that this shifting is again bounded. We finally investigated the effect of statistically rare regions on the value of the coercive field and found a behavior similar to the one observed in the EPM and in the standard ferromagnetic RFIM.

In Chapter 3 we presented the analytical study of the EPM and RFIM in a mean-field limit. Defining a mean-field approximation for the EPM is not straightforward due to the anisotropic nature of the Eshelby kernel. We focused for simplicity on the ferromagnetic version proposed in [4] which allows us to characterize in detail the sample-to-sample fluctuations. We studied the passage of the average evolution curves from a discontinuous to a continuous regime in the two models when changing the strength of the initial disorder. We were able to analytically compute the disconnected susceptibility and to compare it with the connected one to give an estimate of the effective strength of the random field. While in the RFIM the random field coupled to the local variable is explicitly present in the Hamiltonian, in the EPM it emerges in the vicinity of the yielding transition. We characterized how the different sources of disorder present in the EPM contribute to the effective random field by changing the initial distribution of stresses and of stress jumps. We then discussed a direct mapping between the average evolution of the two models. Interestingly, for this mapping to work one has to impose the condition of a single yielding event per site in the EPM, which, as we saw in the weak disorder regime of the finite-dimensional Eshelby-RFIM, is an important difference between the two models. We tried to push forward the mapping by working on a direct analogy between the evolution of the disconnected susceptibilities of the two models, but concluded that this would require the possibility of an evolution-dependent disorder strength in the RFIM.

To summarize, the present work has given arguments that there indeed exists a critical point that separates the brittle and ductile regimes of the athermal quasistatic evolution of sheared amorphous solids and is controlled by the initial degree of stability of the material. Finite-size effects are strong in this problem and one way around them is to develop an effective theory. Elasto-plastic models are a first step for a mesoscopic description of the yielding transition. Besides some debatable weaknesses of this approach, it would be useful to further simplify the problem. We have made progress in this direction by investigating in detail the relevance of the athermally and quasistatically driven random-field Ising model to the description of the yielding transition and more specifically of the disorder-controlled

critical point. We list below some directions that could be fruitfully taken to make further progress.

- To conclude on the persistence or not of an overshoot in the ductile regime of the AQS protocol in the thermodynamic limit, progress is needed on the analytical side. We are exploring this direction by studying a nonuniform Hébraud-Lequeux (HL) model [72] following the derivation in [73]. The model is still mean-field, but its heterogeneous nature allows for the linear shear-band instability proposed in [6] to clearly emerge. Preliminary results suggest that this linear instability is indeed present in the model but is not a long wavelength phenomenon as it is already found in small systems. These results are still in the preliminary phase and they require further examination. We also found the same type of instability in a random-field Ising model with Eshelby interactions treated in a mean-field way analogous to the HL model for elasto-plasticity. This instability appears as a general consequence of the form of the Eshelby propagator.
- Among the approximations listed in Chapter 1 while defining the EPM, we are studying the possibility of lifting the one on the perfect alignment of the Eshelby kernels in the direction of the drive. In reality the strain field generated by a plastic rearrangement can have its positive parts oriented along a slightly different direction each time, as observed in MD simulations (see Fig. I.7 and [155]). It is then interesting to see how the presence of a randomness in the orientation of Eshelby propagators affects the yielding transition and the critical point that separates the brittle and ductile regimes. Preliminary results on small system sizes showed that the brittle regime is still present when the rotation angle of the Eshelby kernels is kept between two small values, while it disappears for completely random orientations. This approach is also relevant for building an EPM able to describe the behavior of dense active matter [184].
- Another condition that would be interesting to relax is the one related to the $T = 0$ dynamics. Real amorphous solids are at an effectively low but nonzero temperature. We discussed how working at $T = 0$ is important in order to get a crisp definition of the avalanches in driven systems. Adding temperature makes the determination of avalanches more complicated, as they are not sharply defined for $T > 0$. Nonetheless one still expects to see large events in response to an increase of the external driving. It has been shown that in the driven ferromagnetic RFIM in 3D the addition of temperature does not preclude the possibility of observing a clear power-law regime of the avalanche-size distribution [136]. One could repeat this study in the EPM and in the Eshelby-RFIM, as it would allow to assess the effect of thermal fluctuations on avalanches and yielding.
- As we saw in Chapter 2, the anisotropic nature of the Eshelby kernel seems an important ingredient to obtain realistic results with the EPM. To get a simpler model and access larger system sizes one could think of keeping this ingredient, while giving up on the long-range nature. (This would also include the possibility that the quadrupole-quadrupole interaction is screened by emerging dipoles [166].) A model with short-range quadrupolar interactions has been studied [185, 186] and it has been shown that this modification of the kernel alters the formation of the band and the avalanche size distribution [185]. The effect of this approximation on

the yielding transition and on its dependence on the initial disorder has not been studied yet and is an interesting direction we would like to explore. Our working hypothesis is that the range of the interaction is not important as far as the universal aspects of the yielding transition are concerned.

Appendix A

The Eshelby kernel

In this appendix we discuss the Eshelby propagator. We start with the derivation of the long-ranged quadrupolar form in Eq. (I.5) following [149] and we discuss the resulting field for a point-like and a spherical inclusion. We then discuss the properties of the kernel and the choice of the values in $\mathbf{r} = 0$ in the real space and in $\mathbf{q} = 0$ in the Fourier space.

1 Fourier transform convention

In the following we make use of the Fourier transforms in both the continuous and discrete spaces. For the continuous case we define the Fourier transform and its inverse in a d-dimensional space as

$$\hat{f}(\mathbf{q}) = \mathcal{F}\{f(\mathbf{r})\}(\mathbf{q}) = \int_{\mathbf{r}} f(\mathbf{r}) e^{i\mathbf{q}\cdot\mathbf{r}} d^d\mathbf{r} \tag{A.1}$$

$$f(\mathbf{r}) = \mathcal{F}^{-1}\{f(\mathbf{q})\}(\mathbf{r}) = \frac{1}{(2\pi)^d} \int_{\mathbf{q}} \hat{f}(\mathbf{q}) e^{-i\mathbf{q}\cdot\mathbf{r}} d^d\mathbf{q}, \tag{A.2}$$

where the subscripts $\mathbf{r}$ and $\mathbf{q}$ stand for the integral over the whole real and reciprocal space, respectively. The standard properties of the Fourier transform follow. The derivative of a function with respect to one component of $\mathbf{r}$, say x, in the real space follows

$$\mathcal{F}\left\{\frac{\partial f(\mathbf{r})}{\partial x}\right\}(\mathbf{q}) = iq_x \mathcal{F}\{f(\mathbf{r})\}(\mathbf{q}). \tag{A.3}$$

The delta functions in both the real space and the Fourier space are defined as

$$\delta^{(d)}(\mathbf{r}) = \frac{1}{(2\pi)^d} \int_{\mathbf{q}} e^{-i\mathbf{q}\cdot\mathbf{r}} d^d\mathbf{q}, \tag{A.4}$$

$$\hat{\delta}^{(d)}(\mathbf{q}) = \frac{1}{(2\pi)^d} \int_{\mathbf{r}} e^{i\mathbf{q}\cdot\mathbf{r}} d^d\mathbf{r}. \tag{A.5}$$

Finally, the convolution between two functions f and g is defined as

$$(f \times g)(\mathbf{r}) = \int_{\mathbf{r}'} g(\mathbf{r} - \mathbf{r}') f(\mathbf{r}') d^d\mathbf{r}' \tag{A.6}$$

and its Fourier transform follows

$$\mathcal{F}\{(f \times g)(\mathbf{r})\}(\mathbf{q}) = \hat{f}(\mathbf{q})\hat{g}(\mathbf{q}). \tag{A.7}$$

2 Derivation of the Eshelby propagator

We generalize the formula in Eq. (I.5) to d-dimensions for homogenous and isotropic materials, following [149] and [162]. The solid is considered to be incompressible and to react only elastically to a plastic perturbation. In the following we make use of the Einstein notation, so that a sum is performed over repeated indices. The stress tensor σ_{ij} obeys the mechanical equilibrium condition at every point in the material:

$$\frac{\partial \sigma_{ij}(\mathbf{r})}{\partial r_i} = 0. \tag{A.8}$$

We decompose the stress tensor into the volumetric and deviatoric terms

$$\sigma_{ij} = \sigma_{\mathrm{M}} \delta_{ij} + \sigma'_{ij}, \tag{A.9}$$

where

$$\sigma_{\mathrm{M}} = \frac{1}{d}\sigma_{ii} \quad \text{and} \quad \sigma'_{ij} = \sigma_{ij} - \sigma_{\mathrm{M}}\delta_{ii}. \tag{A.10}$$

We assume that a plastic event occurs somewhere in the system. The total strain perturbation can be decomposed in two terms: the plastic one, coming from inside the localized event, and the elastic one, coming from the reaction of the material to such a rearrangement out of it. We can write this as $\Delta\varepsilon_{ij} = \Delta\varepsilon^{\mathrm{el}}_{ij} + \Delta\varepsilon^{\mathrm{pl}}_{ij}$. The stress receives a contribution from the elastic strain given by $\Delta\sigma'_{ij} = 2\mu\Delta\varepsilon^{\mathrm{el}}_{ij}$ in a point outside the rearranging region. This elastic strain is just a consequence of the plastic inclusion and it is more useful to rewrite the stress as $\Delta\sigma'_{ij} = 2\mu(\Delta\varepsilon_{ij} - \Delta\varepsilon^{\mathrm{pl}}_{ij})$. In the following, moving to the Fourier space will be convenient. We define

$$\Delta\hat{u}_i = \mathcal{F}(\Delta u_i), \quad \Delta\hat{\varepsilon}_{ij} = \mathcal{F}(\Delta\varepsilon_{ij}) = \frac{i}{2}(q_i\Delta\hat{u}_j + q_j\Delta\hat{u}_i), \quad \Delta\hat{\sigma}_{ij} = \mathcal{F}(\Delta\sigma_{ij}), \tag{A.11}$$

where the conventions for the Fourier transform are specified above, and $\mathbf{q}$ is the vector in the reciprocal space. We use the same hat notation also for the Fourier transform of the other quantities. Our goal is to find a relation between the stress tensor at some point in the material and the strain field generated by the plastic inclusion. This amounts to finding a function $G_{ijkl}(\mathbf{r}-\mathbf{r}')$ such that

$$\Delta\sigma'_{ij}(\mathbf{r}) = 2\mu \int d\mathbf{r}' G_{ijkl}(\mathbf{r}-\mathbf{r}')\Delta\varepsilon^{\mathrm{pl}}_{kl}(\mathbf{r}') \quad \text{(In real space)}, \tag{A.12}$$

$$\Delta\hat{\sigma}'_{ij}(\mathbf{q}) = 2\mu\hat{G}_{ijkl}(\mathbf{q})\Delta\hat{\varepsilon}^{\mathrm{pl}}_{kl}(\mathbf{q}) \quad \text{(In Fourier space)}. \tag{A.13}$$

We start with the mechanical equilibrium equation in Eq. (A.8). Assuming that the system was at the mechanical equilibrium before the plastic event and will be at the mechanical equilibrium afterward we can rewrite this condition as

$$\begin{aligned}
0 = \partial_j \Delta\sigma_{ij} &= \partial_j(\Delta\sigma_{\mathrm{M}}\delta_{ij} + 2\mu\Delta\varepsilon^{\mathrm{el}}_{ij}) && \text{(A.14)}\\
&= \partial_i\Delta\sigma_{\mathrm{M}} + 2\mu\partial_j(\Delta\varepsilon_{ij} - \Delta\varepsilon^{\mathrm{pl}}_{ij}) && \text{(A.15)}\\
&= \partial_i\Delta\sigma_{\mathrm{M}} + \mu\partial_j(\partial_i\Delta u_j + \partial_j\Delta u_i) - 2\mu\partial_j\Delta\varepsilon^{\mathrm{pl}}_{ij} && \text{(A.16)}\\
&= \partial_i\Delta\sigma_{\mathrm{M}} + \mu\partial_i\partial_j\Delta u_j + \partial_j\partial_j\Delta u_i - 2\mu\partial_j\Delta\varepsilon^{\mathrm{pl}}_{ij}. && \text{(A.17)}
\end{aligned}$$

We define an internal force field f_i as

$$f_i = -2\mu\partial_j \Delta\varepsilon^{\mathrm{pl}}_{ij} \quad \text{(In real space)}, \tag{A.18}$$

$$\hat{f}_i = -2i\mu q_j \Delta\hat{\varepsilon}^{\mathrm{pl}}_{ij} \quad \text{(In Fourier space)}. \tag{A.19}$$

We can now make use of the hypothesis of incompressibility, that reads

$$\partial_i \Delta u_i = 0 \quad \text{(In real space)}, \tag{A.20}$$

$$iq_i \Delta\hat{u}_i = 0 \quad \text{(In Fourier space)}. \tag{A.21}$$

Putting this equation inside Eq. (A.14) we get

$$iq_i \Delta\hat{\sigma}_{\mathrm{M}} - \mu q_j q_j \Delta\hat{u}_i + \hat{f}_i = 0 \tag{A.22}$$

in the Fourier space. We proceed by multiplying by q_i both sides of Eq. (A.22) (which amounts to performing a derivative with respect to r_i in the real space) and, using again the incompressibility condition, we get

$$iq^2 \Delta\hat{\sigma}_{\mathrm{M}} = -q_i \hat{f}_i, \tag{A.23}$$

with $q^2 = q_i q_i$ being the squared modulus of vector $\mathbf{q}$. As a consequence for $\mathbf{q} \neq 0$ we have $\hat{\sigma}_{\mathrm{M}} = iq_i\hat{f}_i/q^2$. From this we finally get an equation for the Fourier transform of the displacement:

$$\Delta\hat{u}_i = -2i\left(\frac{q_j}{q^2}\Delta\hat{\varepsilon}^{\mathrm{pl}}_{ij} - \frac{q_i q_j q_k}{q^4}\Delta\hat{\varepsilon}^{\mathrm{pl}}_{jk}\right). \tag{A.24}$$

The resulting stress can be computed using the relation $\Delta\sigma'_{ij} = 2\mu(\Delta\varepsilon_{ij} - \Delta\varepsilon^{\mathrm{pl}}_{ij})$ and reads

$$\Delta\hat{\sigma}'_{ij} = 2\mu\left(\frac{q_i q_k \delta_{jl} + q_j q_l \delta_{ik}}{q^2} - \frac{2q_i q_j q_k q_l}{q^4} - \delta_{ik}\delta_{jl}\right)\Delta\hat{\varepsilon}^{\mathrm{pl}}_{kl}, \tag{A.25}$$

from which we obtain

$$\hat{G}_{ijkl} = \frac{q_i q_k \delta_{jl} + q_j q_l \delta_{ik}}{q^2} - \frac{2q_i q_j q_k q_l}{q^4} - \delta_{ik}\delta_{jl}. \tag{A.26}$$

We consider a plastic inclusion with the same symmetry as the externally applied deformation, which is simple shear on the x-y plane. We then neglect the diagonal components of the plastic strain, namely $\Delta\hat{\varepsilon}^{\mathrm{pl}}_{ii} = 0$, for every i. We only consider the deviatoric contribution to the stress, so that we have

$$\Delta\hat{\sigma}_{xy}(\mathbf{q}) = \Delta\hat{\sigma}'_{xy}(\mathbf{q}) = 2\mu\hat{G}(\mathbf{q})\Delta\hat{\varepsilon}^{\mathrm{pl}}_{xy}(\mathbf{q}), \tag{A.27}$$

with

$$\hat{G}(\mathbf{q}) = -\frac{4q_x^2 q_y^2}{q^4} \quad \text{(In 2D)}, \tag{A.28}$$

$$\hat{G}(\mathbf{q}) = -\frac{4q_x^2 q_y^2 + q_z^2 q^2}{q^4} \quad \text{(In 3D)}. \tag{A.29}$$

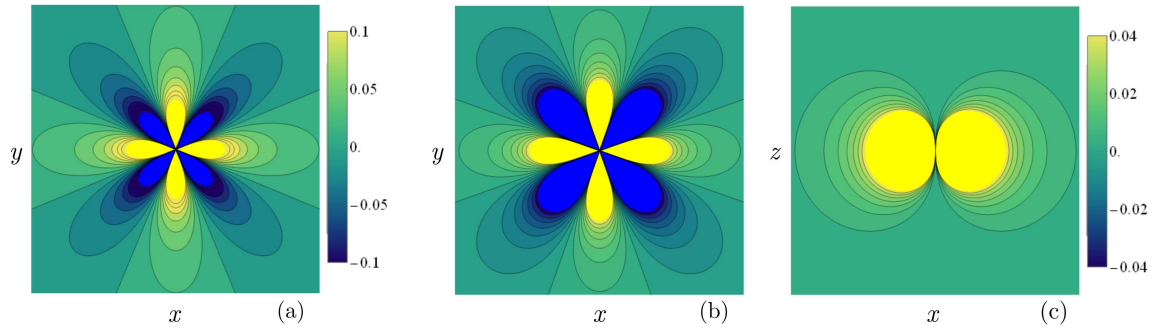

Figure A.1: Eshelby kernel for a homogeneous infinite material in 2D (a) and 3D in the x-y plane (b) and in the x-z plane (c).

Note that in the last steps of the calculation we imposed the condition $\mathbf{q} \neq 0$. The kernel is not defined at the origin in the Fourier space. The value of the propagator in $\mathbf{q} = 0$ is chosen depending on the deformation protocol and is discussed in the next part. This result holds for an infinite elastic medium, but we did not make any assumption on the nature and shape of the plastic strain field $\Delta\varepsilon^{\mathrm{pl}}_{xy}(\mathbf{r})$, except for the hypothesis that it has the shear symmetry. In Eq. (A.28) we found the propagator for the plastic strain, but to conclude on the stress variation that a rearrangement generates on the rest of the material $\Delta\sigma_{xy}(\mathbf{r})$, we need to choose a form for the plastic event. In [149] the shape of the localized event is described as a delta function $\Delta\varepsilon^{\mathrm{pl}}_{xy} = \varepsilon_0 a^d \delta(\mathbf{r})$, with ε_0 being a typical amplitude and a the microscopic linear size (for dimensional reasons). This form is equivalent to a constant in the Fourier space $\Delta\hat{\varepsilon}^{\mathrm{pl}}_{xy} = \varepsilon_0 a^d$. The stress resulting from such an inclusion can be computed, for example in 2D, as

$$\Delta\sigma_{xy}(\mathbf{r}) = 2\mu\mathcal{F}^{-1}\left(\hat{G}(\mathbf{q})\Delta\hat{\varepsilon}^{\mathrm{pl}}_{xy}(\mathbf{q})\right) = -2\mu\varepsilon_0 a^d \int_{\mathbf{q}} \frac{d\mathbf{q}}{(2\pi)^2}\frac{4q_x^2 q_y^2}{q^4} e^{i\mathbf{q}\cdot\mathbf{r}}. \tag{A.30}$$

The integral is however only conditionally convergent and its result changes depending on how the limit to infinity is taken. In order to overcome this issue, we focus on the case of a spherical inclusion, so that $\Delta\varepsilon^{\mathrm{pl}}_{xy}(\mathbf{r}) = \varepsilon_0 I(\mathbf{r})$, with an indicator function

$$I(\mathbf{r}) = \theta(a - r) \tag{A.31}$$

where θ is the Heaviside function, r the modulus of vector $\mathbf{r}$, and a the linear size of the plastic region. The Fourier transforms of the indicator function are

$$\hat{I}(\mathbf{q}) = \frac{2\pi a}{q} J_1(qa) \quad (\text{In 2D}), \tag{A.32}$$

$$\hat{I}(\mathbf{q}) = \frac{4\pi}{q^3}\left[\sin(qa) - (qa)\cos(qa)\right] \quad (\text{In 3D}), \tag{A.33}$$

where we used the definition of Bessel functions of the first kind $J_n(z) = \frac{(-i)^n}{2\pi}\int_0^{2\pi} d\theta e^{i(z\cos\theta + n\theta)}$. The next step in order to find the stress field generated by a spherical plastic event is to

compute the inverse Fourier transform which, in 2D, gives

$$\mathcal{F}^{-1}\left[-\frac{4q_x^2q_y^2}{q^4}\hat{I}(\mathbf{q})\right] = \int \frac{d\mathbf{q}}{(2\pi)^2}\, e^{i\mathbf{q}\cdot\mathbf{r}}\left(-\frac{4q_x^2q_y^2}{q^4}\right)\hat{I}(\mathbf{q}) = -\frac{2a}{\pi}\int d\mathbf{q}\, e^{i\mathbf{q}\cdot\mathbf{r}}\frac{q_x^2q_y^2}{q^5}J_1(qa). \tag{A.34}$$

This integral can be computed with the help of the Bessel function's properties. After a lengthy calculation we finally get

$$\Delta\sigma_{xy}(\mathbf{r}) = 2\mu\varepsilon_0\mathcal{F}^{-1}\left[-\frac{4q_x^2q_y^2}{q^4}\hat{I}(\mathbf{q})\right] = 2\mu\varepsilon_0\cos(4\theta)\left[\left(\frac{a}{r}\right)^2 - \frac{3}{2}\left(\frac{a}{r}\right)^4\right] \tag{A.35}$$

in polar coordinates $\mathbf{r} = (r,\theta)$. This means that if we consider an inclusion with a finite size, the integral can be solved. The indicator function $I(r)$ plays the role of a regulator and allows to compute the integral which was otherwise indeterminate. This form is also confirmed by real-space calculations in [187]. In the far-field approximation the term in $1/r^2$ dominates and one finds the same formula in Eq. (I.5)

$$G(\mathbf{r}) = \frac{\cos(4\theta)}{\pi r^2}, \tag{A.36}$$

multiplied by the size of the region a^2 and the uniform plastic strain ε_0 inside it. The same reasoning can be done for the 3D case, and leads to the form

$$\Delta\sigma_{xy}(\mathbf{r}) = \frac{3\mu}{2\pi}\frac{4\pi a^3}{3}\varepsilon_0\left[\frac{r^2(x^2+y^2)-10x^2y^2}{r^7} + \frac{2}{15}\left(\frac{a}{r}\right)^2\frac{3r^4-15r^2(x^2+y^2)+105x^2y^2}{r^7}\right], \tag{A.37}$$

after assuming that the plastic strain has again the symmetry of the macroscopically applied deformation, which is a shear in the x-y plane. In the far-field approximation with the spherical coordinates (r,θ,ϕ) the formula above becomes

$$\Delta\sigma_{xy}(\mathbf{r}) = \frac{5\mu a^3\varepsilon_0}{2r^3}\sin^2(\theta)\left[\sin^2(\theta)(\cos(4\phi)-1)+\frac{4}{5}\right], \tag{A.38}$$

which conserves a quadrupolar symmetry in the x-y plane and decays as r^{-3}.

2.1 Value at the origin and properties of the Eshelby strain field

The calculations in the reciprocal space performed in the previous section are valid only for the case in which $\mathbf{q} \neq 0$. To choose the value of the propagator at $\mathbf{q} = 0$ we consider the deformation protocol that we want to apply. In the case of a fixed-stress protocol, the macroscopic amount of stress resulting from a plastic event should be 0, since the total stress is imposed from the outside. The macroscopic stress is given by

$$\Delta\sigma_{xy}^{\text{tot}} = \int_{\mathbf{r}}\Delta\sigma_{xy}(\mathbf{r})d\mathbf{r} = 2\mu\hat{G}(0)\hat{\varepsilon}_{xy}^{\text{pl}}(0). \tag{A.39}$$

One has to impose $\hat{G}(\mathbf{q}=0)=0$ in this case. In our study we are interested in the strain-controlled case. When the strain is controlled, the stress should decrease after each plastic event by a quantity proportional to the total amount of plastic strain generated, so that $\hat{G}(0)<0$. Different values can be chosen, and the choice thereof has consequences on the dynamics [147]. In our case we simply choose $\hat{G}(0)=-1$. From the expressions of the propagator in the real space in Eq. (A.36) and in Eq. (A.38) we notice that also in this case the value in $\mathbf{r}=0$ is not defined. We can choose to fix $G(\mathbf{r}=0)=-1$ to decrease the stress at the site that yields. Notice that the choice of the value at the origin in the real (reciprocal) space shifts by a constant the propagator in the reciprocal (real) space, so that the constant term in Eq. (A.38) is not important since it will be changed by the imposition of $G(0)=-1$.

From the form of the propagator in the Fourier space we note an important property. As a plastic event occurs somewhere in the system the stress is modified in the whole sample, but the total stress along each row and column in the x-y plane is conserved. We compute the integral over y at a fixed value of $x=x_0$ in 2D, which, using the properties of the Fourier transform, gives

$$\Delta\sigma^{\mathrm{x}}_{xy}(x_0)=\int_{-\infty}^{\infty}\Delta\sigma_{xy}(x_0,y)dy=2\mu\varepsilon_0\int_{-\infty}^{\infty}\hat{G}(q_x,0)e^{-iq_xx_0}dq_x \tag{A.40}$$

in the case of a point-like plastic event with $a=1$. From Eq. (A.28) we see that $\hat{G}(q_x,0)=0$ everywhere except for $q_x=0$, which does not change the result of the integral. It follows that $\Delta\sigma^{\mathrm{x}}_{xy}(x_0)=0$ for every x_0. This result can be generalized to the situation in which $y=y_0$ and the integral is performed over x, in which case $\Delta\sigma^{\mathrm{y}}_{xy}(y_0)=0$. This means that no plastic event can change the total stress along a line at constant x or y, defined as

$$\sigma^{\mathrm{x}}_{xy}(x_0)=\int_{-\infty}^{\infty}\sigma_{xy}(x_0,y)dy. \tag{A.41}$$

Since the total strain is applied uniformly to the sample, it follows that the difference between the value of this integral at x_0 and $x_1\neq x_0$ does not change from the one at rest, before deformation is applied, so that

$$\sigma^{\mathrm{x}}_{xy}(x_0,\gamma)-\sigma^{\mathrm{x}}_{xy}(x_1,\gamma)=\sigma^{\mathrm{x}}_{xy}(x_0,\gamma=0)-\sigma^{\mathrm{x}}_{xy}(x_1,\gamma=0) \tag{A.42}$$

for any x_0 and x_1. The same result also holds for the 3D case, where the integral should be carried on over planes perpendicular to either x, y, or z. The resulting stress difference along such regions is

$$\Delta\sigma^{\mathrm{x}}_{xy}(x_0)=\int_{-\infty}^{\infty}\int_{-\infty}^{\infty}\Delta\sigma_{xy}(x_0,y,z)dydz=2\mu\varepsilon_0\int_{-\infty}^{\infty}\hat{G}(q_x,0,0)e^{-iq_xx_0}dq_x \tag{A.43}$$

which is again 0 due to the properties of the 3D Eshelby propagator.

3 Implementation of the kernel

The expressions of the kernel that we derived in the previous section is valid for a homogeneous and infinite medium. However, in our case, we deal with a discrete and finite lattice

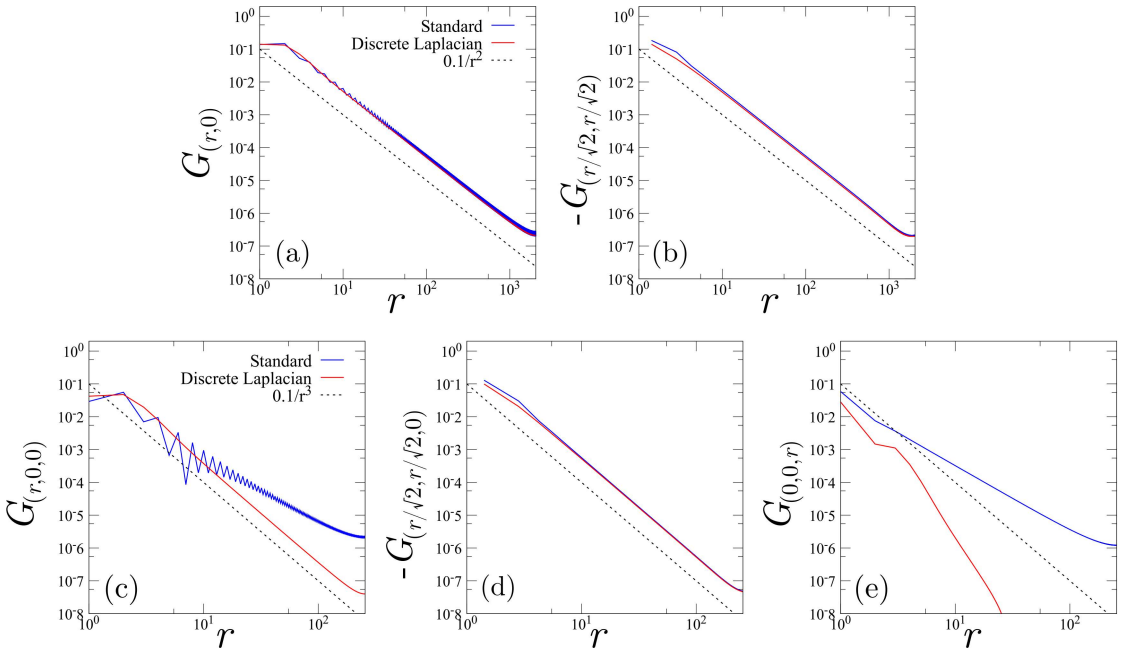

Figure A.2: Scaling of the Eshelby kernel with the distance along x (a) and y (b) in 2D for the FFT with and without the Laplacian correction $q_i^2 \to 2 - 2\cos(q_i)$. In this case the correction adjusts some oscillations that were previously observed in [151]. In (c) and (d) we plot the same thing for the 3D case. Notice that here the correction is even more important since the kernel does not have the right scaling without it. In (e) the behavior of the kernel along the z axis is shown, with the very fast decay observed when correcting the Laplacian.

of size L and lattice constant a. The form of the Eshelby kernel in this case is not known, but as a first approximation one could think of taking the continuous solution and discretize it in the real space as

$$G^{\mathrm{D}}_{\mathbf{r}} = G^{\mathrm{C}}(\mathbf{r}), \tag{A.44}$$

where $\mathbf{r} = (a\, m_x, a\, m_y)$ with $m_{x,y} = 0, \ldots, L$. In the present section we introduced the superscripts D for the propagator defined on the lattice and C for the continuous one, in order to make the discussion clear. The periodic boundary conditions need to be imposed. This procedure requires particular care due to the long-range nature of the interactions. One has to solve two issues: discretization and periodicity. In the real space it is easy to perform the discretization as above, but imposing periodicity is harder. A possible solution to this problem is to consider the kernel in the Fourier space and discretize there, so that

$$\hat{G}^{\mathrm{D}}_{\mathbf{q}} = \hat{G}^{\mathrm{C}}(\mathbf{q}). \tag{A.45}$$

In the Fourier space the finite linear size L of the system with periodic boundary conditions is translated to a discretization of the reciprocal vector. On the other hand the discretization of the real space translates instead to a restriction of the Fourier space around the first Brillouin zone, so that $\mathbf{q} = (\pi\, n_x/L, \pi\, n_y/L)$ with $n_{x,y} = -L/2, \ldots, L/2 - 1$ (in 2D with $a = 1$). From

the expression of $\hat{G}^{\mathrm{D}}_{\mathbf{q}}$ one can easily find the real space kernel in these conditions by means of an inverse Fast Fourier Transform algorithm (FFT).

From the expression of the kernel in the Fourier space in Eq. (A.28) we notice that the explicit dependence on the $\mathbf{q}$ vector comes in form of q_i^2 or q^2. In the real space these terms are related to a second derivative along a certain axis i and a Laplacian, respectively. In the discrete space the second derivative is not defined, but can be approximated via the finite difference method as

$$\frac{\partial^2 f^{\mathrm{C}}(x)}{\partial x^2} \to \frac{f^{\mathrm{D}}_{x+a} + f^{\mathrm{D}}_{x-a} - 2f^{\mathrm{D}}_{x}}{a^2}, \tag{A.46}$$

where a is the lattice constant. This translates to the Fourier space as

$$q_i^2 \to \frac{2 - 2\cos(q_i a)}{a^2}. \tag{A.47}$$

In our work we use this kind of mesh with $a = 1$, as was previously done in [147]. The real space propagator that results from this operation has a very similar behavior to the expression in Eq. (A.36) and in Eq. (A.38) and it shows a better agreement with respect to the one without the discrete Laplacian correction. A couple of issues still persist. First, in both 2D and 3D the agreement with the $1/r^d$ shape of the continuous real space kernel is lost at small r, due to the cutoff of high-frequency modes [151]. When the kernel is tilted by a certain amount (as in Section 4 of Chapter 3 or in [169]), more precision on the short-range interactions is required. In this case we perform the discretization of the real space on a finer grid. We then average the results in the neighboring sites to go back to the original dimension of the lattice. The second problem is that in 3D one can see from Eq. (A.38) that the kernel should be identically zero along the z-direction. This is not the case in the results obtained from the FFT algorithm, but the decrease is still fast enough compared to the other terms and to the first order correction obtained by considering a spherical inclusion.

Other solutions have also been devised to face the summation problem that occurs when imposing periodic boundary conditions. For example, in [151] the propagator is considered in the continuous real space and summed analytically over copies of the system in the y direction. The result depends only on the copies along x. The summation along x cannot be computed analytically, but a sum over the first 5 copies is sufficient.

3.1 The Eshelby kernel in the EPM

In our EPM the system is strain-driven, so we impose $\hat{G}(\mathbf{q} = 0) = -1$. Before applying this kernel we also need to fix the value at the origin of the real space. To this end in the simulations we use the kernel $\hat{G}'_{\mathbf{q}}$ defined as

$$\hat{G}'_{\mathbf{q}} = \begin{cases} \frac{\hat{G}^{\mathrm{D}}_{\mathbf{q}}}{\mathcal{M}} & (\mathbf{q} \neq \mathbf{0}), \\ -1 & (\mathbf{q} = \mathbf{0}), \end{cases} \tag{A.48}$$

with

$$\mathcal{M} = -\frac{1}{L^d} \sum_{\mathbf{q} \neq \mathbf{0}} \hat{G}_{\mathbf{q}} > 0. \tag{A.49}$$

With this choice we assure that $G^{\mathrm{D}}_{\mathbf{r}=0} = -1 - 1/L^d$. Note that all the properties described in the section above still hold true in this discretized case.

3.2 The Eshelby kernel in the Eshelby-RFIM

In the Eshelby-RFIM defined in Chapter 2 we have substituted the usual short-range interactions of the standard RFIM with the Eshelby kernel. We obtain the real-space expression of the Eshelby propagator by inverse Fourier transform of $\hat{G}(\mathbf{q})$, as described above. The choice of $\hat{G}(\mathbf{q}=0)$ and $G(\mathbf{r}=0)$ here is a bit different from the EPM case. As discussed in the main text we choose now $\hat{G}(\mathbf{q}=0)=0$ and $G(\mathbf{r}=0)=0$, so that the spin flipping does not affect its own effective field. This leads to define the kernel

$$\hat{G}''_{\mathbf{q}} = \begin{cases} \frac{\hat{G}^{\mathrm{D}}_{\mathbf{q}}}{\mathcal{M}} + c & (\mathbf{q} \neq \mathbf{0}), \\ 0 & (\mathbf{q} = \mathbf{0}), \end{cases} \tag{A.50}$$

with $c = 1 + 1/(L^d - 1)$ obtained by imposing that the spins do no interact with themselves. As a consequence of this correction, the propagator is not negative in the whole Fourier space, which could lead to instabilities. However, this was the only way we found to avoid self-interaction, and the results are still stable thanks to the fact that each spin can only flip once (no multiple yielding). During the simulations of this model we encountered an issue in the 2D case. A single system spanning band does not form properly and instead many thin (one or two lines thick) bands take place when the magnetization jumps. We checked that the nearest neighbor interaction strength is to blame for this behavior. As we saw in Fig. A.2, the kernel obtained from the IFFT does not display the $1/r^d$ decay at short distance. In the EPM this issue does not affect the resulting band, probably due to the multiple yielding of many sites (even if some effects are observed in the shear band form [151]), while it here causes serious problems. To overcome this issue we decided to manually correct the nearest-neighbor term of the Eshelby kernel in order to restore the $1/r^d$ behavior, which solved the problem.

Appendix B

Details on the code

In this appendix we discuss the details of the code. For all the simulations the code has been written from scratch in C language and compiled with the `gcc` compiler. To generate random numbers we employed the Mersenne Twister algorithm. We describe the code to simulate the elasto-plastic model first, followed by both the standard random-field Ising model and our version with Eshelby-like interactions.

1 Code for the EPM

As we discussed in Chapter 1 the basic ingredients for the EPM are elastic blocks that redistribute part of their stress once they reach a stress threshold. The code for a 2D EPM proceeds as follows. The input parameters for the code are the value of R, the disorder strength, L, the system size, l, the limit value of the applied strain, and s, the seed of the random number generator. We begin by defining the 2D array $\underline{\underline{\sigma}}$ and assigning the starting values at each site $\sigma_{i,j}$, following the distribution P_0 in Eq. (1.7), by means of Monte Carlo sampling. We continue by normalizing the kernel that we are going to use. As explained in Appendix A we need to normalize the expression of $\hat{G}_{\mathbf{q}}$ in the Fourier space to assure $G(\mathbf{r} = 0) = -1$. We compute $\mathcal{M}$ with the expression in Eq. (A.49) and define the 2D array $\underline{\underline{\hat{G}}}'$ as in Eq. (A.48). We enter the main **while** loop, which corresponds to the driving procedure. The code iterates the instructions within this loop until the strain γ reaches the required limit l. Inside the loop we first search for the least stable site, i.e., the one with the largest stress $\sigma_{\max}$. Once this site is found, we increase the external strain γ by the amount necessary to destabilize such block, which is precisely $1 - \sigma_{\max}$ (remember that we chose $\sigma_i^{\text{th}} = 1$ for every i). The stress at every site increases accordingly by the same quantity (as $\mu = 1$). After this driving step we enter in the innermost **while** loop, where the system relaxes to the new equilibrium and the avalanche takes place. We check the stability of each site in the lattice. If there is at least an unstable block, the cycle repeats, otherwise it stops. When an unstable site is found, we associate a stress drop to its position in the 2D array $\underline{\underline{\delta\sigma}}$ and we increase the local plastic strain $\underline{\underline{\gamma^{\text{pl}}}}$ of the same amount. Once we checked every site and $\underline{\underline{\delta\sigma}}$ has been filled with the stress drop of the unstable ones, we compute the Fourier transform of this array, which gives $\underline{\underline{\delta\hat{\sigma}}}$. This step is performed by means of the Fast Fourier Transform (FFT) algorithm [188, 189] using the FFTW library [190]. The stress at each site

is then increased by a quantity which is the Inverse Fast Fourier Transform (IFFT) of the (element-by-element) product of $\underline{\underline{\delta\hat{\sigma}}}$ and $\underline{\underline{\hat{G}'}}$. After this stress redistribution more sites may be unstable and the cycle goes on until the system relaxes completely. The strain is then increased again and the procedure is repeated.

1.1 Adding a seed

In order to understand the behavior of the system at small disorder strength, it is interesting to see the effect that a seed of weak sites has on the rest of the system. Such regions are always present in the thermodynamic limit, but due to the small probability associated to their occurrence they may not be observed in finite-size systems. We add such seeds artificially, as it has been done in the context of MD simulations in [163]. To reproduce the setup in [163] we choose to act both on the thresholds and on the initial stress of the sites inside the seed. Such sites are chosen to have a local threshold σ_i^{th} drawn from a Gaussian distribution of mean $\overline{\sigma_i^{\text{th}}} = 1$ and standard deviation $R_{\text{th}} = 0.2$. After they yield for the first time, their threshold is set back to 1. The initial value of their stress is instead chosen from a distribution which reads

$$P_0^{\text{seed}}(\sigma, \sigma_i^{\text{th}}) = \frac{(\sigma_i^{\text{th}} - \sigma^2)}{\mathcal{N}(\sigma_i^{\text{th}})} \exp\Big\{-\sigma^2/(2R_{\text{seed}}^2)\Big\}, \tag{B.1}$$

which depends on the threshold value assigned to site i. We fix $R_{\text{seed}} = 0.9$. The sites outside the seed are chosen as before. The procedure to find the least stable site is then modified to account for the site-dependent threshold by searching $x_{\min} = \min_i(\sigma_i^{\text{th}} - \sigma_i)$. The external strain is increased accordingly. Similarly, the stress drops after a plastic event are chosen based on the local threshold. The rest of the code stays unchanged. The pseudocode to simulate a system with a weak region defined by length r_x and r_y is given below.

The code for the EPM with a seed is easily modified to obtain the model described in [7].

Algorithm 1: Pseudocode for the simulation of the 2D EPM

Data: R, L, l, s

$\gamma \leftarrow 0$;
$\underline{\underline{\gamma^{\mathrm{pl}}}} \leftarrow \underline{\underline{0}}$;
$\underline{\underline{\delta\sigma}} \leftarrow \underline{\underline{0}}$;
$\underline{\underline{\sigma}} \leftarrow \underline{\underline{0}}$;
for $i < L$ **do**
  for $j < L$ **do**
    $\sigma_{i,j} \leftarrow \mathrm{MCSampling}(P_0, R, s)$; /* Stress initialization */
  end
end
$\mathcal{M} \leftarrow 0$;
for $-L/2 < n_x < L/2$ **do**
  for $-L/2 < n_y < L/2$ **do**
    $\mathcal{M} \leftarrow \mathcal{M} + \hat{G}_{q_x,q_y}$; /* Procedure to normalize the kernel */
  end
end
while $\gamma < l$ **do**
  $\sigma_{\max} \leftarrow \mathrm{FindMaximum}(\underline{\underline{\sigma}})$; /* Find least stable */
  $\gamma \leftarrow \gamma + (1 - \sigma_{\max})$; /* Strain increment */
  $\underline{\underline{\sigma}} \leftarrow \underline{\underline{\sigma}} + (1 - \sigma_{\max})\underline{\underline{1}}$;
  $f_2 \leftarrow 1$;
  while f_2 **do**
    $f_2 \leftarrow 0$;
    $\underline{\underline{\delta\sigma}} \leftarrow \underline{\underline{0}}$;
    for $i < L$ **do**
      for $j < L$ **do**
        if $\sigma_{i,j} > 1$ **then**
          $\delta\sigma_{i,j} \leftarrow \sigma_{i,j} - \mathrm{sign}(\sigma_{i,j})(1 - \mathrm{ExpSampling}(s))$;
          $\gamma^{\mathrm{pl}}_{i,j} \leftarrow \gamma^{\mathrm{pl}}_{i,j} + \delta\sigma_{i,j}$; /* Unstable sites yield */
          $f_2 \leftarrow 1$;
        end
      end
    end
    if f_2 **then**
      $\underline{\underline{\delta\hat{\sigma}}} \leftarrow \mathrm{FFT}(\underline{\underline{\delta\sigma}})$;
      $\underline{\underline{\sigma}} \leftarrow \underline{\underline{\sigma}} + \mathrm{IFFT}(\underline{\underline{\delta\hat{\sigma}}}\ \underline{\underline{\hat{G}'}})$; /* Stress redistribution */
    end
  end
end

Algorithm 2: Pseudocode for the 2D EPM with seed insertion

Data: R, L, l, s, r_x, r_y

$\gamma \leftarrow 0$;
$\underline{\underline{\gamma^{\mathrm{pl}}}} \leftarrow \underline{\underline{0}}$;
$\underline{\underline{\delta\sigma}} \leftarrow \underline{\underline{0}}$;
$\underline{\underline{\sigma}} \leftarrow \underline{\underline{0}}$;
$\underline{\underline{\sigma^{\mathrm{th}}}} \leftarrow \underline{\underline{0}}$;
for $i < L$ **do**
  for $j < L$ **do**
    if $(i,j) \in \mathrm{Seed}(\mathrm{r_x}, \mathrm{r_y})$ **then**
      $\sigma^{\mathrm{th}}_{i,j} \leftarrow \mathrm{GaussianSampling}(R_{\mathrm{th}}, s)$;
      $\sigma_{i,j} \leftarrow \mathrm{MCSampling}(P_0^{\mathrm{seed}}, R_{\mathrm{seed}}, \sigma^{\mathrm{th}}_{i,j}, s)$; `/* Initialization */`
    else
      $\sigma^{\mathrm{th}}_{i,j} \leftarrow 1$;
      $\sigma_{i,j} \leftarrow \mathrm{MCSampling}(P_0, R, s)$;
    end
  end
end
$\mathcal{M} \leftarrow 0$;
for $-L/2 < n_x < L/2$ **do**
  for $-L/2 < n_y < L/2$ **do**
    $\mathcal{M} \leftarrow \mathcal{M} + \hat{G}_{q_x,q_y}$; `/* Procedure to normalize the kernel */`
  end
end
while $\gamma < l$ **do**
  $x_{\min} \leftarrow \mathrm{FindMinimum}(\underline{\underline{\sigma^{\mathrm{th}}}} - \underline{\underline{\sigma}})$; `/* Find least stable */`
  $\gamma \leftarrow \gamma + x_{\min}$; `/* Strain increment */`
  $\underline{\underline{\sigma}} \leftarrow \underline{\underline{\sigma}} + x_{\min}\underline{\underline{1}}$;
  $f_2 \leftarrow 1$;
  while f_2 **do**
    $f_2 \leftarrow 0$;
    $\underline{\underline{\delta\sigma}} \leftarrow \underline{\underline{0}}$;
    for $i < L$ **do**
      for $j < L$ **do**
        if $\sigma_{i,j} > 1$ **then**
          $\delta\sigma_{i,j} \leftarrow \sigma_{i,j} - \mathrm{sign}(\sigma_{i,j})(\sigma^{\mathrm{th}}_{i,j} - \mathrm{ExpSampling}(s))$;
          $\gamma^{\mathrm{pl}}_{i,j} \leftarrow \gamma^{\mathrm{pl}}_{i,j} + \delta\sigma_{i,j}$; `/* Unstable sites yield */`
          $\sigma^{\mathrm{th}}_{i,j} \leftarrow 1$;
          $f_2 \leftarrow 1$;
        end
      end
    end
    if f_2 **then**
      $\underline{\underline{\delta\hat{\sigma}}} \leftarrow \mathrm{FFT}(\underline{\underline{\delta\sigma}})$;
      $\underline{\underline{\sigma}} \leftarrow \underline{\underline{\sigma}} + \mathrm{IFFT}(\underline{\underline{\delta\hat{\sigma}}}\ \underline{\underline{\hat{G}'}})$; `/* Stress redistribution */`
    end
  end
end

2 Code for the standard RFIM

We discuss here the code to perform simulations of the standard Random-Field Ising Model (RFIM) in 2D, following the same approach of [129]. As for the EPM, we consider the AQS protocol, which amounts to increasing the external field, let the avalanche of spin flips relax, and then increase H again. The stability condition at the lattice site i reads $h_i^{\text{eff}} s_i > 0$, so that the spin has to take the sign of its local effective field, defined in Eq. (I.36) (we take $J = 1$ in the following). As an input to the code we give the standard deviation of the random fields R, the system size L, the limiting value for the magnetization l, and the seed s for the random number generator. We start with $H \to -\infty$ so that all the spins point down. We then proceed by initializing the 2D array that contains the local random fields $\underline{\underline{h}}$ and the one containing spin values $\underline{\underline{s}}$. The local random fields are chosen from a Gaussian distribution with zero mean and standard deviation R. Once these quantities have been initialized we enter into the first **while** loop, which corresponds to external driving. The effective field acting on each site is computed, and the one of the least stable spin is used to increase the external field H. We then enter in the second **while** loop, corresponding to avalanches. Here the value of each effective field is computed again (carefully considering the periodic boundary conditions), and the location of the sites for which $s_{i,j} h_{i,j}^{\text{eff}} < 0$ is saved in a 2D array $\underline{\underline{C}}$. If no unstable spins are found, we go back to increasing the external field, while in the other case we flip the sign of one spin at random between the ones saved in $\underline{\underline{C}}$. Since the interactions are ferromagnetic one can alternatively flip all the unstable spins together without altering the dynamics. This parallel update choice proves to be faster than the one in which unstable spins are flipped at random one at a time. This process goes on until the external field reaches the desired limit l (or the magnetization hits 1).

Notice that this algorithm is not the state-of-the art for the simulation of the RFIM. For a more careful study of the standard RFIM via computer simulations see for example [132, 170].

Algorithm 3: Pseudocode for the simulation of the standard 2D RFIM

Data: R, L, l, s

$H \leftarrow -\infty$;
$\underline{\underline{s}} \leftarrow -\underline{\underline{1}}$;
$\underline{\underline{h}} \leftarrow \underline{\underline{0}}$;
$\underline{\underline{h^{\text{eff}}}} \leftarrow \underline{\underline{0}}$;
for $i < L$ **do**
  for $j < L$ **do**
    $h_{i,j} \leftarrow \text{GaussianSampling}(R, s)$; /* Random field initialization */
  end
end
while $H < l$ **do**
  for $i < L$ **do**
    for $j < L$ **do**
      $h^{\text{eff}}_{i,j} \leftarrow s_{i+1,j} + s_{i-1,j} + s_{i,j+1} + s_{i,j-1} + h_{i,j} + H$;
    end
  end
  $h^{\text{eff}}_{\text{max}} \leftarrow \text{FindMaximum}(\underline{\underline{h^{\text{eff}}}} | h^{\text{eff}}_{i,j} < 0)$; /* Find least stable */
  $H \leftarrow H + |h^{\text{eff}}_{\text{max}}|$; /* External field increment */
  $f_2 \leftarrow 1$;
  while f_2 **do**
    $f_2 \leftarrow 0$;
    $\underline{\underline{C}} \leftarrow \underline{\underline{0}}$;
    for $i < L$ **do**
      for $j < L$ **do**
        $h^{\text{eff}}_{i,j} \leftarrow s_{i+1,j} + s_{i-1,j} + s_{i,j+1} + s_{i,j-1} + h_{i,j} + H$;
        if $s_{i,j} h^{\text{eff}}_{i,j} < 0$ **then**
          $C_{i,j} \leftarrow 1$; /* Memorize unstable spins */
          $f_2 \leftarrow 1$;
        end
      end
    end
    if f_2 **then**
      $(i_{\text{chosen}}, j_{\text{chosen}}) \leftarrow \text{ChooseRandom}(\underline{\underline{C}} | C_{i,j} == 1)$;
      $s_{i_{\text{chosen}}, j_{\text{chosen}}} \leftarrow -s_{i_{\text{chosen}}, j_{\text{chosen}}}$; /* Flip random unstable spin */
    end
  end
end

3 Code for the Eshelby-RFIM

We now discuss the code to implement the 2D Eshelby-RFIM. The interactions are given by the Eshelby kernel. The input parameters are the same of the standard RFIM case (see above). The initial field is again $H \to -\infty$. We start by defining the 2D spin array $\underline{s}$, with all spins pointing down, and the local random fields $\underline{h}$ chosen from a Gaussian distribution of 0 mean and standard deviation R. We then perform the operations to prepare the interaction kernel $\hat{G}''_{\mathbf{q}}$ defined in Eq. (A.50). We compute the Inverse Fourier transform of $\hat{G}''_{\mathbf{q}}$ to get its real space expression, and we store it in the 2D array $\underline{\underline{G}}$. Once the real space form of the kernel is defined we correct the interactions between nearest neighbors in order to have a proper $1/r^2$ decay. This is necessary to have a nice and sharp shear band, and should not affect the conclusions on the critical point. The propagator is then normalized again to assure $\hat{G}_{\mathbf{q}=0} = 0$ after this correction. To simplify the notation, we pack all these operations into the function "KernelDefinition" in the pseudocode below. The last step before launching the dynamics is to initialize the effective fields. At the beginning all spins are pointing down and, since $\hat{G}_{\mathbf{q}=0} = 0$, we simply start with $\underline{\underline{h^{\text{eff}}}} \leftarrow \underline{\underline{h}} + H$. We then enter the first **while** loop. We search for the largest effective field among the negative spins and we increase the external field accordingly. We then proceed to flip the relative spin and we propagate the effect of such a spin flip to the rest of the system by changing all the local effective fields. At this point we enter the second **while** loop. We check if there are unstable sites and if there are we flip one of them at random. Once the effective fields have been updated we check again for unstable sites and we go on until the whole system relaxes. Notice that, as discussed in the main text, in this case one cannot employ the parallel update algorithm since the interactions are not purely ferromagnetic, hence the system could potentially end up into an infinite loop in which two or more spins keep flipping at the same time without possibility of stopping. We then resort to the random update scheme, which allows the system to properly relax and does not enter any infinite loops. The drawback of this choice is a larger computational time, as one has to compute the Fourier transform of the whole system even if only one spin flips. To mitigate this effect, we compute the propagation of the spin flip effect to the system directly in the real space. This approach is not convenient when using the parallel update scheme, as many spins flip at the same time, while it is much faster in the random update case. When the system completely relaxes we increase the external field and start again, until we reach the desired limiting value of H.

3.1 Adding a seed

Also in the RFIM case we study what happens when a rare region is present inside the system from the beginning of the dynamics. We insert a seed by forcing some spins to be positive by means of a large random field that is imposed by hand. The pseudocode for the initialization of the 2D-RFIM (both NN and Eshelby ones) with a region of +1 spins characterized by sizes r_x and r_y can be found below. This code should be substituted to lines 2-9 of the pseudocode for the Eshelby-RFIM simulation, while the rest stays unchanged.

Algorithm 4: Pseudocode for the simulation of the 2D Eshelby-RFIM

Data: R, L, l, s

$H \leftarrow -\infty$;
$\underline{\underline{s}} \leftarrow -\underline{\underline{1}}$;
$\underline{\underline{h}} \leftarrow \underline{\underline{0}}$;
$\underline{\underline{h^{\text{eff}}}} \leftarrow \underline{\underline{0}}$;
for $i < L$ **do**
  for $j < L$ **do**
    $h_{i,j} \leftarrow \text{GaussianSampling}(R, s)$; `/* Random field initialization */`
  end
end
$\underline{\underline{h^{\text{eff}}}} \leftarrow \underline{\underline{h}} + H$;
$\underline{\underline{G}} \leftarrow \text{KernelDefinition}(L)$;
while $H < l$ **do**
  $h^{\text{eff}}_{\max} \leftarrow \text{FindMaximum}(\underline{\underline{h^{\text{eff}}}} | h^{\text{eff}}_{i,j} < 0)$; `/* Find least stable */`
  $H \leftarrow H + |h^{\text{eff}}_{\max}|$; `/* External field increment */`
  $s_{i_{\max}, j_{\max}} \leftarrow -s_{i_{\max}, j_{\max}}$;
  for $i < L$ **do**
    for $j < L$ **do**
      $h^{\text{eff}}_{i,j} \leftarrow h^{\text{eff}}_{i,j} + 2G_{i-i_{\max}, j-j_{\max}} + |h^{\text{eff}}_{\max}|$;
    end
  end
  $f_2 \leftarrow 1$;
  while f_2 **do**
    $f_2 \leftarrow 0$;
    $\underline{\underline{C}} \leftarrow \underline{\underline{0}}$;
    for $i < L$ **do**
      for $j < L$ **do**
        if $s_{i,j} h^{\text{eff}}_{i,j} < 0$ **then**
          $C_{i,j} \leftarrow 1$; `/* Memorize unstable spins */`
          $f_2 \leftarrow 1$;
        end
      end
    end
    if f_2 **then**
      $(i_{\text{chosen}}, j_{\text{chosen}}) \leftarrow \text{ChooseRandom}(\underline{\underline{C}} | C_{i,j} == 1)$;
      $s_{i_{\text{chosen}}, j_{\text{chosen}}} \leftarrow -s_{i_{\text{chosen}}, j_{\text{chosen}}}$; `/* Flip random unstable spin */`
      for $i < L$ **do**
        for $j < L$ **do**
          $h^{\text{eff}}_{i,j} \leftarrow h^{\text{eff}}_{i,j} + 2 s_{i_{\text{chosen}}, j_{\text{chosen}}} G_{i-i_{\text{chosen}}, j-j_{\text{chosen}}}$;
        end
      end
    end
  end
end

Algorithm 5: Pseudocode for the seed insertion for the 2D-RFIM

$\underline{\underline{s}} \leftarrow -\underline{\underline{1}}$;
$\underline{\underline{h}} \leftarrow \underline{\underline{0}}$;
$\underline{\underline{\underline{\underline{h}}}}^{\text{eff}} \leftarrow \underline{\underline{0}}$;
for $i < L$ **do**
  for $j < L$ **do**
    if $(i, j) \in \text{Seed}(\text{r}_\text{x}, \text{r}_\text{y})$ **then**
      $h_{i,j} \leftarrow \infty$;
      $s_{i,j} \leftarrow 1$;
    else
      $h_{i,j} \leftarrow \text{GaussianSampling}(R, s)$;
    end
  end
end

Appendix C

Mean-field Calculations

In this appendix we describe more in detail the calculations that lead to the formulas and results described in Chapter 3.

1 Details for the AQS driven mean-field soft-spin RFIM

We consider the mean-field soft-spin RFIM introduced in Section 1.2 of Chapter 3 with Hamiltonian

$$\mathcal{H}[\{s_i\}] = -\frac{J}{2N}\sum_{i,j\neq i} s_i s_j + \sum_i V(s_i) - \sum_{i=1}^{N}(h_i + H)s_i. \tag{C.1}$$

where $V(s_i)$ is the 2-parabola potential defined in Eq. (3.24). In the AQS evolution the system goes through minima of the Hamiltonian, with

$$-\frac{J}{N}\sum_{j\neq i} s_j + V'(s_i) = h_i + H. \tag{C.2}$$

On the ascending branch of the hysteresis curve in which the magnetic field H is adiabatically ramped up when starting from a large negative H, this directly leads to the solution in Eqs. (3.25) and (3.26). The average over the random-field distribution $\rho(h)$, which is equivalent to the average over samples α, then yields the average magnetization given in Eq. (3.27).

More generally, if one wishes to compute the average of quantities that are functions of the sample-dependent magnetization it is convenient to start from the identity $\overline{f(m^\alpha)} = \int_{-\infty}^{+\infty} dm f(m)\delta(m - m^\alpha)$ and after using Eq. (3.26) and standard manipulations,

$$\overline{f(m^\alpha)} \propto \int_{-\infty}^{+\infty} dm f(m) \int_{-i\infty}^{+i\infty} d\lambda e^{N\mathcal{G}(m,\lambda)}, \tag{C.3}$$

with

$$\mathcal{G}(m,\lambda) = \lambda\left[m + 1 - \frac{H + Jm}{k}\right] + \log\int_{-\infty}^{-H-Jm+k} dh e^{-\frac{\lambda}{k}h}\rho(h) + \int_{-H-Jm+k}^{+\infty} dh e^{-\frac{\lambda}{k}h - 2\lambda}\rho(h). \tag{C.4}$$

In the thermodynamic limit $N \to \infty$, the integrals in Eq. (C.3) can be treated via Laplace's method by an expansion around the saddle point (m^*, λ^*) satisfying

$$\mathcal{G}^{(0,1)}(m^*, \lambda^*) = \mathcal{G}^{(1,0)}(m^*, \lambda^*) = 0, \tag{C.5}$$

where the superscript indicate partial derivatives with respect to the arguments. In practice, to expand around the saddle-point, we introduce the fluctuations as

$$\begin{aligned} m &= m^* + \frac{\delta m}{\sqrt{N}} \\ \lambda &= \lambda^* + i\frac{\delta \lambda}{\sqrt{N}} \end{aligned} \tag{C.6}$$

where

$$\begin{aligned} &\lambda^* = 0, \\ &m^*(H) = \frac{k+H}{k-J} - \frac{2k}{k-J}\int_{-\infty}^{-H-Jm^*(H)+k} dh\rho(h). \end{aligned} \tag{C.7}$$

After some algebra, one easily finds that

$$\overline{f(m^\alpha)} = f(m^*) + \frac{f''(m^*)}{2N}[-\mathcal{G}_*^{(2,0)} + \frac{(\mathcal{G}_*^{(1,1)})^2}{\mathcal{G}_*^{(0,2)}}]^{-1}, \tag{C.8}$$

where

$$\begin{aligned} &\mathcal{G}_*^{(2,0)} \equiv \mathcal{G}^{(2,0)}(m^*, \lambda^*) = 0 \\ &\mathcal{G}_*^{(1,1)} \equiv \mathcal{G}^{(1,1)}(m^*, \lambda^*) = \left(1 - \frac{J}{k}\right) - 2J\rho(H + Jm^* - k), \\ &\mathcal{G}_*^{(0,2)} \equiv \mathcal{G}^{(0,2)}(m^*, \lambda^*) = \\ &\frac{\Delta_B^2}{k^2} + 4\int_{-H-Jm^*+k}^{+\infty} dh\rho(h) + \frac{4}{k}\int_{-H-Jm^*+k}^{+\infty} dhh\rho(h) - 4\left[\int_{-H-Jm^*+k}^{+\infty} dh\rho(h)\right]^2, \end{aligned} \tag{C.9}$$

and one can check that $\mathcal{G}_*^{(0,2)} > 0$. Consider now the disconnected susceptibility, $\chi_{\text{disc}}(H) = N\overline{[m^\alpha(H) - \overline{m^\alpha(H)}]^2}$. By applying the above formula in Eq. (C.8), one immediately obtains

$$\chi_{\text{disc}} = \frac{\mathcal{G}_*^{(0,2)}}{(\mathcal{G}_*^{(1,1)})^2}, \tag{C.10}$$

which after using the explicit expressions in Eq. (C.9) and $m^* = m + \mathrm{O}(1/\sqrt{N})$ leads to Eq. (3.33) of the main text.

2 Details for the AQS driven mean-field EPM

In this part of the appendix we detail the calculations that lead to the expression of the disconnected susceptibility, and hence of the effective disorder, for the EPM with different disorder sources.

2.1 Expression of the disconnected susceptibility

We first derive the expressions of the terms appearing in the disconnected susceptibility as given by Eq. (3.44). We start by considering the average of the squared fluctuations, $\overline{\langle \delta\hat{y}^{\alpha,[\hat{x}]_M}(\gamma)^2 \rangle}_{[\hat{x}]_M}$. As already stressed, it is easier to study the evolution as a function of y instead of γ (see Eq. (3.37)). Then, after integrating Eq. (3.2), one has

$$\delta\hat{\gamma}^{\alpha,[\hat{x}]_M}(y) = \frac{-\sqrt{N}}{2(\mu_1+\mu_2)} \sum_{n=1}^{M} \Big[\frac{1}{N} \sum_{i=1}^{N} \theta(dy - x_i^{\alpha,[\hat{x}]_n}(ndy))\hat{x}_i^{n+1} - < \hat{x} > F_{ndy}(dy) \Big], \quad \text{(C.11)}$$

where $y = Mdy$ and we recall that $F_y(x) = (1/N)\sum_i \overline{< \theta(x - x_i^{\alpha,[\hat{x}]_M}(y)) >_{[\hat{x}]_M}}$, so that

$$\begin{aligned} &\frac{4(\mu_1+\mu_2)^2}{N} \overline{\left\langle \left[\delta\hat{\gamma}^{\alpha,[\hat{x}]_M}(y)\right]^2 \right\rangle}_{[\hat{x}]_M} = \\ &\sum_{n',n''=1}^{M} \Big[\overline{\left\langle \frac{1}{N^2} \sum_{i,j=1}^{N} \theta(dy - x_i^{\alpha,[\hat{x}]_{n'}}(n'dy))\hat{x}_i^{n'+1} \theta(dy - x_j^{\alpha,[\hat{x}]_{n''}}(n''dy))\hat{x}_j^{n''+1} \right\rangle}_{[\hat{x}]_{\tilde{n}}} - \\ &< \hat{x} >^2 F_{n'dy}(dy) F_{n''dy}(dy) \Big]. \end{aligned} \quad \text{(C.12)}$$

where $\tilde{n} = \max(n', n'') + 1$. An important property is that the x_i's evolve independently when considering their evolution with y as the control parameter, so that when $i \neq j$ in the sum in the right-hand side of Eq. (C.12) one can factorize the average of the two θ functions. After some manipulations this leads to

$$\begin{aligned} &4(\mu_1+\mu_2)^2 \overline{\left\langle \left[\delta\hat{\gamma}^{\alpha,[\hat{x}]_M}(y)\right]^2 \right\rangle}_{[\hat{x}]_M} = \\ &\sum_{n',n''=1}^{M} \Big[\overline{\left\langle \theta(dy - x_i^{\alpha,[\hat{x}]_{n'}}(n'dy))\hat{x}_i^{n'+1} \theta(dy - x_i^{\alpha,[\hat{x}]_{n''}}(n''dy))\hat{x}_i^{n''+1} \right\rangle}_{[\hat{x}]_{\max(n',n'')+1}} \\ &- < \hat{x} >^2 F_{n'dy}(dy) F_{n''dy}(dy) \Big]. \end{aligned} \quad \text{(C.13)}$$

We need to compute the first term for the two different cases $n' = n''$ and $n' < n''$. When $n' = n''$ one simply has

$$\begin{aligned} &\sum_{n'=1}^{M} \overline{\left\langle \theta(dy - x_i^{\alpha,[\hat{x}]_{n'}}(n'dy))\hat{x}_i^{n'+1} \theta(dy - x_i^{\alpha,[\hat{x}]_{n'}}(n'dy))\hat{x}_i^{n'+1} \right\rangle}_{[\hat{x}]_{n'+1}} = \\ &\sum_{n'=1}^{M} \overline{\left\langle \theta(dy - x_i^{\alpha,[\hat{x}]_{n'}}(n'dy)) \left(\hat{x}_i^{n'+1}\right)^2 \right\rangle}_{[\hat{x}]_{n'+1}} = \int_0^\infty \hat{x}^2 g(\hat{x}) d\hat{x} \int_0^y P_{y'}(0) dy'. \end{aligned} \quad \text{(C.14)}$$

The case $n' < n''$ requires some care. First, the factor $\hat{x}_i^{n''+1}$ can be averaged alone, and

$$\begin{aligned} &\overline{\left\langle \theta(dy - x_i^{\alpha,[\hat{x}]_{n'}}(n'dy))\hat{x}_i^{n'+1} \theta(dy - x_i^{\alpha,[\hat{x}]_{n''}}(n''dy))\hat{x}_i^{n''+1} \right\rangle}_{[\hat{x}]_{n''+1}} = \\ &< \hat{x} > \overline{\left\langle \theta(dy - x_i^{\alpha,[\hat{x}]_{n'}}(n'dy))\hat{x}_i^{n'+1} \left\langle \theta(dy - x_i^{\alpha,[\hat{x}]_{n''}}(n''dy)) \right\rangle_{[\hat{x}]_{n'+2\to n''}} \right\rangle}_{[\hat{x}]_{n'+1}}. \end{aligned} \quad \text{(C.15)}$$

where $[\hat{x}]_{n'+2\to n''}$ means the sequence of random jumps between $\hat{x}_{n'+2}$ and $\hat{x}_{n''}$. From Eq. (3.5), when using the independence of the random jumps from one plastic event to another, one obtains that

$$\begin{aligned}&\left\langle \theta(dy - x_i^{\alpha,[\hat{x}]_{n''}}(n''dy))\right\rangle_{[\hat{x}]_{n'+2\to n''}} = \\ &\left\langle \theta(2dy - x_i^{\alpha,[\hat{x}]_{n''-1}}((n''-1)dy))\right\rangle_{[\hat{x}]_{n'+2\to n''-1}} \\ &- G(dy)\left\langle \theta(dy - x_i^{\alpha,[\hat{x}]_{n''}}((n''-1)dy))\right\rangle_{[\hat{x}]_{n'+2\to n''-1}}\end{aligned} \tag{C.16}$$

where $G(x) =< \theta(\hat{x}-x) >= \int_x^\infty d\hat{x}g(\hat{x})$, and, by repeating the procedure $(n''-n'-1)$ times,

$$\begin{aligned}&\left\langle \theta(dy - x_i^{\alpha,[\hat{x}]_{n''}}(n''dy))\right\rangle_{[\hat{x}]_{n'+2\to n''}} = \\ &\theta((n''-n')dy - x_i^{\alpha,[\hat{x}]_{n'+1}}((n'+1)dy)) - G(dy)\theta((n''-n'-1)dy - x_i^{\alpha,[\hat{x}]_{n'+1}}((n'+1)dy)) \\ &+ \sum_{n'''=1}^{n''-n'-2} S_{n''-n'-2-n'''}(dy)\theta(n'''dy - x_i^{\alpha,[\hat{x}]_{n'+1}}((n'+1)dy)),\end{aligned} \tag{C.17}$$

with $S_n(x)$ given by the self-consistent equation

$$S_n(x) = [g(x+ndy) - g(ndy)G(x) + \sum_{k=1}^{n} g((k-1)dy)S_{n-k}(x)]dy, \tag{C.18}$$

or in the continuum limit with $n\to\infty$, $dy\to 0$ with $ndy = y$ and $S_y(x) = S_n(x)/dy$,

$$S_y(x) = g(x+y) - g(y)G(x) + \int_0^y g(y')S_{y-y'}(x). \tag{C.19}$$

One easily checks that the function $R_y(x)$ introduced in Eq. (3.13) is the derivative of $S_y(x)$ with respect to x. With the above expressions, by using again Eq. (3.5) and then performing the average over $\hat{x}_{n'+1}$, one has

$$\begin{aligned}&\left\langle \hat{x}_i^{n'+1}\theta(dy - x_i^{\alpha,[\hat{x}]_{n''}}(n''dy))\hat{x}_i^{n''+1}\right\rangle_{[\hat{x}]_{n'+1}} =< \hat{x} > \theta((n''-n'+1)dy - x_i^{\alpha,[\hat{x}]_{n'}}(n'dy)) \\ &- T((n''-n')dy)\theta(dy - x_i^{\alpha,[\hat{x}]_{n'}}(n'dy)) - G(dy)[\,< \hat{x} > \theta((n''-n')dy - x_i^{\alpha,[\hat{x}]_{n'}}(n'dy)) \\ &- T((n''-n'-1)dy)\theta(dy - x_i^{\alpha,[\hat{x}]_{n'}}(n'dy))] + \sum_{n'''=1}^{n''-n'-2} S_{n''-n'-2-n'''}(dy)[\,< \hat{x} > \\ &\times \theta((n'''+1)dy - x_i^{\alpha,[\hat{x}]_{n'}}(n'dy)) - T(n'''dy)\theta(dy - x_i^{\alpha,[\hat{x}]_{n'}}(n'dy))]\end{aligned} \tag{C.20}$$

with $T(x) = \int_x^\infty d\hat{x}\hat{x}g(\hat{x})$. The last step is to multiply the above expression by $\theta(dy - x_i^{\alpha,[\hat{x}]_{n'}}(n'dy))$ and to perform the average over the sequence of random jumps $[\hat{x}]_{n'}$ and over the samples α. After some tedious algebra, we find

$$\begin{aligned}&\overline{\left\langle \theta(dy - x_i^{\alpha,[\hat{x}]_{n'}}(n'dy))\hat{x}_i^{n'+1}\theta(dy - x_i^{\alpha,[\hat{x}]_{n''}}(n''dy))\hat{x}_i^{n''+1}\right\rangle}_{[\hat{x}]_{n''+1}} = \\ &[< \hat{x} > -T((n''-n')dy)]F_{n'dy}(dy) - [< \hat{x} > -T((n''-n'-1)dy)]F_{n'dy}(dy) \\ &+ F_{n'dy}(dy)\sum_{n'''=1}^{n''-n'-2} S_{n''-n'-2-n'''}(dy)[< \hat{x} > -T(n'''dy)].\end{aligned} \tag{C.21}$$

Putting everything together and taking the continuum limit we finally obtain

$$\overline{\left\langle \left[\delta\hat{\gamma}^{\alpha,[\hat{x}]_M}(y)\right]^2\right\rangle}_{[\hat{x}]_M} = \left(\frac{1}{2(\mu_1+\mu_2)}\right)^2 \Big(< \hat{x}^2 > \int_0^y dy' P_{y'}(0) - < \hat{x} >^2 \left(\int_0^y dy' P_{y'}(0)\right)^2 \\ + 2 < \hat{x} > \int_0^y dy' P_{y'}(0) \int_{y'}^y dy'' \Big[g(0)[< \hat{x} > -T(y''-y')] - T'(y''-y') \\ + \int_0^{y''-y'} d\hat{y}[< \hat{x} > -T(\hat{y})] R_{y''-y'-\hat{y}}(0) \Big] \Big). \tag{C.22}$$

By passing from the variable y to the variable γ, this then leads to Eq. (3.46). One checks that the above expression is equal to 0 when $y = 0$ and by using the Laplace transform and expanding one finds that when $y \to \infty$,

$$[2(\mu_1+\mu_2)]^2 \overline{\left\langle \left[\delta\hat{\gamma}^{\alpha,[\hat{x}]_M}(y)\right]^2\right\rangle}_{[\hat{x}]_M} \to \Delta_0 - \frac{< \hat{x}^2 >^2}{4 < \hat{x} >^2} + \frac{< \hat{x}^3 >}{3 < \hat{x} >}. \tag{C.23}$$

where $\overline{x} = 1$ and $\Delta_0 = \overline{x^2} - 1$.

We now consider the mixed term $\overline{\langle \delta\hat{y}^{\alpha,[\hat{x}]_M}(\gamma)\delta\hat{m}^{\alpha}(0)\rangle}_{[\hat{x}]_M}$. Changing again from γ to y, we define

$$Q(y) = \overline{\langle \delta\hat{\gamma}^{\alpha,[\hat{x}]_M}(y)\delta\hat{m}^{\alpha}(0)\rangle}_{[\hat{x}]_M} \tag{C.24}$$

From the equation for $\delta\hat{\gamma}^{\alpha,[\hat{x}]_M}(y)$ which we have already used above and some straightforward manipulations, we find

$$\begin{aligned} Q(y) &= -\frac{1}{2(\mu_1+\mu_2)N} \sum_{n=1}^{M} \sum_{i,j=1}^{N} \overline{\left\langle \theta(dy - x_i^{\alpha,[\hat{x}]_n}(ndy))\hat{x}_i^{n+1}\right\rangle_{[\hat{x}]_M} [x_j^{\alpha}(0) - 1]} \\ &= -\frac{< \hat{x} >}{2(\mu_1+\mu_2)N} \sum_{i=1}^{N} \overline{\sum_{n=1}^{M} \left\langle \theta(dy - x_i^{\alpha,[\hat{x}]_n}(ndy))\right\rangle_{[\hat{x}]_n} [x_i^{\alpha}(0) - 1]}. \end{aligned} \tag{C.25}$$

where we have taken advantage of the independence of the site variables when y is the control variable and we have used that by construction $\overline{x_j^{\alpha}(0)} = 1 - \overline{\sigma_j^{\alpha}(0)} = 1$. As for deriving the expression of $\overline{\left\langle \left[\delta\hat{\gamma}^{\alpha,[\hat{x}]_M}(y)\right]^2\right\rangle}_{[\hat{x}]_M}$, we can use the equation relating $\theta(x - x_i^{\alpha,[\hat{x}]_n}(ndy))$ at step n to the same function at earlier steps. After taking the continuum limit, one easily finds that

$$\left\langle \theta(x - x_i^{\alpha,[\hat{x}]_n}(y))\right\rangle_{[\hat{x}]_n} = \theta(x + y - x_i^{\alpha}(0)) - G(x)\theta(y - x_i^{\alpha}(0)) + \int_0^y dy' S_{y-y'}(x)\theta(y' - x_i^{\alpha}(0)), \tag{C.26}$$

with $S_y(x)$ defined in Eq. (C.19). Inserting Eq. (C.26) in Eq. (C.25) and performing the average over the samples, i.e., over the $x_i^{\alpha}(0)$ leads to

$$\begin{aligned} Q(y) = &- \frac{< \hat{x} >}{2(\mu_1+\mu_2)} \int_0^y dy' \Big[(y'-1)P_0(y') + g(0) \int_0^{y'} dy''(y''-1)P_0(y'') \\ &+ \int_0^{y'} dy'' R_{y'-y''}(0) \int_0^{y''} d\hat{y}(\hat{y}-1)P_0(\hat{y}) \Big], \end{aligned} \tag{C.27}$$

from which one finally obtains Eq. (3.47). One finds that the above expression is 0 when $y = 0$ and it goes to

$$Q(y) \to \frac{1}{2(\mu_1 + \mu_2)} \Delta_0 \tag{C.28}$$

when $y \to \infty$.

2.2 Solving different models

In this part we discuss the calculations in models with different sources of disorder.

2.2.1 One- and two-exponential distributions of random jumps

The results are most easily obtained by using a Laplace transform on the variable y. We consider here the 1- and 2-exponential distributions of random jumps defined in Eq. (3.49). Their Laplace transforms read

$$\begin{aligned} \hat{g}^{1\text{exp}}(s) &= \frac{1}{1+ < \hat{x} > s}, \\ \hat{g}^{2\text{exp}}(s) &= \frac{1}{[1+ts][1+(< \hat{x} > -t)s]}. \end{aligned} \tag{C.29}$$

One easily finds from Eqs. (3.12) and (3.13) that

$$\begin{aligned} \hat{R}_s(x) &= -g(x) + se^{sx} \frac{[\hat{g}(s) - \int_0^x dy e^{-sy} g(y)]}{1 - \hat{g}(s)}, \\ \hat{P}_s(x) &= e^{sx}[\hat{P}_0(s) - \int_0^x dy e^{-sy} \hat{P}_0(y)] + \hat{P}_0(s) e^{sx} \frac{[\hat{g}(s) - \int_0^x dy e^{-sy} g(y)]}{1 - \hat{g}(s)}, \end{aligned} \tag{C.30}$$

where a "hat" indicates a Laplace transform with respect to y. It is easy to check that for the single-exponential distribution, $\hat{R}_s(x) = 0$. Furthermore, since from Eq. (C.30) $\hat{P}_s(0) = \hat{P}_0(s)/[1 - \hat{g}(s)]$, one has

$$P_y^{2\text{exp}}(0) = P_0(y) + \frac{1}{< \hat{x} >} \int_0^y dy' P_0(y') [1 - e^{-\frac{< \hat{x} >}{t(< \hat{x} > -t)}(y-y')}] \tag{C.31}$$

which can be solved once an initial distribution $P_0(x)$ has been chosen. (The single-exponential result is simply obtained by dropping the last term in the bracket inside the integral.) The numerical solution for all the averaged quantities (average stress, connected susceptibility) is then easily obtained. The contributions to the sample-to-sample fluctuations can be cast in the form

$$\begin{aligned} &[2(\mu_1 + \mu_2)]^2 \overline{\left\langle [\delta \hat{\gamma}^{\alpha, [\hat{x}]_M}(y)]^2 \right\rangle}_{[\hat{x}]_M} = \\ &\mathcal{L}_y^{-1} \Big\{ < \hat{x}^2 > \frac{\hat{P}_0(s)}{s[1 - \hat{g}(s)]} - < \hat{x} >^2 \int_0^\infty dy e^{-sy} \left(\int_0^y dy' P_{y'}(0) \right)^2 - 2 < \hat{x} > \frac{\hat{P}_0(s)}{s[1 - \hat{g}(s)]^2} g'(s) \Big\}, \end{aligned} \tag{C.32}$$

and

$$(\mu_1 + \mu_2) \overline{\langle \delta \hat{\gamma}^{\alpha, [\hat{x}]_M}(y) \delta \hat{m}^\alpha(0) \rangle}_{[\hat{x}]_M} = \frac{< \hat{x} >}{2} \mathcal{L}_y^{-1} \Big\{ \frac{[\hat{P}_0'(s) + \hat{P}_0(s)]}{s[1 - \hat{g}(s)]} \Big\}. \tag{C.33}$$

where $\mathcal{L}_y^{-1}$ denotes the inverse Laplace transform. Again, since $P_y(0)$ is expressed in terms of $P_0(y)$, one can compute from the above expressions the disconnected susceptibility for the 2-exponential and single-exponential random-jump distributions once an initial distribution $P_0(x)$ is specified.

2.2.2 Fixed-jump model

For the fixed-jump model (see Eq. (3.49)) the only randomness is in the initial condition. Eq. (3.1) simplifies to

$$\begin{aligned} dy^\alpha &= 2\mu_2 d\gamma + \frac{\mu_2 < \hat{x} >}{N(\mu_1+\mu_2)} \sum_{i=1}^{N} \theta(dy^\alpha - x_i^\alpha(\gamma)) \\ &= 2\mu_2 d\gamma + x_c F_y^\alpha(dy^\alpha), \end{aligned} \tag{C.34}$$

and similar simplifications occur for the other equations.

Consider first the averaged quantities. We work with y as the control parameter and we start with the equation for the (averaged) cumulative probability, $F_y(x) = \int_0^x dx' P_y(x')$,

$$\partial_y F_y(x) = \partial_x F_y(x) - P_y(0)\theta(< \hat{x} > -x). \tag{C.35}$$

In this subsection, to alleviate the notation, we replace $< \hat{x} >$ by $\hat{x}$ (there is anyhow no randomness in the jumps). To solve the above equation we have to consider the two cases $x > \hat{x}$ and $x < \hat{x}$ separately.

- $x > \hat{x}$

Eq. (C.35) then reduces to

$$\partial_y F_y(x) = \partial_x F_y(x), \tag{C.36}$$

which implies that $F_y(x)$ is a function of only $x + y$. Using the condition at $y = 0$ gives

$$F_y(x) = F_0(x + y), \tag{C.37}$$

Note that the condition that $F_y(x) \to 1$ when $y \to \infty$ is properly satisfied. The condition comes from the fact that at large strain (or y), all the sites have undergone at least one plastic event, so that their stability cannot be larger than $\hat{x}$ (whereas this could be possible at small y if $P_0(x)$ extends over all values of x). As a result, $F_y(x)$ being the cumulative distribution, it must be equal to 1.

- $x < \hat{x}$

Then,

$$(\partial_y - \partial_x)\, F_y(x) = -P_y(0), \tag{C.38}$$

so that $F_y(x)$ is a function of y and $x + y$. It can be written as $F_y(x) = P(x + y) - H(y)$, with

$$H(y) = \int_0^y dy' P_{y'}(0) \tag{C.39}$$

and $P(x + y)$ yet to be determined. The condition that $F_y(0) = 0$ then imposes that $F_y(x) = H(x + y) - H(y)$. One expects that the function $H(y)$ is piecewise continuous and one easily checks that it takes the form

$$H(y) = H_0(y) + \sum_{n=1}^{\infty} H_0(y - n\hat{x})\theta(y - n\hat{x}), \tag{C.40}$$

with $H_0(y)$ defined between 0 and $\hat{x}$. From the above results, one finds the solution for all values of x as

$$\begin{aligned} F_y(x) =& F_0(y+x) + \theta(\hat{x}-x)\Bigg[- F_0(y) + \sum_{n=1}^{\infty} \big(F_0(y+x-n\hat{x})\theta(y+x-n\hat{x}) \\ & - F_0(y-n\hat{x})\theta(y-n\hat{x})\big)\Bigg], \end{aligned} \tag{C.41}$$

and by deriving with respect to x,

$$P_y(x) = P_0(y+x) + \theta(\hat{x}-x)\sum_{n=1}^{\infty} \theta(y+x-n\hat{x})P_0(y+x-n\hat{x}). \tag{C.42}$$

This solution is a periodic function of y for large values of y since the contribution from the first term vanishes when $y \to \infty$. The periodicity of this function (of period $\hat{x}$) is clearly unphysical and disappears as soon as one introduces randomness in the jumps (or in the thresholds).

The expressions of the average stress and of the connected susceptibility versus the strain γ are then derived by using the general formulas given in the main text. Note that by combining Eq. (C.42) and Eqs. (3.17) and (3.19) one finds

$$\begin{aligned} \gamma(y+\hat{x}) - \gamma(y) &= \frac{1}{2\mu_2}[\hat{x} - x_c \int_0^{y+\hat{x}} dx' P_0(x')], \\ \sigma(y+\hat{x}) - \sigma(y) &= \int_{y+\hat{x}}^{\infty} dx' P_0(x')[\hat{x} + 2(1+y-x')], \end{aligned} \tag{C.43}$$

so that when $y \gg 1$, $\gamma(y+\hat{x}) - \gamma(y) \to \hat{x}\frac{\mu_1}{2\mu_2(\mu_1+\mu_2)}$ and $\sigma(y+\hat{x}) - \sigma(y) \to 0$.

We next study the disconnected susceptibility,

$$\chi_{\rm dis}(\gamma) = \Delta_0 + \left(\frac{\mu_1}{\mu_2}\right)^2 \overline{\delta\hat{y}^\alpha(\gamma)^2} + 2\left(\frac{\mu_1}{\mu_2}\right)\overline{\delta\hat{y}^\alpha(\gamma)\delta\hat{m}^\alpha(0)}, \tag{C.44}$$

by considering as before the fluctuations with y as the control parameter.

We first calculate the squared-fluctuation term. One has

$$\overline{\delta\hat{\gamma}^\alpha(y)^2} = \left(\frac{x_c}{2\mu_2}\right)^2 N \sum_{n'=0}^{M}\sum_{n''=0}^{M} \Big[\overline{F^\alpha_{n'dy}(dy)F^\alpha_{n''dy}(dy)} - F_{n'dy}(dy)F_{n''dy}(dy)\Big], \tag{C.45}$$

where $Mdy = y$. The function $F_{y',y''}(x',x'') = \overline{F^\alpha_{y'}(x')F^\alpha_{y''}(x'')}$ satisfies evolution equations that generalize Eq. (C.35):

$$\begin{aligned} \partial_{y'}F_{y',y''}(x',x'') &= \partial_{x'}F_{y',y''}(x',x'') - \partial_{x'}F_{y',y''}(x,x')\Big|_{x'=0}\theta(\hat{x}-x') \\ \partial_{y''}F_{y',y''}(x',x'') &= \partial_{x''}F_{y',y''}(x',x'') - \partial_{x''}F_{y',y''}(x,x')\Big|_{x''=0}\theta(\hat{x}-x''). \end{aligned} \tag{C.46}$$

Furthermore, one can introduce the function $H_{y',y''}(x',x'')$ through

$$F_{y',y''}(x',x'') = \left(1-\frac{1}{N}\right)F_{y'}(x')F_{y''}(x'') + \frac{1}{N}H_{y',y''}(x',x''), \tag{C.47}$$

where we have used the independence of the evolution with y of the variables on different sites. The above equations for $F_{y',y''}(x',x'')$ translate into equations for $H_{y',y''}(x',x'')$. They can be solved by using the procedure followed above or $F_y(x)$ and considering separately the cases $x',x'' < \hat{x}$, $x' < \hat{x} < \hat{x}''$ or $x'' < \hat{x} < \hat{x}'$, and $\hat{x} < x',x''$. One can then show that

$$H_{y',y''}(x',x'') = U(y'+x',y''+x'') - U(y'+x',x'') - U(x',y''+x'') + U(y',y''), \tag{C.48}$$

with

$$\begin{aligned} U(z',z'') =& F_0(\min(z',z'')) + \sum_{n=1}^{\infty} F_0(\min(z'-n\hat{x},z''))\theta\Big(z'-n\hat{x}\Big) \\ &+ \sum_{n=1}^{\infty} F_0(z',\min(z''-n\hat{x}))\theta\Big(z''-n\hat{x}\Big) \\ &+ \sum_{n'=1}^{\infty}\sum_{n''=1}^{\infty} F_0(\min(z'-n'\hat{x},z''-n''\hat{x}))\theta\Big(z'-n'\hat{x}\Big)\theta\Big(z''-n''\hat{x}\Big). \end{aligned} \tag{C.49}$$

From Eqs. (C.45) and (C.47), one can write the averaged squared fluctuations as

$$\overline{\delta\hat{\gamma}^{\alpha}(y)^2} = \left(\frac{x_c}{2\mu_2}\right)^2 \sum_{n'=0}^{M}\sum_{n''=0}^{M}\Big[H_{n'dy,n''dy}(x',x'') - F_{n'dy}(dy)F_{n''dy}(dy)\Big], \tag{C.50}$$

which after expanding in dy and taking the continuum limit gives

$$\overline{\delta\hat{\gamma}^{\alpha}(y)^2} = \left(\frac{x_c}{2\mu_2}\right)^2 [U(y,y) - H(y)^2], \tag{C.51}$$

where $H(y)$ has been defined before. We now compute the cross term $\overline{\delta\hat{\gamma}^{\alpha}(y)\delta\hat{m}^{\alpha}(0)}$ which can be expressed as

$$\overline{\delta\hat{\gamma}^{\alpha}(y)\delta\hat{m}^{\alpha}(0)} = \frac{x_c\sqrt{N}}{2\mu_2}\sum_{n=1}^{M}\overline{\Big[F_{n\,dy}(dy) - F^{\alpha}_{n\,dy}(dy)\Big][m^{\alpha}(0)-1]}, \tag{C.52}$$

with

$$m^{\alpha}(0) = \int_0^{\infty} dx'x'\frac{\partial}{\partial x'}F_0^{\alpha}(x'). \tag{C.53}$$

After some lengthy but straightforward manipulations, we find that

$$\overline{\delta\hat{\gamma}^{\alpha}(y)\delta\hat{m}^{\alpha}(0)} = \frac{x_c}{2\mu_2}\sum_{n=0}^{\infty}\int_0^{y-n\hat{x}} dy'P_0(y')(1-y'). \tag{C.54}$$

Using the formulas to switch from fluctuations at constant y to fluctuations at constant γ and collecting all the terms, we finally obtain an expression for the disconnected susceptibility.

2.3 Annealed average over the random jumps

We go back to the generic case where the local stress jumps are random and we consider an annealed calculation in which one first averages all quantities over the random jumps, i.e.,

$$A_y^{\alpha,[\hat{x}]_M}(x) \to A_y^{\alpha}(x) = \left\langle A_y^{\alpha,[\hat{x}]_M}(x) \right\rangle_{[\hat{x}]_M}. \tag{C.55}$$

Clearly, this procedure does not change the result for the average stress nor for the connected susceptibility. However, this modifies the sample-to-sample fluctuations and the disconnected susceptibility, which is now written

$$\chi_{\rm disc}^{\rm (ann)}(\gamma) = \Delta_0 + \left(\frac{\mu_1}{\mu_2}\right)^2 \overline{\langle \delta\hat{y}^\alpha(\gamma)\rangle_{[\hat{x}]_M}^2} + 2\left(\frac{\mu_1}{\mu_2}\right) \overline{\langle \delta\hat{y}^\alpha(\gamma)\rangle_{[\hat{x}]_M}^2 \, \delta\hat{m}^\alpha(0)}, \tag{C.56}$$

One can see that the only term that is different from the quenched-average calculation is the squared-fluctuation term (the second one in the right-hand side). We thus compute this term by changing again from γ to y for the control parameter. We introduce the random-jump averaged fluctuation

$$\delta\hat{\gamma}^\alpha(y) = \left\langle \delta\hat{\gamma}^{\alpha,[\hat{x}]_M}(y) \right\rangle_{[\hat{x}]_M} = \frac{x_c}{2\mu_2} \sum_{n=1}^{M} \left(F_{ndy}^\alpha(dy) - F_{ndy}(dy) \right), \tag{C.57}$$

with

$$F_y^\alpha(x) = \left\langle F_y^{\alpha,[\hat{x}]_M}(x) \right\rangle_{[\hat{x}]_M} = F_0^\alpha(x+y) - G(x)F_0^\alpha(y) + \int_0^y dy' F_0^\alpha(y') S_{y-y'}(x). \tag{C.58}$$

When computing the sample-averaged squared fluctuations we will have to consider the average of products of functions $F_y^\alpha(x)$. We therefore derive the general formula

$$\begin{aligned}
\overline{F_{y'}^\alpha(x) F_{y''}^\alpha(x)} &= \left(1 - \frac{1}{N}\right) F_{y'}(x) F_{y''}(x) + \frac{1}{N}\Big[\frac{1}{2}\Big(F_0(\min(y', y'') + x) + G^2(x) F_0(\min(y', y'')) \\
&+ \int_0^{y'}\int_0^{y''} d\hat{y}' d\hat{y}'' F_0(\min(\hat{y}', \hat{y}'')) S_{y'-\hat{y}'}(x) S_{y''-\hat{y}''}(x)\Big) - G(x) F_0(\min(x+y', y'')) \\
&+ \int_0^{y''} d\hat{y} [F_0(\min(y'+x, \hat{y})) - G(x) F_0(\min(y', \hat{y}))] S_{y''-\hat{y}}(x) + y' \leftrightarrow y''\Big],
\end{aligned} \tag{C.59}$$

where $y' \leftrightarrow y''$ denotes the term obtained by exchanging y' and y''. To simplify the calculation, we restrict ourselves to the single-exponential random-jump distribution. Then,

$$F_y^\alpha(x) = F_0^\alpha(x+y) - e^{-\frac{x}{<\hat{x}>}} F_0^\alpha(y). \tag{C.60}$$

and

$$\begin{aligned}
\overline{F_{y'}^\alpha(x) F_{y''}^\alpha(x)} &= \left(1 - \frac{1}{N}\right) F_{y'}(x) F_{y''}(x) + \frac{1}{N}\Big[F_0(x + \min(y', y'')) \\
&+ e^{-\frac{2x}{<\hat{x}>}} F_0(\min(y', y'')) - e^{-\frac{x}{<\hat{x}>}} \left(F_0(\min(y', x+y'')) + F_0(\min(y'', x+y''))\right)\Big].
\end{aligned} \tag{C.61}$$

We can now compute the fluctuations as

$$\begin{aligned}\overline{\delta\hat{\gamma}^{\alpha}(y)^2} &= N\left(\frac{<\hat{x}>}{2(\mu_2+\mu_1)}\right)^2 \sum_{n',n''=1}^{M}\left(\overline{F^{\alpha}_{n'dy}(dy)F^{\alpha}_{n''dy}(dy)} - F_{n'dy}(dy)F_{n''dy}(dy)\right)\\ &= \left(\frac{<\hat{x}>}{2(\mu_2+\mu_1)}\right)^2 \sum_{n',n''=1}^{M}\Big[F_0(dy+dy\min(n',n'')) + e^{-\frac{2dy}{<\hat{x}>}}F_0(dy\min(n',n''))\\ &-e^{-\frac{dy}{<\hat{x}>}}\left(F_0(dy\min(n',1+n'')) + F_0(dy\min(n'',1+n'))\right) - F_{n'dy}(dy)F_{n''dy}(dy)\Big].\end{aligned} \tag{C.62}$$

Some care is needed to consider separately the cases $n'=n''$ and $n'<n''$ (or $n''<n'$), and we finally arrive at the sought-for expression,

$$\overline{\delta\hat{y}^{\alpha}(\gamma)^2} = \left(\frac{<\hat{x}>}{2(\mu_2+\mu_1)}\right)^2\left[F_0(y) + \frac{2}{<\hat{x}>}\int_0^y dy' P_{y'}(0)(y-y') - \left(\int_0^y dy' P_{y'}(0)\right)^2\right]. \tag{C.63}$$

From this and previous results we can compute the annealed disconnected susceptibility as a function of γ.

3 Direct mapping between correlation functions in MF-EPM and MF-RFIM

In this section of the appendix we push further the idea of a direct mapping between correlation functions in the mean-field EPM and a mean-field RFIM which was discussed in Section 1.3 of Chapter 3. As already explained, this can only be done in a restricted range of the driving parameter, in the vicinity of the yielding transition. In particular, the range must be small enough that (i) the connected susceptibility of the mean-field EPM is positive and large (region (iii) in the main text, i.e., between the overshoot and the steady state) and that, moreover, (ii) the sites in the EPM yield only once. We define this range as $[\gamma_0, \gamma_{\rm m}]$, which translates in an interval $[H_0, H_{\rm m}]$ for the RFIM. At γ_0 the state of the EPM is given by the exact evolution starting from $\gamma = 0$. However, we have more freedom for the RFIM. The only requirement is that the system be in a metastable state at H_0, and we can relax the condition used in the main text that this state is the one obtained by ramping up the external field from $-\infty$ and by following the ascending (lower) branch of the hysteresis loop. In the following we first express the evolution of the mean-field EPM and mean-field RFIM in terms of the initial condition at γ_0 or H_0 only. Once the evolution equations for the two models starting from an arbitrary value of the external field are obtained, we compare the results in order to check the similarities between the two. By forcing some conditions we are able to find an exact mapping between the average evolution of the two models.

3.1 Mean-field EPM starting from finite strain

For simplicity, as in Section 1.3 of Chapter 3, we consider a model in which randomness is only in the initial condition, with $g(\hat{x}) = \delta(\hat{x} - <\hat{x}>)$. This is not expected to alter the qualitative behavior of the system in the close vicinity of the yielding transition (of course, as shown in Fig. 3.5, it does for the steady state). We again switch the control parameter from

γ to y and then study the evolution between y_0 and y_m, with $y_0 = \overline{y^\alpha(\gamma_0)}$ and $y_\mathrm{m} = \overline{y^\alpha(\gamma_\mathrm{m})}$. Due to the assumption of a single jump per site, the local stability evolves according to

$$\begin{aligned} x_i^\alpha(y) &= x_i^\alpha(y_0) - (y - y_0), && \text{when } (y - y_0) < x_i^\alpha(y_0), \\ &= x_i^\alpha(y_0) - (y - y_0) + < \hat{x} >, && \text{when } (y - y_0) > x_i^\alpha(y_0), \end{aligned} \tag{C.64}$$

which is the equivalent of Eq. (3.28) in main text, with the local stability as a function of y instead of γ. One immediately derives for the volume-averaged quantity (compare with Eq. (3.14))

$$\widetilde{m}^\alpha(y) = \widetilde{m}^\alpha(y_0) - (y - y_0) + < \hat{x} > \int_0^{y-y_0} dx P_{y_0}^\alpha(x), \tag{C.65}$$

where $P_{y_0}^\alpha(x) = (1/N) \sum_i \delta(x - x_i^\alpha(y_0))$, and, after averaging over the samples,

$$\widetilde{m}(y) = \overline{x}(y_0) - (y - y_0) + < \hat{x} > \int_0^{y-y_0} dx P_{y_0}(x), \tag{C.66}$$

To go back from y to the original control parameter γ, we use

$$\begin{aligned} 2\mu_2[\gamma^\alpha(y) - \gamma^\alpha(y_0)] &= y - y_0 - \frac{x_c}{N} \sum_i \int_{y_0}^{y} dy' \delta(-x_i^\alpha(y')) \\ &= y - y_0 - \frac{x_c}{N} \sum_i \int_{y_0}^{y} dy' \delta(-x_i^\alpha(y_0) + y' - y_0) \end{aligned} \tag{C.67}$$

where the second equation is obtained by taking into account the fact that only one jump per site is allowed. This is true provided $y - y_0$ is small enough (in particular, one should have $y - y_0 \ll < \hat{x} >$). After averaging, one has

$$2\mu_2[\gamma(y) - \gamma_0] = (y - y_0) - x_c \int_0^{y-y_0} dy' P_{y_0}(y'), \tag{C.68}$$

which can be inverted to give

$$\Delta y(\gamma) = y(\gamma) - y_0 = 2\mu_2(\gamma - \gamma_0) + x_c \int_0^{\Delta y(\gamma)} dy' P_{y_0}(y'), \tag{C.69}$$

and by derivation,

$$\frac{\partial \Delta y(\gamma)}{\partial \gamma} = \frac{2\mu_2}{1 - x_c P_{y_0}(\Delta y(\gamma))}, \tag{C.70}$$

where one should keep in mind that Δy also depends on γ_0. The connected susceptibility $\chi_\mathrm{conn}(\gamma) = m'(\gamma)$ can then be expressed as

$$\chi_\mathrm{conn}(\gamma) = \frac{\partial \widetilde{m}(\Delta y)}{\partial \Delta y} \frac{\partial \Delta y(\gamma)}{\partial \gamma} = \frac{2\mu_2(-1 + < \hat{x} > P_{y_0}(\Delta y(\gamma)))}{1 - x_c P_{y_0}(\Delta y(\gamma))}. \tag{C.71}$$

One can notice by comparing with the exact expression in Eq. (3.35) that the single-jump approximation leads to the substitution of $P_{y_0+\Delta y}(0)$ with $P_{y_0}(\Delta y)$. This makes sense, since if a site is unstable at y, with $x_i(y) = 0$, it should be the first time since y_0, meaning that

it evolved only elastically with, as a consequence, $x_i(y_0) = y - y_0$. The condition that the connected susceptibility is positive in the relevant interval of γ or y implies that

$$P_{y_0}(\Delta y) > \frac{1}{< \hat{x} >}, \tag{C.72}$$

and puts a bound on the possible values of y_0 and $y_{\rm m}$. We now proceed with the computation of the sample-to-sample fluctuations. In what follows we set $2\mu_2 = 1$ to simplify the notation. Following the same procedure as in the main text, we introduce the reduced fluctuations $\delta\hat{m}^\alpha(\gamma)$, $\delta\hat{\tilde{m}}^\alpha(y)$, $\delta\hat{y}^\alpha(\gamma)$, and $\delta\hat{\gamma}^\alpha(y)$. One still has

$$\delta\hat{m}^\alpha(\gamma) = \delta\hat{\tilde{m}}^\alpha(y(\gamma)) + \tilde{m}'(y(\gamma))\delta\hat{y}^\alpha(\gamma), \tag{C.73}$$

and therefore,

$$\delta\hat{m}^\alpha(\gamma) - \delta\hat{m}^\alpha(\gamma_0) = \delta\hat{\tilde{m}}^\alpha(y(\gamma)) - \delta\hat{\tilde{m}}^\alpha(y_0) + \tilde{m}'(y(\gamma))\delta\hat{y}^\alpha(\gamma) - \tilde{m}'(y_0)\delta\hat{y}^\alpha(\gamma_0). \tag{C.74}$$

By combining Eqs. (C.65) and (C.67), we derive

$$\gamma^\alpha(y) - \gamma^\alpha(y_0) = \left(1 - \frac{x_c}{< \hat{x} >}\right)\Delta y - \frac{x_c}{< \hat{x} >}[\tilde{m}^\alpha(y) - \tilde{m}^\alpha(y_0)], \tag{C.75}$$

which can be inverted to give

$$y^\alpha(\gamma) - y_0 = \frac{< \hat{x} >}{< \hat{x} > - x_c}(\gamma - \gamma_0) + \frac{x_c}{< \hat{x} > - x_c}[m^\alpha(\gamma) - m^\alpha(\gamma_0)]. \tag{C.76}$$

The fluctuations of y can then be rewritten as

$$\delta\hat{y}^\alpha(\gamma) = \delta\hat{y}^\alpha(\gamma_0) + \frac{x_c}{< \hat{x} > - x_c}\left[\delta\hat{m}^\alpha(\gamma) - \delta\hat{m}^\alpha(\gamma_0)\right], \tag{C.77}$$

from which we get

$$\delta\hat{m}^\alpha(\gamma) = \delta\hat{m}^\alpha(\gamma_0) + \frac{\delta\hat{\tilde{m}}^\alpha(y(\gamma)) - \delta\hat{\tilde{m}}^\alpha(y_0) + (\tilde{m}'(y(\gamma)) - \tilde{m}'(y_0))\delta\hat{y}^\alpha(\gamma_0)}{1 - \frac{x_c}{<\hat{x}> - x_c}\tilde{m}'(y(\gamma))}. \tag{C.78}$$

The disconnected susceptibility $\chi_{\rm disc}(\gamma) = \overline{\delta\hat{m}^\alpha(\gamma)^2}$ can then be expressed as

$$\begin{aligned}\chi_{\rm disc}(\gamma) =& \chi_{\rm disc}(\gamma_0) + 2\chi_{\rm conn}(\gamma)\overline{\frac{\delta\hat{m}^\alpha(\gamma_0)[\delta\hat{\tilde{m}}^\alpha(y(\gamma)) - \delta\hat{\tilde{m}}^\alpha(y_0) + (\tilde{m}'(y(\gamma)) - \tilde{m}'(y_0))\delta\hat{y}^\alpha(\gamma_0)]}{\frac{<\hat{x}>}{<\hat{x}> - x_c}\tilde{m}'(y(\gamma))}} \\ &+ \chi_{\rm conn}(\gamma)^2\overline{\frac{[\delta\hat{\tilde{m}}^\alpha(y(\gamma)) - \delta\hat{\tilde{m}}^\alpha(y_0) + (\tilde{m}'(y(\gamma)) - \tilde{m}'(y_0))\delta\hat{y}^\alpha(\gamma_0)]^2}{\left(\frac{<\hat{x}>}{<\hat{x}> - x_c}\tilde{m}'(y(\gamma))\right)^2}},\end{aligned} \tag{C.79}$$

where we have introduced the connected susceptibility given by Eq. (C.71). As already stressed, we are interested in a range $[\gamma_0, \gamma_{\rm m}]$ such that $\chi_{\rm conn}(\gamma) \gg 1$. Then the variance of the effective random field $\Delta_{\rm eff}(\gamma) = \chi_{\rm disc}(\gamma)/\chi_{\rm conn}(\gamma)^2$ is obtained as

$$\Delta_{\rm eff}(\gamma) \approx \overline{\frac{(\delta\hat{\tilde{m}}^\alpha(y(\gamma)) - \delta\hat{\tilde{m}}^\alpha(y_0) + (\tilde{m}'(y(\gamma)) - \tilde{m}'(y_0))\delta\hat{y}^\alpha(\gamma_0))^2}{\left[\frac{<\hat{x}>}{<\hat{x}> - x_c}\tilde{m}'(y(\gamma))\right]^2}}, \tag{C.80}$$

where all quantities can be calculated as done in the main text and in the previous sections of this appendix.

3.2 Mean-field RFIM starting from a finite field

We consider a starting point H_0 which is finite and between the two coercive fields, so that the sites can be either on the upper or lower branch of their hysteresis loop, since they both represent local minima of the Hamiltonian. The sites that have already flipped (upper branch) can only contribute elastically to the magnetization curve (remember however that the RFIM has a "negative elasticity" compared to the EPM), so that the plastic-like behavior associated with changes of local minimum depends only on the fraction of sites that start on the lower branch. (Notice that, as mentioned above, such an initial configuration is not reachable by starting from a magnetic field that goes to $-\infty$.)

We start by introducing a variable y, analogous to that used in the EPM,

$$y^\alpha(H) = H + Jm^\alpha(H) = H + \frac{J}{Nk}\sum_i \phi_i^\alpha(H). \tag{C.81}$$

where we have defined for convenience $\phi_i^\alpha = ks_i^\alpha$. Inverting the above relation gives

$$H^\alpha(y) = y - \frac{J}{Nk}\sum_i \phi_i^\alpha(y). \tag{C.82}$$

To describe the initial preparation of the system at $H = H_0$ or $y = y_0$ we consider that all the site variables are independently distributed according to the distribution $P_{y_0}(\phi)$, which plays the same role as $P_{y_0}(x)$ in the EPM. The constraint that the site with local magnetization ϕ correspond to a local minimum of the Hamiltonian imposes the following form:

$$\begin{aligned} P_{y_0}(\phi) &= \theta(\phi - 2k)\left[\rho_-(\phi - k - y_0) + \rho_+(\phi - k - y_0)\right] \\ &+ \theta(-\phi - 2k)\left[\rho_-(\phi + k - y_0) + \rho_+(\phi + k - y_0)\right] \\ &+ \theta(\phi)\theta(2k - \phi)\rho_+(\phi - k - y_0) + \theta(-\phi)\theta(2k + \phi)\rho_-(\phi + k - y_0), \end{aligned} \tag{C.83}$$

where we have defined the probability distributions $\rho_-(h)$ and $\rho_+(h)$ for having a random field h and being in the lower and upper branch, respectively (which, again, means that the local magnetization has or has not flipped from the left minimum of the 2-parabola potential to the right one: see also Fig. 3.3). The situation considered in the main text corresponds to taking $y_0 \to -\infty$ and $\rho_+(h) = 0$. The two distributions ρ_- and ρ_+ satisfy

$$\begin{aligned} &\int_{-\infty}^{\infty} dh\rho_-(h) = a, \ \int_{-\infty}^{\infty} dh\rho_+(h) = 1 - a, \\ &\int_{-\infty}^{\infty} dh\, h\rho_-(h) = \int_{-\infty}^{\infty} dh\, h\rho_+(h) = 0, \\ &\rho_+(h < -k - y_0) = 0, \ \rho_-(h > k - y_0) = 0, \end{aligned} \tag{C.84}$$

where the last two conditions come from the fact that a large negative (respectively, a large positive) local random field forces the local magnetization to be in the lower (respectively, the upper branch). Note that $a \in [0, 1]$ is a free parameter. In what follows we will consider the case $y_0 > 0$, which we anticipate to be the relevant one. Taking Eq. (C.84) into account, the expression of $P_{y_0}(\phi)$ then simplifies to

$$\begin{aligned} P_{y_0}(\phi) &= \theta(\phi - 2k)\left[\rho_-(\phi - k - y_0) + \rho_+(\phi - k - y_0)\right] \\ &+ \theta(\phi)\theta(2k - \phi)\rho_+(\phi - k - y_0) + \theta(-\phi)\rho_-(\phi + k - y_0). \end{aligned} \tag{C.85}$$

The evolution of the local magnetization ϕ_i^α as a function of y reads

$$\begin{aligned}\phi_i^\alpha(y) &= \phi_i^\alpha(y_0) + y - y_0, \quad \text{when} \quad \phi_i^\alpha(y_0) > 2k \text{ or } \phi_i^\alpha(y_0) < -(y - y_0) \\ &= \phi_i^\alpha(y_0) + y - y_0 + 2k, \quad \text{when} \quad 0 > \phi_i^\alpha(y_0) > -(y - y_0),\end{aligned} \tag{C.86}$$

if i belongs to the sites on the lower branch between y_0 and y, and

$$\phi_i^\alpha(y) = \phi_i^\alpha(y_0) + y - y_0 \tag{C.87}$$

otherwise. As in the EPM, if one considers y as our control parameter, each site evolves independent from the others. After averaging, one finds

$$\begin{aligned}\phi(y) = k\widetilde{m}(y) &= \overline{\phi_1^\alpha}(y_0) + y - y_0 + 2k \int_{-(y-y_0)}^{0} \mathrm{d}x P_{y_0}(x) \\ &= \overline{\phi_1^\alpha}(y_0) + y - y_0 + 2k \int_{-(y-y_0)}^{0} \mathrm{d}x \rho_-(x + k - y_0).\end{aligned} \tag{C.88}$$

From this expression and the average of Eq. (C.81), $y(H) = H + (J/k)\phi(y(H))$ one can compute the connected susceptibility

$$\chi_{\text{conn}}(H) = \frac{1}{k}\phi'(y)y'(H) = \frac{\phi'(y(H))}{k - J\phi'(y(H))}. \tag{C.89}$$

We now consider the disconnected susceptibility $\chi_{\text{disc}}(H) = \overline{[\delta\hat{m}^\alpha(H)]^2}$. We again use the same procedure of relating the fluctuations at constant H to the fluctuations at constant y. If the bare disorder (random-field distribution) is independent of the applied magnetic field H, the sample-to-sample fluctuations at a given H can be formally expressed in a way that do not explicitly depend on the starting point H_0, and one has

$$\Delta_{\text{eff}}(H) = \frac{\overline{[\delta\hat{\widetilde{m}}^{\,\alpha}(y(H))]^2}}{\widetilde{m}'(y(H))^2}. \tag{C.90}$$

Actually, the disconnected susceptibility $\chi_{\text{disc}}(H)$ can be cast as the sum of three terms as in Eq. (C.79) for the EPM, but in the present case $\delta\hat{y}^\alpha(H_0)$ is simply given by $J\delta\hat{\widetilde{m}}^{\,\alpha}(y_0)$ and the sum of three terms simplifies to the above equation. Note however that $\delta\hat{\widetilde{m}}^{\,\alpha}(y(H))$ and $\widetilde{m}'(y(H))$ do depend on the choice of initial condition in H_0, as we show below.

The sample-to-sample fluctuations at fixed y can be calculated by using the evolution equations given above and after some lengthy but straightforward manipulations we arrive at

$$\begin{aligned}&\overline{[\delta\hat{\widetilde{m}}^{\,\alpha}(y(H))]^2} = \left(\frac{1}{k}\right)^2 [\overline{\phi_i^\alpha(y)^2} - \overline{\phi_i^\alpha(y)}^2] \\ &= 1 - (1-2a)^2 + \frac{1}{k^2}\int_{-\infty}^{\infty} dh h^2[\rho_-(h) + \rho_+(h)] \\ &+ \frac{4}{k}\int_{k-y(H)}^{\infty} dh h\rho_-(h) - 4\int_{k-y(H)}^{\infty} dh\rho_-(h)[2a - 1 + \int_{k-y(H)}^{\infty} dh\rho_-(h)]\end{aligned} \tag{C.91}$$

which is valid for $H \geq H_0$. By combining this expression with Eq. (C.90) one obtains the disconnected susceptibility. Note that when $y_0 \to -\infty$, $\rho_+(h) = 0$, $\rho_-(h) = \rho(h)$ (as a result, $a = 1$), and one exactly recovers the expression in Eq. (3.33), after using $y(H) = H + Jm(H)$ and $\Delta_B = \int_{-\infty}^{\infty} dh h^2\rho(h)$.

3.3 Tentative mapping between the two models

We first consider the mapping of the mean-field EPM to a mean-field RFIM at the average level, i.e., for the stress-strain curve and the connected susceptibility. It is convenient to look at the expressions parametrized by the control parameter y (which is then taken as the identical in both models). For the EPM, one has

$$\begin{aligned} m'(y) &= -1 + < \hat{x} > P_{y_0}^{\mathrm{EPM}}(y - y_0) \\ \frac{\partial \gamma}{\partial y} &= \left(\frac{1 - \frac{x_c}{<\hat{x}>}}{2\mu_2} \right) [1 - \frac{x_c}{< \hat{x} > - x_c} m'(y)]. \end{aligned} \tag{C.92}$$

and for the RFIM,

$$\begin{aligned} m'(y) &= \frac{1}{k} + 2P_{y_0}^{\mathrm{RFIM}}(-(y - y_0)) \\ H'(y) &= 1 - Jm'(y). \end{aligned} \tag{C.93}$$

To map the EPM on the RFIM we then define an interaction and a magnetic field in the RFIM as

$$\begin{aligned} J &= \frac{x_c}{< \hat{x} > - x_c} \\ H &= \frac{2\mu_2}{1 - \frac{x_c}{<\hat{x}>}} \gamma, \end{aligned} \tag{C.94}$$

and we choose the initial distribution such that

$$2P_{y_0}^{\mathrm{RFIM}}(-(y - y_0)) = 2\rho_-(-y + k) = < \hat{x} > P_{y_0}^{\mathrm{EPM}}(y - y_0) - (1 + \frac{1}{k}). \tag{C.95}$$

The choice for $\rho_+(h)$ is still free and will not affect the evolution of the average magnetization, but the above equation puts a constraint on the maximum value of y: the right-hand side should indeed always be larger than 0, since on the left there is a probability. This restricts intervals $[y_0, y_{\mathrm{m}}]$ over which the analogy can hold.

To pursue the analogy one would like to describe the sample-to-sample fluctuations and tune the mean-field RFIM such that $\chi_{\mathrm{disc}}^{\mathrm{RFIM}}(y) \approx \chi_{\mathrm{disc}}^{\mathrm{EPM}}(y)$, in the limit where $\chi_{\mathrm{conn}} \gg 1$. Since $\rho_-(h)$ is already essentially fixed by the mapping at the level of the averaged quantities, we have some freedom with $\rho_+(h)$. This turns out not to be sufficient to match the two disconnected susceptibilities. A possible solution to this issue could be to consider an effective RFIM in which the bare disorder evolves with the applied magnetic field, i.e., with a variance $\Delta_B(H)$. This seems reasonable but we have not tried to implement this scenario. Note again that this mapping at the level of correlation functions or susceptibilities does not imply a direct mapping between individual dynamical trajectories.

3.4 Results and test of the hypothesis of a single plastic event per site

We illustrate the mapping of the mean-field EPM with the assumption of a single jump per site in the vicinity of the yielding transition to the mean-field RFIM at the average level in Fig. C.1. We display in panel (a) a weak-disorder case with a brittle (discontinuous) yielding and and in panel (b) a value of the disorder close to the critical point. In both cases we also show the exact solution for the EPM. One can see that the assumption of a single jump per site is virtually exact from the initial condition at γ_0 up to yielding and then

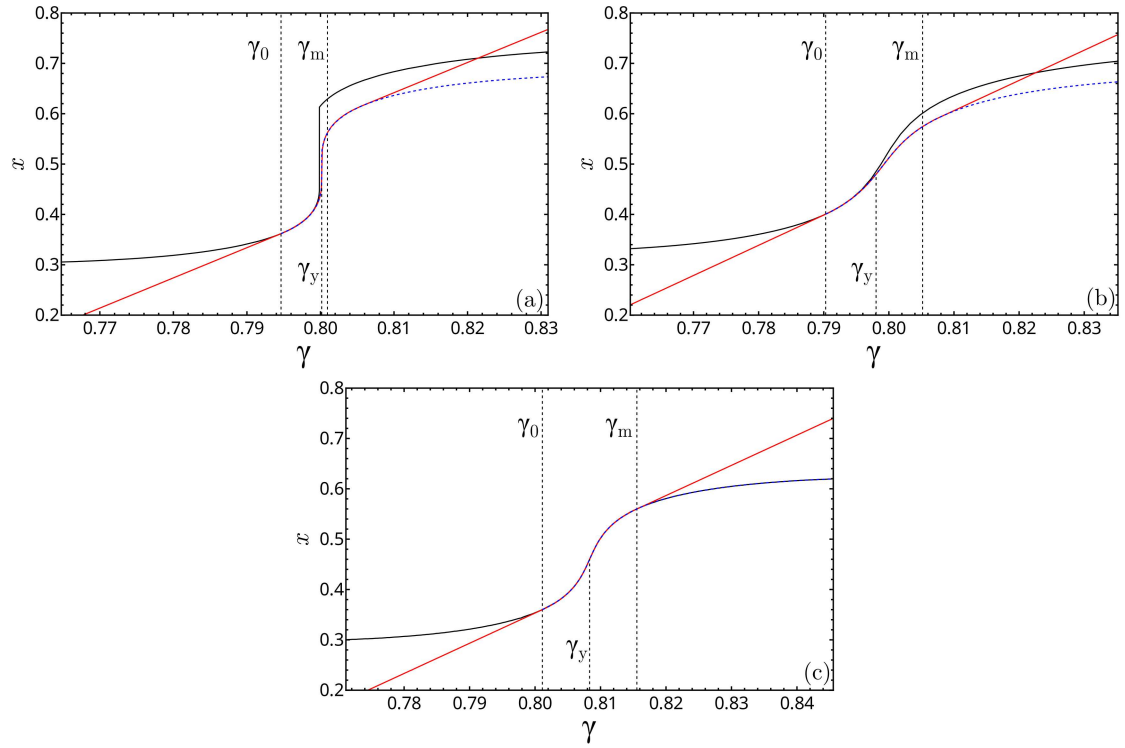

Figure C.1: Average stability $x(\gamma) = 1 - \sigma(\gamma)$ for the mean-field EPM. We focus on the elastic branch and the yielding region. Top row: Model with a 2-exponential distribution of random jumps, in the weak-disorder (brittle) case (a) and in the continuous case with a ductile yielding (b). Here, $2\mu_2 = 1$, $\mu_1 = 0.7$ and $< \hat{x} >= 0.92$. Bottom row (c): Model with randomness only in the initial conditions (no random jumps). In all cases the exact solution is displayed as a full black curve and the solution obtained under the assumption of a single jump per site as a dashed blue curve (they coincide in (c)). The red curve represents the equivalent RFIM which exactly coincides with the single-jump EPM curve between the two vertical lines at γ_0 and γ_m. We also indicate the location γ_y of the (discontinuous) yielding transition in (a) or the maximum of the connected susceptibility in (b) and (c).

starts to deteriorates, as expected. The direct mapping to the RFIM is found to hold in a narrow region around yielding. The "negative elasticity" of the RFIM prevents a broader application.

We also note that the single-jump hypothesis is correct for a wide range of values of y in the case without random jumps (see Fig. C.1(c), where the full black curve and the dashed blue one superimpose). A direct calculation shows that it is exact for $y \leq \hat{x}$.

Appendix D

Avalanches

In this appendix we discuss the avalanche-size distribution of the two models that we described in Chapter 1 (an EPM) and Chapter 2 (the Eshelby-RFIM). In athermally and quasistatically (AQS) driven systems the dynamics proceeds intermittently by discontinuous jumps (see Figs. 1.1 and 2.1). Such bursts of activity arise from more or less collective phenomena called avalanches and it is interesting to characterize their distribution. One usually defines the probability distribution $P(S)$ for having an avalanche of size S, defined as $S = N\delta s$, with N the number of sites in the system and δs the jump in the (intensive) quantity under study (stress for sheared solids and magnetization per spin for Ising models). For finite systems close to criticality (either self-organized, as in the steady-state of sheared amorphous solids, or conventional, as in the RFIM) $P(S)$ typically takes a scaling form,

$$P(S) \sim S^{-\tau}\mathcal{P}(S/S_c), \tag{D.1}$$

where τ is the power-law exponent and $\mathcal{P}$ is a scaling function that decreases very fast for $S > S_c$. In a finite system the cutoff size S_c grows with the system size as $S_c \sim L^{d_f}$, with d_f the fractal dimension of the largest avalanches, so that a collapse of the avalanche-size distribution for different system sizes is obtained by plotting $P(S)L^{\tau d_f}$ vs S/L^{d_f}. These exponents have been extensively studied for various AQS driven systems, e.g., in the standard RFIM [129, 132], in the depinning of an elastic manifold [127], and in the sheared amorphous solids [144, 191]. We now discuss the avalanche statistics of the two models that we have studied in the main text.

1 Avalanche size distribution for the EPM

The avalanche size distribution of the EPM has already been much studied in different setups. This type of numerical studies were performed for example to determine whether the "dynamical" yielding transition (i.e., that observed by imposing a certain amount of stress and measuring the resulting strain rate) can be described by interface depinning [144]. Usually the determination of the exponents that characterize the avalanche distribution is carried out in the steady state, which is independent of the initial conditions and of the value of γ. We have performed a similar measurement in our model. In order to compare the results with the Eshelby-RFIM defined in Chapter 2, which does not have a proper steady state, we

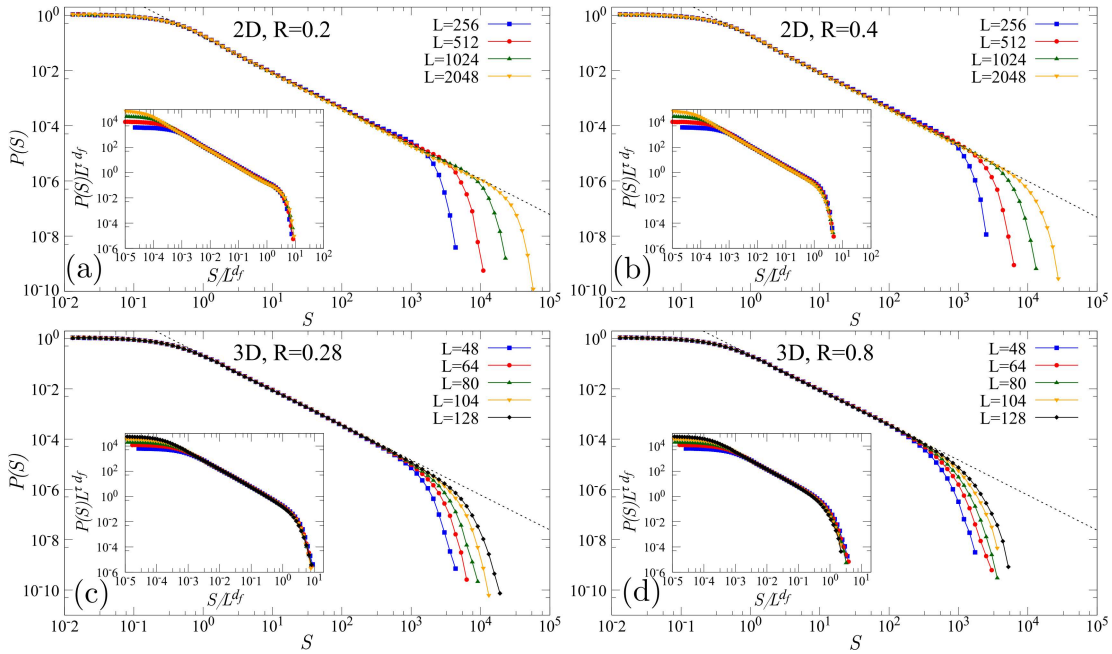

Figure D.1: Scaling of the avalanches for 2D (a,b) and 3D (c,d) EPM. In (a) and (c) the model is in the brittle regime, while in (b) and (d) it is in the monotonic stress-vs-strain curve regime. The black dashed lines are obtained by fitting the largest system size. They give $\tau = 1.309$ and $\tau = 1.308$ in 2D for respectively $R = 0.20$ and $R = 0.40$, and $\tau = 1.390$ and $\tau = 1.394$ in 3D for respectively $R = 0.28$ and $R = 0.80$. The insets show the collapse obtained with $\tau = 1.3$ and $d_f = 1.1$ in 2D, and $\tau = 1.4$ and $d_f = 1.6$ in 3D.

have studied the avalanche size distribution while the system is still in the transient regime, but still after yielding. (We define the steady state as the state that the system attains when each site has experienced at least one event, resulting in the complete erasure of the initial condition's memory.) It follows that the distribution of avalanche sizes is actually dependent (at least in principle) on γ and R. We define $\tilde{P}(S, R, \gamma)$ as the probability distribution of having an avalanche of size S at strain γ with initial disorder strength R, and the avalanche size is defined as $S = N\Delta\sigma$. In order to collect a large number of avalanches for estimating their distribution we measure the integral between two values of γ, namely $\gamma_{\min}$ and $\gamma_{\max}$. The resulting distribution that we measure is then

$$P(S, R) = \frac{1}{\mathcal{N}} \int_{\gamma_{\min}}^{\gamma_{\max}} \tilde{P}(S, R, \gamma) d\gamma, \tag{D.2}$$

with $\mathcal{N}$ the appropriate normalization constant. This quantity still depends on the choice of $\gamma_{\min}$ and $\gamma_{\max}$ and R, as we are not at the steady state. In the following analysis we take $\gamma_{\min} = 0.7$ and $\gamma_{\max} = 1$. In this range of γ, for a small value of R, the system has already formed a shear band, but the band has not widened to invade the whole system yet. On the other hand, for large values of R, the stress curve has not yet reached its plateau value (see Fig. 1.1) and some sites have not yielded.

The results of our analysis are shown in Fig. D.1. The power-law scaling is observed for both 2D and 3D EPM, for different values of R. For large values of S the distribution

decreases to 0 very quickly, with a cutoff to the power-law behavior that increases with the system size. From the fit we extract $\tau \approx 1.31$ in 2D and $\tau \approx 1.40$ in 3D, which are close to the values found in the literature [144, 147, 192] despite the fact that the system is not in the steady state. We have then performed the curve collapse, from which we obtain an estimate of the value of the fractal dimension d_f, which is found close to 1.1 in 2D and close to 1.6 in 3D. As expected the avalanches are more compact in higher dimensions. We notice that the collapse works well for both values of R, less so however for the strong disorder case in 3D, meaning that the appropriate value of d_f may be slightly smaller. The evolution of the system for the two values of R is qualitatively different due to the presence for the $R < R_c$ case and the absence for $R > R_c$ of a shear band. Nonetheless, the fit gives exponent values that are similar in the two cases, and similar to the steady state values given in the literature.

2 Avalanche size distribution for the Eshelby-RFIM

We now move to the case of the Eshelby-RFIM. As we pointed out in the main text, this model does not reach a true steady-state, and its evolution ends once all the spins are pointing in the upward direction. As before, we restrict our attention to a range of values between $m_{\min} = -0.5$ and $m_{\max} = 0$ (the range is unchanged when changing R). Analogously to what is done in the study of the standard RFIM, we define the avalanche size $S = N\Delta m$ and we study its distribution $\tilde{P}(S, R, m)$ at total magnetization m and random field strength R. We perform the same analysis as above, studying

$$P(S, R) = \frac{1}{\mathcal{N}} \int_{m_{\min}}^{m_{\max}} \tilde{P}(S, R, m) dm, \tag{D.3}$$

with $\mathcal{N}$ the normalization constant. We have then measured this quantity for different system sizes and different values of the disorder strength. In this case there is a large number of events in which the magnetization does not change. This type of events come from the anisotropy of the Eshelby kernel, which makes it possible for a spin to flip to a positive value and interact antiferromagnetically with another spin which is then forced to flip from a positive to a negative value. As the number of such events changes with the system size, it can blur the scaling behavior of the avalanche size distribution. In order to circumvent this effect we only focus on avalanches in which at least 10 spins have flipped up, cutting out the contribution of small avalanches. (Note that a similar issue is also found in random-field Ising models with long-range antiferromagnetic interactions in [171], where the authors employed a different definition of the avalanche size to address the problem.)

The outcome of our analysis is shown in Fig. D.2. The distribution of avalanche sizes displays a power-law behavior for intermediate values of S and then sharply decreases after a cutoff that increases with the system size. We have estimated the exponents τ and d_f in order to compare them with those obtained in the EPM. In 2D we obtain $\tau \approx 1.25$, with a slightly smaller value for $R < R_c$, not far from the value in the EPM case, while $\tau \approx 1.58$ in 3D, which is quite different from the EPM counterpart. (In [147] a dependence of τ on the value of $\hat{G}_{\mathbf{q}=0}$ has been shown, which could partly explain the differences between EPM and Eshelby-RFIM.) The value of the fractal dimension seems instead larger ($d_f = 1.3$) for $R < R_c$ than for $R > R_c$. This could be a consequence of the different treatment of the nearest-neighbor

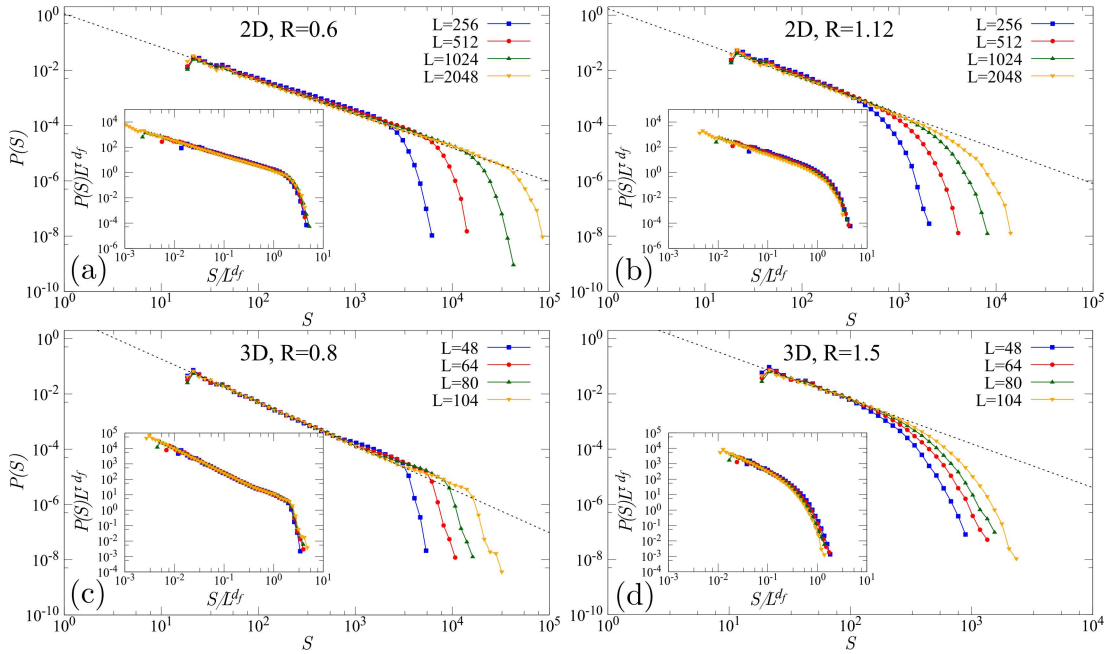

Figure D.2: Scaling of the avalanches for 2D (a,b) and 3D (c,d) Eshelby-RFIM. In (a) and (c) the model displays a macroscopic jump in the magnetization curve, while in (b) and (d) its magnetization increases continuously. The black dashed lines are obtained by fitting the largest system size. They give $\tau = 1.22$ and $\tau = 1.25$ in 2D for respectively $R = 0.60$ and $R = 1.12$, and $\tau = 1.57$ and $\tau = 1.58$ in 3D for respectively $R = 0.80$ and $R = 1.50$. The insets show the collapse obtained with $\tau = 1.22$ and $d_f = 1.3$ in 2D for $R = 0.60$ and $\tau = 1.25$ and $d_f = 1.1$ for $R = 1.12$. In 3D we plot the collapse with $\tau = 1.58$ and $d_f = 1.9$ in 3D for $R = 0.80$ while $\tau = 1.58$ and $d_f = 1.6$ for $R = 1.5$.

correction to the Eshelby kernel. It has been shown that such modifications of the Eshelby kernel have an effect on the avalanches shape [151], so that it would not be surprising to find more compact avalanches here. For $R > R_c$ the value of the fractal dimension seems to be smaller, which may indicate that the precise value of the nearest-neighbor interaction have a smaller role in this case.

Up to this point we have assumed the avalanche-size distribution is scale free in the thermodynamic limit, an hypothesis which is not at all obvious. From results on the driven ferromagnetic RFIM [170] one observes several decades of scaling behavior of the integrated avalanche-size distribution even quite far from the critical point. In that case however, the avalanche-size distribution is scale-free only at the critical point, contrary to the EPM where it is scale free for all the values of R. Concluding on whether or not the avalanches observed in the Eshelby-RFIM are actually scale-free away from the critical point is not easy. In the EPM the distribution of avalanche sizes is intimately related in the EPM to the probability distribution $P_{\rm st}(x)$ of the local stability $x = 1 - \sigma$ close to $x = 0$. For this distribution it has been argued [193] that in systems in which the kernel is monotonic, as in the case of an elastic interface, one has $P_{\rm st}(x) \sim x^{\theta}$ with $\theta = 0$. On the other hand, for the long-range and quadrupolar symmetry of the Eshelby kernel one observes a pseudogap with $\theta > 0$,

which means that the system is marginally stable [50, 144, 193]. Determining the value of θ in the case of the Eshelby-RFIM woulc be an interesting approach to this problem. It has been recently shown that in a 1D RFIM the addition of long-range antiferromagnetic interactions make the system marginally stable [171]. Measuring the distribution $P_{\rm st}(x)$ for the Eshelby-RFIM is not straightforward and is left for future work.

Bibliography

[1] Peter J. Lu and David A. Weitz. Colloidal particles: Crystals, glasses, and gels. *Annual Review of Condensed Matter Physics*, 4(1):217–233, 2013.

[2] P. N. Pusey and W. van Megen. Observation of a glass transition in suspensions of spherical colloidal particles. *Phys. Rev. Lett.*, 59:2083–2086, Nov 1987.

[3] Ali S. Argon and H. Y. Kuo. Plastic flow in a disordered bubble raft (an analog of a metallic glass). *Materials Science and Engineering*, 39:101–109, 1979.

[4] Misaki Ozawa, Ludovic Berthier, Giulio Biroli, Alberto Rosso, and Gilles Tarjus. Random critical point separates brittle and ductile yielding transitions in amorphous materials. *Proceedings of the National Academy of Sciences*, 115(26):6656–6661, 2018.

[5] Alexandre Nicolas, Ezequiel E. Ferrero, Kirsten Martens, and Jean-Louis Barrat. Deformation and flow of amorphous solids: Insights from elastoplastic models. *Rev. Mod. Phys.*, 90:045006, Dec 2018.

[6] Hugh J. Barlow, James O. Cochran, and Suzanne M. Fielding. Ductile and brittle yielding in thermal and athermal amorphous materials. *Phys. Rev. Lett.*, 125:168003, Oct 2020.

[7] Marko Popović, Tom W. J. de Geus, and Matthieu Wyart. Elastoplastic description of sudden failure in athermal amorphous materials during quasistatic loading. *Phys. Rev. E*, 98:040901, Oct 2018.

[8] L. X. Hayden, Archishman Raju, and James P. Sethna. Unusual scaling for two-dimensional avalanches: Curing the faceting and scaling in the lower critical dimension. *Phys. Rev. Res.*, 1:033060, Oct 2019.

[9] Jie Lin and Matthieu Wyart. Mean-field description of plastic flow in amorphous solids. *Phys. Rev. X*, 6:011005, Jan 2016.

[10] Karin Dahmen and James P. Sethna. Hysteresis, avalanches, and disorder-induced critical scaling: A renormalization-group approach. *Phys. Rev. B*, 53:14872–14905, Jun 1996.

[11] Mingwei Chen. A brief overview of bulk metallic glasses. *NPG Asia Materials*, 3:82–90, 2011.

[12] Daniel Bonn, Morton M. Denn, Ludovic Berthier, Thibaut Divoux, and Sébastien Manneville. Yield stress materials in soft condensed matter. *Rev. Mod. Phys.*, 89:035005, Aug 2017.

[13] P J Withers. Residual stress and its role in failure. *Reports on Progress in Physics*, 70(12):2211, nov 2007.

[14] S. Chandrasekar and M. M. Chaudhri. The explosive disintegration of prince rupert's drops. *Philosophical Magazine B*, 70(6):1195–1218, 1994.

[15] Jan Kirkegaard Lauridsen, Michael Twardos, and Michael Dennin. Shear-induced stress relaxation in a two-dimensional wet foam. *Physical review letters*, 89 9:098303, 2002.

[16] N. Koumakis, M. Laurati, S. U. Egelhaaf, J. F. Brady, and G. Petekidis. Yielding of hard-sphere glasses during start-up shear. *Phys. Rev. Lett.*, 108:098303, Mar 2012.

[17] L.F. Liu, L.H. Dai, Y.L. Bai, B.C. Wei, and J. Eckert. Characterization of rate-dependent shear behavior of zr-based bulk metallic glass using shear-punch testing. *Journal of Materials Research*, 21(1):153–160, 2006.

[18] Hideyuki Mizuno, Stefano Mossa, and Jean-Louis Barrat. Acoustic excitations and elastic heterogeneities in disordered solids. *Proceedings of the National Academy of Sciences*, 111:11949 – 11954, 2014.

[19] J. Lubliner. *Plasticity Theory*. Dover books on engineering. Dover Publications, 2008.

[20] Geoffrey Ingram Sir Taylor. The mechanism of plastic deformation of crystals. part i. theoretical. *Proceedings of The Royal Society A: Mathematical, Physical and Engineering Sciences*, 145:362–387, 1934.

[21] Anne-Laure Biance, Sylvie Cohen-Addad, and Reinhard Höhler. Topological transition dynamics in a strained bubble cluster. *Soft Matter*, 5:4672–4679, 2009.

[22] K. E. Jensen, D. A. Weitz, and F. Spaepen. Local shear transformations in deformed and quiescent hard-sphere colloidal glasses. *Phys. Rev. E*, 90:042305, Oct 2014.

[23] Kenneth W. Desmond and Eric R. Weeks. Measurement of stress redistribution in flowing emulsions. *Phys. Rev. Lett.*, 115:098302, Aug 2015.

[24] Peter Schall, David A. Weitz, and Frans Spaepen. Structural rearrangements that govern flow in colloidal glasses. *Science*, 318(5858):1895–1899, 2007.

[25] D. Pan, A. Inoue, T. Sakurai, and M. W. Chen. Experimental characterization of shear transformation zones for plastic flow of bulk metallic glasses. *Proceedings of the National Academy of Sciences*, 105(39):14769–14772, 2008.

[26] Q. Wei, D. Jia, K. T. Ramesh, and E. Ma. Evolution and microstructure of shear bands in nanostructured fe. *Applied Physics Letters*, 81:1240–1242, 8 2002.

[27] P. Coussot, J. S. Raynaud, F. Bertrand, P. Moucheront, J. P. Guilbaud, H. T. Huynh, S. Jarny, and D. Lesueur. Coexistence of liquid and solid phases in flowing soft-glassy materials. *Phys. Rev. Lett.*, 88:218301, May 2002.

[28] John Douglas Eshelby. The determination of the elastic field of an ellipsoidal inclusion, and related problems. *Proceedings of the royal society of London. Series A. Mathematical and physical sciences*, 241(1226):376–396, 1957.

[29] Alexandre Kabla and Georges Debrégeas. Local stress relaxation and shear banding in a dry foam under shear. *Phys. Rev. Lett.*, 90:258303, Jun 2003.

[30] Chandana Mondal, Michael Moshe, Itamar Procaccia, Saikat Roy, Jin Shang, and Jie Zhang. Experimental and numerical verification of anomalous screening theory in granular matter. *Chaos, Solitons & Fractals*, 164:112609, 2022.

[31] Harish Charan, Michael Moshe, and Itamar Procaccia. Anomalous elasticity and emergent dipole screening in three-dimensional amorphous solids, 2022.

[32] Ratul Dasgupta, H. George E. Hentschel, and Itamar Procaccia. Microscopic mechanism of shear bands in amorphous solids. *Phys. Rev. Lett.*, 109:255502, Dec 2012.

[33] A.L. Greer, Y.Q. Cheng, and E. Ma. Shear bands in metallic glasses. *Materials Science and Engineering: R: Reports*, 74(4):71–132, 2013.

[34] Thibaut Divoux, David Tamarii, Catherine Barentin, and Sébastien Manneville. Transient shear banding in a simple yield stress fluid. *Phys. Rev. Lett.*, 104:208301, May 2010.

[35] Thibaut Divoux, Marc A. Fardin, Sebastien Manneville, and Sandra Lerouge. Shear banding of complex fluids. *Annual Review of Fluid Mechanics*, 48(1):81–103, 2016.

[36] Joachim Bokeloh, Sergiy V. Divinski, Gerrit Reglitz, and Gerhard Wilde. Tracer measurements of atomic diffusion inside shear bands of a bulk metallic glass. *Phys. Rev. Lett.*, 107:235503, Nov 2011.

[37] John Lauridsen, Gregory Chanan, and Michael Dennin. Velocity profiles in slowly sheared bubble rafts. *Phys. Rev. Lett.*, 93:018303, Jul 2004.

[38] J. Lu, G. Ravichandran, and W.L. Johnson. Deformation behavior of the zr41.2ti13.8cu12.5ni10be22.5 bulk metallic glass over a wide range of strain-rates and temperatures. *Acta Materialia*, 51(12):3429–3443, 2003.

[39] R. Raghavan, P. Murali, and U. Ramamurty. On factors influencing the ductile-to-brittle transition in a bulk metallic glass. *Acta Materialia*, 57(11):3332–3340, 2009.

[40] Thibaut Divoux, Catherine Barentin, and Sébastien Manneville. Stress overshoot in a simple yield stress fluid: An extensive study combining rheology and velocimetry. *Soft Matter*, 7:9335–9349, 2011.

[41] Jun Shen and J.F. Sun. Plasticity of a ticu-based bulk metallic glass: Effect of cooling rate. *Journal of Materials Research - J MATER RES*, 22, 11 2007.

[42] Golden Kumar, Pascal Neibecker, Yan Hui Liu, and Jan Schroers. Critical fictive temperature for plasticity in metallic glasses. *Nature Communications*, 4(1):1536, feb 2013.

[43] Jittisa Ketkaew, Wen Chen, Hui Wang, Amit Datye, Meng Fan, Gabriela Pereira, Udo Schwarz, ze Liu, Rui Yamada, Wojciech Dmowski, Mark Shattuck, Corey O'Hern, Takeshi Egami, Eran Bouchbinder, and Jan Schroers. Mechanical glass transition revealed by the fracture toughness of metallic glasses. *Nature Communications*, 9, 08 2018.

[44] Beatrice Ruta, Eloi Pineda, and Zach Evenson. Topical review: Relaxation processes and physical aging in metallic glasses. *Journal of Physics: Condensed Matter*, 29, 11 2017.

[45] H. G. E. Hentschel, Smarajit Karmakar, Edan Lerner, and Itamar Procaccia. Do athermal amorphous solids exist? *Phys. Rev. E*, 83:061101, Jun 2011.

[46] S M Fielding. Shear banding in soft glassy materials. *Reports on Progress in Physics*, 77:102601, 10 2014.

[47] Jan K. G. Dhont. A constitutive relation describing the shear-banding transition. *Phys. Rev. E*, 60:4534–4544, Oct 1999.

[48] Gaël Combe and Jean-Noël Roux. Strain versus stress in a model granular material: A devil's staircase. *Phys. Rev. Lett.*, 85:3628–3631, Oct 2000.

[49] Giulio Biroli and Pierfrancesco Urbani. Breakdown of elasticity in amorphous solids. *Nature Physics*, 12(12):1130–1133, aug 2016.

[50] Baoshuang Shang, Pengfei Guan, and Jean-Louis Barrat. Elastic avalanches reveal marginal behavior in amorphous solids. *Proceedings of the National Academy of Sciences*, 117(1):86–92, 2020.

[51] Timothy Foecke. Metallurgy of the rms titanic, 1998-02-01 1998.

[52] Gary L Hunter and Eric R Weeks. The physics of the colloidal glass transition. *Reports on Progress in Physics*, 75(6):066501, may 2012.

[53] A W Lees and S F Edwards. The computer study of transport processes under extreme conditions. *Journal of Physics C: Solid State Physics*, 5(15):1921, aug 1972.

[54] Andrea Ninarello, Ludovic Berthier, and Daniele Coslovich. Models and algorithms for the next generation of glass transition studies. *Phys. Rev. X*, 7:021039, Jun 2017.

[55] A. Tanguy, F. Leonforte, and J. L. Barrat. Plastic response of a 2d lennard-jones amorphous solid: Detailed analysis of the local rearrangements at very slow strain rate. *The European Physical Journal E*, 20:355–364, 7 2006.

[56] Tristan Albaret, Francesca Boioli, and David Rodney. Time-resolved shear transformations in the transient plastic regime of sheared amorphous silicon. *Phys. Rev. E*, 102:053003, Nov 2020.

[57] Ashwin J., Eran Bouchbinder, and Itamar Procaccia. Cooling-rate dependence of the shear modulus of amorphous solids. *Phys. Rev. E*, 87:042310, Apr 2013.

[58] Anaël Lemaître and Christiane Caroli. Rate-dependent avalanche size in athermally sheared amorphous solids. *Phys. Rev. Lett.*, 103:065501, Aug 2009.

[59] Craig E. Maloney and Anaël Lemaître. Amorphous systems in athermal, quasistatic shear. *Phys. Rev. E*, 74:016118, Jul 2006.

[60] M. L. Falk and J. S. Langer. Dynamics of viscoplastic deformation in amorphous solids. *Phys. Rev. E*, 57:7192–7205, Jun 1998.

[61] F. Puosi, J. Rottler, and J-L. Barrat. Time-dependent elastic response to a local shear transformation in amorphous solids. *Phys. Rev. E*, 89:042302, Apr 2014.

[62] Gaurav Prakash Shrivastav, Pinaki Chaudhuri, and Jürgen Horbach. Yielding of glass under shear: A directed percolation transition precedes shear-band formation. *Phys. Rev. E*, 94:042605, Oct 2016.

[63] Antina Ghosh, Zoe Budrikis, Vijayakumar Chikkadi, Alessandro L. Sellerio, Stefano Zapperi, and Peter Schall. Direct observation of percolation in the yielding transition of colloidal glasses. *Phys. Rev. Lett.*, 118:148001, Apr 2017.

[64] Meng Fan, Minglei Wang, Kai Zhang, Yanhui Liu, Jan Schroers, Mark D. Shattuck, and Corey S. O'Hern. Effects of cooling rate on particle rearrangement statistics: Rapidly cooled glasses are more ductile and less reversible. *Phys. Rev. E*, 95:022611, Feb 2017.

[65] Marcel Utz, Pablo G. Debenedetti, and Frank H. Stillinger. Atomistic simulation of aging and rejuvenation in glasses. *Phys. Rev. Lett.*, 84:1471–1474, Feb 2000.

[66] David Richard, Edan Lerner, and Eran Bouchbinder. Brittle-to-ductile transitions in glasses: Roles of soft defects and loading geometry. *MRS Bulletin*, 2021.

[67] Gaurav Prakash Shrivastav, Pinaki Chaudhuri, and Jürgen Horbach. Heterogeneous dynamics during yielding of glasses: Effect of aging. *Journal of Rheology*, 60:835–847, 9 2016.

[68] Sylvain Patinet, Damien Vandembroucq, and Michael L. Falk. Connecting local yield stresses with plastic activity in amorphous solids. *Phys. Rev. Lett.*, 117:045501, Jul 2016.

[69] D. Richard, M. Ozawa, S. Patinet, E. Stanifer, B. Shang, S. A. Ridout, B. Xu, G. Zhang, P. K. Morse, J.-L. Barrat, L. Berthier, M. L. Falk, P. Guan, A. J. Liu, K. Martens, S. Sastry, D. Vandembroucq, E. Lerner, and M. L. Manning. Predicting plasticity in disordered solids from structural indicators. *Phys. Rev. Mater.*, 4:113609, Nov 2020.

[70] Prabhat K. Jaiswal, Itamar Procaccia, Corrado Rainone, and Murari Singh. Mechanical yield in amorphous solids: A first-order phase transition. *Phys. Rev. Lett.*, 116:085501, Feb 2016.

[71] Giorgio Parisi, Itamar Procaccia, Corrado Rainone, and Murari Singh. Shear bands as manifestation of a criticality in yielding amorphous solids. *Proceedings of the National Academy of Sciences*, 114(22):5577–5582, 2017.

[72] P. Hébraud and F. Lequeux. Mode-coupling theory for the pasty rheology of soft glassy materials. *Phys. Rev. Lett.*, 81:2934–2937, Oct 1998.

[73] Lydéric Bocquet, Annie Colin, and Armand Ajdari. Kinetic theory of plastic flow in soft glassy materials. *Phys. Rev. Lett.*, 103:036001, Jul 2009.

[74] Peter Sollich, Fran çois Lequeux, Pascal Hébraud, and Michael E. Cates. Rheology of soft glassy materials. *Phys. Rev. Lett.*, 78:2020–2023, Mar 1997.

[75] S. Fielding, Peter Sollich, and M. Cates. Ageing and rheology in soft materials. *Journal of Rheology - J RHEOL*, 44:323–369, 03 2000.

[76] C. Monthus and Jean-Philippe Bouchaud. Models of traps and glass phenomenology. *Journal of Physics A*, 29:3847–3869, 1996.

[77] Elisabeth Agoritsas, Eric Bertin, Kirsten Martens, and Jean-Louis Barrat. On the relevance of disorder in athermal amorphous materials under shear. *The European Physical Journal E*, 38(7), jul 2015.

[78] Guillemette Picard, Armand Ajdari, Lydéric Bocquet, and Fran çois Lequeux. Simple model for heterogeneous flows of yield stress fluids. *Phys. Rev. E*, 66:051501, Nov 2002.

[79] Robyn L. Moorcroft, Michael E. Cates, and Suzanne M. Fielding. Age-dependent transient shear banding in soft glasses. *Phys. Rev. Lett.*, 106:055502, Feb 2011.

[80] V V Bulatov and A S Argon. A stochastic model for continuum elasto-plastic behavior. i. numerical approach and strain localization. *Modelling and Simulation in Materials Science and Engineering*, 2(2):167, mar 1994.

[81] Corrado Rainone, Pierfrancesco Urbani, Hajime Yoshino, and Francesco Zamponi. Following the evolution of hard sphere glasses in infinite dimensions under external perturbations: Compression and shear strain. *Phys. Rev. Lett.*, 114:015701, Jan 2015.

[82] Pierfrancesco Urbani and Francesco Zamponi. Shear yielding and shear jamming of dense hard sphere glasses. *Phys. Rev. Lett.*, 118:038001, Jan 2017.

[83] Joseph Pollard and Suzanne M. Fielding. Yielding, shear banding, and brittle failure of amorphous materials. *Phys. Rev. Res.*, 4:043037, Oct 2022.

[84] David Richard, Corrado Rainone, and Edan Lerner. Finite-size study of the athermal quasistatic yielding transition in structural glasses. *The Journal of Chemical Physics*, 155(5), 08 2021. 056101.

[85] Kenneth G. Wilson and J. Kogut. The renormalization group and the ϵ expansion. *Physics Reports*, 12(2):75–199, 1974.

[86] Kenneth G. Wilson. The renormalization group: Critical phenomena and the Kondo problem. *Rev. Mod. Phys.*, 47:773–840, Oct 1975.

[87] R. Peierls. On ising's model of ferromagnetism. *Mathematical Proceedings of the Cambridge Philosophical Society*, 32(3):477–481, 1936.

[88] Lars Onsager. Crystal statistics. i. a two-dimensional model with an order-disorder transition. *Phys. Rev.*, 65:117–149, Feb 1944.

[89] Filip Kos, David Poland, David Simmons-Duffin, and Alessandro Vichi. Precision islands in the ising and o(n) models. *Journal of High Energy Physics*, 2016, 2016.

[90] Martin Hasenbusch. Finite size scaling study of lattice models in the three-dimensional ising universality class. *Phys. Rev. B*, 82:174433, Nov 2010.

[91] VL Ginzburg. Some remarks on phase transitions of the second kind and the microscopic theory of ferroelectric materials. *Soviet Phys. Solid State*, 2:1824–1834, 1961.

[92] Alexander L. Efros and Vitaly Kisin. *Physics and Geometry of Disorder: Percolation Theory.* MRI, 1986.

[93] Robert B. Griffiths. Nonanalytic behavior above the critical point in a random ising ferromagnet. *Phys. Rev. Lett.*, 23:17–19, Jul 1969.

[94] S F Edwards and P W Anderson. Theory of spin glasses. *Journal of Physics F: Metal Physics*, 5(5):965, may 1975.

[95] James P Sethna, Karin A Dahmen, and Christopher R Myers. Crackling noise. *Nature*, 410(6825):242–250, 2001.

[96] S. Lemerle, J. Ferré, C. Chappert, V. Mathet, T. Giamarchi, and P. Le Doussal. Domain wall creep in an ising ultrathin magnetic film. *Phys. Rev. Lett.*, 80:849–852, Jan 1998.

[97] E. Agoritsas, V. Lecomte, and T. Giamarchi. Disordered elastic systems and one-dimensional interfaces. *Physica B: Condensed Matter*, 407(11):1725–1733, 2012. Proceedings of the International Workshop on Electronic Crystals (ECRYS-2011).

[98] Daniel S. Fisher. Collective transport in random media: from superconductors to earthquakes. *Physics Reports*, 301(1):113–150, 1998.

[99] J J Hopfield. Neural networks and physical systems with emergent collective computational abilities. *Proceedings of the National Academy of Sciences*, 79(8):2554–2558, 1982.

[100] Marc Mézard and Andrea Montanari. *Information, Physics, and Computation.* Oxford University Press, 2009.

[101] Moshe Schwartz and A. Soffer. Exact inequality for random systems: Application to random fields. *Phys. Rev. Lett.*, 55:2499–2501, Nov 1985.

[102] Daniel S. Fisher. Scaling and critical slowing down in random-field ising systems. *Phys. Rev. Lett.*, 56:416–419, Feb 1986.

[103] T. Nattermann. Theory of the random field ising model, 1997.

[104] Gilles Tarjus and Matthieu Tissier. Nonperturbative functional renormalization group for random field models and related disordered systems. i. effective average action formalism. *Phys. Rev. B*, 78:024203, Jul 2008.

[105] Amnon Aharony. Tricritical points in systems with random fields. *Phys. Rev. B*, 18:3318–3327, Oct 1978.

[106] Yoseph Imry and Shang-keng Ma. Random-field instability of the ordered state of continuous symmetry. *Phys. Rev. Lett.*, 35:1399–1401, Nov 1975.

[107] K. Binder. Random-field induced interface widths in ising systems. *Z. Physik B - Condensed Matter*, 50:343–352, Dec 1983.

[108] Th. Schneider and Erling Pytte. Random-field instability of the ferromagnetic state. *Physical Review B*, 15:1519–1522, 1977.

[109] J. Bricmont and A. Kupiainen. Lower critical dimension for the random-field ising model. *Phys. Rev. Lett.*, 59:1829–1832, Oct 1987.

[110] Ivan Balog, Gilles Tarjus, and Matthieu Tissier. Criticality of the random field ising model in and out of equilibrium: A nonperturbative functional renormalization group description. *Phys. Rev. B*, 97:094204, Mar 2018.

[111] Matthieu Tissier and Gilles Tarjus. Nonperturbative functional renormalization group for random field models and related disordered systems. iv. supersymmetry and its spontaneous breaking. *Physical Review B*, 85:104203, 2011.

[112] Nikolaos G. Fytas and Víctor Martín-Mayor. Universality in the three-dimensional random-field ising model. *Phys. Rev. Lett.*, 110:227201, May 2013.

[113] Nikolaos G. Fytas, Víctor Martín-Mayor, Marco Picco, and Nicolas Sourlas. Phase transitions in disordered systems: The example of the random-field ising model in four dimensions. *Phys. Rev. Lett.*, 116:227201, Jun 2016.

[114] R L C Vink, K Binder, and H Löwen. Colloid–polymer mixtures in random porous media: finite size scaling and connected versus disconnected susceptibilities. *Journal of Physics: Condensed Matter*, 20(40):404222, sep 2008.

[115] Benjamin Guiselin, Ludovic Berthier, and Gilles Tarjus. Random-field ising model criticality in a glass-forming liquid. *Phys. Rev. E*, 102:042129, Oct 2020.

[116] P. C. Martin, E. D. Siggia, and H. A. Rose. Statistical dynamics of classical systems. *Phys. Rev. A*, 8:423–437, Jul 1973.

[117] H. Janssen. On a lagrangean for classical field dynamics and renormalization group calculations of dynamical critical properties. *Zeitschrift für Physik B Condensed Matter and Quanta*, 23:377–380, 01 1976.

[118] C de Dominicis. Techniques de renormalisation de la théorie des champs et dynamique des phénomenes critiques. In *J. Phys., Colloq*, volume 37, page 247, 1976.

[119] Tarjus, Gilles and Tissier, Matthieu. Random-field ising and o(n) models: theoretical description through the functional renormalization group. *Eur. Phys. J. B*, 93(3):50, 2020.

[120] Amos Maritan, Marek Cieplak, Michael R. Swift, and Jayanth R. Banavar. Spin-flip avalanches and dynamics of first order phase transitions. *Phys. Rev. Lett.*, 72:946–946, Feb 1994.

[121] Francisco J. Pérez-Reche and Eduard Vives. Spanning avalanches in the three-dimensional gaussian random-field ising model with metastable dynamics: Field dependence and geometrical properties. *Phys. Rev. B*, 70:214422, Dec 2004.

[122] Jean Zinn-Justin. *Quantum Field Theory and Critical Phenomena*. Oxford University Press, 1989.

[123] Ivan Balog and Gilles Tarjus. Activated dynamic scaling in the random-field ising model: A nonperturbative functional renormalization group approach. *Phys. Rev. B*, 91:214201, Jun 2015.

[124] Kay Joerg Wiese and Pierre Le Doussal. Functional renormalization for disordered systems, basic recipes and gourmet dishes, 2006.

[125] A. I. Larkin. Effect of Inhomogeneties on the Structure of the Mixed State of Superconductors. *Soviet Journal of Experimental and Theoretical Physics*, 31:784, January 1970.

[126] Pascal Chauve, Thierry Giamarchi, and Pierre Le Doussal. Creep and depinning in disordered media. *Phys. Rev. B*, 62:6241–6267, Sep 2000.

[127] Kay Jörg Wiese. Theory and experiments for disordered elastic manifolds, depinning, avalanches, and sandpiles. *Reports on Progress in Physics*, 85(8):086502, aug 2022.

[128] Thierry Giamarchi. *Disordered Elastic Media*, pages 2019–2038. Springer New York, New York, NY, 2009.

[129] James P. Sethna, Karin A. Dahmen, and Olga Perkovic. Random-field ising models of hysteresis. *arXiv: Materials Science*, pages 107–179, 2004.

[130] Karin Dahmen and James P. Sethna. Hysteresis, avalanches, and disorder-induced critical scaling: A renormalization-group approach. *Phys. Rev. B*, 53:14872–14905, Jun 1996.

[131] Olga Perkovic, Karin A. Dahmen, and James P. Sethna. Disorder-induced critical phenomena in hysteresis: A numerical scaling analysis, 1996.

[132] Djordje Spasojević, Sanja Janićević, and Milan Knežević. Numerical evidence for critical behavior of the two-dimensional nonequilibrium zero-temperature random field ising model. *Phys. Rev. Lett.*, 106:175701, Apr 2011.

[133] Saroj Kumar Nandi, Giulio Biroli, and Gilles Tarjus. Spinodals with disorder: From avalanches in random magnets to glassy dynamics. *Phys. Rev. Lett.*, 116:145701, Apr 2016.

[134] K Binder. Theory of first-order phase transitions. *Reports on Progress in Physics*, 50(7):783, jul 1987.

[135] Hong Ji and Mark O. Robbins. Percolative, self-affine, and faceted domain growth in random three-dimensional magnets. *Phys. Rev. B*, 46:14519–14527, Dec 1992.

[136] Liheng Yao and Robert L Jack. Thermal vestiges of avalanches in the driven random field ising model. *Journal of Statistical Mechanics: Theory and Experiment*, 2023(2):023303, feb 2023.

[137] Misaki Ozawa, Ludovic Berthier, Giulio Biroli, and Gilles Tarjus. Role of fluctuations in the yielding transition of two-dimensional glasses. *Phys. Rev. Res.*, 2:023203, May 2020.

[138] Saverio Rossi, Giulio Biroli, Misaki Ozawa, Gilles Tarjus, and Francesco Zamponi. Finite-disorder critical point in the yielding transition of elastoplastic models. *Phys. Rev. Lett.*, 129:228002, Nov 2022.

[139] Damien Vandembroucq and Stéphane Roux. Mechanical noise dependent aging and shear banding behavior of a mesoscopic model of amorphous plasticity. *Phys. Rev. B*, 84:134210, Oct 2011.

[140] Jean-Christophe Baret, Damien Vandembroucq, and Stéphane Roux. Extremal model for amorphous media plasticity. *Phys. Rev. Lett.*, 89:195506, Oct 2002.

[141] Zoe Budrikis, David Fernández Castellanos, Stefan Sandfeld, Michael Zaiser, and Stefano Zapperi. Universal features of amorphous plasticity. *Nature Communications*, 15928:1–10, 07 2017.

[142] Alexandre Nicolas, Kirsten Martens, Lydéric Bocquet, and Jean-Louis Barrat. Universal and non-universal features in coarse-grained models of flow in disordered solids. *Soft matter*, 10 26:4648–61, 2014.

[143] Jie Lin, Thomas Gueudré, Alberto Rosso, and Matthieu Wyart. Criticality in the approach to failure in amorphous solids. *Phys. Rev. Lett.*, 115:168001, Oct 2015.

[144] Jie Lin, Edan Lerner, Alberto Rosso, and Matthieu Wyart. Scaling description of the yielding transition in soft amorphous solids at zero temperature. *Proceedings of the National Academy of Sciences*, 111:14382–14387, 10 2014.

[145] Jack T. Parley, Srikanth Sastry, and Peter Sollich. Mean-field theory of yielding under oscillatory shear. *Phys. Rev. Lett.*, 128:198001, May 2022.

[146] Chen Liu, Ezequiel E. Ferrero, Eduardo A. Jagla, Kirsten Martens, Alberto Rosso, and Laurent Talon. The fate of shear-oscillated amorphous solids. *The Journal of Chemical Physics*, 156(10):104902, 2022.

[147] Ezequiel Ferrero and Eduardo A. Jagla. Criticality in elastoplastic models of amorphous solids with stress-dependent yielding rates. *Soft matter*, 2019.

[148] I. Fernández Aguirre and E. A. Jagla. Critical exponents of the yielding transition of amorphous solids. *Phys. Rev. E*, 98:013002, Jul 2018.

[149] Guillemette Picard, Armand Ajdari, François Lequeux, and Lyderic Bocquet. Elastic consequences of a single plastic event: A step towards the microscopic modeling of the flow of yield stress fluids. *The European physical journal. E, Soft matter*, 15:371–81, 01 2005.

[150] Botond Tyukodi, Damien Vandembroucq, and Craig E. Maloney. Avalanches, thresholds, and diffusion in mesoscale amorphous plasticity. *Phys. Rev. E*, 100:043003, Oct 2019.

[151] Zoe Budrikis and Stefano Zapperi. Avalanche localization and crossover scaling in amorphous plasticity. *Phys. Rev. E*, 88:062403, Dec 2013.

[152] Armand Barbot, Matthias Lerbinger, Anier Hernandez-Garcia, Reinaldo García-García, Michael L. Falk, Damien Vandembroucq, and Sylvain Patinet. Local yield stress statistics in model amorphous solids. *Phys. Rev. E*, 97:033001, Mar 2018.

[153] Armand Barbot, Matthias Lerbinger, Anaël Lemaître, Damien Vandembroucq, and Sylvain Patinet. Rejuvenation and shear banding in model amorphous solids. *Phys. Rev. E*, 101:033001, Mar 2020.

[154] Neng Wang, Jun Ding, F. Yan, Mark Asta, Robert Ritchie, and Lin Li. Spatial correlation of elastic heterogeneity tunes the deformation behavior of metallic glasses. *Computational Materials Science*, 4:19, 04 2018.

[155] Alexandre Nicolas and Jörg Rottler. Orientation of plastic rearrangements in two-dimensional model glasses under shear. *Phys. Rev. E*, 97:063002, Jun 2018.

[156] David Fernández Castellanos, Stéphane Roux, and Sylvain Patinet. Insights from the quantitative calibration of an elasto-plastic model from a lennard-jones atomic glass. *Comptes Rendus. Physique*, 22(S3):135–162, 2021.

[157] Chen Liu, Suman Dutta, Pinaki Chaudhuri, and Kirsten Martens. Elastoplastic approach based on microscopic insights for the steady state and transient dynamics of sheared disordered solids. *Phys. Rev. Lett.*, 126:138005, Apr 2021.

[158] Anaël Lemaître, Chandana Mondal, Michael Moshe, Itamar Procaccia, Saikat Roy, and Keren Screiber-Re'em. Anomalous elasticity and plastic screening in amorphous solids. *Phys. Rev. E*, 104:024904, Aug 2021.

[159] E. A. Jagla, François P. Landes, and Alberto Rosso. Viscoelastic effects in avalanche dynamics: A key to earthquake statistics. *Phys. Rev. Lett.*, 112:174301, Apr 2014.

[160] Anaël Lemaître. Structural relaxation is a scale-free process. *Phys. Rev. Lett.*, 113:245702, Dec 2014.

[161] Hua Tong, Shiladitya Sengupta, and Hajime Tanaka. Emergent solidity of amorphous materials as a consequence of mechanical self-organisation. *Nature communications*, 11:4863, 09 2020.

[162] Chen Liu. *Critical dynamics at the yielding transition and creep behavior of amorphous systems: mesoscopic modeling.* PhD thesis, Université Grenoble Alpes, 2016.

[163] Misaki Ozawa, Ludovic Berthier, Giulio Biroli, and Gilles Tarjus. Rare events and disorder control the brittle yielding of well-annealed amorphous solids. *Phys. Rev. Research*, 4:023227, Jun 2022.

[164] Jean-Yves Fortin and Maxime Clusel. Applications of extreme value statistics in physics. *Journal of Physics A: Mathematical and Theoretical*, 48(18):183001, 2015.

[165] Ashivni Shekhawat, Stefano Zapperi, and James P. Sethna. From damage percolation to crack nucleation through finite size criticality. *Phys. Rev. Lett.*, 110:185505, Apr 2013.

[166] Chandana Mondal, Michael Moshe, Itamar Procaccia, and Saikat Roy. Dipole screening in pure shear strain protocols of amorphous solids, 2023.

[167] Hong Ji and Mark O. Robbins. Transition from compact to self-similar growth in disordered systems: Fluid invasion and magnetic-domain growth. *Phys. Rev. A*, 44:2538–2542, Aug 1991.

[168] Belita Koiller, Hong Ji, and Mark O. Robbins. Effect of disorder and lattice type on domain-wall motion in two dimensions. *Phys. Rev. B*, 46:5258–5265, Sep 1992.

[169] Misaki Ozawa and Giulio Biroli. Elasticity, facilitation and dynamic heterogeneity in glass-forming liquids, 2022.

[170] Olga Perković, Karin A. Dahmen, and James P. Sethna. Disorder-induced critical phenomena in hysteresis: Numerical scaling in three and higher dimensions. *Phys. Rev. B*, 59:6106–6119, Mar 1999.

[171] Jishnu N. Nampoothiri, Kabir Ramola, Sanjib Sabhapandit, and Bulbul Chakraborty. Gaps between avalanches in one-dimensional random-field ising models. *Phys. Rev. E*, 96:032107, Sep 2017.

[172] Saverio Rossi and Gilles Tarjus. Emergence of a random field at the yielding transition of a mean-field elasto-plastic model. *Journal of Statistical Mechanics: Theory and Experiment*, 2022(9):093301, sep 2022.

[173] Anaël Lemaître and Christiane Caroli. Plastic response of a 2d amorphous solid to quasi-static shear : Ii - dynamical noise and avalanches in a mean field model, 2007.

[174] E A Jagla. The prandtl–tomlinson model of friction with stochastic driving. *Journal of Statistical Mechanics: Theory and Experiment*, 2018(1):013401, jan 2018.

[175] E. E. Ferrero and E. A. Jagla. Elastic interfaces on disordered substrates: From mean-field depinning to yielding. *Phys. Rev. Lett.*, 123:218002, Nov 2019.

[176] Botond Tyukodi, Sylvain Patinet, Stéphane Roux, and Damien Vandembroucq. From depinning transition to plastic yielding of amorphous media: A soft-modes perspective. *Phys. Rev. E*, 93:063005, Jun 2016.

[177] A. Alan Middleton. Asymptotic uniqueness of the sliding state for charge-density waves. *Phys. Rev. Lett.*, 68:670–673, Feb 1992.

[178] M. L. Rosinberg and T. Munakata. Hysteresis and complexity in the mean-field random-field ising model: The soft-spin version. *Phys. Rev. B*, 79:174207, May 2009.

[179] M L Rosinberg and G Tarjus. A statistical mechanical description of metastable states and hysteresis in the 3d soft-spin random-field model at t = 0. *Journal of Statistical Mechanics: Theory and Experiment*, 2010(12):P12011, dec 2010.

[180] Francisco-José Pérez-Reche, Lev Truskinovsky, and Giovanni Zanzotto. Driving-induced crossover: From classical criticality to self-organized criticality. *Phys. Rev. Lett.*, 101:230601, Dec 2008.

[181] Hudson Borja da Rocha and Lev Truskinovsky. Rigidity-controlled crossover: From spinodal to critical failure. *Phys. Rev. Lett.*, 124:015501, Jan 2020.

[182] Hudson Borja da Rocha and Lev Truskinovsky. Mean field fracture in disordered solids: Statistics of fluctuations. *Journal of the Mechanics and Physics of Solids*, 158:104646, 2022.

[183] Ian Williams, Erdal C. Oğuz, Hartmut Löwen, Wilson C. K. Poon, and C. Patrick Royall. The rheology of confined colloidal hard disks. *The Journal of Chemical Physics*, 156(18), 05 2022. 184902.

[184] Peter Morse, Sudeshna Roy, Elisabeth Agoritsas, Ethan Stanifer, Eric Corwin, and M. Lisa Manning. A direct link between active matter and sheared granular systems. *Proceedings of the National Academy of Sciences of the United States of America*, 118, 05 2021.

[185] Botond Tyukodi. *A depinning approach of amorphous plasticity and dewetting.* PhD thesis, Université Pierre et Marie Curie, 2016.

[186] Kirsten Martens, Lydéric Bocquet, and Jean-Louis Barrat. Spontaneous formation of permanent shear bands in a mesoscopic model of flowing disordered matter. *Soft Matter*, 8:4197–4205, 2012.

[187] Ratul Dasgupta, H. George E. Hentschel, and Itamar Procaccia. Yield strain in shear banding amorphous solids. *Phys. Rev. E*, 87:022810, Feb 2013.

[188] James W. Cooley and John W. Tukey. An algorithm for the machine calculation of complex fourier series. *Mathematics of Computation*, 19:297–301, 1965.

[189] Michael T. Heideman, Don H. Johnson, and C. Sidney Burrus. Gauss and the history of the fast fourier transform. *Archive for History of Exact Sciences*, 34:265–277, 1985.

[190] Matteo Frigo and Steven G. Johnson. The design and implementation of FFTW3. *Proceedings of the IEEE*, 93(2):216–231, 2005. Special issue on "Program Generation, Optimization, and Platform Adaptation".

[191] K. Michael Salerno and Mark O. Robbins. Effect of inertia on sheared disordered solids: Critical scaling of avalanches in two and three dimensions. *Phys. Rev. E*, 88:062206, Dec 2013.

[192] Chen Liu, Ezequiel E. Ferrero, Francesco Puosi, Jean-Louis Barrat, and Kirsten Martens. Driving rate dependence of avalanche statistics and shapes at the yielding transition. *Phys. Rev. Lett.*, 116:065501, Feb 2016.

[193] Jie Lin, Alaa Saade, Edan Lerner, Alberto Rosso, and Matthieu Wyart. On the density of shear transformations in amorphous solids. *Europhysics Letters*, 105(2):26003, feb 2014.